CosmicRayGroup
Dept. of Physics, Kyoto Univ

March 2004

A high altitude observation for sub 100 GeV gamma-rays

Akihiro Asahara

Department of Physics, Graduate School of Science, Kyoto University, Sakyo-ku, Kyoto, 606-8502, Japan

Abstract

The energy spectrum of a gamma-ray pulsar has a cutoff at at high energies, due to physical phenomenon occurring in the pulsar magnetosphere. This cutoff energy is inferred from models which predict different values for the same pulsar, between 5 - 200 GeV. Thus, this energy region is quite important to study the emission mechanism of gamma-rays emitted from pulsars. However, only a few detectors have been exploring in this energy region until now.

The performance of a single gamma-ray telescope is discussed based on the Imaging Atmospheric ČerenkovTechnique (IACTech) at high altitudes. Observations at a high altitude are quite suitable for the IACTech because the density of Čerenkovlight caused by gamma-rays is several-times larger than at sea level. To observe gamma-ray pulsars at high altitude, a gamma-ray camera, designated CheSS (Čerenkovlight detecting System on Subaru) based on the IACT, has been developed for the Subaru infrared-optical telescope at an altitude of 4200 m. Using CheSS, the Crab nebula/pulsar was observed for three days in December 2001. From a comparison between the simulated and observed shower events, it was found that the Night-Sky Background (N.S.B.) and muon showers have significant effects on the detection rate below 80 GeV in spite of the small Field Of View (FOV) of CheSS (0.75 degrees). The simulated spectrum, which includes muon shower events, is consistent with the observed spectrum.

Based on this study, the performance of a camera with a larger FOV of 3.0 degrees is discussed. Although the effects of muon showers and the N.S.B. become serious, the simulation results indicate that an 8.2 m IACT with a FOV of 3.0 degrees at an altitude of 4200 m could detect 15 GeV energy gamma-rays.

Contents

Chapter1

Gamma-ray astronomy for Pulsars

> "If you knew Time as well as I do," said the Hatter, "you wouldn't talk about wasting *it*. It's *him*."
>
> "I don't know what you mean," said Alice.
>
> "Of course you don't!" the Hatter said, tossing his head contemptuously. "I dare say you never even spoke to Time!"
>
> "Perhaps not," Alice cautiously replied; "but I know I have to beat time when I learn music." — *A Mad Tea-Party* —

The discovery of the first radio pulsar, PSR B1919+21, triggered further large-scale search for pulsars. Recently, more than 1500 pulsars have been known in the radio band, and we have ~ 50 positive detections in X-rays. However, in gamma-ray band, we have known only 10 pulsars which is detected by the Compton Gamma-Ray Observatory (*CGRO*). Seven pulsars of them have the high confidence level (*the major seven*) and other three pulsars have the moderate significance.

Six of pulsars detected by *EGRET* on-board *CGRO* show a clear evidence of pulsed emission above 100 MeV. Spectral energy distributions (SED) of the emission from the high-energy pulsars peak in the hard x-ray or gamma-ray range, and a few of them show the break around 1 GeV energies. Therefore, the energy region above 10 GeV is quite important to study the emission mechanism of gamma-ray pulsars.

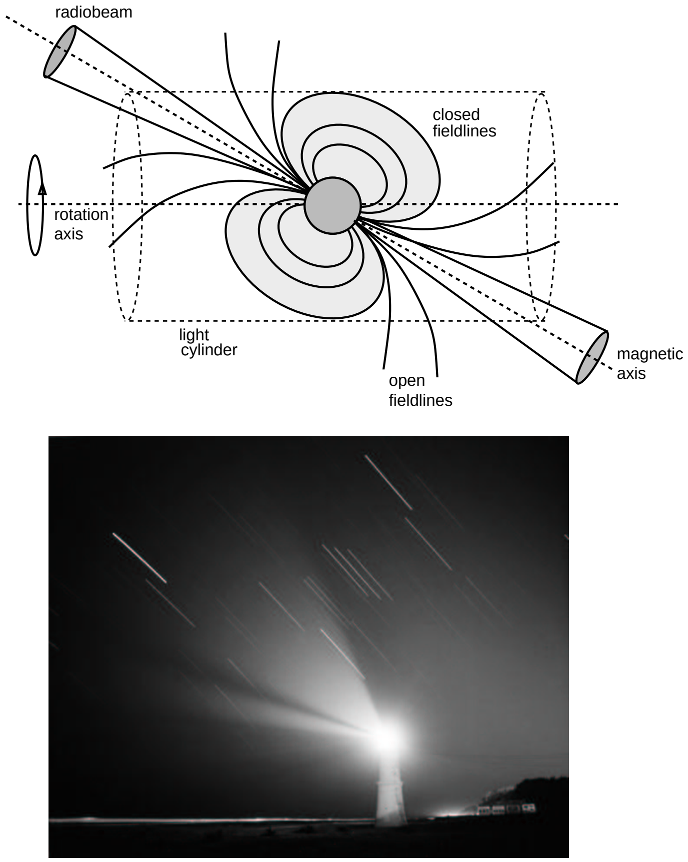

Figure 1.1: Top: schematic diagram of the rotating neutron star model (or "lighthouse model") for pulsar emission. Bottom: Real lighthouse,"kaketuka tohdai".

§ 1 What is pulsar ?

First Pulsar was discovered in late 1967 by Jocelyn Bell Burnell as radio sources which blink on and off at a constant frequency (Hewish et al. 1968). Now we observe the brightest ones (e.g. the Crab pulsar) at almost every wavelength of light. Pulsars are spinning neutron stars that have jets of particles moving almost at the speed of light streaming out their two magnetic poles. These jets produce very powerful beams of photon. It is generally accepted that the magnetic and rotational axes of a pulsar are also misaligned, and thus, the beam of light from the jet sweeps around as the pulsar rotates, just as the spotlight in a lighthouse does (Fig. 1.1). We see pulsars turn on and off as the beam sweeps over the Earth.

Why can we assure that pulsars are neutron stars ? The characteristics of pulsars are following:

- The pulse period distributes between 0.001 and 10 sec (Fig. 1.2).
- The integrated pulse profiles occupy between 2 % and 10 % of the period, and thus the time width of each pulse is quite small (Fig. 1.3).
- The pulse periodicity is extremely regular; $P/\dot{P} \sim 10^{11}$.
- Period increase very slowly, and never decrease, except for occasional "glitches" (see section § 2).

In a time 0.001 sec light travels roughly 300 km. This sets an upper limit to the size of the emitting region. The so-called compact stars, white dwarfs or neutron stars are candidates of pulsars, and three possibilities immediately are suggested: rotation, vibration, or a binary system.

1. The rotating white dwarfs should satisfy

$$\Omega^2 R \sim \frac{GM}{R^2}, \tag{1.1}$$

where Ω is the angular velocity of rotation. This equation is rewritten in terms of the mean density ρ as

$$\Omega^2 \sim G\rho. \tag{1.2}$$

Taking a maximum mean density of 10^8 g cm^{-3} gives a period

$$P = \frac{2\pi}{\Omega} > 1 \text{ sec.} \tag{1.3}$$

This result rules out rotating white dwarfs.

2. Consider the vibrating white dwarfs. Accurate calculations show that the shortest period for the fundamental mode is $\sim$ 2 sec(Shapiro and Saul 1983). Higher harmonics could have shorter periods, but are ruled out for two reason: first, it requires special conditions to excite a harmonic without exciting the fundamental mode. Any small nonlinearity will lead to mixing and destroy the sharpness of the period. Second, the loss of energy in a vibrating system usually leads to a decrease in the period.

3. The density of a neutron star are $\sim 10^6$ times larger than that of a white dwarf. Thus the fundamental mode of a vibrating neutron star is $\sim 10^{-3}$. This is too short.

4. Binary white dwarfs should satisfy

$$\Omega^2 r \sim \frac{GM}{r^2}, \tag{1.4}$$

where r is the orbital radius. Since r > R, we again recover the result (1.3).

5. The binary neutron star system can have the period in the observed range between 0.1 and 2.5 sec by a suitable choice of radius. However, such a system would be a copious emitter of gravitational waves(Weber 1960), with a lifetime

$$\tau \sim 10^{-3} \ \ \mathrm{yr} \ \left(\frac{P}{1 \ \mathrm{sec}}\right)^{8/3}. \tag{1.5}$$

The timescale on which pulsar periods are observed to change is typically $P/\dot{P} \sim 10^4$ yr. In addition, gravitational wave emission causes the period to decrease, not increase.

Consequently, only a rotating neutron start meets all the above objections.

§ 2 Pulsar 101

Pulsars are strongly magnetized and fast rotating neutron stars, with a mass of M $\sim 1.4\mathrm{M}_\odot$, a radius of R $\sim$ 15 km, and periods from 1 ms to 10 seconds. In this section, we review the basic properties of pulsars.

2.1 Period

The periods of all pulsars known at present range within the interval 1 ms to 10 sec. Most of them lies between 0.3 sec and 1.5 sec, as shown in Fig.1.2. The mean period of a pulsar is constant up to six and more digits. For example, the period of the Crab pulsar is measured by

$$P = 0.0335312051841 \cdots \quad [\mathrm{sec}]. \tag{1.6}$$

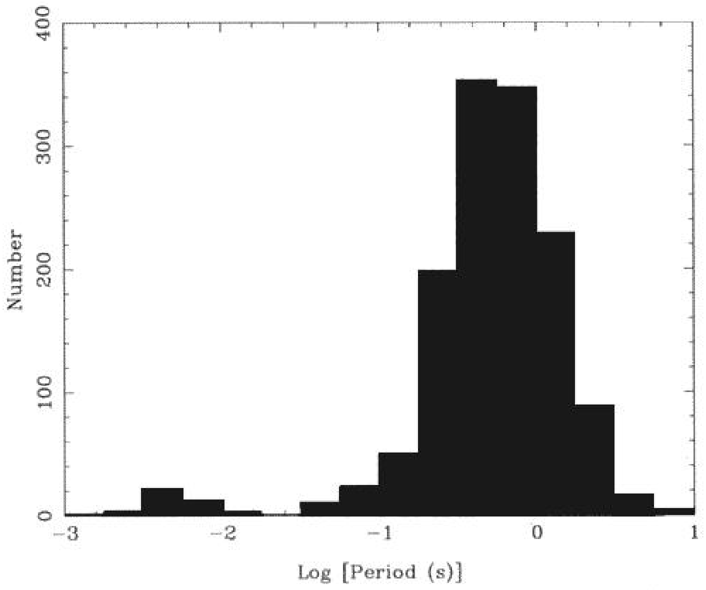

Figure 1.2: The distribution of the periods of pulsars(Manchester 2003).

Fluctuations of pulsar period are random, but characteristic values of RMS deviations do not usually amount to more than several milliseconds (Lyne and Smith 1998). The statistical analysis shows that this activity is represented by unresolvable "glitches" of the phase, period P and period derivative $\dot{P}$ (Downs 1982). "glitches" are observed in ~ 20 young pulsars (Shemar and Lyne 1996), and during a glitch event, the pulsar period decreases in a step function, with amplitude from a few parts in 10^9 to a part in 10^6. At the same time, the spin-down rate increases, and the pulsar recovers over a time period of weeks to months to a period close to the pre-glitch value. Smaller glitches may be caused by a sudden cracking of the crust of the neutron star and its relaxation to a more spherical shape; larger glitches are probably due to variations in the coupling between the super-fluid interior of the star and its independently rotating crust(Cordes et al. 1988). These fluctuations are, however, not large. Therefore, pulsars are exceedingly exact clocks. Indeed, some millisecond pulsars are more stable than existing atomic clocks (Fig. 1.4).

It is exceedingly significant that the period of all pulsars is regularly increasing. The period increase rate $\dot{P}$ is stable and ranges between 10^{-14} and 10^{-16} for most pulsars. Some of pulsars in globular clusters have the small negative values of $\dot{P}$.

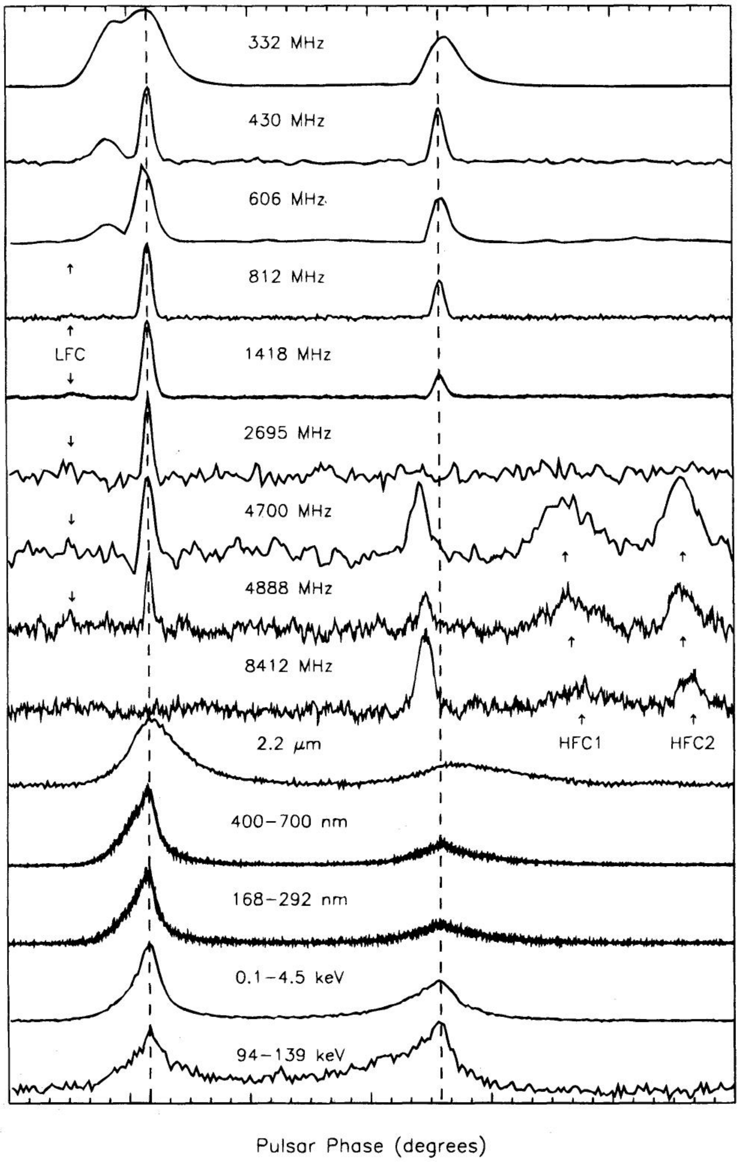

Figure 1.3: Pulse profile for the Crab Pulsar over the radio range 322 MHz to 8.4 GHz, with profiles at infrared, optical, UV, and X-ray (Moffett and Hankins 1996).

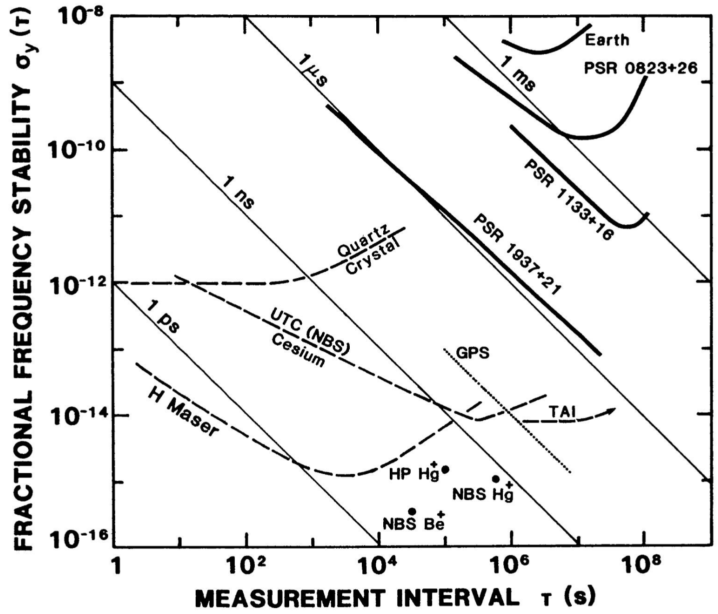

Figure 1.4: Fractional frequency stability. The heavy solid lines give estimates of the fractional frequency stability of the rotation of the Earth based on UT1 mesurements and of several pulsars. The dashed lines give the stabilities of several laboratory standards and International Atomic Time (TAI). The dotted line gives the stability of the Global Positioning System (GPS). Circles indicate the stability of seeral trapped-ion atomic clocks(Backer and Hellings 1986).

For example, PSR B2127+11 in the globular cluster M15 has $\dot{P} = -(20 \pm 1) \times 10^{-18}$ (Wolszczan et al. 1989). This $\dot{P}$ value is obviously due to the Doppler shift caused by the neuron star's acceleration in the globular cluster and is not connected with the real pulsar rotation acceleration(Beskin et al. 1993).

2.2 Distance

Most of the pulsars are strongly concentrated about the Milky Way . In other words, they are sources in the disk of our spiral galaxy and are seen at distances comparable to the thickness of that disk, and thus the distance is roughly several hundred pc.

If the source moves across the sky relative to the background stars at an appreciable rate (proper motion), it must be quite close. The same follows if it moves back and forth relative to very distant stars as the Earth orbits the Sun (parallax). However, most of the pulsars have neither detectable parallax nor proper motion.

The pulsed nature of the pulsar emission together with the slightly dispersive nature of the interstellar medium combine to provide an index (the Dispersion Measure, DM), which allows the distance estimates to be made for individual pulsars. The index of the refraction of a plasma is just

$$n = \left(1 - \frac{\omega_p^2}{\omega^2}\right)^{1/2} \sim 1 - \frac{\omega_p^2}{2\omega^2}, \tag{1.7}$$

where ω_p is the plasma frequency:

$$\omega_p^2 \equiv \frac{4\pi n_e e^2}{m_e}, \tag{1.8}$$

and in practical units

$$\omega_p \sim 5.64 \times 10^4 n_e^{1/2} \quad \text{[rad/s]}, \tag{1.9}$$

with n_e the electron density in electrons/cm^3. This form for the index of refraction neglects finite temperature and magnetic fields. However, it is an excellent approximation for the low densities and weak field strengths appropriate for the interstellar medium. Typical value for n_e are determined to be about 0.03 cm^{-3}, giving $\omega_p \sim 10^4$ rad/s. Since the index of refraction is less than unity, the phase velocity slightly exceeds the velocity of light and the group velocity is slightly less,

$$v_g = nc \sim \left(1 - \frac{\omega_p^2}{2\omega^2}\right) c = \left(1 - \frac{n_e e^2}{2\pi m_e \nu^2}\right) c. \tag{1.10}$$

Consequently, a sharp pulse of radio emission is dispersed, and thus the high frequency components reach the Earth before the low frequency components. The travel time T over distance L is,

$$T = \int_0^L \frac{dl}{v_g} \sim \frac{L}{c} + \frac{e^2 \int_0^L n_e dl}{2\pi m_e c \nu^2} = \frac{L}{c} + 1.345 \times 10^{-3} \nu^{-2} \int_0^L n_e dl \quad [\mathrm{s}]. \tag{1.11}$$

The first term here is just the free space travel time and the second is the additional dispersive delay t. Customary units in astrophysics are parsecs (3×10^{18} cm) for distance and cm^{-3} for density: the integral $\int_0^L n_e dl$, which measures the total electron content between the pulsar and the observer, is known as DM with units cm^{-3} pc. Observers usually quote radio frequencies in megahertz, so that the delay t becomes,

$$t = \frac{\mathrm{DM}}{2.410 \times 10^{-4} \nu_M^2 \ \mathrm{Hz}} \quad [\mathrm{s}]. \tag{1.12}$$

For example, from the measured delay t at various radio bands, the DM for the Crab pulsar is 57 pc cm^{-3}. Although the distance calculated by the DM depends on n_e models, we can find the distance to the Crab pulsar is about $\sim$ 2 kpc. The Crab pulsar is in the center of a supernova remnant. The distance to this remnant is known since it is young enough[1] to expand perceptibly in a few years, and the Doppler shift of radiating filaments moving toward and away from us can also be measured. These two pieces of information immediately give the distance to the nebula, which come out to be about 2 kpc (Trimble 1968). This is consistent with the distance calculated by the DM.

2.3 Magnetic field

To estimate the magnetic field on the surface of a pulsar, we discuss the magnetic dipole model that accounts for many observed properties of pulsars. In order to

---

[1] 950 years since its apparent origin in the supernova of 1054.

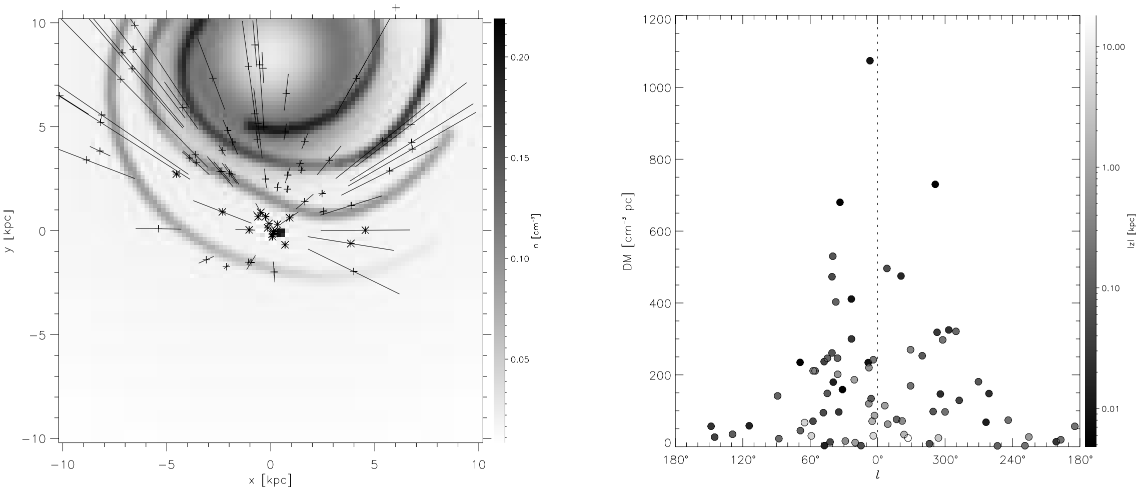

Figure 1.5: Projection of the positions of the pulsars onto the Galactic plane (Gómez et al. 2001). Uncertainties in the distance from the Sun are also shown. The location and density of the spiral arms, central annulus, and Gum Nebula in the Taylor-Cordes model are noted in gray scale. Pulsars marked with a star are those considered to be in the "interarm direction" as seen from the Sun, although this neglects the potential contribution of the Local arm.

produce pulsed radiation from the magnetic poles of the neutron star, the magnetic dipole must be oriented at an angle with respect to the rotation axis(Lyne and Smith 1998), and then the magnetic dipole displays a varying dipole moment at a large distance.This results in the radiation of electromagnetic energy from the dipole, which is extracted from the rotational energy of the neutron star.

A magnetic dipole, of magnetic dipole moment p_m, radiates electromagnetic radiation at a rate

$$-\frac{dE}{dt} = -\frac{2|\ddot{\boldsymbol{P}}_m|^2}{3c^3}. \tag{1.13}$$

Writing

$$\boldsymbol{P}_m = \frac{1}{2}B_pR^3(\boldsymbol{e}_{||}\cos\alpha + \boldsymbol{e}_{\perp}\sin\alpha\cos\Omega t + \boldsymbol{e}'_{\perp}\sin\alpha\sin\Omega t), \tag{1.14}$$

where α is the angle between the rotation axis and the magnetic axis, $\boldsymbol{e}_{||}$ is a unit vector parallel to the rotation axis, $\boldsymbol{e}_{\perp}$ and $\boldsymbol{e}'_{\perp}$ are fixed mutually orthogonal unit vectors perpendicular to $\boldsymbol{e}_{||}$. Equation 1.14 substitutes Eq. 1.13, and then we can find

$$-\frac{dE}{dt} = \frac{{B_p}^2\ R^6\ \Omega^4\sin^2\alpha}{6c^3}\ . \tag{1.15}$$

Let us turn to the calculation of the rotational energy loss. Using the moment of inertia of the neutron star I, we can write the rotational energy loss,

$$E_{rot} = \frac{1}{2}I\Omega^2\ . \tag{1.16}$$

Thus,

$$-\frac{dE_{rot}}{dt} = -I\Omega\dot{\Omega}\ . \tag{1.17}$$

Now, if we assume that the magnetic dipole radiation extracts rotational energy from the neutron star, we can estimate the magnetic field at the surface of a neutron star using Eqs. 1.15 and 1.17,

$$-I\Omega\dot{\Omega} = \frac{{B_p}^2\ R^6\ \Omega^4\sin^2\alpha}{6c^3} \tag{1.18}$$

$$B_p = 2\times10^5\cdot\frac{\sqrt{IP\dot{P}}}{R^3\sin\alpha}\quad[\mathrm{G}] \tag{1.19}$$

Assuming the following typical values for neutron stars: $R = 10$km, $I = 10^{45}$ gcm^2, $\alpha = 30$ degree, and then Eq.1.19 gives

$$B_p = 3.1\times10^{19}\ \sqrt{P\dot{P}}\quad[\mathrm{G}], \tag{1.20}$$

or about 10^{12} gauss for typical parameters ($P \sim 1s$; $\dot{P} \sim 10^{-15}$).

Let us suppose that the radius of the Sun collapses from 7×10^5 km to 10 km. The general magnetic field of the Sun is uncertain, but should be $\sim 10^2$ G. The magnetic flux, $\oint BdS$, must be conserved, and thus

$$B(R = R_\odot) \ \rightarrow \ B(R = 10 \text{ km}) \sim 10^2 \times \left(\frac{7 \times 10^5}{10}\right)^2 = 5 \times 10^{11} \quad [\text{G}]. \tag{1.21}$$

This estimation is quite simple, but well consistent with the magnetic dipole model.

The dipole magnetic field generated by $\boldsymbol{m}$ is

$$\boldsymbol{H} = \frac{3\boldsymbol{e}_r(\boldsymbol{m} \cdot \boldsymbol{e}_r) - \boldsymbol{m}}{r^3} \tag{1.22}$$

at the distance r. That is a textbook equation of the basic electro-magnetics(Sunagawa 1964). Using the polar coordinate, we can write

$$H_r = \frac{2m\cos\theta}{r^3}, \quad H_\theta = \frac{m\sin\theta}{r^3} \ . \tag{1.23}$$

Here, we defined the "light cylinder" as the radius where objects co-rotate with the pulsar at the light speed; $r_L = c/\Omega$. We substitute r_L for Eq. 1.15, and then

$$\frac{dE}{dt} = 4\pi {r_L}^2 \cdot c \cdot \frac{{B_p}^2 \ R^6 \sin^2\alpha}{24\pi {r_L}^6} \ . \tag{1.24}$$

The magnetic field strength is $H(r) \sim |\boldsymbol{m}|/r^3$, and thus

$$\frac{dE}{dt} \sim 4\pi {r_L}^2 \cdot c \cdot \frac{H(r_L)^2}{8\pi}. \tag{1.25}$$

$H(r_L)^2/8\pi$ is the energy density of the magnetic field at the light cylinder. Therefore, This equation implies that the magnetic energy flows from the region of $4\pi {r_L}^2$ at the light speed.

2.4 The breaking index and charactristic age

It is generally accepted that a pulsar is formed with a high angular velocity Ω_i, subsequently evolving according to a simple power law

$$\dot{\Omega} = -k\Omega^n \tag{1.26}$$

where k is a constant and n is referred to as the "braking index". Integration of Eq.1.26 gives the relation between Ω, $\dot{\Omega}$ and the age, t:

$$t = -\frac{\Omega}{(n-1)\dot{\Omega}}\left(1 - \frac{\Omega^{n-1}}{\Omega_i^{n-1}}\right). \tag{1.27}$$

Assuming $n \neq 1$, and $\Omega_i >> \Omega$, we can approximate to a characteristic age τ given by

$$\tau = -\frac{1}{(n-1)}\frac{\Omega}{\dot{\Omega}} = \frac{1}{(n-1)}\frac{P}{\dot{P}}. \tag{1.28}$$

According to Eq. 1.18, $\dot{\Omega} \propto \Omega^3$. Therefore, for the magnetic dipole braking, the braking index equals to 3, and it gives a characteristic age $\tau = P/2\dot{P} = -\nu/2\dot{\nu}$; this is the accepted definition of characteristic age, even though the braking index of n may differ from 3. The nominal parameters ($P \sim 1s; \dot{P} \sim 10^{-15}$) give the characteristic lifetime, $\sim 6 \times 10^6$ years. Since the total number of pulsars in our Galaxy is estimated by 5×10^4(Lyne and Smith 1998), one pulsar must form every $\sim$ 100 years. The estimated rate of core collapse supernova explosions (Type II and Type Ib/c) in the Galaxy is one every 20 - 50 years(Woltjer 1968). Since not all SN may produce pulsars, the birth rate of pulsars we estimated above seems to be consistent with the rate of supernova explosions. However, we have to pay attention that the both estimated rates have many uncertainties.

Differentiation of the spin-down law (Eq. 1.26) shows that a direct measurement of breaking index n is possible if the second differential can be measured,

$$n = \frac{\Omega\ddot{\Omega}}{\dot{\Omega}^2} = 2 - \frac{P\ddot{P}}{\dot{P}^2}. \tag{1.29}$$

However, there are only a few pulsars of which second differentials have been measured. Significant values have been found for the Crab pulsar, $n = 2.515 \pm 0.005$ (Lyne et al. 1988)). The deviations from the value $n = 3$ expected for purely magnetic dipole radiation may indicate that part of the torque on the pulsar is due to outflow of particles.

§ 3 Gamma-ray pulsars

The telescopes on the Compton Gamma Ray Observatory, *BATSE*(10keV - 1 MeV), *OSSE*(10 keV - 100 keV), *COMPTEL*(1 MeV - 10 MeV), and *EGRET*(100MeV - 1GeV), identified a number of gamma-ray pulsars, seven of them with very high confidence and others with less certainty(Thompson 2004). The weakest (PSR B1951+32) among the major 7 has the statistical probability of occurring by chance of $\sim 10^{-9}$. Not all seven pulsars are seen at the highest energies. PSR B1509-58 is seen only up to 10 MeV, detected by *COMPTEL*(Kuiper et al. 1999), and not above 100 MeV by *EGRET*. For this reason, the answer to the question, “How many high-energy gamma-ray pulsars are seen ?” is, “at least six.” Table 1.1 shows the specifications of the major 7 pulsars. In this section, we review the observation results of gamma-ray pulsars.

Table 1.1: The property of *major 7* Gamma-ray pulsars(Schönfelder et al. 2000)

Pulsar	P [msec]	$\dot{P}$ [10^{-15}]	Distance [kpc]
Crab	33.34	421.2	2.0
PSR B1509-58	150.65	1537	4.4
Vela	89.29	124.3	0.5
PSR B1706-44	102.4	93.0	1.8
PSR B1951+32	39.53	5.849	2.5
Geminga	237.1	10.98	0.16
PSR B1055-32	197.1	5.8	1.5

3.1 Light curves

The regular brightness variation (“light-curves”) with periods ranging from $\sim$ ms to nearly 10s, was the primary characteristic of pulsars. The light-curve of a pulsar can be regarded as the cross-section through a rotating beaming pattern cut along the line of sight to the observer. The pattern of the light-curves would give us a direct view of the sites of origin and beaming directions, and allow us to derive the luminosity of such a non-isotropic source.

The pattern of light-curves is quite different each pulsar, but we want to construct the singular view for the pulsed emission of each source. At the present moment, we can not do the population study, due to the limited number of detections. However, some common features for the gamma-ray emission from young pulsars become already apparent.

Figure 1.6 displays the lightcurves of the *major 7* gamma-ray pulsars. We note that the pulsed emission extends over more than 50% of rotation and sharp peaks (generally double) limit the pulsed phase interval. The width and dominance of the peaks led to the conventional assumption of a beaming solid angle of 1 str for luminosity estimates. The beaming pattern inferred from these lightcurves at the gamma-ray band is in the shape of a cone with high intensity on the rim and lower levels inside ("hollow cone", shown in Fig.**??**.) (Leahy 2003).

In Fig. 1.6, we can see that the light curves at the high energy band significantly differ from those at the radio band. These multi-wavelength comparisons serve to distinguish different emission processes. For the Crab pulsar, the shape of the double-peaked light-curve remains all over energy bands, but some components in the light-curve is different each energy band: the bridge region between the two peaks and the second peak are very strong only at Hard X/gamma-ray region. In the radio range (Fig. 1.3), we find additional structures besides the two peaks: two trailing peaks around 5 GHz and a so-called precursor peak at frequencies below 400 MHz. We don't have the comprehensive model that can explain this complex spatial and spectral emission, but it is apparent that several components must exist in the radiation zones of the Crab pulsar.

The same double-peak shape is detected for the older pulsars, Vela and Geminga. However, in contrast to the Crab pulsar, the light-curves of these pulsars are completely at different phase angles of emission below the gamma-ray energy, and especially for the Geminga, significant pulsed emission has only been detected in the X- and gamma-ray region. The present optical and radio detections of Geminga

(Shearer et al. 1998; Gil et al. 1998) are considered to be of marginal significance and need to be confirmed.

3.2 Luminosities

The luminosities of most pulsars observed in the high energy band (X-ray and gamma-ray) seem to have a linear relationship with their spin-down luminosities, $L_{sd} \equiv 4\pi^2 I\dot{P}/P^3$ (Becker and Truemper 1997). This relationship suggests that the bulk of the observed pulse X-ray and gamma-ray emissions are indeed emitted at the expense of rotational energy of the neutron star and thus of non-thermal origin. The empirical relation between the X-ray luminosity and the spin down luminosity was found, $L_x \sim 0.001 L_{sd}$(Becker and Truemper 1997), and it also suggests that most of the X-ray emission results from the rotational energy loss. A similar origin was found to the gamma-rays.

However, the detailed physics of energy dissipation through pulsar magnetosphere, such as the broad band synchrotron emission from the radio to the gamma-ray band, has not been understood yet. Indeed, in the recent study, Andrea et al. re-examined the relationship between the L_x and L_{sd} using resent data from *ASCA*, *RXTE*, *Beppo-SAX*, *Chandra*, and *XMM-Newton*, and concluded that L_x is uncorrelated with P and $\dot{P}$.

3.3 Spectra

Thompson et al. have compiled multi-wavelength spectra for the pulsed emission of gamma-ray pulsars as shown in Fig. 1.7. The spectral intensities are displayed in terms of νF_ν , which is equivalent to the power emitted per unit interval of $\ln(\nu)$. The spectra emphasize that emission in the X- and gamma-ray regions dominates the radiation budget of these pulsars and that the pulsed emissions are generally harder than power-laws with index = -2 (which would be a horizontal line in this spectral display). In several cases, the spectra are curved in the gamma-ray range and lead up to a cut-off or turn over at a few GeV. The pulsar spectra are arranged

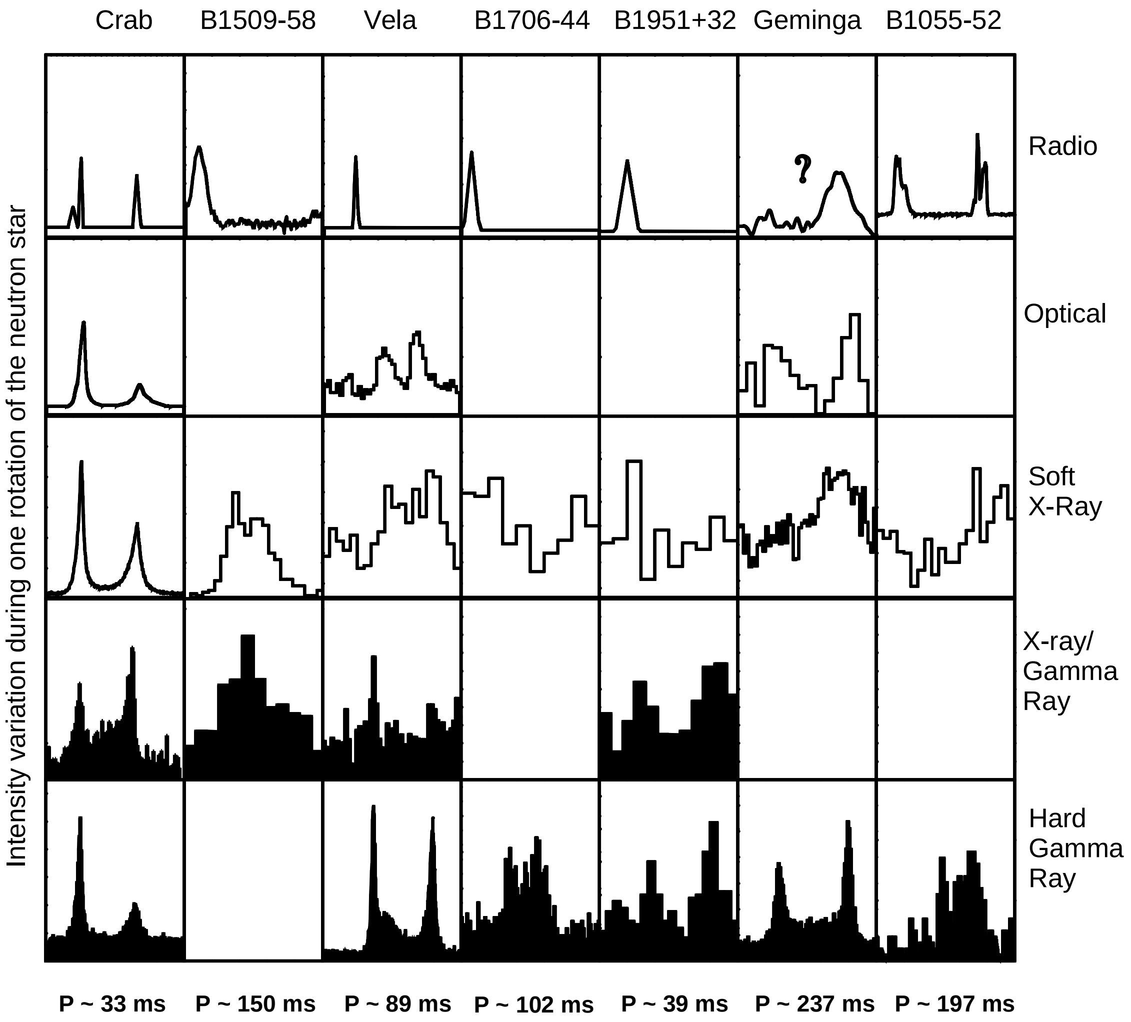

Figure 1.6: Light curves of seven gamma-ray pulsars in five energy bands, from left to right in order of characteristic age. Each panel shows one full rotation of the neutron star(Thompson 2004).

in order of increasing charactristic age ($\tau \sim P/\dot{P}$) with Crab ($\tau \sim 10^3$ year) as the youngest, and PSR B1055-52 ($\tau \sim 5 \times 10^5$ year) as the oldest object. In the following sentence, let us review the spectra of each pulsar briefly.

The Crab pulsar emits the maximum power at about 100 keV and the spectrum can be described by a broad peak extending from the optical band ($\sim$ 1 eV) to about 100 MeV. Above 100 MeV the pulsed spectrum continues with a harder power law distribution up to a few GeV, where the spectrum goes into a steep decline (Kuiper et al. 2001). Above GeV, all instruments report upper limits, and thus we need the instrument which has higher sensitivity.

PSR B1509-58 was first detected in the X-ray band by the *Einstein*(Seward and Harnden 1982), and at the low energy gamma-ray band up to 30 MeV by *BATSE*, *OSSE* and *COMPTEL* (Carraminana and Bennett 1995). *EGRET* may have a marginal detection of this pulsar between 30-70 MeV, but show significant upper limits on the flux above this energy range. This fact indicates that the spectrum must turn over in the $\sim$ 10 MeV range. This low energy cut-off has been explained as an absorption effect for high-energy photons in the strong magnetic field. Indeed, PSR B1509-58 has one of the strongest inferred magnetic fields ($\sim 2 \times 10^{13}$ Gauss). Harding et al. showed that the second order quantum-mechanical process of "photon splitting" ($\gamma \rightarrow \gamma\gamma$) in such a strong magnetic field, would limit the energy of emitted gamma-rays to several tens of MeV(Harding et al. 1997).

The Vela pulsar has a pronounced spectral break at 2 GeV. Since this is a strong and steady gamma-ray emitter, the detailed spectra for the individual phase components (e.g. the peaks and the interpulse emission) are available. The spectra of the emission peaks are generally softer than the spectra of the inter-peak regions. The softest components are observed in the leading and trailing wings of the peaks, which has been explained as a low-energy spill-out from the main gamma-ray cascades in the outer magnetosphere.

PSR B1706-44 was detected by *COS-B* 25 years ago(Swanenburg et al. 1981), and identified in 1992 as a pulsar with a 102 ms pulsation period by *EGRET* (Thompson et al. 1992). The gamma emission forms a single broad peak within the pulsar period, in contrast to the two narrow peaks seen in the other gamma-ray pulsars(Thompson et al. 1992). The maximum power of PSR1706-44 is emitted around 1 GeV. At soft X-ray band, the same pulsation have been found recently. At TeV energies, the unpulsed photons emitted this source is detected by CANGAROO I(Kifune et al. 1995) and II(Kushida 2003), but its pulsation is not found.

PSR B1951+32 is found as a weak gamma-ray source at energies above 300 MeV. After extended *EGRET*observations, the pulsating of B1951+32 was found in gamma-rays at E $>$ 100 MeV with the same 39.5 ms periodicity as in the radio band (Ramanamurthy et al. 1995). Although seen only as a weak source amid the high background of the galactic disk emission, the pulsation in high-energy gamma-rays is clearly seen. The pulsed radiation has a photon spectral index of -1.74 ± 0.11. The spectrum of this pulsar seems to have the characteristic spectral break above several GeV. However, we need to confirm it by other missions because of the limited statistics for this source.

Geminga (PSR B0633+17) has been the most enigmatic gamma-ray source since it was detected by *SAS-2*in 1972 (Maraschi and Treves 1977). These days, *ROSAT*has revealed a 237 ms pulsations in Geminga (Halpern and Holt 1992), and the corresponding gamma-ray signal was found in data from *EGRET*, *COS-B*, and *SAS-2*(Mayer-Hasselwander et al. 1994). The spectrum of the pulsed emission is generally quite hard and shows remarkable variations over the rotation period. The maximum power of Geminga is emitted at about 1 GeV. Above a few GeV, the spectrum breaks off sharply. The power in optical ($m_v \sim 25.5$, pulsation marginally detected) and radio emissions (marginal detections of pulsed emission at 102 MHz) is lower than the gamma-ray emission by more than 6 orders of magnitude, justifying the designation “radio-quiet pulsar” for Geminga.

PSR B1055-52 also has a quite hard photon spectral index of - 1.18 ± 0.16 that seems to extend from X-rays to the gamma-ray range(Fierro et al. 1993). Again the maximum power is emitted around 1 GeV. No clear break in the spectrum is visible up to 4 GeV.

From the multi-wavelength light-curves, pulsars show spectral changes as they rotate, i.e. the light-curves look different for adjacent energy bands. This phase dependent spectroscopy can be extended to the gamma -ray range. Figure 1.8 shows the hardness ratio as a function of the pulsar's rotation, where hardness ratio is defined as the ratio between the number of photons above 300 MeV to that in the band 100-300 MeV. For "double-peak" pulsars, the first peak has a softer spectrum than that in the interval region, and the second peak also has a harder spectrum than that the first peak. Model calculations (polar cap model and outer gap model, see § 5) have successfully reproduced these phase-dependent spectra for Vela.

3.4 P-P diagram

As we mentioned in section § 2, P and $\dot{P}$ teach us many physical features of pulsars. Figure 1.9 is a distribution of pulsars as a function of their period and period derivative, with the gamma-ray pulsars shown as large dots. Also shown are some of the derived physical parameters. The gamma-ray pulsars tend to be concentrated in a region with high magnetic field shown by the dashed lines, and relatively young ages shown by the solid lines (with the exception of the one millisecond candidate). All gamma-ray pulsars share a third characteristic, shown by the dotted line, of having the open field line voltage high compared to most pulsars. This is not surprising, since the particles are being accelerated by the electromagnetic force.

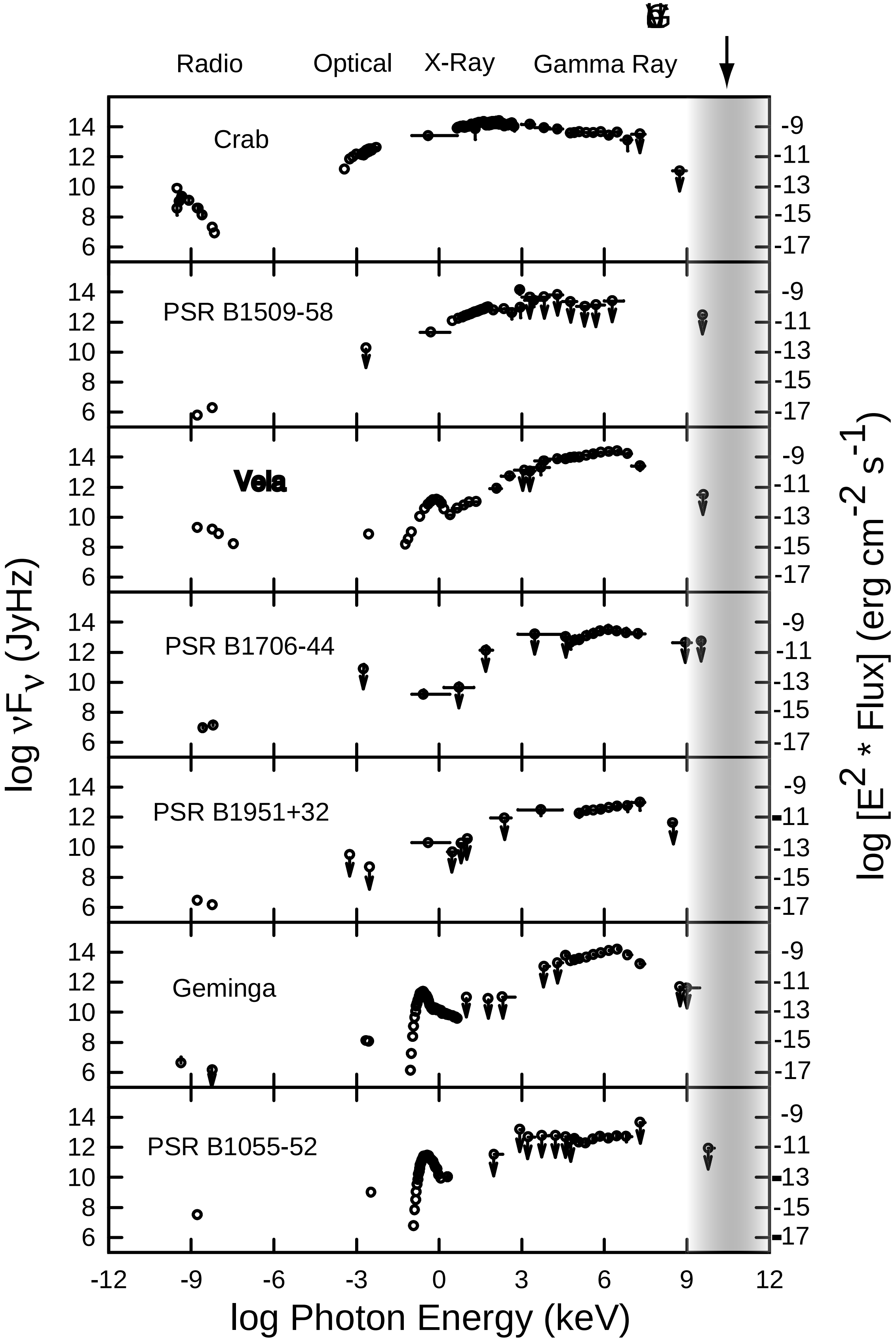

Figure 1.7: Multiwavelength energy spectra for the known gamma-ray pulsars(Thompson et al. 1999).

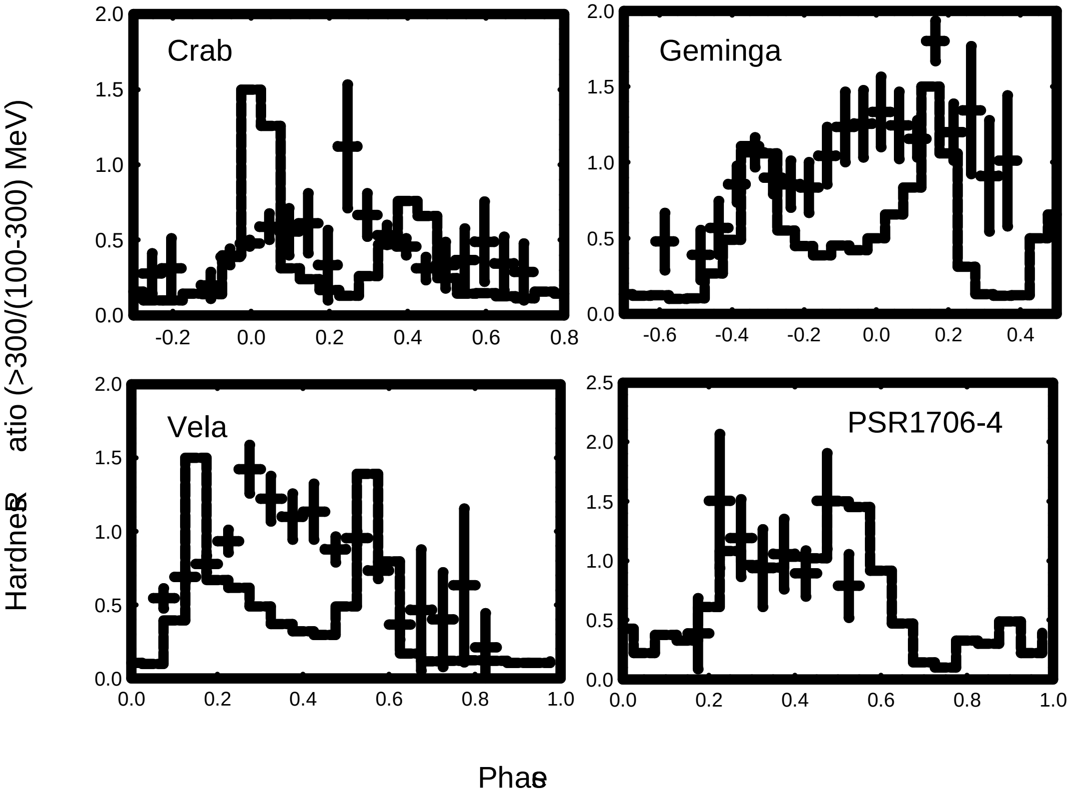

Figure 1.8: The hardness ratio as a function of rotation phase for 4 bright gamma-ray pulsars (Kanbach 2002).

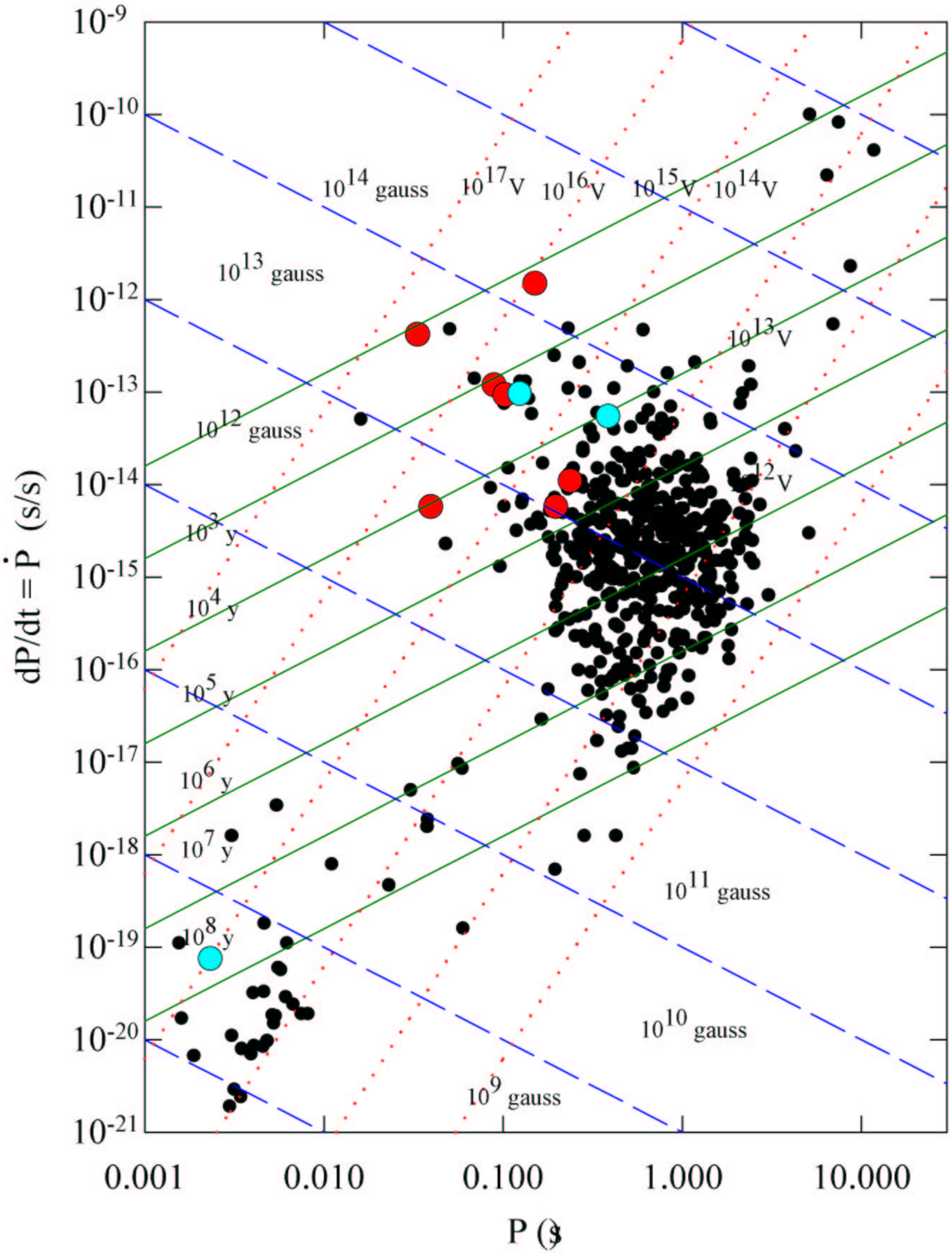

Figure 1.9: Period versus period derivative for a large sample of pulsars. Small dots: no gamma-ray emission. Large dark dots: seven high-confidence gamma-ray pulsars. Large light dots: three lower-confidence gamma-ray pulsars. Solid lines: characteristic age. Dotted line: open field line voltage. Dashed line: surface magnetic fields (Thompson 2004).

§ 4 Pulsar magnetosphere: the aligned rotator

What's going on in the space surrounding a rotating magnetic neutron star ? Hoyle et al. and Pacini concluded that the plasma density near a pulsar must be quite low (Hoyle et al. 1964; Pacini et al. 1967). However, Goldreich and Julian pointed out that conclusion is incorrect, and postulated that strong electric fields parallel to the pulsar's surface will invariable rip off charged particles from the star (Goldreich and Julian 1969). Consequently, the space surrounding the neutron star get filled with a charged separated plasma, and a pulsar must possess a dense magnetosphere which co-rotates with it. This model is the foundation of latest models for high energy pulsed emittion from gamma-ray pulsars. In this section, we show that the space surrounding a neutron star will not be vaccume.

The stellar material is assumed to be an excellent conductor, so that inside the star, an electric field must satisfy the Ohm's law,

$$\rho \left(\boldsymbol{E} + \frac{\boldsymbol{v}}{c} \times \boldsymbol{B} \right) = \boldsymbol{J} = 0 \ . \tag{1.30}$$

That is,

$$\boldsymbol{E}^{in} + \frac{\boldsymbol{\Omega} \times \boldsymbol{r}}{c} \times \boldsymbol{B}^{in} = 0 \ , \tag{1.31}$$

where Ω is the rotation velocity. This equation implies that $\boldsymbol{E} \cdot \boldsymbol{B} = 0$ inside the star.

From the Maxwell equation, $\nabla \cdot \boldsymbol{E} = 4\pi\rho_e$, we can calculate the charge density

$$\nabla \cdot \boldsymbol{E} = -\frac{1}{c} \nabla \cdot (\boldsymbol{v} \times \boldsymbol{B}) = -\frac{\boldsymbol{\Omega}}{c} \cdot (2\boldsymbol{B} - \boldsymbol{r} \times (\nabla \times \boldsymbol{B})) = 4\pi\rho_e \ , \tag{1.32}$$

$$\text{i.e.} \qquad \rho_e = -\frac{\boldsymbol{\Omega}}{2\pi c} \left(\boldsymbol{B} - \frac{1}{2} \boldsymbol{r} \times (\nabla \times \boldsymbol{B}) \right) \ . \tag{1.33}$$

To simplyfy, we assume that a spining neutron star has an aligned dipole external magnetic field, and we can write the magnetic field using Eq.1.23

$$\boldsymbol{B}^{out} = (B_r, B_\theta) = \left(\ B_p \left(\frac{R}{r} \right)^3 \cos\theta, \ \frac{B_p}{2} \left(\frac{R}{r} \right)^3 \sin\theta \ \right) \tag{1.34}$$

Let us assume that the exterior region is a vacuum for the moment, and then

$$\boldsymbol{E}^{out} = -\nabla\phi \ , \tag{1.35}$$

where

$$\nabla^2 \phi = 0 \ . \tag{1.36}$$

In this case, we can solve Laplace's equation for the external electrostatic potential which must be continuous at the stellar surface. The result of this calculation would be

$$\Phi^{out} = -\frac{B_p R^5 \Omega}{3cr^3} P_2(\cos\theta) = -\frac{B_p R^5 \Omega}{6cr^3}(3\cos^2\theta - 1) \ , \tag{1.37}$$

where r, θ, ϕ are the usual polar coordinates with θ mesured from the rotation axis, P_2 is the Legendre polynominal of second degree, and B_p is the polar magnetic field.

From Eq. 1.37 and 1.35, we can find

$$\boldsymbol{E}^{out} = (E_r, E_\theta) = (\frac{B_p \Omega R^5}{cr^3} \ \frac{3\cos^2\theta - 1}{2r}, \ \frac{B_p \Omega R^5}{cr^3} \ \cos\theta \sin\theta) \ . \tag{1.38}$$

As we mentioned above, $\boldsymbol{E} \cdot \boldsymbol{B} = 0$ inside the star, but outside the star, Eqs. 1.38 and 1.34 give

$$\boldsymbol{E} \cdot \boldsymbol{B} = -\frac{B_p^2 \Omega R}{c^2} \left(\frac{R}{r}\right)^7 \cos^3\theta \ . \tag{1.39}$$

Threfore, the magnitude of the electric field parallel to $\boldsymbol{B}$ at the surface is approximately

$$E_{\|} = \frac{(\boldsymbol{E} \cdot \boldsymbol{B})}{|\boldsymbol{B}|} \sim -\frac{R\Omega}{c} B_p \sim 2 \times 10^8 P^{-1} B_{12} \quad [\text{volt cm}^{-1}] \ , \tag{1.40}$$

where B_{12} is the magnetic field strength in units of 10^{12} G. Such a strong field will impart a force to both electrons and ions at the surface that greatly exceeds the gravitational force. For protons,

$$\frac{electricforce}{gravitationalforce} \sim \frac{eR\Omega B_p/c}{GMm/R^2} \sim 10^9 \ . \tag{1.41}$$

Cleary, the surface charge layer could not be in dynamical equilibrium. From this contradiction, Goldreich and Julian conclude that a rotating magnetic neutron star connot be surrounded by a vacuum. Figure 1.10 shows the space charge distribution, according to the analysis of them.

In this situation, the Larmor radius of charged particles is given by:

$$r_c = \frac{pc}{eB} = 3 \times 10^{-5} B_{12} \frac{pc}{10^{10} \text{ eV}} \quad [\text{cm}] \tag{1.42}$$

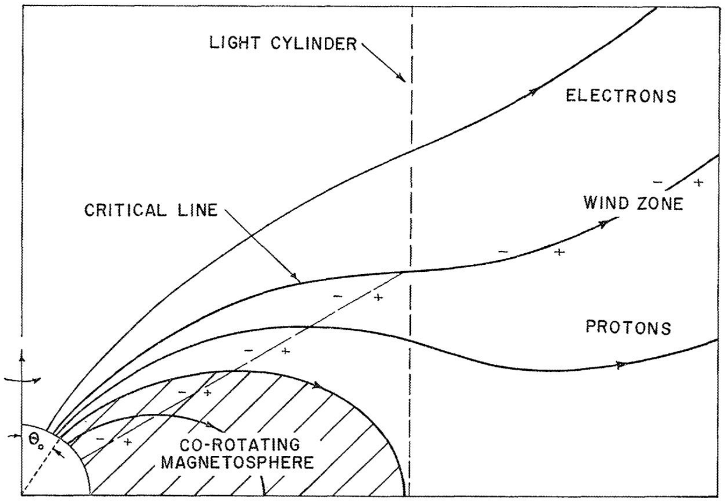

Figure 1.10: Schematic diagram showing the co-rotating magnetsphere and the wind zone (Goldreich and Julian 1969).

Therefore, they cannot across the magnetic field lines, but can flow out to the parallel direction to the magnetic field. The induced electric field is neutralized by the flow of charges in the plasma, and then, the electric fileld outside the star also satisfies $\boldsymbol{E} \cdot \boldsymbol{B} = 0$. Therefore, $\nabla \times \boldsymbol{B}$ equals to zero, and thus Eq. 1.33 gives

$$\rho_e = -\frac{\boldsymbol{\Omega} \cdot \boldsymbol{B}}{2\pi c} \; . \tag{1.43}$$

§ 5 Emission mechanisms

The emission mechanisms of gamma-rays from pulsars have been studied in a number of papers. Currently, two classes of acceleration models have been proposed. In both of them, the pulsed emission originates from radiation by charged particles accelerated in $\boldsymbol{E} \cdot \boldsymbol{B} \neq 0$ "gaps" where a vaccum gap or a deficit of charge density from the Goldrich-Julian charge density is created.

One class of models, called "polar cap", assumes pulsed emission comes from high-energy electrons accelerated near the surface of a neutron star. The other class, called "outer gap", postulates it comes from high energy electrons accelerated

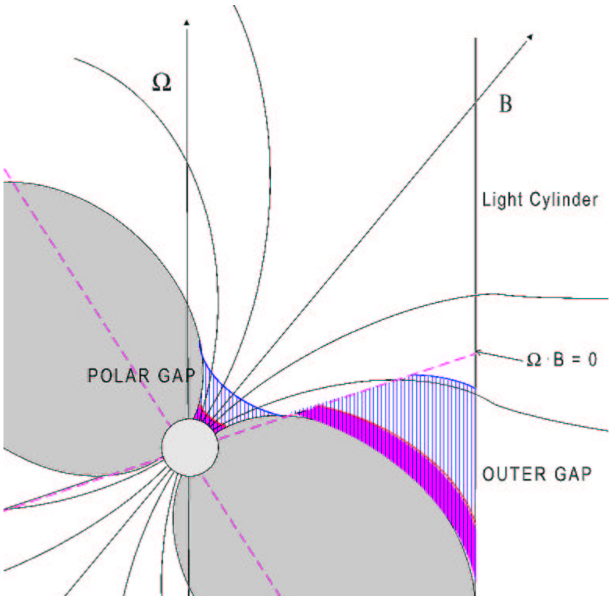

Figure 1.11: Schematic geometry of polar and outer gaps. Dark solid regions are thin gaps of younger pulsars. Hatched regions are thick gaps of older pulsar (Harding 2001).

in potential gaps between the last open field lines of magnetic field and a neutral sheet ($\mathbf{\Omega} \cdot \boldsymbol{B} = 0$ line. see Eq. 1.43).

5.1 Polar cap model I: the gap just above the steller surface

How is the "gap" created ? Here complete solutions for pulsar magnetosphere are not yet available, but it appears that there is mainly an outward flow of relativistic charge particles through the light cylinder. The open magnetic field lines which penetrate the light cylinder play a role analogous to that of conducting wires in ordinary circuits. If the wire is broken near the pulsar surface, the entire potential drop could be developed across the gap(Fig. 1.12).

Open field lines occupy a large region only at considerable distances from the star, $r \sim R_L$. Near the star, these lines form a rather narrow conical zone. They emerge from small regions near the magnetic poles of the star. As in the Earth's and planetary magnetosphere, these regions are called "polar caps". The radius R_{pc} of the polar cap of a neutron star is not large. For the dipole magnetic field (Eq.

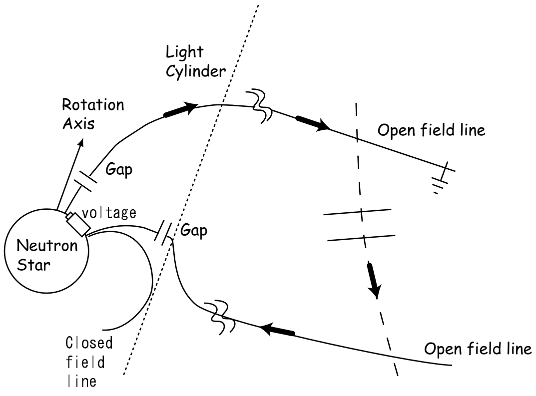

Figure 1.12: Schematic geometry of gaps.

1.23), the equation of the field lines is

$$r = R(\sin\theta / \sin\theta_R)^2 \tag{1.44}$$

where R is the radius of a neutron star, θ_R is the angle of the magnetic field line at the surface of a neutron star. Assuming $r = R_L >> R$, this equation leads

$$\theta_R \sim \sqrt{\frac{\Omega R}{c}} \ . \tag{1.45}$$

Thus,

$$R_{pc} \sim R\theta_R = R\sqrt{\frac{\Omega R}{c}} \ . \tag{1.46}$$

For the typical pulsar ($P = 1$ sec; $R = 10$ km), $R \sim 150$ m. We shall point out the two basic properties which lead to a substantial difference in plasma behavior on closed and open field lines. For closed lines, both ends of field lines come onto the neutron star. Therefore, the co-rotation condition always holds, and thus, the electric field potential Φ coincides with the co-rotation potential Φ_c:

$$\Phi = \Phi_c = \frac{1}{c}(\boldsymbol{\Omega} \times \boldsymbol{r}) \cdot \boldsymbol{A} \tag{1.47}$$

where $\boldsymbol{A}$ is the vector potential of the magnetic field $\boldsymbol{B}$. For open field lines, one of their ends comes onto the neutron star, while the other goes to infinity. Hence, on open field lines the electric field potential, which reflects conditions both on the neutron star and far from it, does not necessarily coincide with the co-rotation potential. It may differ substantially from Φ_c, and thus it could be represented in the form

$$\Phi(\boldsymbol{r}_\perp) = \Phi_c(\boldsymbol{r}_\perp) + \Psi(\boldsymbol{r}_\perp) \tag{1.48}$$

We have taken into account here that the electric field potential is always constant along the magnetic field line ($\boldsymbol{E}\cdot\boldsymbol{B} = 0$). The potential $\Psi(\boldsymbol{r}_\perp)$ reflects the interaction of the magnetic field and currents with plasma; it is the most important characteristic of an open magnetosphere. The presence of a non-zero potential $\Psi(\boldsymbol{r}_\perp)$ implies that on open field lines the plasma does not rotate along with the star as a solid body (Fig. 1.13).

Second, along open field lines plasma may leave the neutron star freely and escape from the magnetosphere. The charge ρ_e (Eq.1.43) goes along with plasma, but then the condition of $\boldsymbol{E} \cdot \boldsymbol{B} = 0$ will be violated near the polar caps. In the vacuum region near the star that appears due to escape of plasma there arises a strong potential electric field $E = -\nabla\Psi$. On the scale of the order of the polar cap (Eq.1.46), the longitudinal potential difference reaches the value

$$|\Psi_{max}| \sim R_{pc}\frac{\Omega R B_p}{c} = \left(\frac{\Omega R}{c}\right)^{\frac{3}{2}} R B_p \sim 10^{13} - 10^{15} \quad [\mathrm{Volt}] \,. \tag{1.49}$$

Let us lead the gap potential more precisely. We assume that the stellar surface is flat and the magnetic field lines is normal to the surface. The geometry is cylindrical (Fig. 1.14). Using the Eq. 1.37, we can lead the potential difference between the center of the open field lines ($\theta = 0,\ r = R$) and the conductive "wall" of the closed field lines ($\theta = \theta_R,\ r = R$),

$$\Delta\phi = \frac{1}{2} B_p \theta_R \left(\frac{\Omega R}{c}\right)^2 \,. \tag{1.50}$$

Below the surface of the star, the electric field is represented by Eq. 1.40. In the polar cap just above the stellar surface, we assume that there is a complete vacuum,

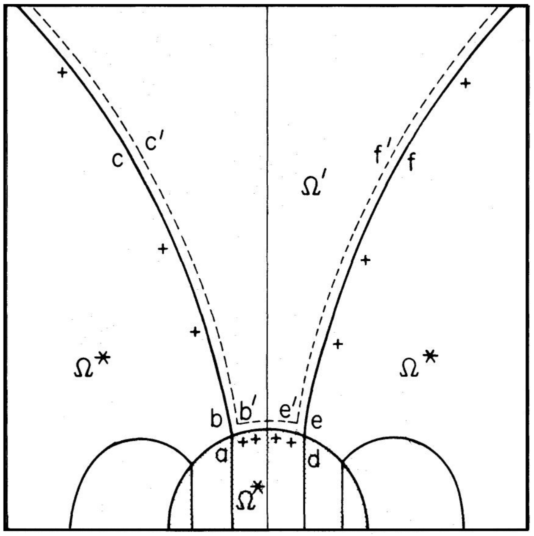

Figure 1.13: Magnetosphere of a rotating neutron star (angular velocity Ω^*) with an anti-parallel dipole field and a polar gap above the surface in the polar region ad. There is zero charge in the magnetosphere between the solid and dashed lines; additional charge is designated only within the star. The magnetosphere between the equator and the cone of abc and def co-rotates with the star. The magnetosphere within the cone of $c'b'e'f'$ rotates with angular velocity $\Omega' < \Omega^*$: Ω' is constant only along magnetic field lines. Significant departures of $\boldsymbol{E} \cdot \boldsymbol{B}$ from zero occur only within the polar gap $ab'e'd$ (Ruderman and Sutherland 1975).

and thus the electric field is a solution of Poisson's equation [2],

$$E_z \sim B_p \left(\frac{\Omega R}{c}\right)^{\frac{3}{2}} \exp\left\{-\frac{z-R}{R}\left(\frac{c}{\Omega R}\right)^{\frac{1}{2}}\right\}\left(1-\frac{\theta^2}{{\theta_c}^2}\right) , \tag{1.51}$$

where we calculate the potential only at the center of the open field lines. As you can see, E_z exists between just above the stellar surface(z=0) and the $z \sim R_{pc}$, and shows the exponential decrease above $z \sim R_{pc}$. The generalized electric potential as the function of r and θ was calculated by many theorists, e.g. (Beskin et al. 1993) (Fig. 1.14:right).

In such a strong electric field, the vacuum becomes unstable, since an electron-positron plasma is generated in it. Consequently, active process associated with electron-positron plasma generation are permanently maintained in the narrow conic region near magnetic poles of the star. Supporters for the polar gap model believe that these process are the source of pulsar activity.

5.2 Polar cap model II: the electron-positron cascade

In the gap just above the stellar surface, gamma-ray emission mechanism is proposed by Sturrock (Sturrock 1971). The huge induced electric field pulls out charged particles from the stellar surface, and accelerate them along the magnetic field lines. The charged particle generate photons via curvature or synchrotron radiation in their instantaneous direction of motion. For young pulsars, like the Crab, curvature radiation is dominant since the Lorentz's factor is $\gamma > 10^6$.

These photons move through the strong magnetic field of the pulsar, and gradually reaches the critical electron-positron pair production angle ($\gamma + B \rightarrow e^+ + e^-$) which depends on the photon energy and on the magnitude of the magnetic field. One of produced particles (positron) goes on moving away from the star, while the other particles (electron) becomes accelerated by the electric field in the opposite direction. It also emits curvature photons, which produce pairs near the stellar surface (Fig. 1.15). One of the newly born particles (positron) begins accelera-

---

[2] e.g. *Classical electricity and magnetism* p.86 - (Barger and Olsson 1991) is the useful guide for you.

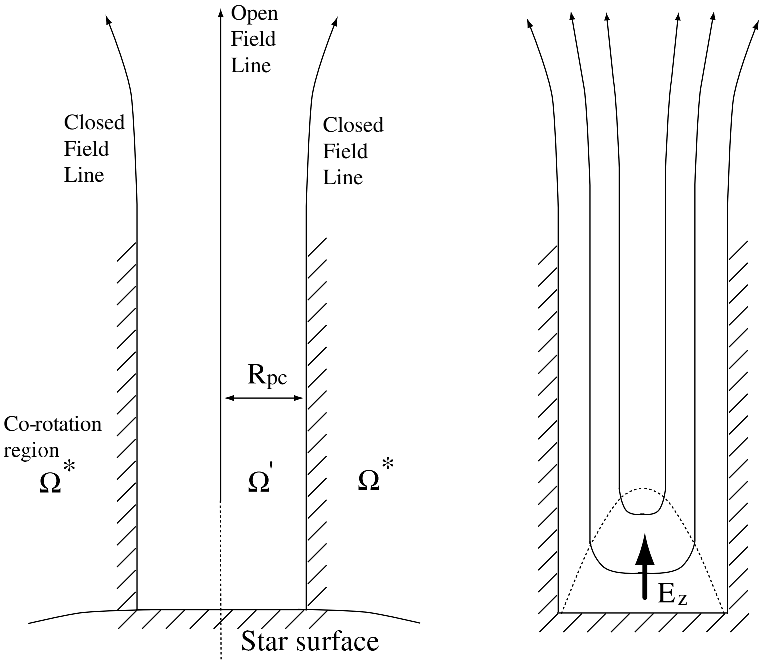

Figure 1.14: Left: Schematic geometry of the polar gap. Right: Equipotential line (dotted) calculated by (Beskin et al. 1993).

tion away from the star, and the acceleration and pair production processes are repeated. This is how there arises a chain reaction of multiplication of electrons, positrons and gamma-ray quanta near a neutron star. If the charged particles gains significant high energy, the energy of their radiation photons may be in the GeV to TeV energy range (Ruderman and Sutherland 1975).

5.3 Outer gap model

Primary electrons accelerated to energies above 10^{12} eV would be needed to explain the emission observed above 100 MeV. These models explored the region above the polar cap as the acceleration and emitting site, but it became clear that the TeV photons cannot escape to the observer, since they are absorbed by the strong magnetic field near the stellar surface. Therefore, the non-detections in the TeV band are entirely consistent with the polar cap model, but it cannot account for the optical spectra of the Crab pulsar(Ruderman 1989). A number of alternative regions

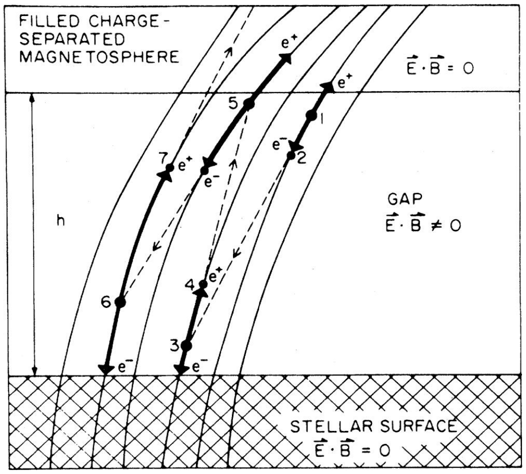

Figure 1.15: Nature of a pair-production discharge (Ruderman and Sutherland 1975).

in the magnetosphere have been proposed for the pulsar emission only against the high energy radiation. Among these, one of the most plausible model is the outer gap model. Cheng, Ho and Ruderman (Cheng et al. 1986) proposed a mechanism for producing the observed emission from the Crab and Vela pulsars in the energy range from gamma-ray to optical wavelengths, in which high-energy pulsar emission is generated in vacuum gaps existing in the outer regions of the magnetosphere.

This gap is formed between the "null surface" ($\boldsymbol{\Omega} \cdot \boldsymbol{B} = 0$, see Eq. 1.43) and the light cylinder, along the last closed field line (see Fig. 1.16). For this model, there are three important regions which contribute to the emission mechanism in a bootstrap manner. Inside the gap (region I of Fig. 1.16), $\boldsymbol{E} \cdot \boldsymbol{B} \neq 0$, and electrons and positrons are accelerated along the curved magnetic field lines by the large potential difference across the gap, radiating curvature gamma-rays and/or boosting soft photons via inverse Compton scattering. Unlike the case in polar cap models, the magnetic fields in the outer gap are too weak for one-photon pair production to play a significant role in the cascade. Instead, these primary gamma-rays move away from the closed-field-line region and collide with ambient photons to produce secondary $\mathrm{e}^{\pm}$ pairs in the region II, just above the vacuum gap boundary, via $\gamma + \gamma \rightarrow \mathrm{e}^+ + \mathrm{e}^-$. These secondary electrons and positrons will typically have a substantial component

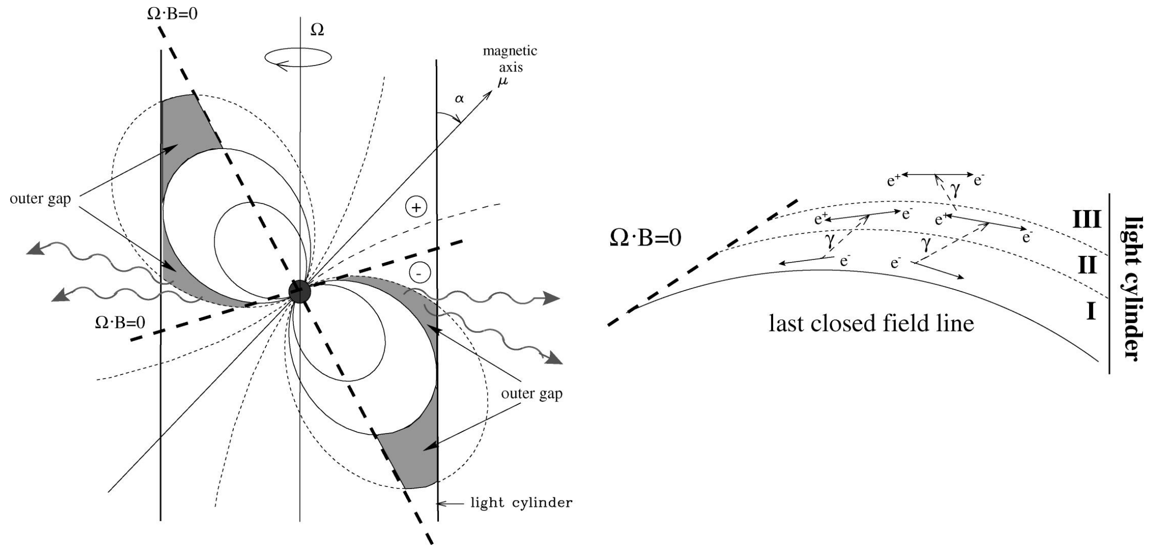

Figure 1.16: Pulsar magnetosphere according to the outer gap model. The four outer gaps, drawn in bold, form along the last closed field lines between the null surface defined by c/ B = 0 (indicated by dashed lines), and the light cylinder. Beams from one hemisphere are mirrored in the opposite hemisphere.

of their momenta perpendicular to the local magnetic field, and they will emit synchrotron radiation (and/or boost photons by inverse Compton scattering), which cover the energies from optical to gamma-rays. The secondary photons move beyond the region II to form tertiary pairs in the region III. These pairs have insufficient energy for formation of X-ray or gamma-rays, but provide a sea of infrared and optical photons which illuminate the entire open magnetosphere and refuel the gap. This is how the mechanism in region I can continue.

5.4 Energy spectrum above 10 GeV

Observations of pulsars in the unexplored energy region above 20 GeV and/or more sensitive measurements above 1 GeV may be able to discriminate in favor of polar cap or outer gap models. Polar cap models predict that the gamma-ray spectra cutoff very sharply (as a “super exponential”) due to one-photon pair production attenuation at the strong magnetic field. In contrast, for the outer gap model, the cut off of spectra is more slowly (as a simple exponential) due to a particle acceleration limit.

The highly relativistic particles emit photons at quite small ($\theta \sim 1/\gamma$) angles to the open magnetic field lines. The photons of energy ϵ (in units of mc^2), emitted near the neutron star surface, are initially below the threshold for one-photon pair production ($\epsilon_{th} = 2/\sin\theta$), but may reach threshold by increasing θ in the course of propagating across curved field lines. For the polar cap model, the gamma-ray spectrum will exhibit a cutoff at the pair escape energy (cf. Harding et al. 1997), i.e. the highest energy that photons can escape from the magnetosphere without pair producing. Assuming emission along the polar cap outer rim, $\theta \sim (2\pi R/cP)^{1/2}$, at radius R, the estimate of cutoff energy is (see Zhang & Harding 2000a, Eqn. 28)

$$E_c \sim 2 \text{ GeV } P^{1/2} B_{0,12}^{-1} \left(\frac{R}{R_0}\right)^{5/2}, \qquad B_{0,12} \gtrsim 10(R/R_0)^2 \tag{1.52}$$

$$E_c \sim 0.2 \text{ GeV } P^{1/2} \left(\frac{R}{R_0}\right)^{1/2}, \qquad B_{0,12} \lesssim 10(R/R_0)^2 \tag{1.53}$$

where P, R_0 and $B_{0,12}$ are the neutron star period, radius and surface magnetic field in units of 10^{12} G, respectively.

Figure 1.17 shows a more accurate calculation of the predicted high-energy cutoff energy as a function of surface field strength for different radii of photon emission, computed by numerically propagating photons through a neutron star magnetosphere and taking into account general relativistic effects of a Schwarzschild metric (Harding et al. 1997). The observed cutoff energies of eight gamma-ray pulsars versus their surface fields derived from P and $\dot{P}$, assuming $R_0 = 10^6$ cm, are also plotted.

From Fig. 1.17, it appears that long period pulsars with low magnetic fields ("old" pulsars) will be the best candidates for detection above 20 GeV. However, the curvature radiation energy of the primaries decreases with increasing period, due to both an increasing radius of curvature of the last open field line and a decreasing particle acceleration energy. The maximum CR energy starts to move below the photon escape energy, and thus determines the cutoff energy. If the present version of the polar cap model is correct, the pulsed emission will be difficult to detect with

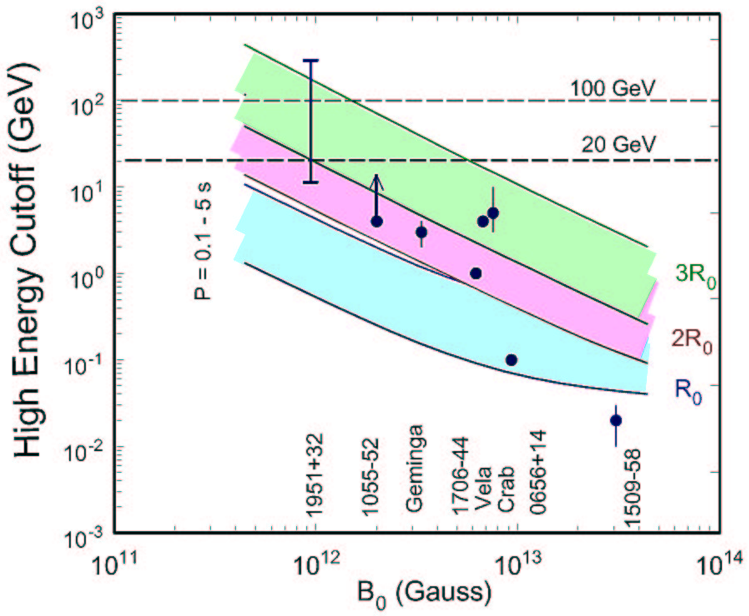

Figure 1.17: Calculated high-energy spectral cutoff energies due to magnetic pair production attenuation vs. surface field strength for a range of periods at different photon emission radii. Also shown are measured turnover energies of detected pulsars.

the Imaging Atmospheric Čerenkov Telescopes (IACTs), even from short-period, low-field pulsar like PSR 1951+32.

The picture is quite different in outer gap models, and much more hopeful for ground-based observers. When the high-energy photons are emitted in the outer magnetosphere, where the local magnetic field is orders of magnitude lower than the surface magnetic field, and thus one-photon pair production plays no role in either the pair cascade or the spectral attenuation. In this case, the high-energy cutoffs in the spectrum come from the upper limit of the accelerated particle spectrum, due to the radiation reaction. Therefore, the shape of the cutoff is a simple exponential, more gradual than that in polar cap model spectra. Figure 1.18 shows the broad-band outer-gap model spectrum of Vela (Romani 1996), superimposed on the measured spectrum from optical to VHE gamma-rays and the polar cap model spectrum (Harding & Daugherty 1996). Due to the large errors of the *EGRET*data

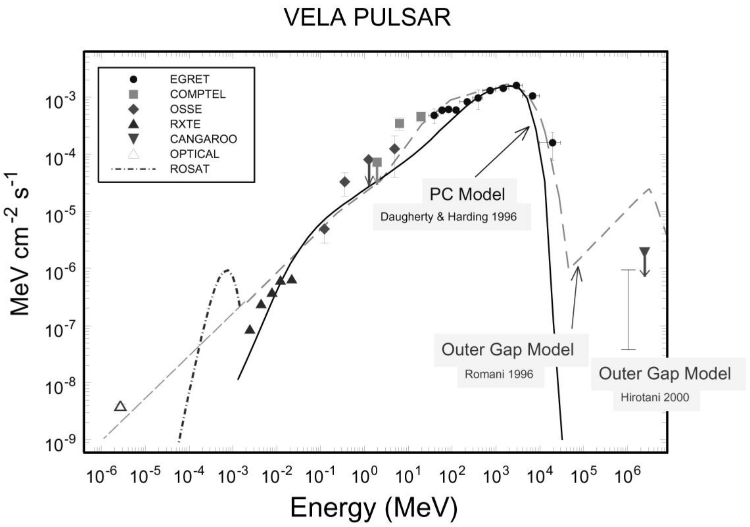

Figure 1.18: Observed optical to VHE gamma-ray spectrum of the Vela pulsar with polar cap (solid line) and outer gap (dashed line) model spectra. Data points are from (Thompson et al. 1999).

points above 1 GeV, the measurements at present can not discriminate between two model spectra.

§ 6 Current situation of instruments

During the last decade, the development of gamma-ray detectors made remarkable progress, and provided us exciting views of our universe. Below 10 GeV, a space-based detector, Compton Gamma Ray Observatory (*CGRO*) revealed high-energy phenomena(Gehrels et al. 1993). Above 100 GeV, ground-based detectors using the IACTech have detected very high-energy gamma-rays emitted from several galactic and extragalactic objects(Ong 1998). In the 10 GeV to 100 GeV region, however, only a few detectors have been exploring until now(de Naurois et al. 2002; Oser et al. 2001).

Polar Cap and Outer Gap model can explain the wide-band pulsed emission below the GeV region fairly well, but as mentioned above, they predict clearly different behaviors between 10 and 100 GeV region (Harding 2001). In Fig. 4.17, the current status of observations is shown for the Crab pulsar/nebula, which is the most famous gamma-ray pulsar and the "standard candle" for gamma-ray astronomy.

Observing the gamma-ray spectrum in the 10-100 GeV energy region has proved to be elusive for both ground-based and satellite-based instruments. Satellite detectors have collection areas that are too small to detect gamma-rays above 10 GeV. In contrast, ground-based detectors can achieve much larger collection areas, but detection of Čerenkov light caused by gamma-ray showers below 100 GeV is difficult because the Čerenkov light density is too low.

However, new generation Čerenkov telescopes, such as CANGAROO-III(Asahara et al. 2004; Kubo et al. 2004), H.E.S.S(Hofmann et al. 2003), and VERITAS(Wakely et al. 2003), are under construction or have just come into operation. The key concept of this new generation is a stereoscopic observation with 10 m class telescopes. These telescopes will be able to achieve good angular resolutions ($\sim$ 0.05 degrees) and moderate energy resolutions ($\Delta E/E \sim 0.2$), but can't really improve the energy threshold ($\sim$ 100 GeV). On the other hand, a new generation space-based detector, to be launched in 2006, GLAST, will be able to detect gamma-rays with energies of up to $\sim$ 100 GeV(Kamae et al. 2000). GLAST will improve the *EGRET*sensitivity by about two orders of magnitude. However, the capability of GLAST at energies above 10 GeV will be quite limited because of the small detection area. Therefore, to cover the energy band between 10 - 100 GeV, we must develop a detector that will have a sufficient sensitivity in this energy band. Although the density of Čerenkov photons induced by gamma-rays is quite low in the sub 100 GeV energy region, there are two methods to detect such low energy particles. One of the methods is to use a "larger mirror".

Two projects with a low-energy threshold, STACEE(Oser et al. 2001) and CELESTE(de Naurois et al. 2002), which use a wave-front sampling technique with many mirrors in a solar power plant, have succeeded to detect detecting gamma-rays below 100 GeV from the Crab nebula/pulsar, but can not detect other GeV/TeV sources, except from a few strong variable sources, such as Mrk 421, because they cannot analyze Čerenkov light images. Among the new generation of projects, only

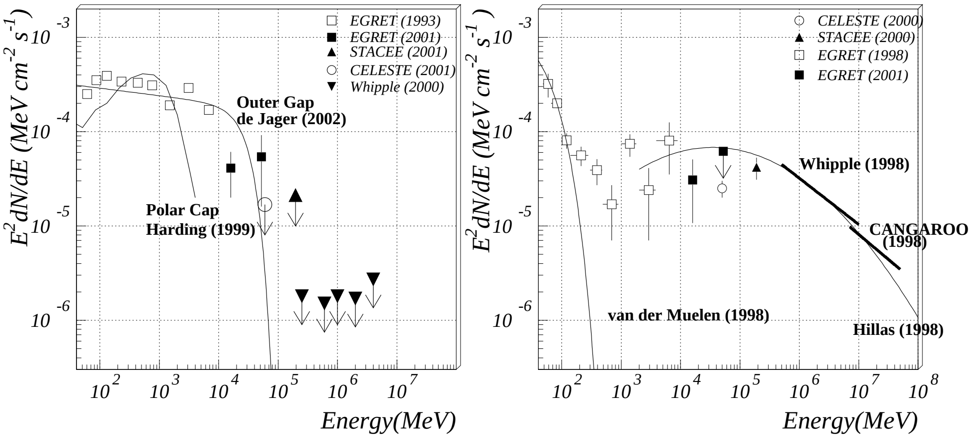

Figure 1.19: The differential flux of the Crab pulsar reported by several instruments. (Harding et al. 1997; Lessard et al. 2000; de Naurois et al. 2002; Oser et al. 2001; Nolan et al. 1993; de Jager 2002). Theoretical curves are superimposed.

the MAGIC group's 17m diameter mirror is expected to detect 30-GeV gamma-rays(Martinez et al. 2003).

The other method for detecting low energy particles is observing them at a "high altitude". The Čerenkov light density caused by cosmic rays is 4-times larger at a high altitude of 4200 m than at sea level(Tanimori et al. 1995). Our simulation shows that a telescope with an 8 m diameter mirror at 4200 m a.s.l can achieve a sub 100 GeV energy threshold level (Asahara et al. 2003). To observe the 10 - 100 GeV energy region, we developed a compact gamma-ray camera, designated CheSS (Čerenkov light detecting System on Subaru) based on the IACTech, for the Subaru infrared-optical telescope(Asahara et al. 2003). This is a specialized camera for detecting gamma-rays emitted from pulsars. Presently, Subaru is the most suitable optical telescope to detect gamma-rays by IACTech, because it has a monolithic 8.2m mirror and a 0.75-degree field of view, and it is located on the top of Mt. Mauna Kea at an altitude of 4200 m. In December 2001, we observed the Crab nebula/pulsar for three days using CheSS installed at the primary focus of the Subaru telescope. This was the first observation using the IACTech at a high altitude. In this work, we show the result of that observation.

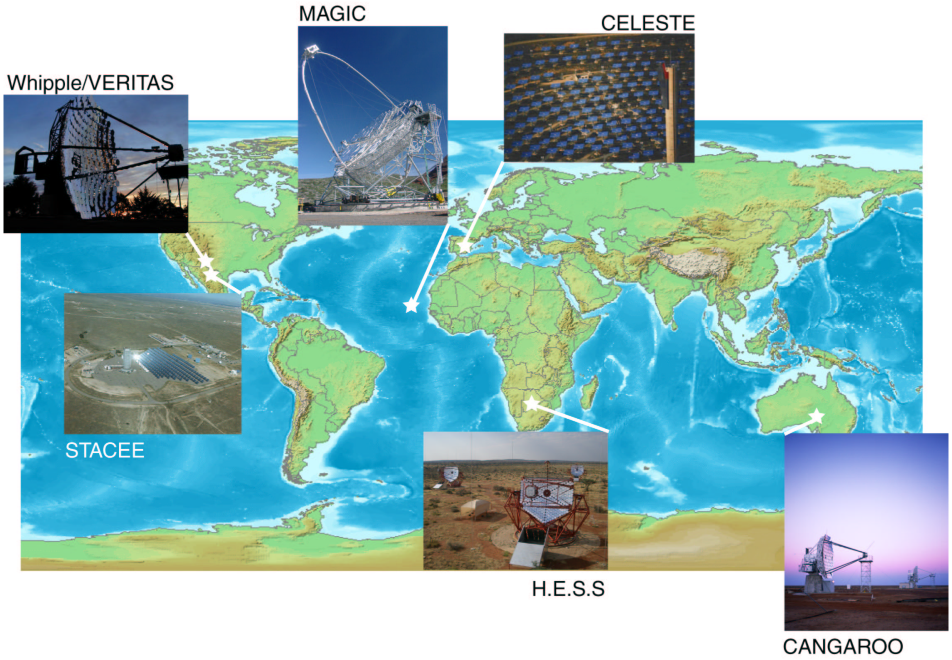

Figure 1.20: Imaging Atmospheric Čerenkov Telescopes.

Chapter2

Techniques for the detection of high-energy gamma-rays

> While she was trying to fix on one, the cook took the cauldron of soup off the fire, and at once set to work throwing everything within her reach at the Duchess and the baby – the fire-irons came first; then followed a shower of saucepans, plates, and dishes. The Duchess took no notice of them even when they hit her; and the baby was howling so much already, that it was quite impossible to say whether the blows hurt it or not. — *Pig and Pepper* —

The term “gamma-ray” is a generic one and is used to describe photons of energy from about 100 keV to $>$ 100 EeV. A wide variety of detection techniques is, therefore, necessary to cover this huge band. This work concentrates on the somewhat restricted gamma-ray band from 1 GeV to 10 TeV. This energy band is usually divided into two energy ranges: High Energy (HE) up to 10 GeV and Very High Energy (VHE) from 10 GeV to 100 TeV.

As mentioned in section 1, below 10 GeV observations are carried out by satellite detectors. In VHE region, their sensitivity is limited by very low count statistics, because fluxes of gamma-rays from cosmic sources steeply fall with increasing their energy. Therefore, for VHE gamma-rays, observations are made by the ground-based detectors. In this chapter, we introduce techniques of ground-based gamma-ray observation.

§ 1 Atmospheric Air Shower Technique

VHE particles striking the earth's atmosphere interact with air molecules , and generate the showers composed of secondary particles. Those are called Extensive Air Showers (EAS). Ground-based instruments for VHE or UHE region detect the products of these interactions or the different types of radiation associated to their interactions with the atmosphere (Čerenkov light, fluorescence, etc.).

For gamma-rays, the EAS is produced by an electro-magnetic cascade. The dominant process at the VHE region is the pair production. A primary gamma-ray produces a electron-positron pair at first. If the energy is sufficient, the electron-positron pair lose only a little energy via ionizationg interactions. Instead, they emit secondary gamma-rays via bremsstrahlung, and in turn, these gamma-rays produce another electron-positron pair(Fig. 2.1). By repeating such processes, an electro-magnetic shower develops, and the number of $e^{\pm}$ and γcontinues increasing exponentially until the energy of the electrons and positrons drop below the critical energy, E_c ($\sim$ 80.3 MeV at 1 atm (Oda, Nishimura, and Sakurai 1989)). At this point, electrons and positrons preferentially lose their energy via ionization rather than via bremsstrahlung. Further multiplication don't occurs except for the ionaization loss. For gamma-rays, the critical energy corresponds to the energy where Compton scattering begins to be more important than the pair production. Thus, the shower reaches its maximum development when the average energy of the cascade particles equals the critical energy. The total number of photons and electrons at the shower maximum is then given by the total energy E_0 divided by the critical energy E_c.

High energy cosmic rays, prontons and nuclei, also interact with atmospheric nuclei (N or 0), and produce EAS consists of furher particles, such as $\pi^0, \pi^{\pm}, K^{\pm}$, and nucleons. A major component of secondaries is pions. A neutral pion, π^0 decays into two gamma rays;

$$\pi^0 \rightarrow 2\gamma \tag{2.1}$$

with very short lifetime (1.78×10^{-16} s) and it initiates an electromagnetic cascade.

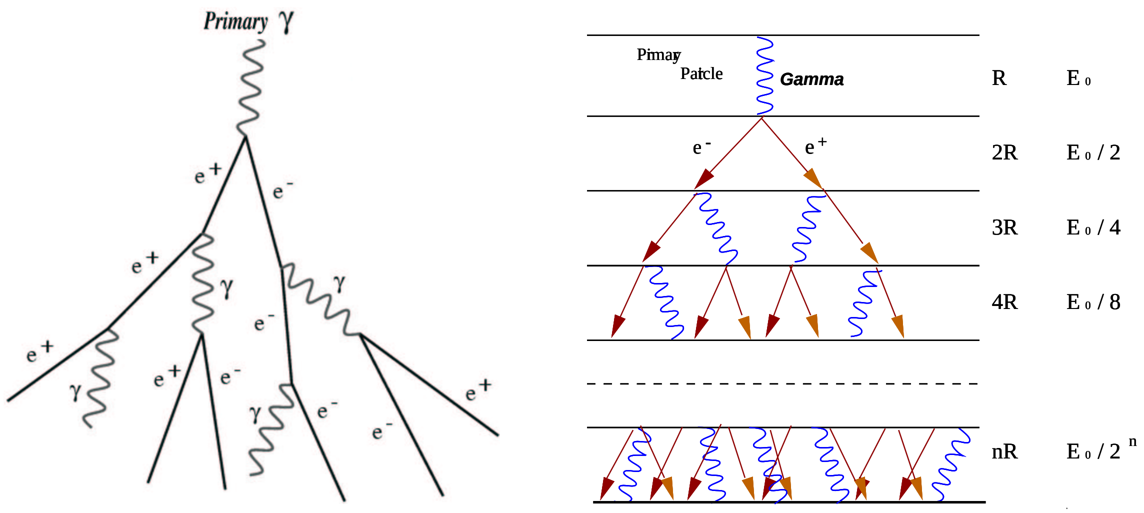

Figure 2.1: Left: Diagram of an gamma-ray initiated shower. Right: Simple model of an electromagnetic shower (Longair 1997).

Many of charged pions interact with nuclei of the atmosphere and produce more pions. Almost all pions decay in flight into muons via:

$$\pi^+ \rightarrow \mu^+ + \nu_\mu \, , \qquad (2.2)$$

$$\pi^- \rightarrow \mu^- + \bar{\nu_\mu} \, , \qquad (2.3)$$

with the mean lifetime of 2.551×10^{-8} s. Decayed muons are slowed down only through the ionization loss. Low energy muons sometimes decay in flight into positrons, electrons and neutrinos:

$$\mu^+ \rightarrow e^+ + \nu_e + \bar{\nu_\mu} \, , \qquad (2.4)$$

$$\mu^- \rightarrow e^- + \bar{\nu_e} + \nu_\mu \, , \qquad (2.5)$$

with the mean lifetime of 2.2×10^{-6} s.

Almost all secondary pions have an enough time to decay in flight in the uppermost layers of the atmosphere before making further nuclear interactions, and thus produce very high energy muons. Most of high energy muons arrive at the surface of the Earth before decaying. Interactions involved in a nucleonic cascade are illustrated in Fig. 2.2.

There are several important differences in the development of EAS between gamma-ray showers and nucleonic showers. First, nucleonic showers initiate in

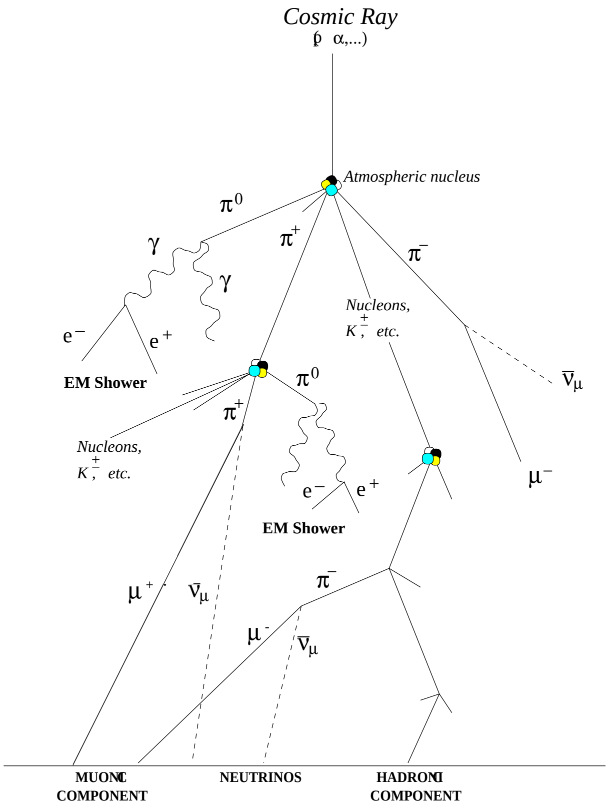

Figure 2.2: Diagram of the development of a nucleonic cascade in the atmosphere (Longair 1997).

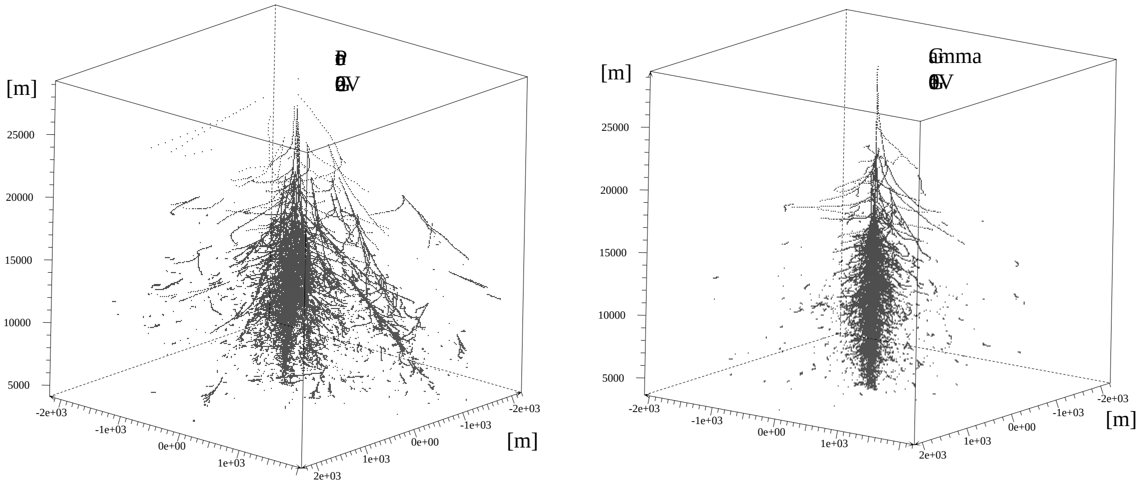

Figure 2.3: Development profiles of MC simulated EASs from a 100 GeV gamma ray (left) and a 200 GeV proton (right).

the deeper atmosphere because of the longer interaction length than those in the radiation length. Second, nuclear cascades have larger transverse momenta than electromagnetic cascades. These two features results in larger fluctuations in the development of nucleonic showers. Figure 2.3 shows the development profiles of a gamma-ray and a nucleonic shower calculated by a Monte Carlo (MC) simulation. The nucleonic shower is extended more transversely than the gamma-ray shower.

Since a major component of nucleonic showers is pions of which neutral pions initiates the electromagnetic cascade, roughly one thirds of particles in a nucleonic shower is those of gamma-ray showers; π^0, π^+ and π^- are produced in almost equal numbers in multi-particle production because of the iso-spin symmetry.

§ 2 Čerenkov Radiation

The Čerenkov radiation is the electromagnetic radiation emitted when a charged particle moves in a dielectric transparent medium at a speed v which is higher than the speed of light in that medium, c/n, where n is the refractive index.

This radiation is not emitted by the particle itself, but by the medium as a result of the reorientation of the instant electrical dipoles induced by the charged particle moving in it. That is why this radiation is only emitted when the velocity of the particle is high enough.

When a charged particle goes across a dielectric medium, it always induces instant electric dipoles in the medium. If the velocity of the particle is less than c/n, the induced dipoles arrange themselves symmetrically around the instantaneous position of the particle (as shown in Fig. 2.4 (a)). This is because the electric field produced by a particle reach all the molecules around the instantaneous position of the charge at almost the same time, since $v << c/n$. There is not a net polarization of the medium at large distances, and thus no radiation is emitted. But if the velocity of the particle is higher than the velocity of the light in the medium, no instant dipoles are set in the region ahead of the moving particle, since the particle travels faster than its own electromagnetic field (see 2.4(b)). Thus, the net polarization of medium is produced along the particle's path, which consequently radiates brief electromagnetic pulses. These pulses are only coherent and combine to form a wave front in those points where they get with the same phase. It can be shown with a simple geometrical interpretation of this emission mechanism (Fig. 2.4 (c)), that Čerenkov radiation is only observed at a particular angle θ, called Čerenkov angle, with respect to the track of the particle. Coherence takes place when the particle travels from A to B in the same time that the light travels from A to C. If $\beta = v \cdot c$ and c/n is the velocity of the Čerenkov light in the medium with n(λ) the refractive index, then, from geometrical considerations the Čerenkov angle is:

$$\cos\theta = \frac{1}{n\beta} \tag{2.6}$$

When a gamma ray with its energy of > GeV enters the top of the atmosphere, it initiates an electro-magnetic cascade, and the electron-positron pairs move with velocities faster than c'. Thus, electrons and positrons in the showers radiate Čerenkov light mainly in the UV and optical region. The threshold for the emission of Čerenkov light depends upon the refractive index n of the atmosphere. At the wavelength of 400 nm, the refractive index of the atmosphere at the temperature of

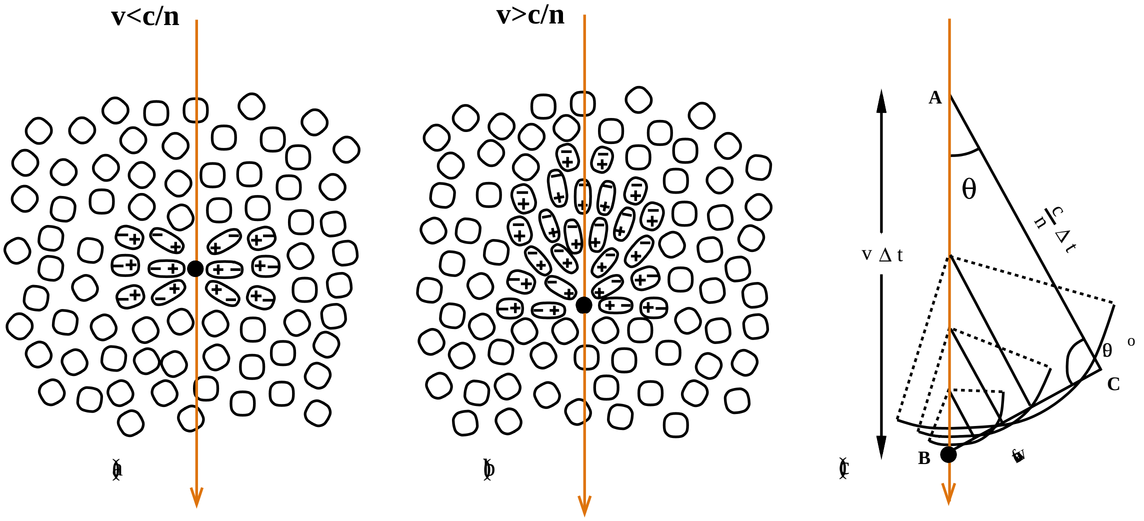

Figure 2.4: The polarization set up in a dielectric when a charged particle passes through. (a) Low velocity. (b) High velocity. (c) Huygens construction to ilustrate coherence and to obtain the Čerenkov angle θ.

T [K] is given by:

$$n = 1.0 + 0.000296 \cdot \left(\frac{x}{1030\,\mathrm{g\,cm^{-2}}}\right) \cdot \left(\frac{\mathrm{T}}{273.2\,\mathrm{K}}\right)^{-1} \tag{2.7}$$

where x is the atmospheric depth in g/cm^2, and T is the atmospheric temperature expressed as a function of x as T $= 204 + 0.091\,x$ [K] (Hillas 1982). At the standard temperature and pressure (1 atm), the refractive index n is estimated to be $\sim$ 1.00027. Since the atmospheric pressure decreases as the altitude goes up (0.1 atm at the altitude of 10 km), the Čerenkov angle is smaller than $\theta \leq 1.3°$ for relativistic particles ($\beta \sim 1$) in an EAS from equation (2.6). Therefore, the Čerenkov radiation from the EAS is emitted within a few degrees from the shower axis. The threshold energy, the opening angle, and the intensity of Čerenkov radiation as a function of the depth (inverse of the altitude) are shown in Fig. 2.5. The threshold energy of Čerenkov radiation for a relativistic electron (positron) is 21 MeV at the sea level and increases to 35 MeV at 7.5 km above the sea level. For $\mu^{\pm}$ and $\pi^{\pm}$, threshold energies are $\mathrm{E}_{\mu^{\pm}}$ ~4.4 GeV and $\mathrm{E}_{\pi^{\pm}}$ ~5.8 GeV, respectively.

The energy loss by the Čerenkov radiation per unit path length is expressed as

$$\frac{dE}{dl} = \frac{z^2 e^2}{c^2} \int_{\beta n > 1} (1 - \frac{1}{\beta^2 n^2}) \nu \, d\nu, \tag{2.8}$$

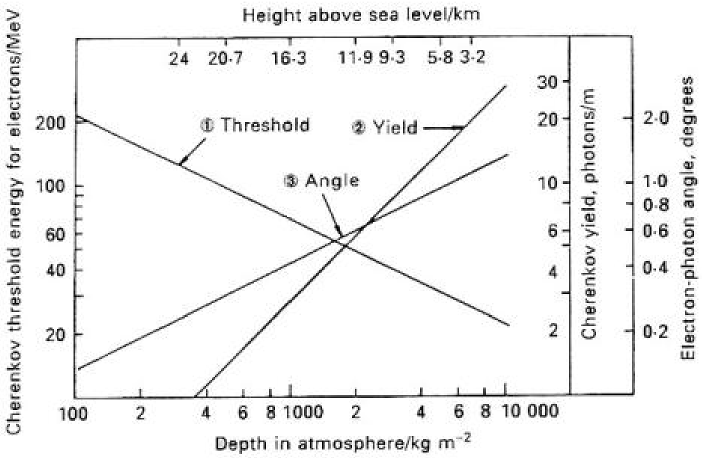

Figure 2.5: Depth dependence of (1)the threshold energy; (2)the intensity of Čerenkov radiation; (3)the angle of Čerenkov radiation for electrons (V. and Wolfendale 1986).

where ze is the particle charge and ν is the frequency of Čerenkov radiation (Jelley 1958). From Eq. 2.8, the number of photons N radiated into the wavelength range between λ_1 and λ_2 is given by:

$$N = 2\pi\alpha z^2 l(\frac{1}{\lambda_1} - \frac{1}{\lambda_2})(1 - \frac{1}{\beta^2 n^2}), \tag{2.9}$$

where $\alpha = e^2/\hbar c \simeq 1/137$ is the fine structure constant and l is the path length of the charged particle. For example, when a relativistic electron travels 1 m, twenty-seven Čerenkov photons are radiated into the wavelength range between 350 and 550 nm. The total number of Čerenkov photons radiated from an EAS is approximately proportional to the number of electrons and positrons produced in the EAS.

The angular cone of the Čerenkov radiation becomes smaller at high altitudes, since the index of refraction of the atmosphere is smaller. Because of this variation, Čerenkov light generated at the height between 7 and 20 km above sea level would fall within a ring of 110 $\sim$ 145 m radius from the shower core if electrons do not undergo multiple scattering. Multiple scattering of electrons broadens the "Čerenkov ring". Figure 2.6 (b) shows the Čerenkov lateral distribution without electron multiple scattering and (a) shows the same distribution taking into account of electron multiples scattering. The lateral distribution of Čerenkov light depends on the details of the longitudinal development of an EAS (Sokolsky 1989).

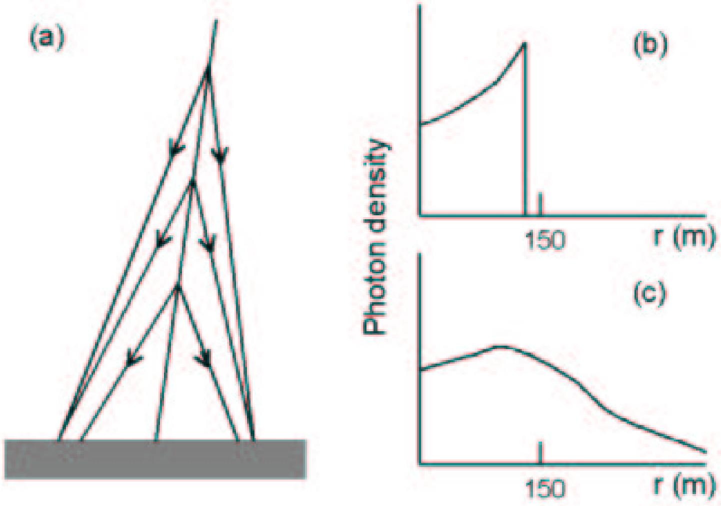

Figure 2.6: Longitudinal development of Čerenkov light. (a)Čerenkov light emission from an EAS at three different atmospheric heights, showing the effect of changing Čerenkov angle due to the variation of the atmospheric index of refraction, (b)illustration of the distribution of resultant photon density at the surface for the case of no electron multiple scattering, and (c)distribution taking into account of multiple scattering of realistic electron (Sokolsky 1989).

Figure 2.7 shows the lateral distribution of Čerenkov light initiated by a 1 TeV gamma ray and a 3 TeV proton at sea level in MC simulation. The lateral distribution of Čerenkov light initiated by a gamma ray is almost flat out to a radius of $\sim 150\,\mathrm{m}$ at sea level and the detection area reaches the order of $10^4\,\mathrm{m}^2$. Moreover, the Čerenkov photon density detected at sea level is approximately proportional to the primary gamma-ray energy, and thus gives us the appropriate estimation for it. However, at high altitudes, the Čerenkov angular cone is smaller and there are a large number of particles moving parallel to the shower axis, so that the distribution of Čerenkov radiation is not Gaussian but has a sharp peak at zero degree (Fig. 2.8)(Asahara et al. 2003).

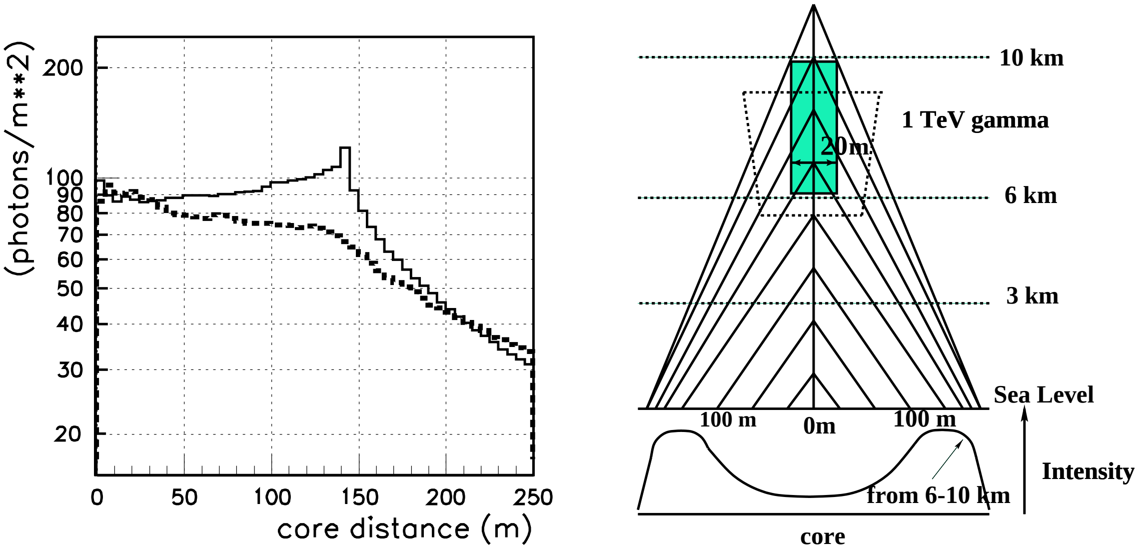

Figure 2.7: Left: Lateral distribution of the Čerenkov light yield on the ground for typical gamma-ray(solid line) and hadron showers(dotted line). The gamma-ray-induced shower shows a relatively flat lateral distribution of light out to about 150m radial distance from the center. Right: Geometric model of the emission of the Čerenkov radiation for gamma-ray and hadron showers. The stippled region encloses the main emission region for production of Čerenkov light from gamma-ray showers. The intensity profiles on the ground reflect the peaking in the Čerenkov lateral distribution for gamma-ray showers at distances to about 150 m from the center of the light pool. For a proton cascade of the same primary energy, its emission region is represented in dashed line.

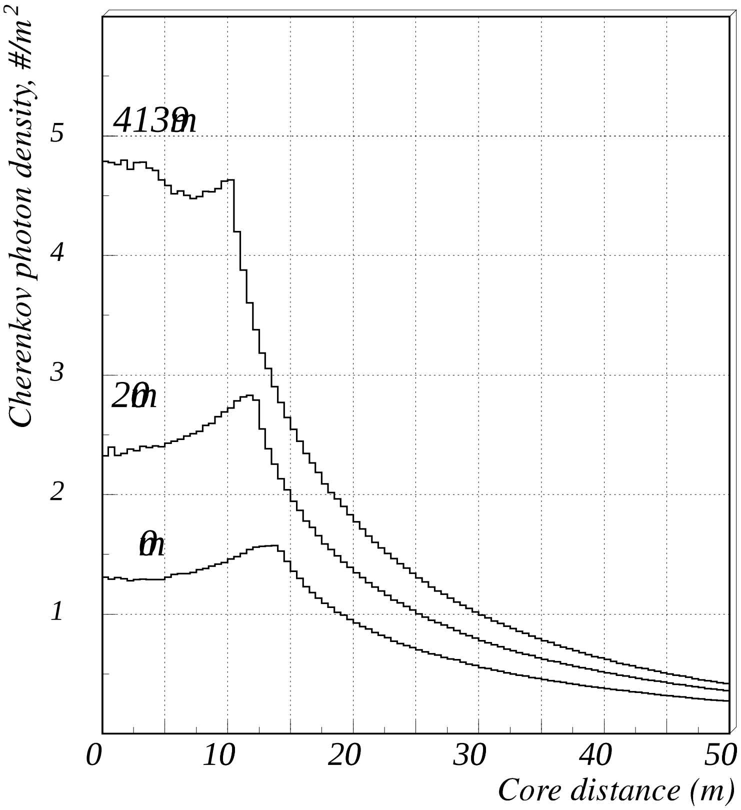

Figure 2.8: Lateral distribution of Čerenkov light from a 10 GeV gamma ray at three different observation levels above sea level: 0 m, 2000 m and 4139 m (MC simulation) (Asahara et al. 2003).

§ 3 Imaging Technique

The rejection of the cosmic-ray background is the main difficulty of the ground-based detectors, since more than 99 % of the atmospheric air showers are caused by the isotropic flux of hadronic cosmic-rays. The flux of a typical gamma-ray source such as the Crab pulsar/nebula is $\sim 10^{-11}\,\mathrm{cm}^{-2}\,\mathrm{sec}^{-1}$ above 1 TeV, while the flux of the cosmic ray (as background) is $\sim 10^{-5}\,\mathrm{cm}^{-2}\,\mathrm{sec}^{-1}\,\mathrm{str}^{-1}$ above the same energy. Assuming a small effective field of view of a telescope with 1° radius ($\sim 10^{-3}$ str), the signal to noise ratio in the detected events is estimated to be $\sim 1/1000$. Therefore, it is nesessary for ground based detectors to reject the hadronic showers effectively. In 1977, efficient technique for the cosmic-ray backgroud rejection was developed by

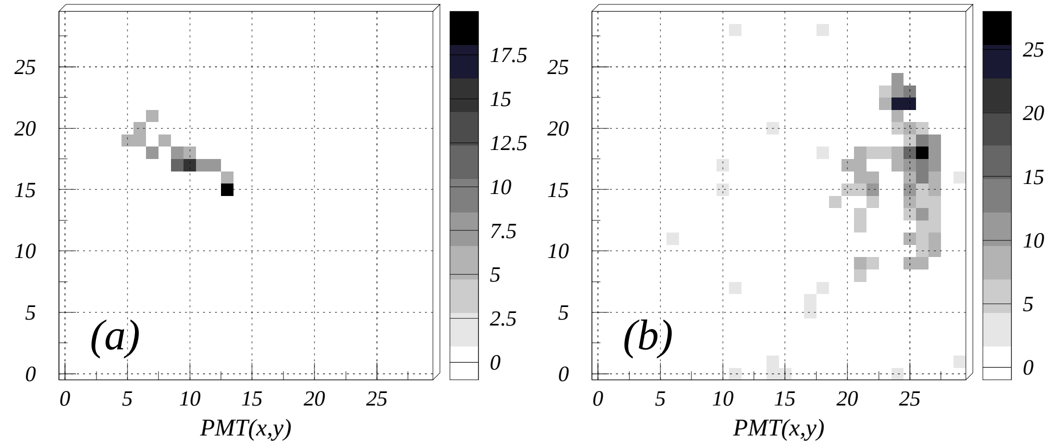

Figure 2.9: Simulated Čerenkov images. (a): 100 GeV gamma-ray. (b): 300 GeV proton.

the Whipple Observatory group. Nowadays, this technique is called by “Imaging technique”.

In this technique, Čerenkov images on the focal plane are recorded with an imaging camera consisting of many photomultiplier tubes (PMTs), and the obtained images well reflect the profile of the longitudinal and lateral developments of the EAS. There are several differences in the development between the EASs initiated by gamma-ray and cosmic-rays, thus Čerenkov images of both kind of showers are also differeces in the orientation and shape. Figure 2.9 shows typical Čerenkov images of an 1 TeV gamma ray and of a 3 TeV proton in MC simulation, respectively. The gamma-ray image elongates to the source position in the field of view, and thus directs toward the center of the camera pointing to the source. On the other hand, the hadronic image has a random direction in the field of view reflecting the random directions of the primary nuclei and the irregularity of the shower development. As the results, the “Imaging technique” provides us the efficient suppression of hadron showers, which improves dramatically the signal to noise ratio by about 100 times.

In 1985, Hillas developed a parameterization of Čerenkov images by fitting an ellipse to those images, and showed that this technique is very effective to enhance gamma-ray signals (Hillas 1985). In 1989, the Whipple group succeeded in detecting TeV gamma rays from Crab Nebula at the 9 σ level using this technique (Weekes 1988). The image parameters generally used in the imaging technique are as follows, and schematically shown in Fig. 2.10.

Width The root mean square (RMS) spread of Čerenkov photons along the minor axis of the image, a measure of the lateral development of the cascade.

Length The RMS spread of Čerenkov photons along the major axis of the image, a measure of the longitudinal development of the cascade.

Distance The distance between the centroid of the image and the source position. Gives information on the core (impact point) distance of the shower with respect to the telecope.

Conc The parameter representing the light concentration in the particular part of an image, as determined from the ratio of the several largest tube signals to the sum of all signals.

Alpha The orientation angle of the image, which is defined as an angle between the major axis and a line joining the centroid of the image to the source.

The gamma-ray showers develop on a parallel with the light axis and elongate to the source position in the field of view. On the other hand, the hadronic showers have a random direction, as shown in Fig. 2.9. Thus the distribution of Distance of protons becomes broader than that of gamma rays. Alpha values of gamma-ray images should be concentrated near Alpha=0°, while Alpha of hadron images should be uniform. Fig. 2.11 (a) shows distributions of ALPHA in MC simulations. Solid and dashed lines show gamma-rays (100 GeV) and Protons (300 GeV), respectively. The Alpha distribution caused by hadrons seems to be increasing slightly above 50 degrees, which is due to the restricted Field of View.

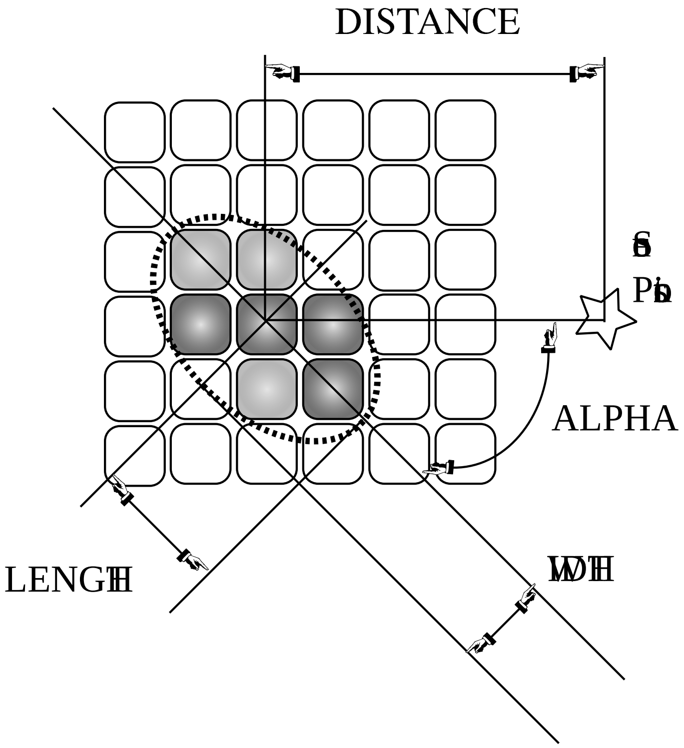

Figure 2.10: Definition of image parameters.

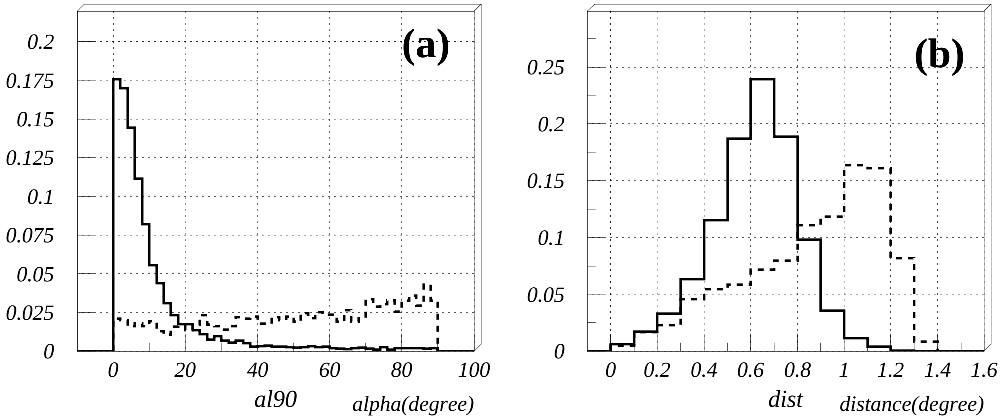

Figure 2.11: Distribution of ALPHA and DIATANCE in simulations. Solid and Dashed line show the image induced by gamma-ray (100 GeV) and Proton (300 GeV), respectively.

Chapter3

Instruments

> "Oh, how I wish I could shut up like a telescope! I think I could, if I only knew how to begin." For, you see, so many out-of-the-way things had happened lately, that Alice had begun to think that very few things indeed were really impossible.
>
> — *Down the Rabbit-Hole* —

Nowadays, there are several 10m-class-mirrors at high altitude, but most of those telescopes have only cassegrain and/or nasmyth foci, and their FOV are too small for IACTs. In general, IACTs need large FOV, at least 1 degree, in order to apply the imaging analysis for the reduction of the night sky background and protons.

The Subaru telescope(Iye and Yamashita 2000), located at the 4,200m summit of Mauna Kea on the island of Hawaii, is the only one telescope which has the primary focus. Its FOV is the largest among 10m class mirrors, about 0.75 degree. This field of view is not large enough to apply the detailed image analysis, such as CANGAROO with a high resolution and large FOV camera. However, a Čerenkovlight image in tens GeV energy is much smaller than that in several 300 GeV which is typical energy threshold of IACT at sea level (See Ch. 4, Fig. 4.1). Even if FOV is small, multi PMTs with small pixel size of $\sim 0.1^\circ$ can reduce N.S.B efficiently and reduce proton events to some extent. Moreover, at high altitude, Signal to Noise ratio (defined by gamma-ray counting rate over hadron counting rate) is higher than at sea level. According to our simulation, we could observe sub 100 GeV energy gamma-rays using 10m class mirror at 4000m altitudes (Ch. 4). At this time, the

Subaru telescope is only one telescope to do such a high altitude observation.

We developed a gamma-ray camera, designated CheSS (Čerenkovlight detecting System on Subaru)(Asahara et al. 2003) based on IACT, for the Subaru telescope. In this chapter, I show the properties of CheSS.

§ 1 Telescope

The Subaru Telescope is an optical-infrared telescope at the 4,200m summit of Mauna Kea on the island of Hawaii. This is a new generation telescope not only because of the size of its mirror with an effective aperture of 8.2 meters, but also because of the various revolutionary technologies used to achieve an outstanding observational performance. An active support system that maintains an unprecedentedly high mirror surface accuracy, a new dome design to suppress local atmospheric turbulence, an extremely accurate tracking mechanism using magnetic driving systems, seven observational instruments installed at the four foci, and an auto-exchanger system to use the observational instruments effectively are just some of the unique features associated with this telescope.

The Subaru telescope also has the good features as an imaging air Chrenkov telescope. The large FOV and long focal length are characters of an IACT, and the Subaru telescope has both of them (FOV: 0.75°, Focal length: 15m). Moreover, other specifications, such as a mirror accuracy, tracking accuracy, and so on, are quit excellent and may be overmuch for an IACT. I listed up the specifications of the Subaru telescope in table 3.1.

§ 2 Overview

Size, weight, and power consumption of the instruments at the Subaru prime focus are severely restricted. Thus, CheSS for the prime focus is one of the most compact detectors among the instruments of Subaru. The chassis has a cylindrical shape with a base radius of 0.5m, a height of 1m, a weight of about 200kg, and a power

Table 3.1: The specifications of the Subaru telescope

Mounting	altitude-azimuth configuration
Primary mirror	
Effective diameter	8.2 m
Thickness	200 mm
Weight	22.8 t
Material	ULE (ultra-low thermal expansion glass)
Mean surface error	1.4×10^{-5} mm
Focal length	15 m
Four foci	
Primary focus	F2.0 with corrector
Cassegrain focus	F12.2
Nasmyth foci	F12.6 (optical and infrared)
Telescope size	
Height	22.2 m
Max width	27.2 m
Weight	555 t
Telescope characteristics	
Max pointing speed	0.5 deg/sec
Tracking accuracy	0.1 arcsec -
Elevation	10 - 89.5 deg.
Total angular resolution	0.2 arcsec @ 2.15 micron

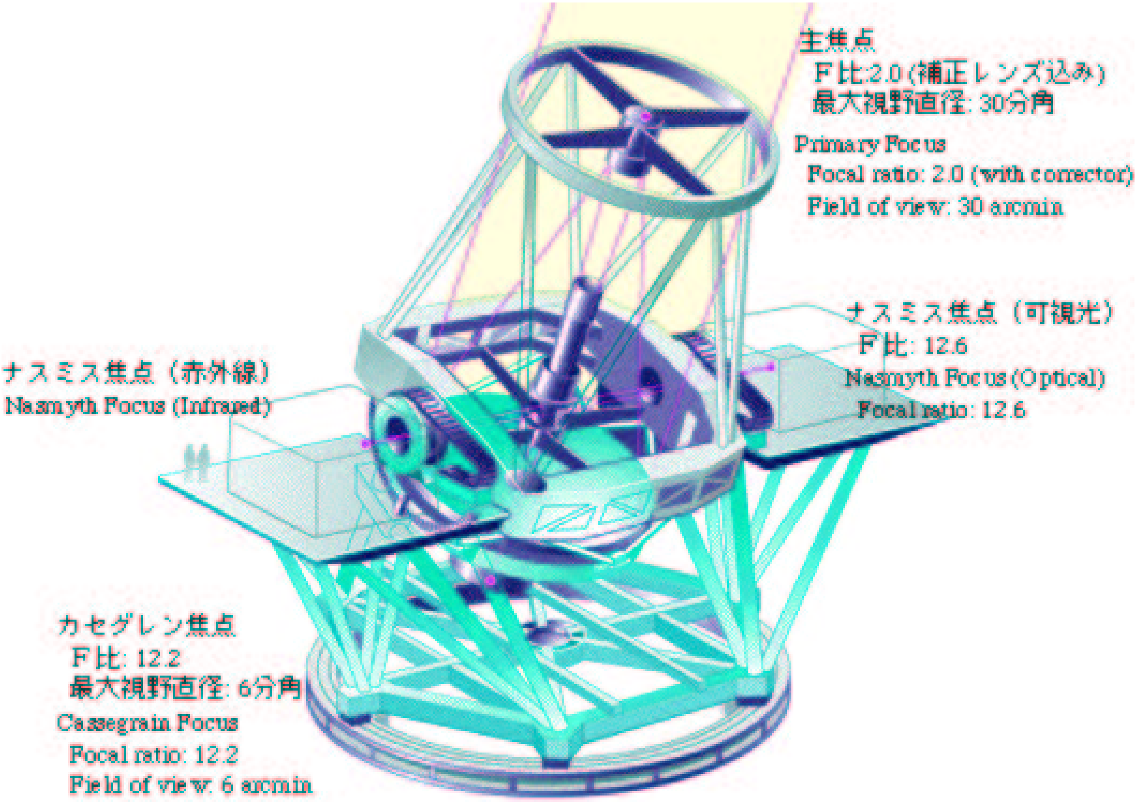

遠藤孝悦・画　日経サイエンス1996年2月号より
Illustration by Takaetsu Endo, taken from Nikkei Science 1996

Figure 3.1: The illustration of the Subaru telescope.

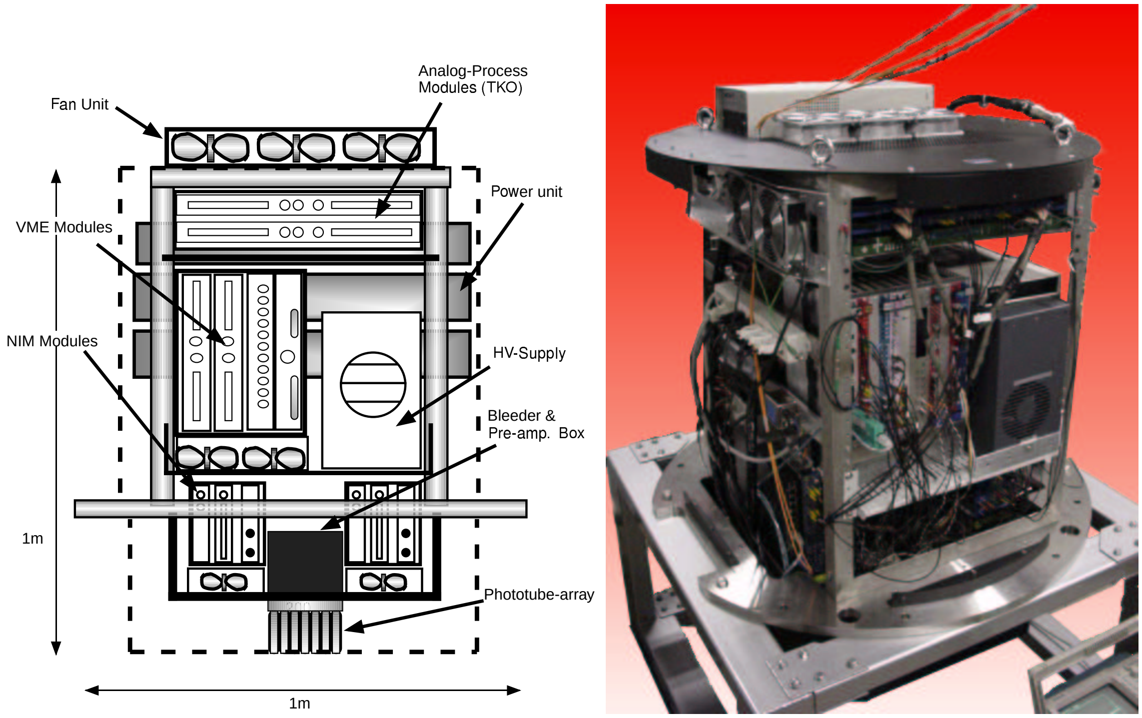

Figure 3.2: CheSS Overview.

consumption under 700W (Fig. 3.2). DC power lines for the electronics units are supplied by six low-noise switching power supplies inside CheSS. CheSS is installed to the Subaru telescope through the Prime Focus Unit (PFU) of which size is larger than CheSS and provides the main power line (AC120V) and optical fiber cables for networking (10Base-T). Figure 3.3 shows how to install CheSS in PFU and how to install PFU on the primary focus.

§ 3 Camera

The focal plane detector consists of an array of 44 separate photomultiplier tubes (PMTs) (Fig. 3.4), and covers a field of view of $0.75° \times 0.75°$. This PMT (Hamamatsu 2497UV) is sensitive to photons between 350nm and 450nm, and its quantum efficiency is about 20 % in this region (Fig. 3.7). The size of the photo-cathode is 23mm × 23mm in square shape, without light guides. The photo-cathodes of 44 PMTs have a total size of 2.3×10^4 mm^2, and cover the ~ 60% of FOV.

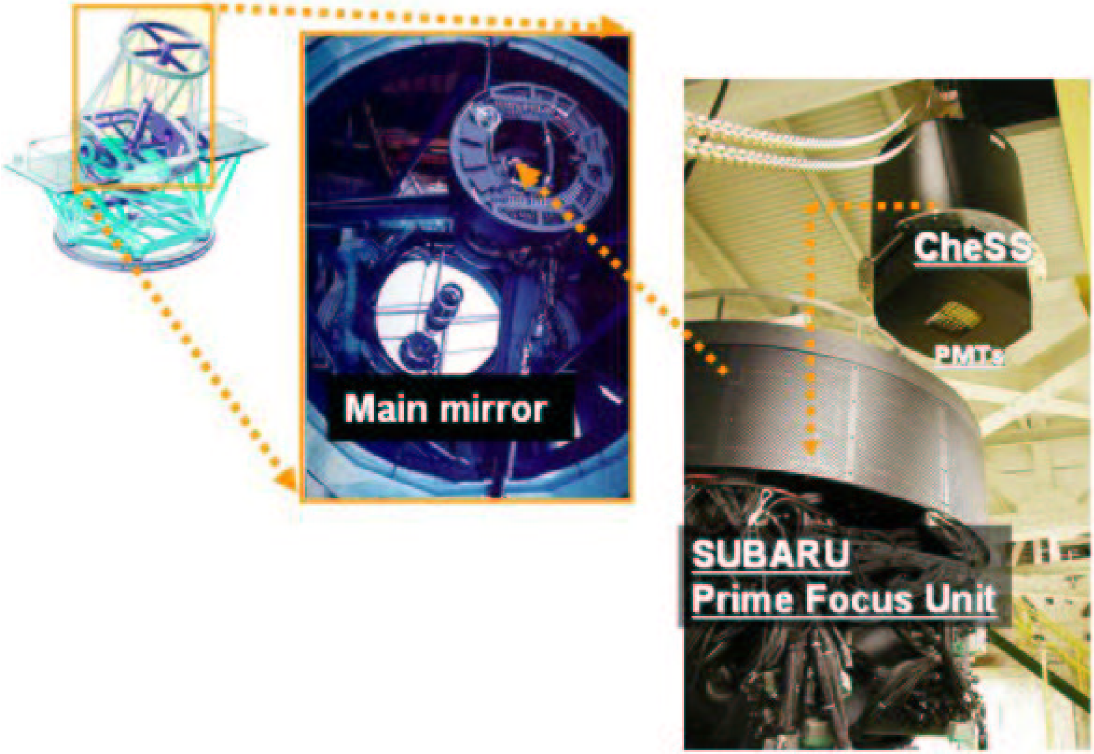

Figure 3.3: How to install CheSS on the prime focus.

Figure 3.4: Photo Multiple Tube array which covers a field of view 0.75° × 0.75°. The size of each PMT is 26mm × 26mm (the photo-cathode is 23mm × 23mm). The black box behind PMTs is AMP-BOX which consists of amplifier chips (LeCroy TRA402S).

High voltages are applied to blocks of 5 PMTs from the HV power supply units (LeCroy 1451) which are remote-controlled via an optical-RS232C converter. The high voltage values are around -1500V, but slightly different from block to block in order to equalize PMT gains whose average value is about 4×10^5. Signals from PMTs are amplified in AMP-BOX which consists of amplifier chips (LeCroy TRA402S), and sent to Discriminator & Summing Modules (DSMs).

§ 4 Photon collection efficiency

Not all Čerenkov photons coming down Subaru telescope are detected by CheSS. The number of Čerenkov photons is decreased (i) on the mirror, (ii) in the transmittance of the correction lenses of PFU, and (iii) at the photo-cathode. In this section, we collectively call these three factor "photon collection efficiency", and discuss it.

Figure 3.5 shows the reflectivity of mirror. A number of microscope slides were placed in the coating chamber when the primary mirror was aluminized. These slides were then brought down to the Base Facility, where their reflectivity was measured in the laboratory by a spectrophotometer. The reflectivity of two such samples coated in August 1999 is indicated in this figure. As shown in this figure, the reflectivity of the Subaru main mirror is much higher than that of standard 10m class IACT.

Figure 3.6 shows the transmittance of the correction lenses of PFU. The correction lenses installed in PFU reduce aberration and give us high quality images, but obscure the Čerenkovphotons to PMTs because Čerenkovphotons are mostly in the ultra violet band and lenses are designed to translate the optical or infrared light. The transmittance was measured in the laboratory only in the wavelength between 360 to 700nm, thus we fitted the decrease of transmittance with the exponential curve. As shown in this figure, even in the UV band, the lenses have sufficient transmittance, which is is about 50 % at 360nm.

Figure 3.7 shows the quantum efficiency of PMT (Hamamatsu 2497UV) as a function of wavelength. The maximum quantum efficiency is about 0.25 at 360nm.

The photon collection efficiency is defined as, (i)×(ii)×(iii). Figure 3.8 shows the results of the calculation.

§ 5 Electronics

Figure 3.9 shows an overview of the electronics. At first, PMT signals are amplified and sent to DSMs. DSM was originally developed for the CANGAROO telescope, and it has multi functions useful for IACT (Fig. 3.10). In the DSM, signals are amplified with fast shaping amplifiers, and fed to two independent discriminators. One is an updating discriminator for measuring the hit timings by Time to Digital Converters (TDCs), and the other is non-update discriminator whose digital output

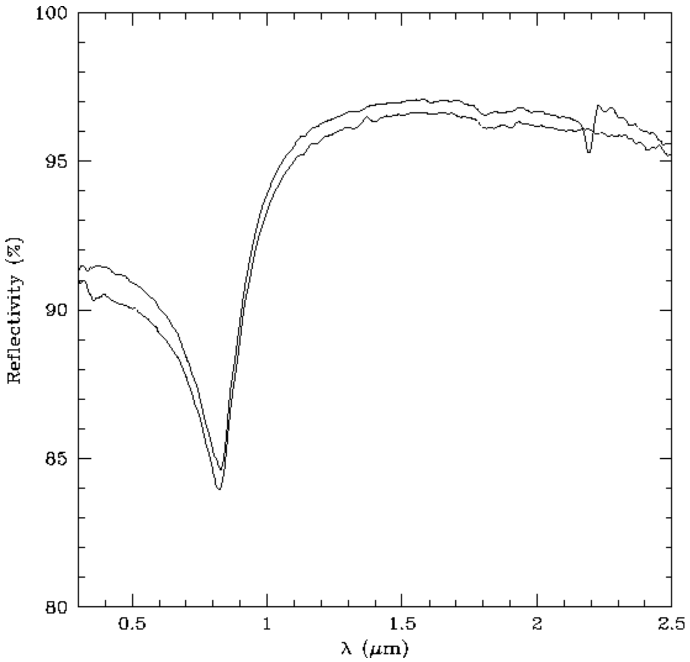

Figure 3.5: The reflectivity of the Subaru main mirror.

is counted by 12bit scaler, and used for the event trigger logic which we call as "Liner SUM" or "LSUM". Its pulse width is set to be about 20nsec, to caver the time dispersion of Čerenkovlight photons emitted by air showers. In addition, DSM outputs the summed signal of 16 channel (hereafter "ASUM"). ASUM signals are also used for the trigger logic. Setting the thresholds of two discriminators and readout of 12bit scaler data are conducted via the VME bus.

The data acquisition trigger scheme is shown in Fig. 3.10. LSUM signals from DSMs are summed, and discriminated to determine how many PMTs hit within the gate time width of 20 nsec. On the other hand, ASUM signals are also summed, and discriminated to determine how much number of photoelectrons are detected. Thresholds of these two discriminators (CAEN V253) are adjustable via VME-bus. The coincidence of both discriminator outputs becomes the event trigger. In order to check the DAQ system, a pulse from a GPS receiver is added to a DAQ trigger every second. This is how we can put a trigger condition, such as "Trigger when 2PMTs detects 3 photoelectrons simultaneously".

The main measurement device of CheSS is TDC (CAEN V667) for each PMT

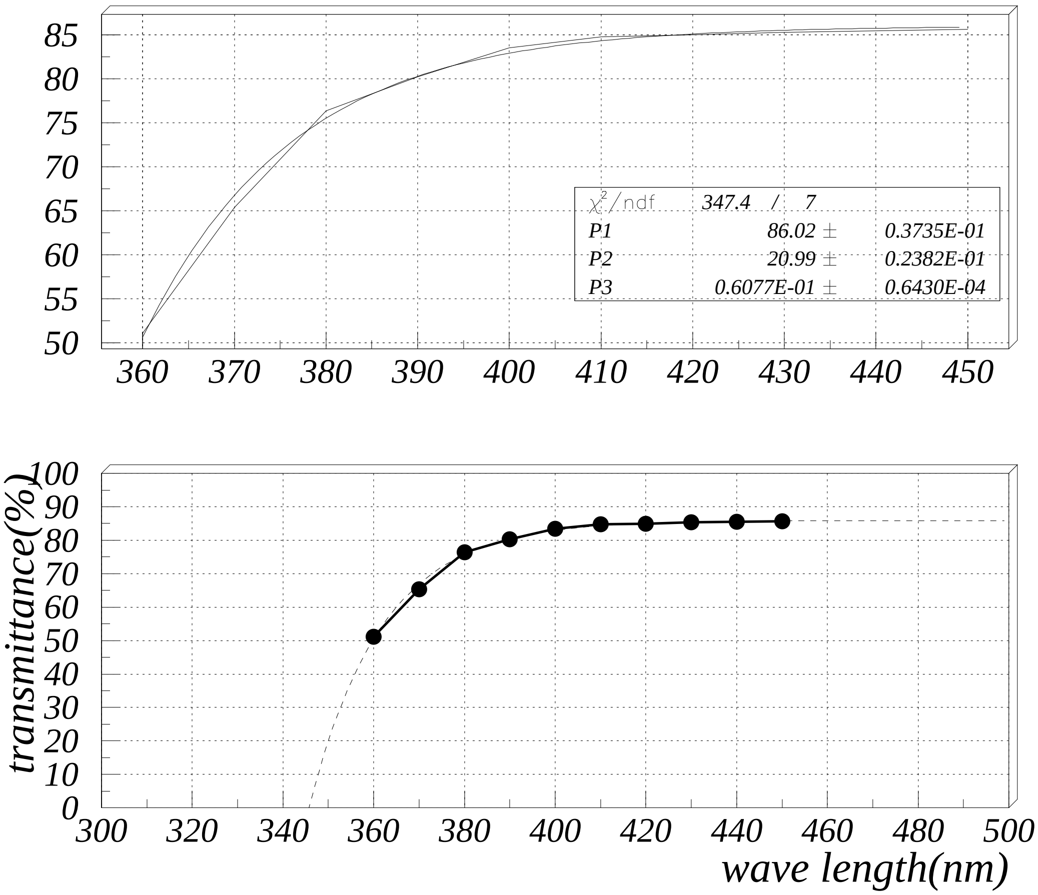

Figure 3.6: The transmittance of the correction lenses of PFU.

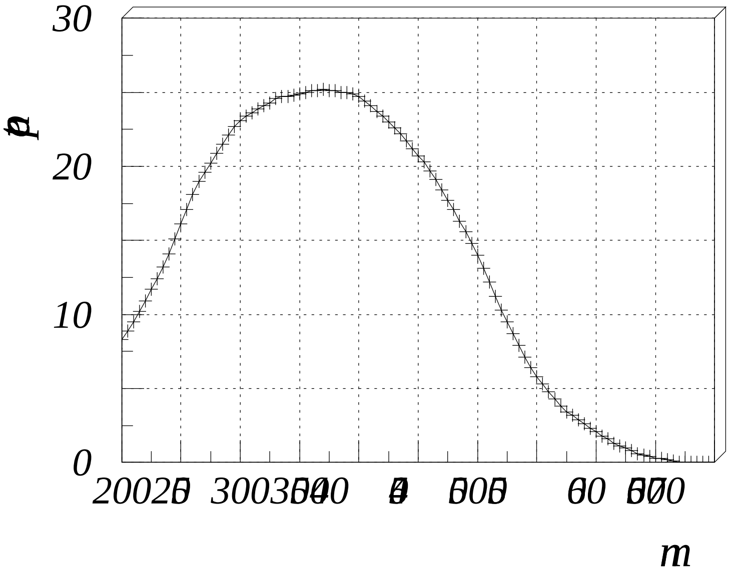

Figure 3.7: The quantum efficiency of the Hamamatsu 2497UV.

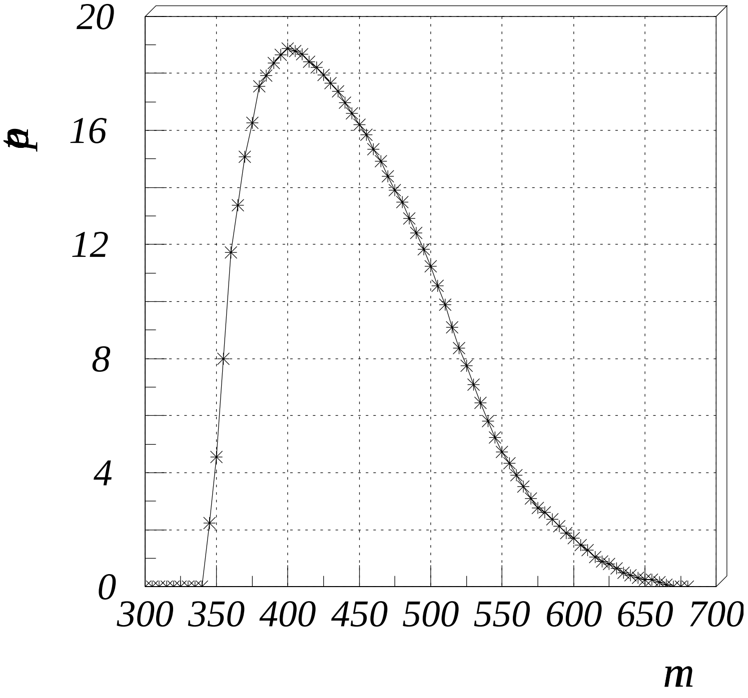

Figure 3.8: The photon collection efficiency of CheSS.

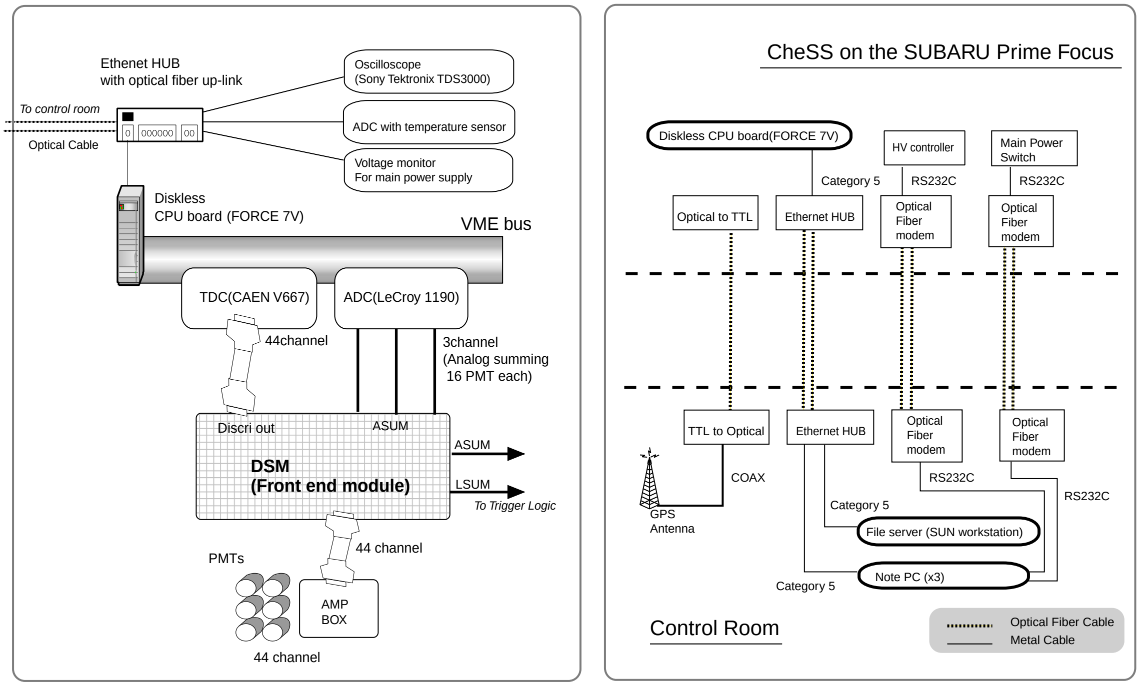

Figure 3.9: Left: Diagram of electronics inside CheSS. The CPU board controls all the electronics, readouts the data in the memory of VME modules, and sends it to the file server. Right: Diagram of connection between CheSS and Control room.

channel. TDC records rising and falling time of PMT signals. Its time resolution is 0.75 nsec, and time window is 840 ns. TDC can recode multi-hit event, and features the double hit resolution of 10 ns.

Total number of photo-electrons is measured by 3 channel Analog to Digital Converters (ADC, Lecroy 1182). 3 channels are corrrespoinding to 3 ASUM signals from DSMs. CheSS is not equiped on ADC for each PMT, but we can estimate the number of photo-electron using TDC width (see section 2.3).

§ 6 Internal clocks

A precise time stamp is necessary to analyze the pulsed component of the Crab pulsar. CheSS has three independent clocks. The first clock is the CPU system time, which is adjusted by Network Time Protocol (NTP) server via Ethernet. NTP is designed specifically for use in a large, diverse Internet system. Therefore, it has

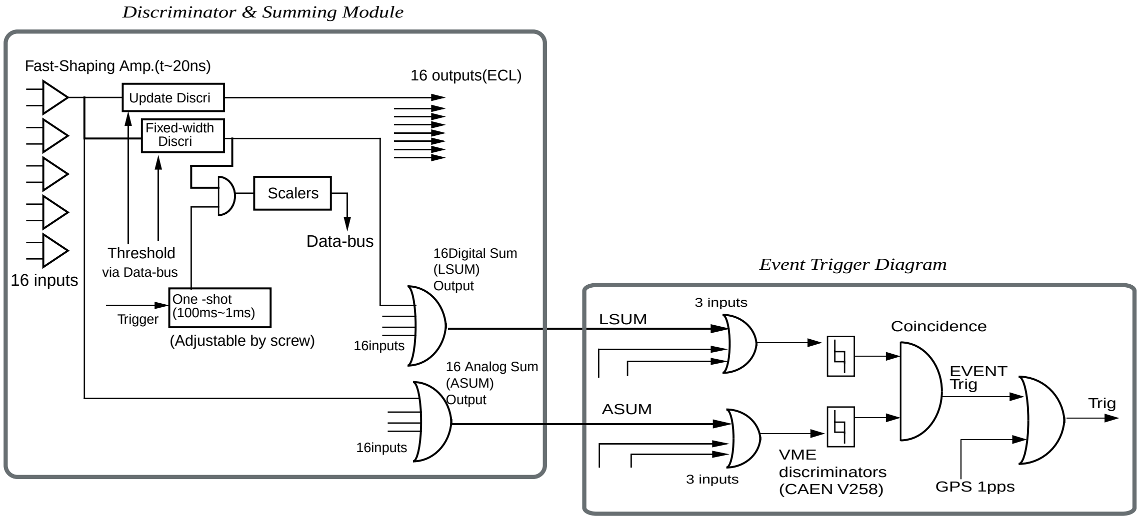

Figure 3.10: The diagram of Discriminator & Summing Module (DSM) and Event trigger logic. Threshold for update discriminators and fixed-width discriminators (non-update) are set by the diskless CPU board via VME-bus. The 12bit scaler data is also read out via VME-bus.

a modest accuracy of a few tens of milliseconds, but we can trust at least a second time scale of the CPU system time. The second clock is the 1MHz quartz oscillator. The VME latching scaler, CAEN V830, has counted 1MHz oscillator pulses since the main power supply is turned on. The latching scaler writes counts of the moment in its internal memory at just the same time when triggers are generated (Fig. 3.11). Thus, we can use that count data as a micro-second accuracy clock. The third and the most accurate clock is inside of the GPS time server module. This module receives the 1pps signal from the GPS antenna, and tell us the high accuracy time using its internal high-precision quartz. According to the manual, This module has the accuracy of μsec order.

Figure 3.12 shows the accuracy of each clock. As mentioned above, 1pps pulse from the GPS antenna are added to the DAQ trigger every second to check the DAQ system. We analyzed the time difference between two contiguous time stamps recorded at the time when 1pps trigger generated. If you use an ideal clock, the difference of the time stamps are just 1 sec. In figure 3.12, we shows "the time difference - 1.0 sec" recorded by each clock to focus the stability of msec order. GPS time server module gives the most accurate time, and that is about ±1 μsec.

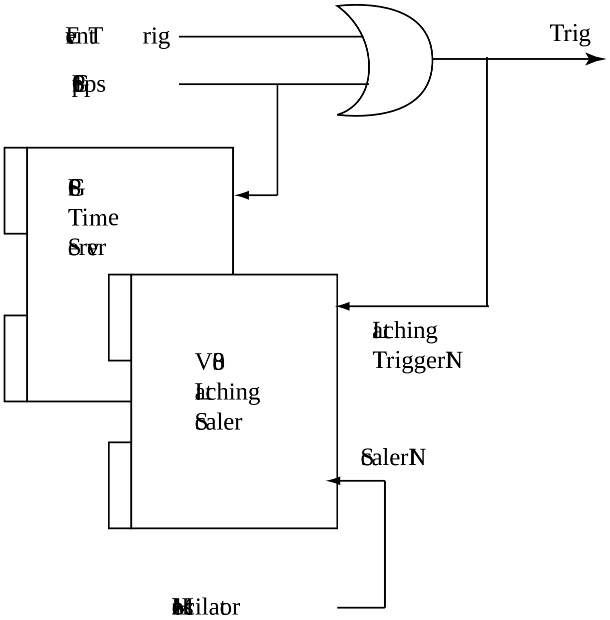

Figure 3.11: The diagram of the V830 latching scaler and GPS time server

§ 7 Data Acquisition

Inside CheSS and the control room are networked via optical fiber cables which is compliant with IEEE 802.3 10Base-T Ethernet Protocol. The disk-less CPU board (FORCE 7V) inside CheSS controls all electronics except high voltage modules[1], readouts the digital data from fast VME-bus modules, and then, sends the data to the control room via optical fiber cables (Fig. 3.9 right panel). The file server for disk-less CPU is a SUN Solaris^{TM} 2.6 based UNIX workstation. The file server is installed in the control room, and receives the data from disk-less CPU board inside CheSS. The environment inside the astro-dome is quite severe for a hard disk. The air temperature is always near 0 °C, and the telescope is always moving to track the target. Therefore, a VME board CPU cannot use a hard disk. Instead, it mounts a

---

[1] On the point of security, another independent PC controls high voltage modules via optical-RS232C converter.

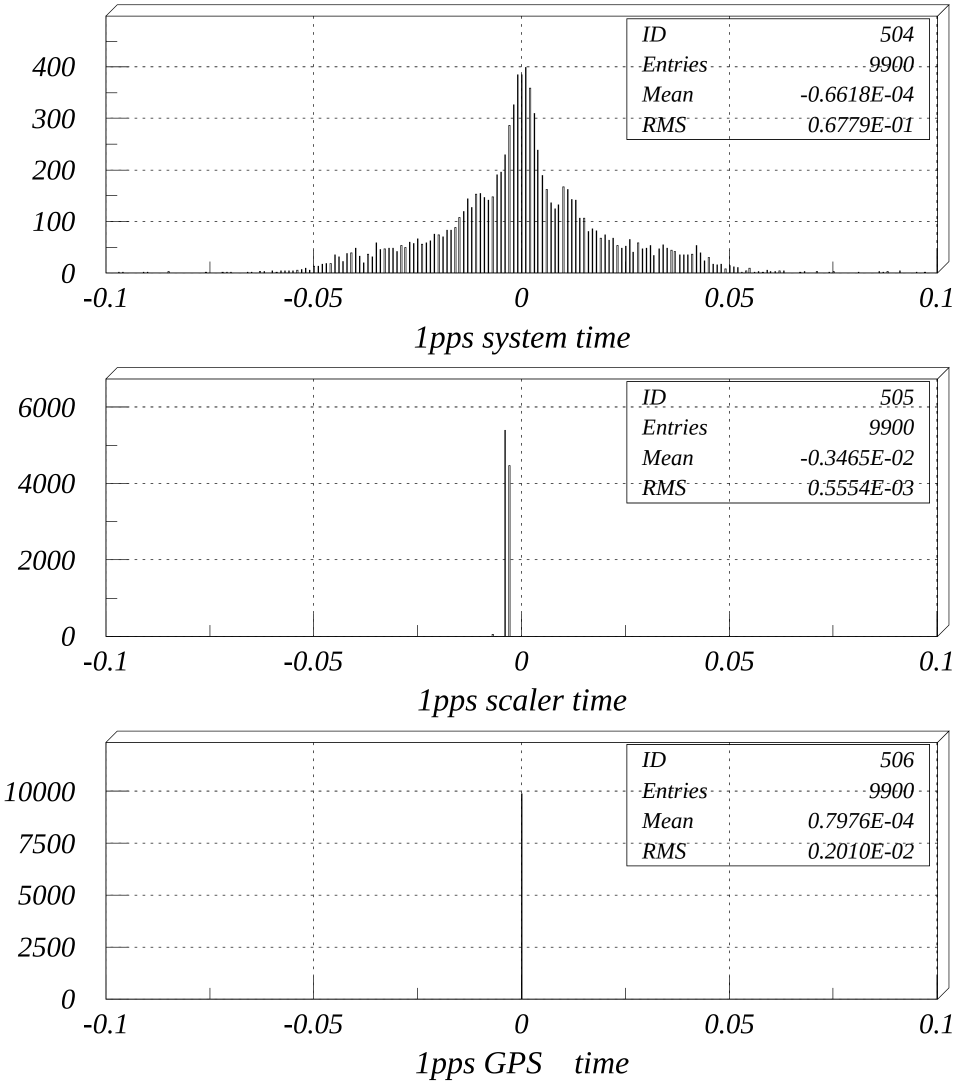

Figure 3.12: The time accuracy of each clocks. Top, middle, and bottom figure show the time stamp recorded by CPU system time, 1MHz qurts oscillater, and the GPS time server module. Note that Unit is msec.

system disk via NFS (Network File System) from a file server located in the control room. This is so called “Diskless client - File server” system.

The software for the data acquisition (DAQ) is based on the “UNIDAQ package” (Ball et al. 1993). UNIDAQ is a reasonably portable, modular, UNIX based, data acquisition system. Its implementation for a given user can cover from a simple two-process system, to a large system which runs on multiple processors with multiple data sources and a variety of analysis and display activities. There are 3 main process working on CheSS CPU during DAQ (Fig. 3.13). “Collector” fetches the binary data from the memory of various VME modules, and write the data on the shared memory which is the dynamic storage allocated on the physical memory in the diskless CPU. “Recorder” reads the data from the shared memory at intervals, and writes it on the NFS mounted hard disk. “Buffer Manager” manages the shard memory, and asks Recorder to readout the data before the run out of memory. “Analyzer” runs on the file server in the control room. This is the quick-look analysis program, and provides the real-time event monitor. “Subaru OBS” is the monitor program of the movement of Subaru telescope. Its data is also recoded on the hard disk inside the file server.

This cliant - server system is secure on the point of the damege of hard disks, but the trade-off is the performance of data acquisition speed. In this case, however, it does not matter since the data size of CheSS is quite small, about 500 Byte per event. According to our test of the data acquisition performance, CheSS CPU can deal with event triggers at 300Hz with dead time of 20% (Fig. 3.14).

§ 8 Calibration of the pulse width measured by TDC

The number of photoelectrons detected with CheSS is estimated using the width of TDC data(Fig. 3.15). We calibrated the TDC width vs. ADC channel using a blue LED (Nichia NSPB320BS). The result of this calibration is shown in Fig. 3.15. The ADC channel has roughly linear correlation with the number of photoelectron. In

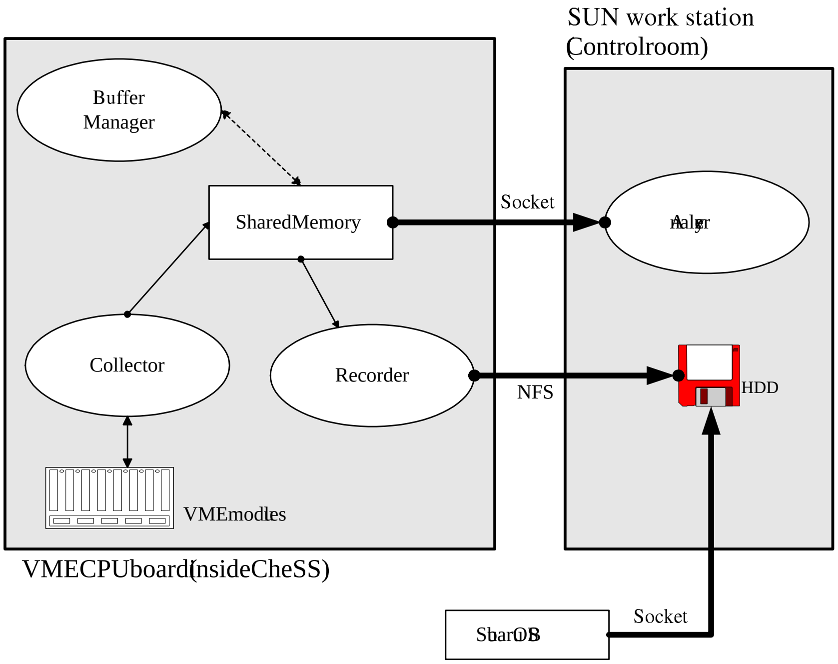

Figure 3.13: The schematic diagram of processes running during data acquisition.

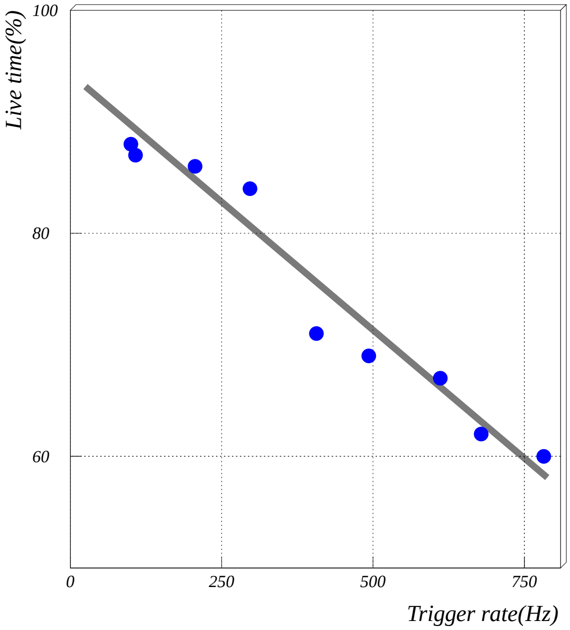

Figure 3.14: The data acquisition speed of CheSS.

this case, one photoelectron is estimated to be about 35 ADC channel.

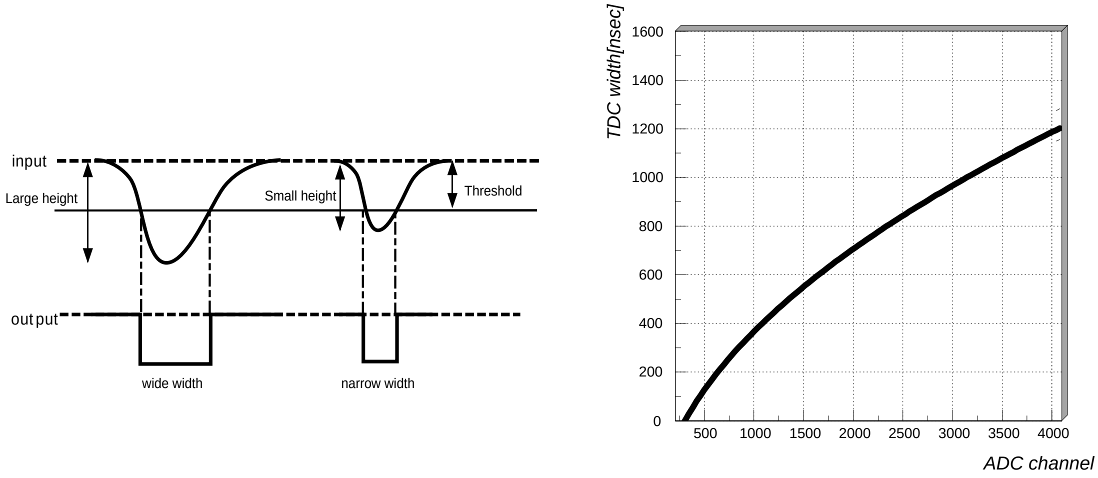

Figure 3.15: TDC width (hit over threshold) calibration. The number of photoelectrons detected with CheSS is estimated using the width of TDC data. Left: the concept of this method. Right: the result of the calibration.

§ 9 Inspection modules

To monitor the status of instruments, CheSS has some auxiliary modules shown in Fig. 3.16. The network oscilloscope provides us 4 channel waveforms via Ethernet. We chose 4 outputs which are most important ones for the CheSS' DAQ, and checked those 4 outputs at 1 sec intervals. If necessary, we can also record those waveforms on a hard disk.

The voltage monitor is consisted of the voltage transducer (AC 120V → DC 2V) and 8bit ADC, and monitor the voltage fluctuation of the main power line. The output of the transducer is insulated with the input (main power line), and thus the short circuit is never happened. The ADC is remote controlled by Windows^{TM} note PC in the control room. Therefore, we can use the voltage monitor even if the disk-less CPU inside CheSS were stalled.

CheSS also equips the two blue LEDs with the pulser which is able to generate rectangular waves at 100 or 1000 kHz frequency. The pulse width of the rectangular waves is fixed at 50 nsec, and the pulse hight is adjustable by remote control via optical fibers in the range between 0 and 5 Volt We can not access inside CheSS once it is installed, because it is installed on the prime focus which is 15 m above the floor. Therefore, this LED unit is quite important since it enable us to check the DAQ and calculate PMTs during observation.

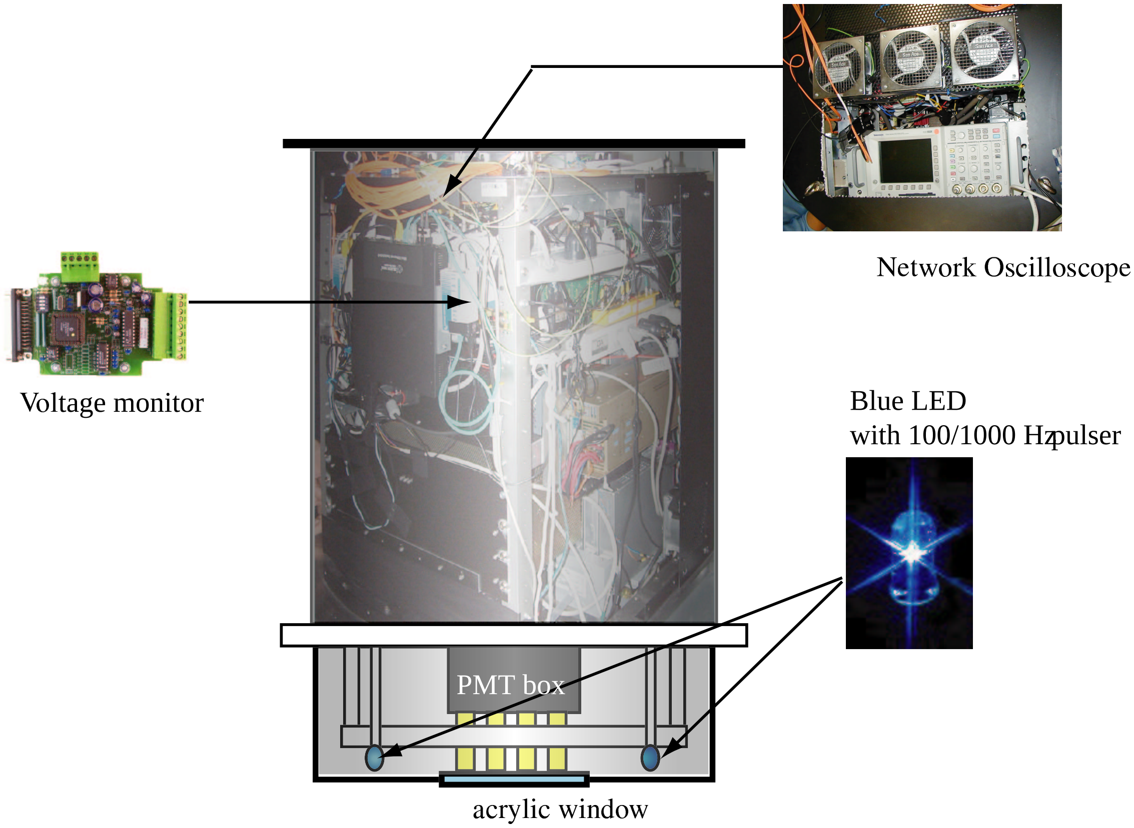

Figure 3.16: Inspection modules installed in CheSS.

Chapter4

Simulation

> "I'm very sorry you've been annoyed," said Alice, who was beginning to see its meaning.
>
> "And just as I'd taken the highest tree in the wood," continued the Pigeon, raising its voice to a shriek, "and just as I was thinking I should be free of them at last, they must need come wriggling down from the sky! Ugh, Serpent!"
>
> — *Advice from a Caterpillar* —

In this chapter, the performance of CheSS is described, based on the Monte-Carlo simulation. Although CheSS' 0.75 degree FOV camera is relatively small for IACTech, a Čerenkovlight image for tens of GeV energy is much smaller than that for several 100 GeV, which is the typical energy threshold of a 10 m class IACT at sea level (Fig. 4.1). We use the CORSIKA package (Heck et al. 1998) to simulate extensive air showers generated by gamma-rays, protons, and electrons. CORSIKA is a detailed Monte-Carlo simulation program used to study the evolution and properties of extensive air showers in the atmosphere.

From a comparison between the simulated and observed shower events, it was found that the N.S.B. and muon showers have significant effects on the detection rate below 80 GeV in spite of the small FOV of CheSS. The simulation result, which includes muon shower events, suggests that CheSS has the capability of sub-100 GeV energy gamma-rays.

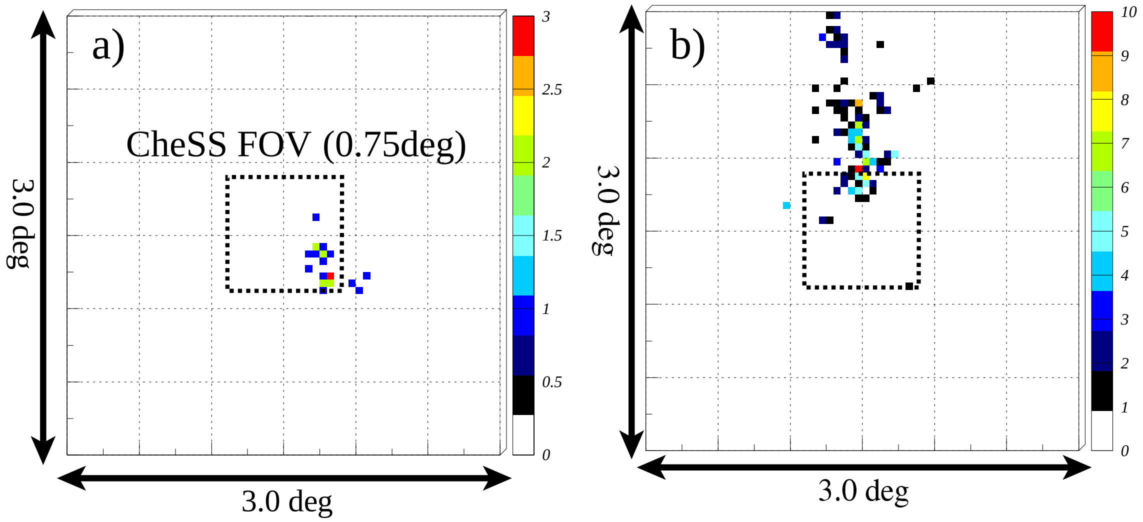

Figure 4.1: Example images of typical gamma-ray showers at 4200 m a.s.l.(simulation). (a) 30 GeV gamma-ray; (b) 300 GeV gamma-ray.

§ 1 Field of view

The Field of view is one of the principal parameters for IACTs. Let us estimate how much events CheSS can detect on the focal plane using Imaging Parameters (See Ch.2 § 3). Figure 4.2 shows the distributions of the DISTANCE, WIDTH, and LENGTH parameters as a function of the energy of gamma-rays. For 30 GeV gamma-ray showers, the DISTANCE, WIDTH, and LENGTH distribute from 0 to 1.2 degrees, from 0 to 0.1, and from 0 to 0.4, respectively. To capture whole Čerenkovimages, we need a FOV of following value

$$\mathrm{DISTANCE} + \sqrt{\mathrm{WIDTH}^2 + \ \mathrm{LENGTH}^2}\ . \tag{4.1}$$

Figure 4.3 shows the distributions of this value for 30 and 500 GeV gamma-ray showers. According to this figure, a 0.75 degree camera can detect only sim 15% of the total events for 30 GeV gamma-ray showers.

However, at 4200 m a.s.l, the density of Čerenkovlight within a core distance of $\geq$ 100m is 3.4-times larger for gamma-ray showers than at sea level (Fig. 4.4). Moreover, at high altitudes, the signal-to-noise ratio (defined by gamma-ray counting rate over proton counting rate) is improved. The density of Čerenkovlight at 4200 m induced by proton showers is only 1.8-times larger than at sea level (Fig. 4.4). Consequently, even with such a small FOV of 0.75 degrees, it has the capability to detect sub 100 GeV gamma-rays. The simulated evidence is described in following sections.

Figure 4.5 shows the distributions of the ALPHA parameter for gamma-ray showers with an energy between 10 and 50 GeV, detected by a camera with FOV values of 1.0, 1.5, 2.0, and 3.0 degrees. This figure indicates that a 0.75 degree FOV camera is not large sufficient to apply the "Imaging Method" for proton rejection. Therefore, we estimate the gamma-ray flux using ON-OFF chopping methods. To reduce the systematic error, we need to reject N.S.B. as much as possible. The 44 PMTs with a small pixel size of $\sim 0.1^\circ$ installed on CheSS, can reduce the N.S.B. efficiently and reduce the proton events to some extent (See Ch. 6).

As mentioned in Ch. 3, the primary focus of the SUBARU telescope gives us the largest FOV among 10m class mirrors at the present moment. If we constructed 10 m class telescope(s) specialized for the IACTech, how much FOV were sufficient to provide the high detection efficiency for γ-rays? From the standpoint of ALPHA parameter, at least 1.5-degree FOV is necessary, as shown in Fig. 4.5. From the standpoint of the parameter defined as Eq.4.3, 3.0-degree FOV camera seems to be the best since it can detect almost all events in the energy range between 30 and 500 GeV (Fig. 4.3). We discuss the performance such a large FOV camera at high altitudes in Ch. 8.

§ 2 Simulation parameters

Table 4.1 lists the specification of CheSS. The focal plane detector consists of an array of 44 separate PMTs, and covers a field of view of $0.75^\circ \times 0.75^\circ$ (Ch.3 § 3). The hardware trigger is generated when N PMTs have signals above Q photo-electrons within a gate time of 20 nsec. We call such a trigger condition "N PMT × Q ph.-e.", for simplicity. Other simulation parameters are listed in Table 4.1.

We discuss simulated air showers within the core distance of 100 m. In Fig.

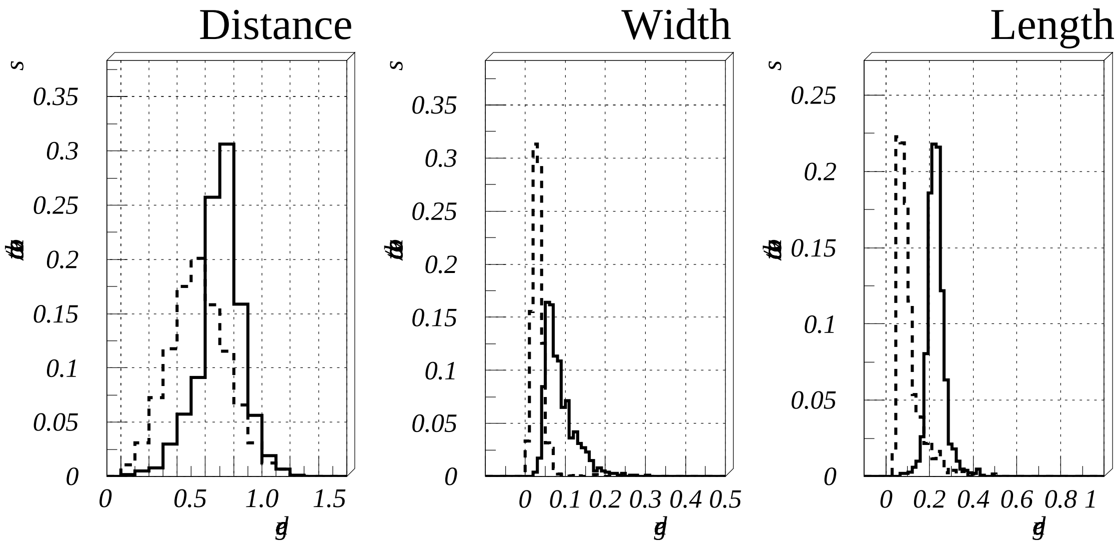

Figure 4.2: DISTANCE, WIDTH, and LENGTH parameters of a standard 10 m class IACT at 4200 m a.s.l. The solid line shows 500 GeV, and the dashed line shows a 30 GeV energy gamma-ray seed.

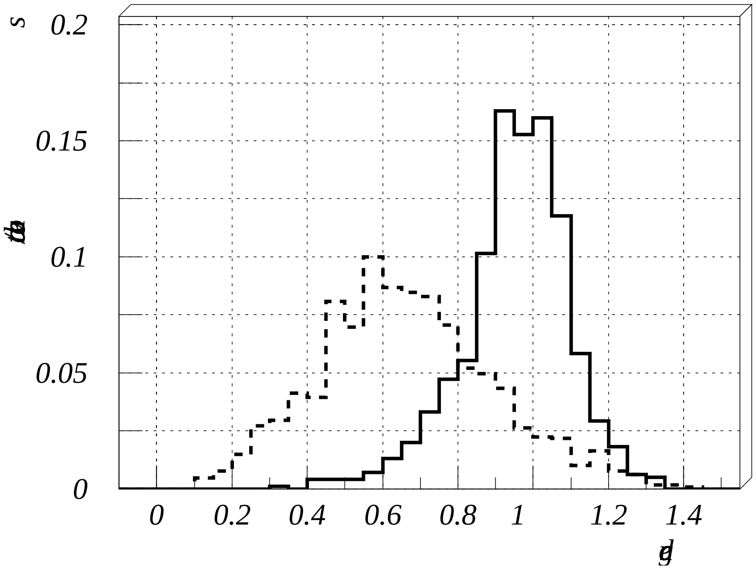

Figure 4.3: Distributions of, DISTANCE + $\sqrt{\text{WIDTH}^2 + \text{LENGTH}^2}$ at 4200 m a.s.l. The solid line shows 500 GeV, and the dashed line shows a 30 GeV energy gamma-ray seed.

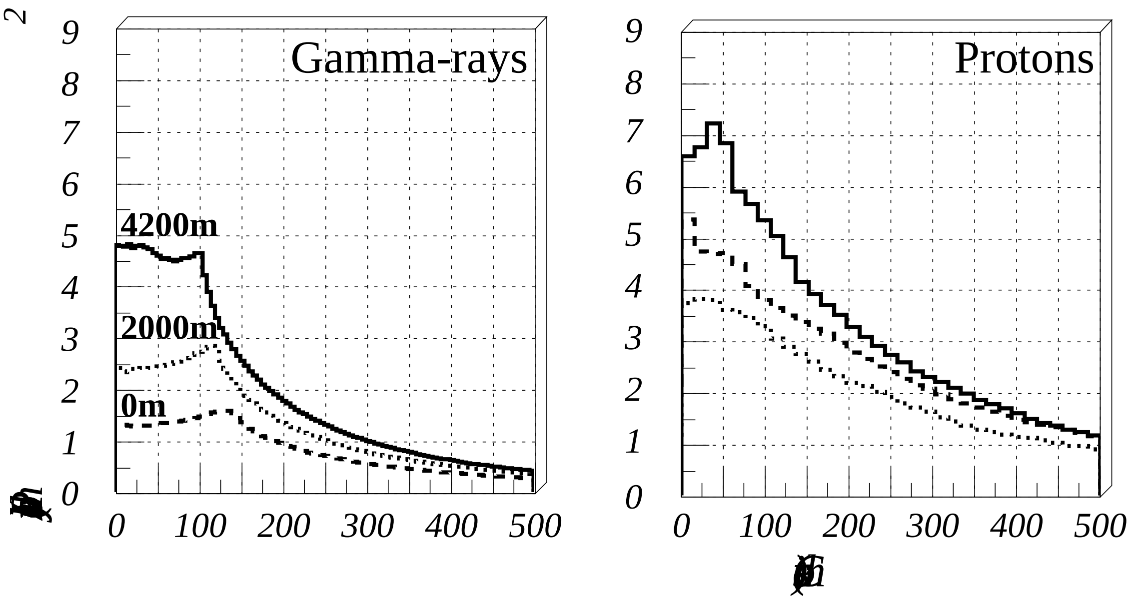

Figure 4.4: Density distribution of Čerenkovlight photons caused by 10 GeV gamma-rays (Left) and 100 GeV protons (Right) at various altitudes, which were averaged over 1000 showers. The solid, dashed, and dotted line show 4200, 2000, and 0 m a.s.l.

Table 4.1: Simulation parameters of CheSS.

Mirror dimensions	$8.2m\phi$, $52.8m^2$ area, monolithic
Focal length	15m
Mirror Reflectivity	Ref. Subaru data(NAOJ 2001)
Transmittance of correction lenses	> 80%(400nm-600m) (Komiyama 2001)
Field of view	0.75 degrees
Camera pixels	44
Quantum efficiency	Ref. HAMAMATSU R2497 spec sheet (Hamamatsu Photonics K.K. 2004)
Site	Hawaii(4200m)
Atmospheric model	U.S. standard atmosphere(Linsley 1988)

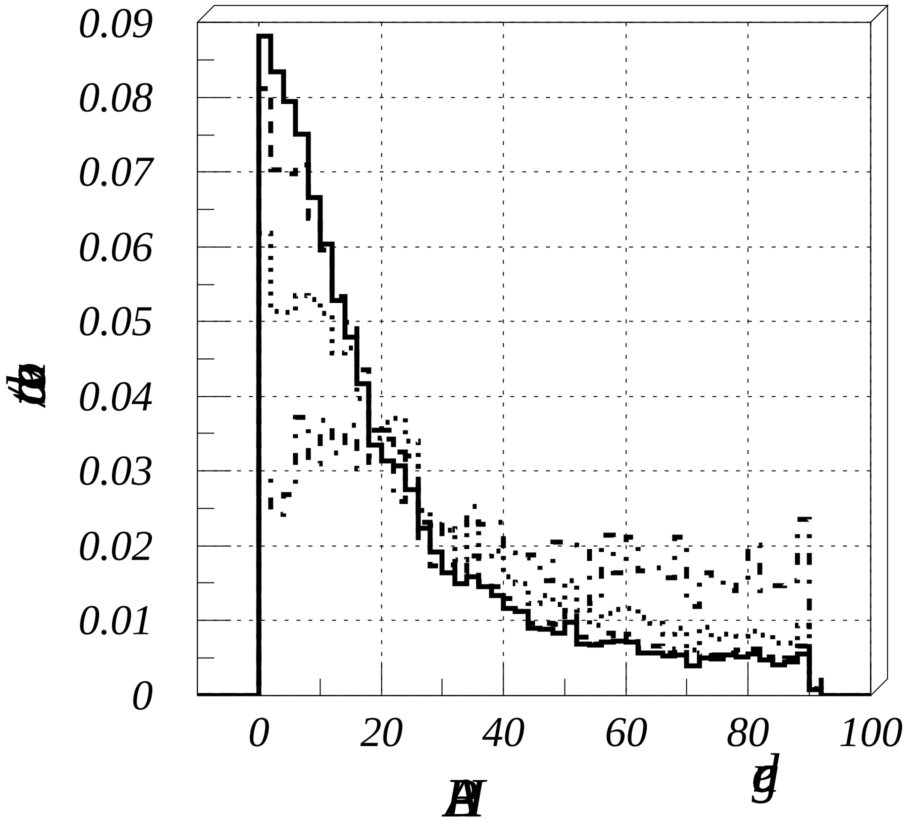

Figure 4.5: Distributions of the ALPHA parameters for gamma-ray showers detected by a camera with a FOV values of 3.0 (sold line), 2.0 (dashed line), 1.5 (dotted line), and 1.0 (dash-dotted line) degrees for a point-like source. We assumed energy bands between 15 GeV and 50 GeV (slope of the energy spectrum is -2.0), and a trigger condition of 2/616 $\geq$ 5 ph.-e.(this notation is explained in the main text).

4.4, the edge of the "Čerenkovpool" (the turning point where the Čerenkovphoton density dramatically decreases) at 4200 m a.s.l. is slightly closer to the center (about 100 m) than at sea level. Moreover, the FOV of CheSS is so small that CheSS can not detect showers with a large core distance. Figure 4.6 shows the detection probability as a function of the core distance for gamma-ray showers, where the detection probability is $< 5 \times 10^{-3}$ when the core distance is over 100 m. Therefore, limiting the core distance to 100 m does not affect the simulation results.

Background particles arrive isotropically to the camera, and its solid angle for the pointing direction of a telescope also affects the simulation results. We confirmed that when the angle is over 4 degrees, the trigger efficiency for protons is $< 1 \times 10^{-5}$. We set the maximum solid angle to 4.0 degrees for the background particles.

In addition, we assumed the observation of the Crab (Ra: 5h34m31s, Dec: 22°00'52") at Mt. Mauna Kea, Hawaii (155°28'48.8"W, 19°49'42.6"N) in December, and the zenith angle was fixed at 10 degrees.

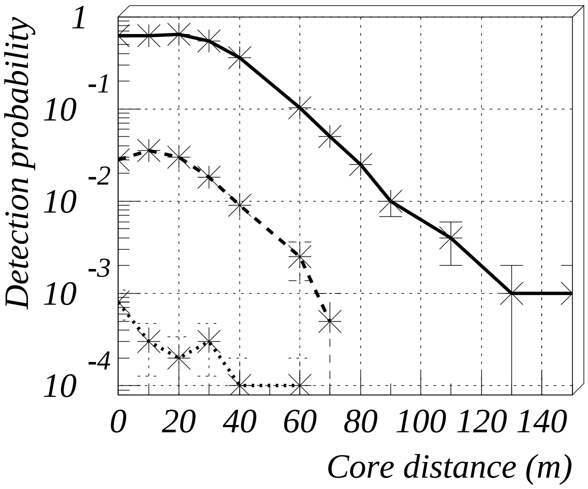

Figure 4.6: Detection probability as a function of the core distance, assuming the trigger condition of 3PMT × 4ph.-e. The solid, dashed, and dotted line show 100 GeV, 30 GeV, and 10 GeV gamma-rays, respectively.

§ 3 Night Sky Background

We calculated the number of photo-electrons induced by the N.S.B. using the following data: the transmittance of correction lenses, the reflectivity of the mirror, the quantum efficiency of the PMTs, the gate time width of the trigger circuit, and the N.S.B. flux taken by the optical telescope (CFHT) at Mt. Mauna Kea(CFHT group 2004); which is about 13 ph.-e. within the gate time of 20 nsec. In this section, we consider the Poisson distributed N.S.B. to have a mean value of 13 ph.-e. in each event.

In order to measure the background, the telescope was pointed at three different OFF points, which were 5, 10 and 12 minutes away from the Crab pulsar/nebula at the same declination. Figure 4.7 shows the expected counting rates with several N.S.B. levels (simulation) and the mean counting rates at three different OFF source points (observation). Assuming the trigger condition to be 3PMT×3ph.-e., which we requested in the observation, the trigger rate at each OFF point corresponded to 8 - 14 ph.-e. However, the trigger circuit of CheSS for "N ph.-e." is quite loose due to the fluctuations of the analog sum of PMT signals (Asahara et al. 2003). Our required trigger condition was considered to be fluctuating between 3PMT×3ph.-e. and 3PMT×4ph.-e. Therefore, the N.S.B. background level seems to be slightly higher than 13 ph.-e.

§ 4 Effective area

Figure 4.8 shows the effective area of gamma-rays and background particles (protons, electrons, and muons), assuming the trigger condition of 3PMT × 3ph.-e., × 4ph.-e., and × 5ph.-e. The effective area depends on the energy of the particles. For gamma-rays, it is proportional to $\sim E^{3.8}$ below 70 GeV, and $\sim E^{0.4}$ above 150 GeV (3PMT × 4ph.-e.). We can see that the effective area of electrons is different from that of gamma-rays, since electrons arrive isotropically to the camera, and are affected by the geomagnetic fields.

The effective areas of the electrons and protons become flat at low energy for the

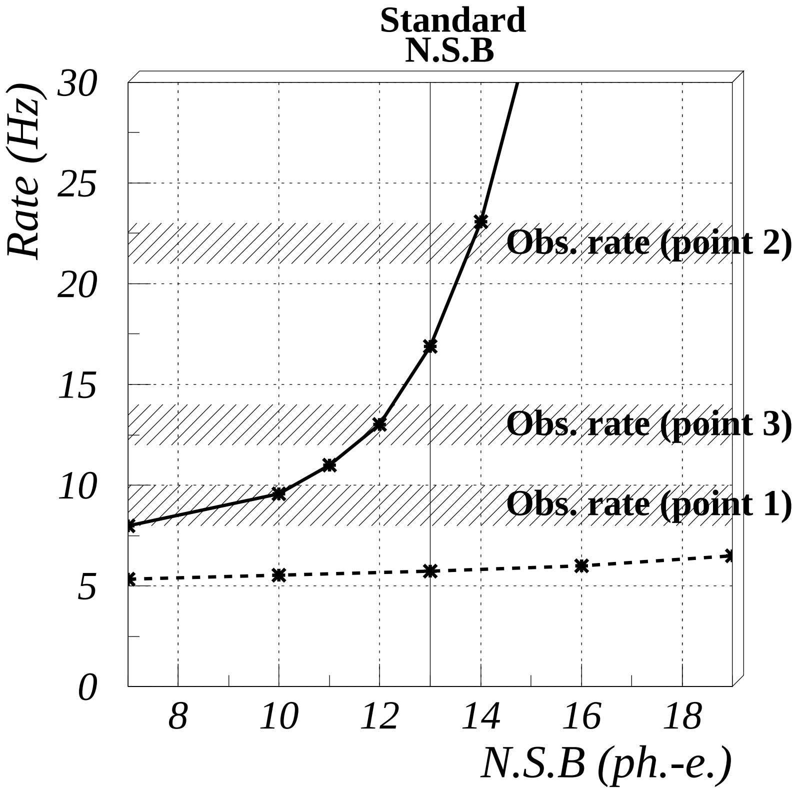

Figure 4.7: Expected counting rates with an N.S.B. level of 7 - 20 ph.-e. within 20 ns, and the mean counting rates at three different OFF source points (observation). The solid and dashed lines represents the assumed trigger conditions of 3PMT×3ph.-e. and 3PMT×4ph.-e.

trigger condition of 3PMT × 3ph.-e. This means that these hardware thresholds are too low to reject the effects of the N.S.B., and thus the event rate becomes quite high. We need to adjust the hardware thresholds to be higher than that of 3PMT × 3ph.-e. to suppress the trigger rate during an observation.

§ 5 Differential detection rates

Figure 4.9 shows the simulated detection rates for gamma-rays, where three trigger conditions (3PMT × 3ph.-e., × 4ph.-e., and × 5ph.-e.) were examined. We assumed the following data for the input flux: the extrapolated flux of the Crab nebula calculated by Hillas(Hillas et al. 1998) for unpulsed gamma-rays and the theoretical flux based on the Polar Cap Model calculated by de Jager(de Jager 2002) for pulsed gamma-rays (shown in Fig. 4.17).

Here, we define the energy threshold as the energy at the maximum point of the event rate (we use this definition throughout this paper). Figure 4.9 shows that the energy threshold of CheSS is 15 GeV for 3PMT×3ph.-e., 60 GeV for 3PMT×4ph.-e., and 100 GeV for 3PMT×5ph.-e. The small change of trigger condition (from 3 ph.-e. to 5 ph.-e.) causes a significant change in the energy threshold (from 15 GeV to 100 GeV).

Figure 4.10 shows the simulated detection rates for three kinds of background particles (protons, electrons, and muons) under the N.S.B. The total flux of pulsed and unpulsed gamma-rays is superimposed. We used the observed flux of protons(Boezio et al. 1999), electrons(Torii et al. 2001), and muons(Gaisser 1997) in this calculation. In this work, we used the flux of muons at the sea level. The flux of muons depends on the atmospheric depth, but above 10 GeV, it is almost constant in atmospheric depth from 1000 g/cm^2 ($\sim$ sea level) to 300 g/cm^2 ($\sim$ 10000 m a.s.l.) (Boezio et al. 2000).

In general, because muons are generated by cosmic-ray protons, we have to estimate how much the muon shower events are included in the proton shower events that we have already simulated. Our simulation shows a proton with an energy of 80

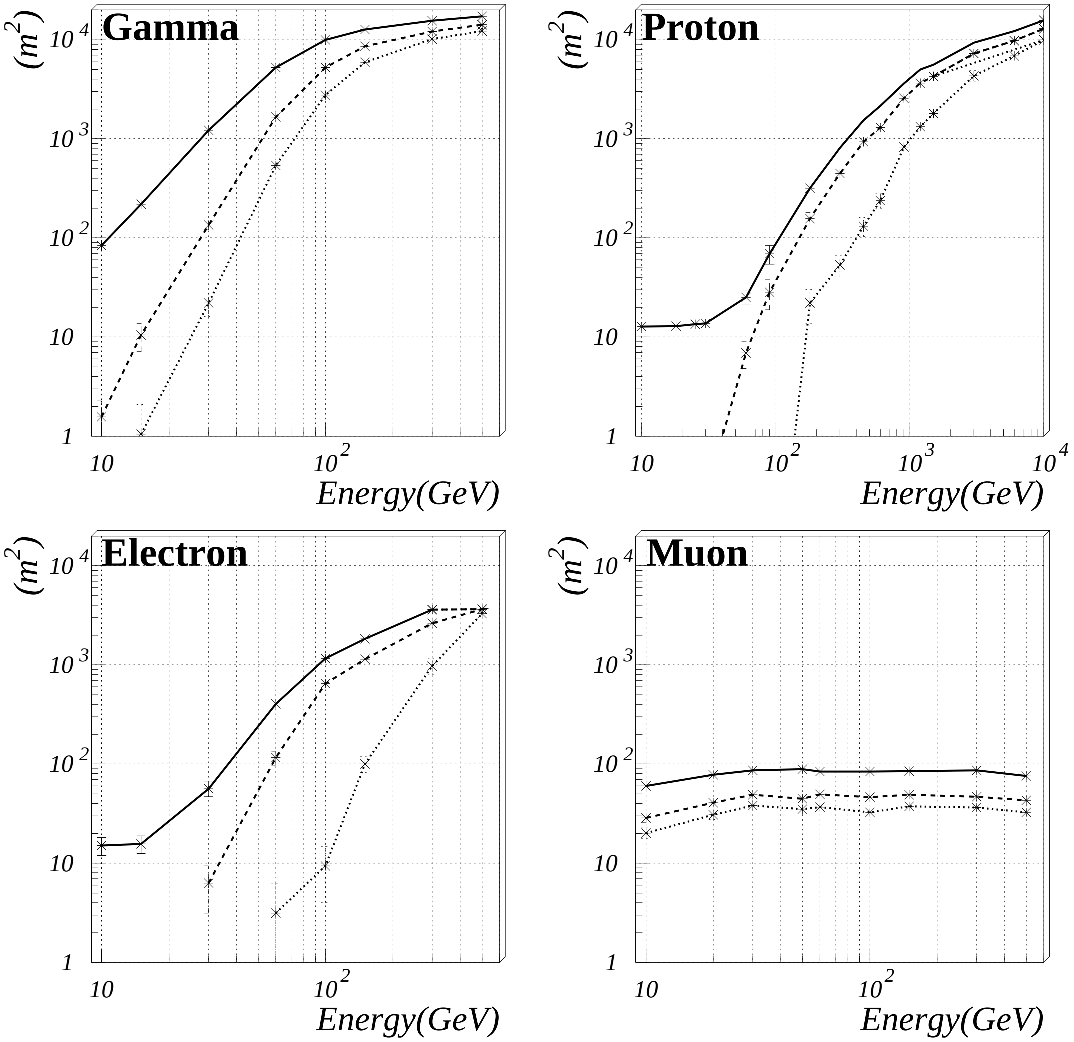

Figure 4.8: Effective area of gamma-rays, protons, electrons, and muons as a function of energy. The solid, dashed, and dotted line show 3PMT×3ph.-e., 3PMT×4ph.-e., 3PMT×5ph.-e., respectively.

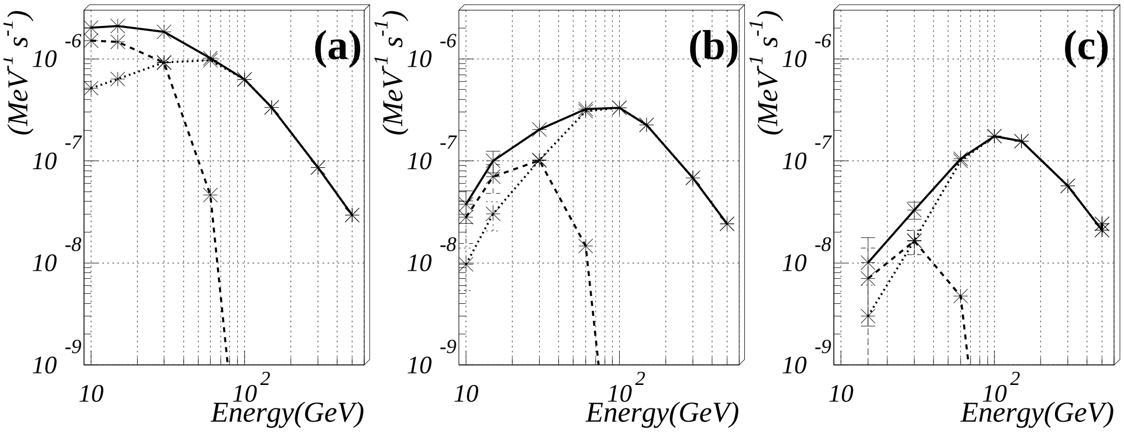

Figure 4.9: Simulated differential detection rates for gamma-rays from the Crab nebula/pulsar under the N.S.B. (a) 3PMT×3ph.-e.; (b) 3PMT×4ph.-e.; (c) 3PMT×5ph.-e. The dotted, and dashed line show the unpulsed component (nebula) and the pulsed component (pulser) of Crab respectively. The solid-line shows the sum of the unpulsed and pulsed components.

GeV generated 3.7 ± 2.0 muons at 4000 m a.s.l., where we assume that the proton comes to the center of the FOV in the vertical direction. Figure 4.11 shows the distribution of their angle to the telescope pointing direction. We can see that the angle of the muon is too large to be detected in the 0.75 degree FOV. Consequently, we can estimate the detection rate for muon showers independently of that for proton showers.

Like gamma-rays, the detection rates of protons and electrons are also quite sensitive to a small change in the trigger condition. For 3PMT×3ph.-e., the detection rates of protons and electrons increase at the low-energy band due to the N.S.B. However, if we change the trigger condition to 3PMT×4ph.-e., the detection rates of protons and electrons can be effectively suppressed. This fact implies that detection rates below 100 GeV are strongly affected by the fluctuation of the N.S.B.

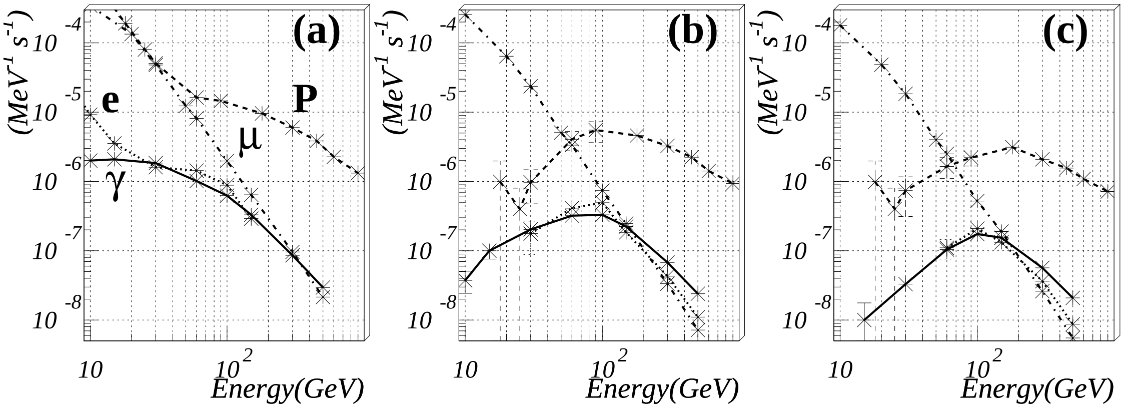

Figure 4.10: Simulated differential detection rates for gamma-rays (solid line), protons (dashed line), electrons (dotted line), and muons (dash-dotted line). The solid-line shows the total flux of the unpulsed and pulsed components of gamma-rays. We assume three trigger conditions: 3PMT×3ph.-e. (a); 3PMT×4ph.-e. (b); 3PMT×5ph.-e. (c).

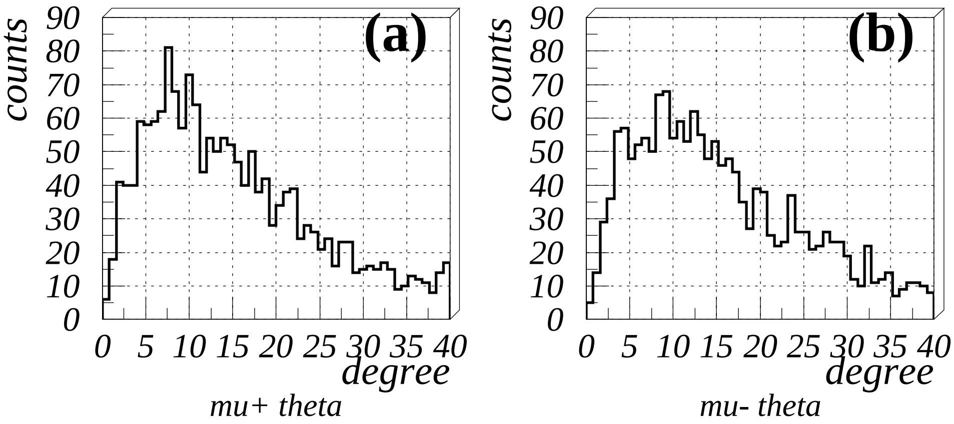

Figure 4.11: Distributions of the angle between the telescope pointing direction and the track of muons that are generated by 80 GeV protons at 4000 m a.s.l. Figures (a) and (b) show μ^+ and μ^-, respectively.

§ 6 Proton backgrounds

At low energies below 100 GeV, a proton can not produce a sufficient number of secondary particles through hadronic interactions, and it rarely generates enough Čerenkovphotons to trigger the telescope. Therefore, the detection rate strongly depends on the N.S.B. level at such a low-energy band.

Figure 4.12(a) shows the mean number of photo-electrons on the camera for gamma-rays and protons. The number of photo-electrons of the proton becomes constant below 100 GeV, and is equal to the sum of accidental N.S.B. photons within a gate time of 20 nsec. This result suggests that accidental events due to the N.S.B. become the dominant background below 100 GeV. Figure 4.12(b) shows the events obtained by the hardware trigger of 3PMT×4ph.-e., assuming that the N.S.B. level is 13 ph.-e. Above 300 GeV, the mean number of photo-electrons induced by gamma-ray primaries is about 2.5-times larger than that by protons. However, at about 80 GeV, both two primaries generate almost the same number of photo-electrons, because it is determined by the N.S.B. photons.

§ 7 Electron backgrounds

The background induced by electrons is not negligible below 100 GeV(Cortina and González 2001). Electrons make showers that are practically indistinguishable from gamma-ray induced ones, and thus can not be eliminated using conventional γ/hadron discrimination methods. Most proposals for next-generation Čerenkovdetectors have discussed this problem. However, for CheSS, the effect is not serious compared to that for IACTs with a large FOV.

The event rate of gamma-ray showers emitted from point-like sources does not depend on the FOV if the FOV is sufficiently large for the spread of Čerenkovphotons. On the other hand, the electrons arrive isotropically, and their event rate is proportional to the FOV squared. Therefore, the detection rate of electrons is small for CheSS.

Moreover, unlike gamma-rays, electrons are affected by the Geomagnetic Field

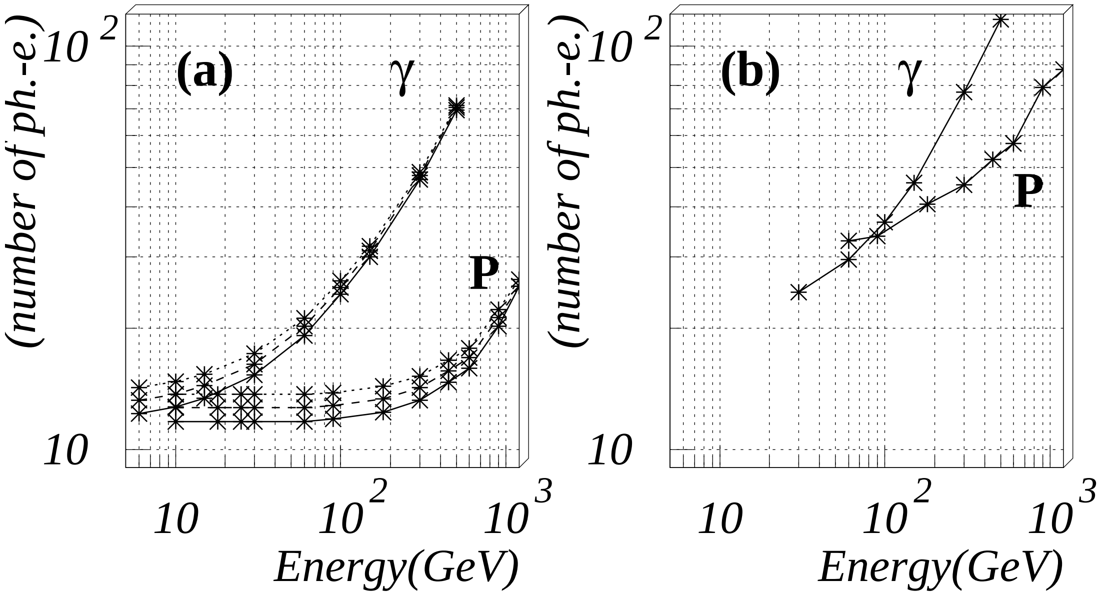

Figure 4.12: Total number of photo-electrons on the camera as a function of the energy; (a) raw data without any cut. The solid, dashed, and dotted line represent the N.S.B. level of 12 ph.-e., 13 ph.-e., and 14 ph.-e. (b) The surviving events after the hardware trigger of 3PMT×4ph.-e., where we assume an N.S.B. level of 13 ph.-e.

(GF). The GF bends the cosmic-ray trajectories and prevents low-rigidity particles from reaching the Earth's surface. The allowed minimum rigidity is known as "cut-off rigidity". According to the dipole approximation of GF, the cut-off rigidity is about 11 GeV/c at the Subaru telescope site (19°49'42.6"N, 155°28'48.8"W) in the vertical direction. Therefore, the detection rate of electrons around 10 GeV becomes much lower than that shown in Fig.4.10. For the trigger condition of 3PMT×4ph.-e. and 3PMT×5ph.-e., the detection rate of electrons is already well suppressed below 30 GeV, and thus the rigidity cut-off does not affect our simulation results. For 3PMT×4ph.-e., however, the integral detection rate becomes 30% lower (from 0.33Hz to 0.23Hz) than that shown in Fig. 4.10, by assuming a cut-off rigidity of 11 GeV/c.

Besides the cut-off rigidity, the local GF also affects the development of secondary particles generated by electrons, and reduces the detection rate to below 100 GeV. Figure 4.13 shows the differential detection rates of electrons expected by CheSS with and without the GF. We estimate that the counting rates are 6.6×10^{-2} Hz with the GF, and 1.7×10^{-1} Hz without the GF. The local GF reduces the integral detection rate of electrons by more than 60%.

§ 8 Muon backgrounds

In a previous proceeding(Asahara et al. 2003), we did not discuss the effects of muon background, because the FOV of CheSS is relatively small. However, we considered the air showers induced by muons, and found that the muon background is not negligible at several tens of GeV energy. For the trigger condition of 3PMT×4ph.-e., the number of photo-electrons induced by a muon shower is 38 ± 12 ph.-e. (Fig. 4.14) independently of its energy, because the number of Čerenkovphotons induced by muons is determined not by the energy of muons, but by the path length that muons pass through within the FOV. Although the effective area for muon showers is much smaller than that for electrons and protons at high energy, muons keep an effective area of $\sim$100 m^2 in the overall energy observed (Fig. 4.8). It follows that

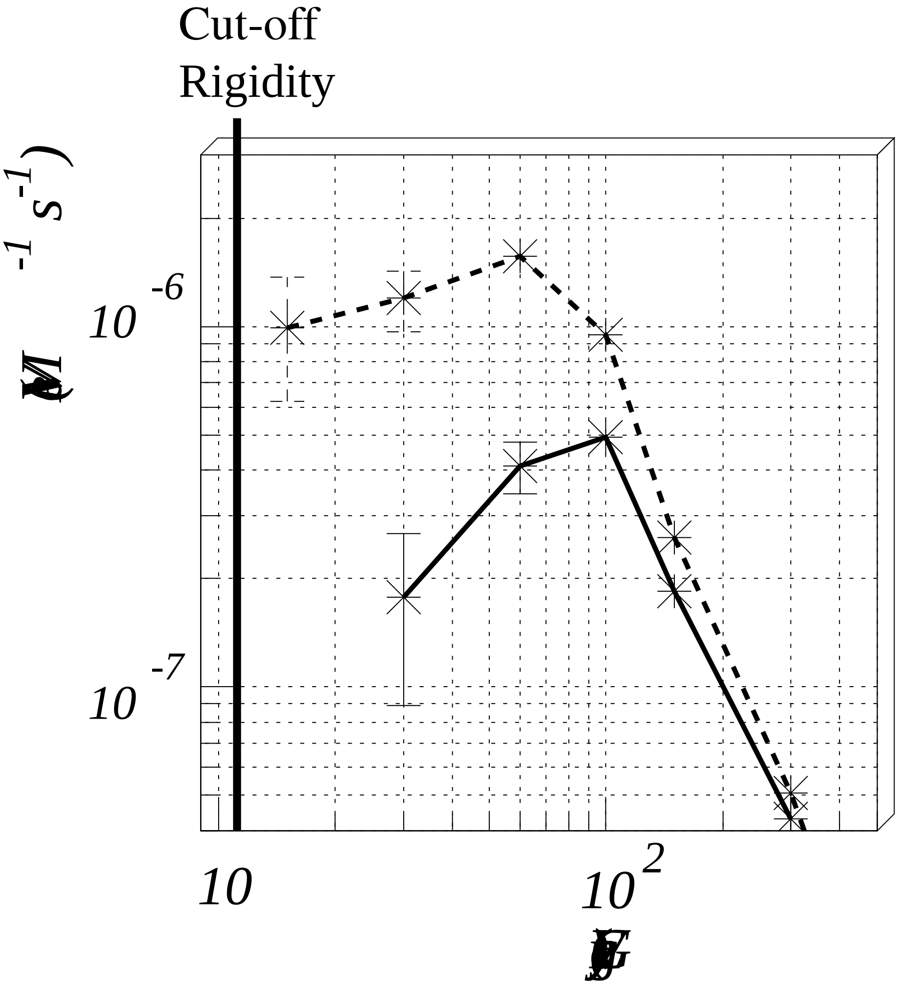

Figure 4.13: Differential direction rate of electrons of the SUBARU site, which has a geomagnetic field of $(B_x,B_z)=(27.7\ \mu T, 20.8\ \mu T)$ (solid line), and in an ideal location that has no geomagnetic field (dotted line), where B_x is the horizontal component of the geomagnetic field to the north direction, and B_z is the vertical component of the GF downward.

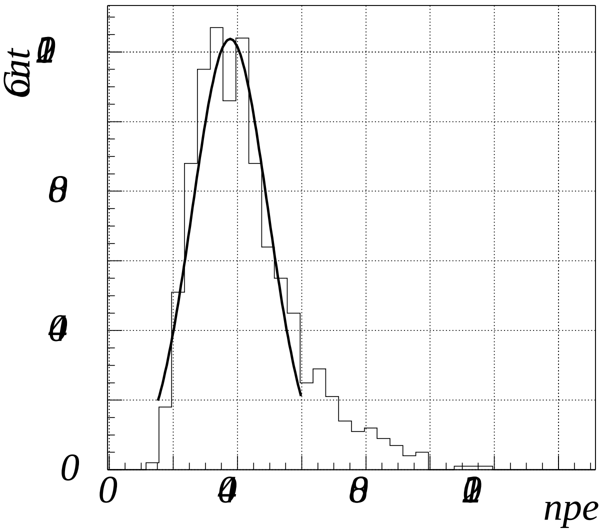

Figure 4.14: Simulated distribution of the number of photo-electrons induced by muon showers, assuming the trigger condition of 3PMT × 4 ph.-e. The energy of muons is between 1 and 300 GeV.
The fitting line is a Gaussian distribution curve with a mean of 37.7 and a σ of 11.8.

muon showers become dominant background below 50 GeV.

The minimum energy of muons that can trigger the telescope is worth estimating. Figure 4.15 shows the effective area of muons below 50 GeV. We can see that the effective area dramatically decreases below 10 GeV, but strongly depends on the N.S.B. level. The flux of muon seeds is quite high ($\sim 10^{-3}$ cm^{-2} s^{-1} sr^{-1} (GeV/c)$^{-1}$) below 10 GeV. Therefore, small changes in the N.S.B. level cause sharp increases in the event rate.

§ 9 Sensitivity of CheSS

Figure 4.16 shows the integral detection rate of gamma-rays, protons, electrons, and muons, assuming the trigger condition, 3PMT × 4ph.-e. Above an energy threshold of 60 GeV, the expected detection rates are 5.8×10^{-2} Hz for gamma-rays, 3.1 Hz for protons, and 5.8×10^{-2} Hz for electrons. For muons, we integrated the differential event rate for the overall energy, since muon showers generate the same number of

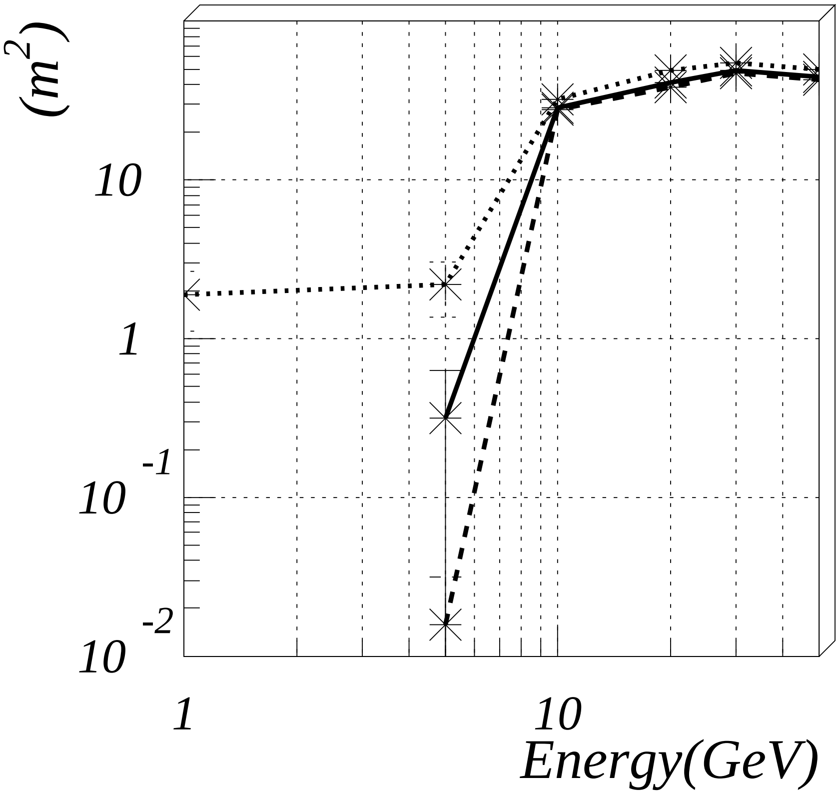

Figure 4.15: Effective area of muons that have an energy below 50 GeV. The solid, dashed, and dotted lines show the N.S.B. level of 7 ph.-e., 13 ph.-e.(standard level), and 20 ph.-e.

Čerenkovphotons in all energy bands. The expected integral detection rate of muons is 2.5 Hz. Consequently, the signal rate is 5.8×10^{-2} Hz and the noise rate is 5.7 Hz. The significance defined as,

$$\text{Significance} = \frac{N_{ON} - N_{OFF}}{\sqrt{N_{ON} + N_{OFF}}} = \frac{Rate_{signal}}{\sqrt{2Rate_{noise}}}\sqrt{t_{obs}} \qquad (4.2)$$

results $\sim$ 4 sigma by 10-hour-ON and 10-hour-OFF observation. In Eq.4.2, t_{obs} is an observation time; N_{ON} and N_{OFF} are the number of events in the ON and OFF source run.

Figure 4.17 shows the 4 σ sensitivity lines of CheSS for 10 hours of observations at a zenith angle of 10 degrees. Regarding the trigger condition of 3PMT × 4ph.-e., we could effectively suppress the background events, and also reduce the pulsed gamma-ray events that have a quite small number of ph.-e. In order to extract pulsed gamma-ray events efficiently, we should set the threshold level to be as low as possible. For 3PMT × 3ph.-e., which is the hardware threshold level in an observation, the integral event rate of pulsed gamma-rays is expected to 0.045 Hz. In this trigger condition, the background rate is also large ($\sim$ 16 Hz), but we can remove the large number of ph.-e. if we focus only on pulsed gamma-ray events. After we cut those events that have a number of ph.-e.$>$ 25, the integral event rate of pulsed gamma-rays and that of the background particles (protons, electrons, muons, and unpulsed gamma-rays) becomes 0.040 Hz and 11.1 Hz. If we assume that the duty cycle of pulse is 25% in one phase, we can reduce the background events by one forth because they come uniformly in one phase. Therefore, 10 hours ON-OFF observation also produces $\sim$ 4 sigma detection from the Crab pulsar (Fig. 4.17). In this case, the epoch folding method is assumed for the timing analysis, because the period of the Crab pulsar is already known to be 33 msec. However, since the number of pulsed gamma-ray events is small ($\sim$ 1400 events), we must carefully choose the number of phase bins in the epoch folding method.

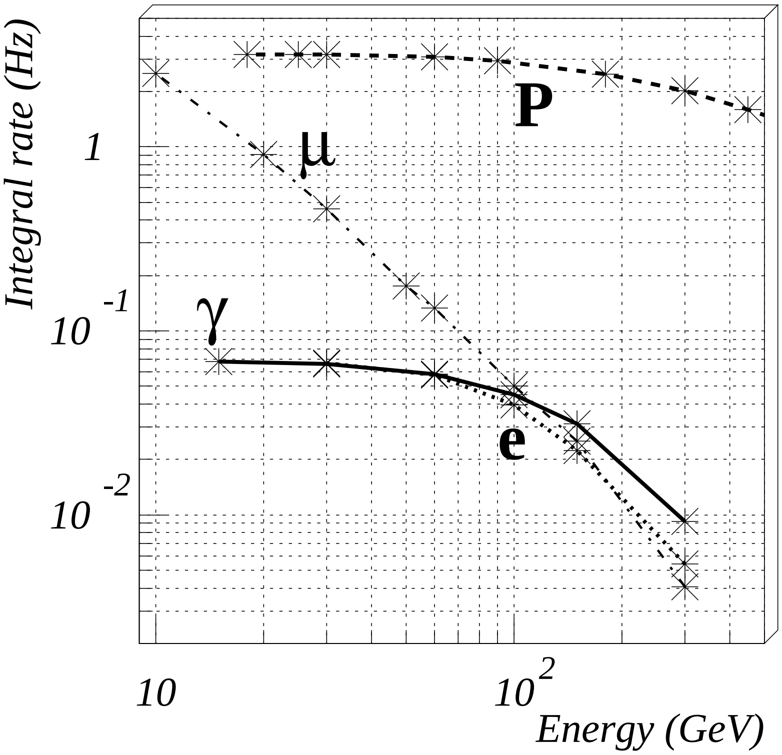

Figure 4.16: Integral flux of gamma-rays (solid line), protons (dashed line), electrons (dotted line), and muons (dash-dotted line). The trigger condition is 3PMT × 4ph.-e.

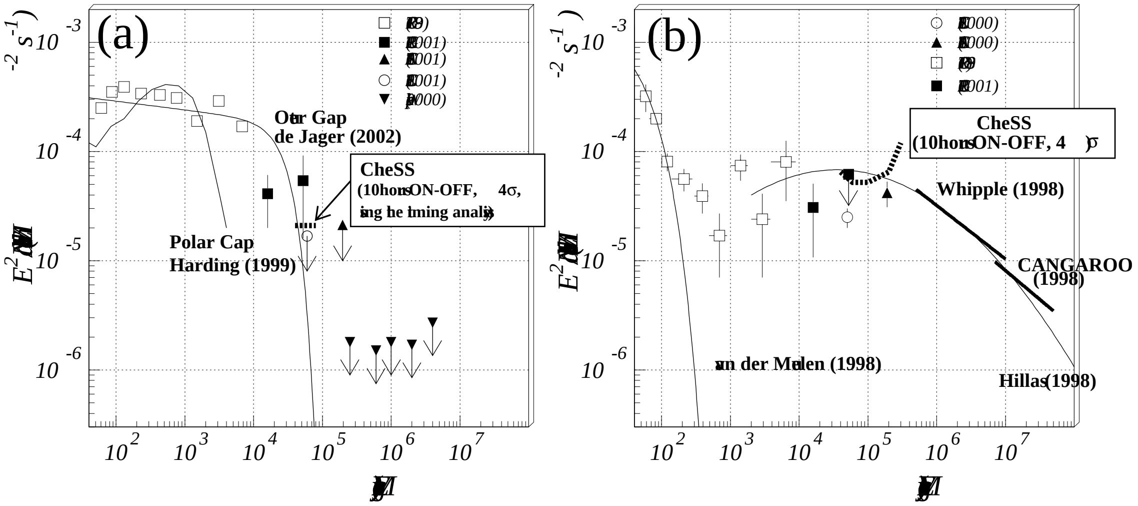

Figure 4.17: Spectra of the Crab reported by several instruments. Theoretical curves and the expected sensitivities of CheSS are superimposed (Harding et al. 1997; Lessard et al. 2000; de Naurois et al. 2002; Oser et al. 2001; Nolan et al. 1993; de Jager 2002; Mori 2001);

(a) pulsed component. The sensitivity line shows 10 hours of observation at the zenith angle of 10 degrees. In this calculation, we assumed a hardware threshold of 3PMT×3ph.-e., and an improvement in sensitivity due to the timing analysis for a pulse with a duty cycle of 25% in one phase; (b) unpulsed component. The sensitivity also shows 10 hours of observation at a zenith angle of 10 degrees. This line was calculated from the ON and OFF source counting rates with a threshold of 3PMT×4ph.-e. (described in detail in subsection § 9).

Chapter5

Observation

> And the Gryphon added "Come, let's hear some of your adventures."
>
> "I could tell you my adventures – beginning from this morning." said Alice a little timidly; "but it's no use going back to yesterday, because I was a different person then."
>
> "Explain all that," said the Mock Turtle.
>
> "No, no! The adventures first," said the Gryphon in an important tone: "explanations take such a dreadful time." — *The Lobster-Quadrille* —

§ 1 Observations of the Crab pulsar/nebula

The SUBARU telescope equipped with CheSS was pointed in the direction of the Crab pulsar/nebula on 17th, 18th, and 19th December 2001. The averaged zenith angle is $\sim 30°$.

These three days were around the new of the moon. Weather was fine for three days, but humidity was rise up on 17th Dec. Temprature inside astro-doom is well controlled, about 0 °C. Weather conditios are listed in Table 5.1.

We observed Crab with ON-OFF chopping mode, which was the method that observe alternatively the target point for gamma rays and the OFF point which has same declination but several minutes difference to the target in right ascension. The purpose of observing OFF point is to mesure the background cosmic-rays. We observed three OFF points to reduce the systematic error due to the difference between night sky background levels. Figure 5.1 shows the position of the Crab pulsar/nebula and three OFF points which we observed. The precious values of

Crab and OFF points are listed in Table 5.3, and the total observation time is summarized in Table 5.2. In addition, the calibration runs were done to measure the variation of PMTs gains using a blue LED several times per day.

The trigger conditions in observation is listed in Table 5.4. Large part of observation was conducted at 3 PMT × 3 ph.-e. In the beginning of 17th night. We set higher threshold level for safe starting. On the way of 19th night, we set lower threshold level because the event rate decreased due to the high humidity.

	Temperature	Humidity	Wind Speed	Pressure	Seeing
17th Dec	-0.9 (°C)	22 (%)	0.3 (m/s)	621.3 (hPa)	0".75 (deg)
18th Dec	0.4	18	0.1	621.8	0".65
19th Dec	3.1	21	0.1	622.9	1".00

Table 5.1: Summary of weather conditions.

	ON	5min OFF	10min OFF	12min OFF
17Dec	3h30m	20m	0m	3h10m
18Dec	3h20m	3h20m	0m	0m
19Dec	4h00m	0m	4h00m	0m
Total	10h50m	3h40m	4h00m	3h10m

Table 5.2: Summary of the observation time.

Target name	position (RA, Dec)
Crab	(05:34:31.974, 22:00:52.049)
OFF 1	(05:29:31.974, 22:00:52.049)
OFF 2	(05:24:31.974, 22:00:52.049)
OFF 3	(05:22:00.000, 22:00:52.049)

Table 5.3: Tracking positions (RA, Dec).

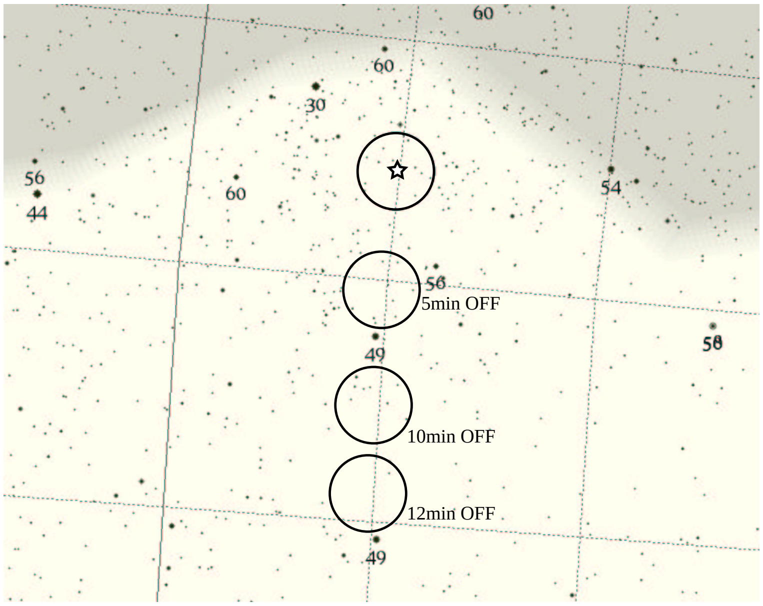

Figure 5.1: Star field map around the Crab nebula/pulsar. Bright Stars are annexed these magnitudes. The circle means the field of view of 0.75°.

		# of hit	# of ph.-e.	TDC th (ph.-e.)	ASUM th (ph.-e.)
17th	1h20min	3.0	3.5	1.2	320
	5h40min	3.0	3	1.2	320
18th	6h40min	3.0	3	1.2	320
19th	2h20min	3.0	3	1.2	320
	5h40min	2.5	3	1.2	320

Table 5.4: Trigger conditions.

§ 2 Test run

We conducted two kinds of test runs several times per one night. One of the test runs is called “LED run”. The purpose of this test run is to confirm for the DAQ system working normally, and to calibrate the gain of 44 PMTs. In LED run, we use the blue LED unit installed in CheSS (Fig.3.16).

The other kind of test runs is called “N.S.B. run”. In this run, the periodic external trigger (1 - 1M Hz) to DAQ is generated independently of the analog pulses from the pre-amplifier of PMTs (Fig. 5.2). This means that the events recorded in this run reflect only the N.S.B. background level. To analyze N.S.B. run data, we can find the nature of N.S.B. background at ON and OFF points where CheSS observed.

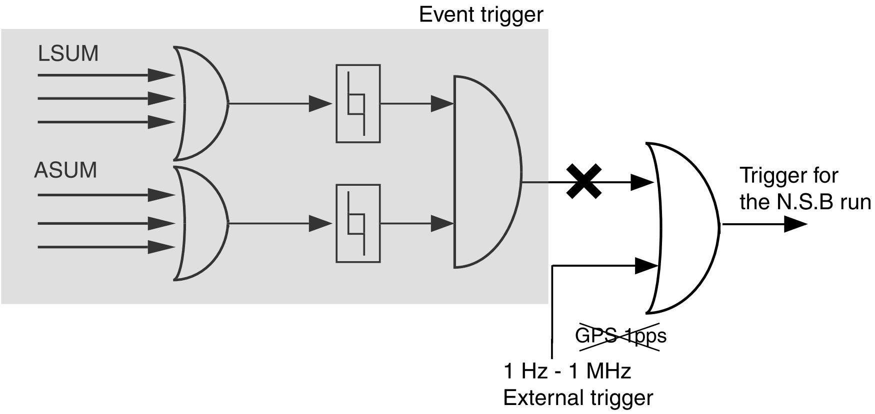

Figure 5.2: The diagram of event trigger logic during N.S.B run. We can choice the frequency of the external trigger between 1 and 1M Hz.

§ 3 Night Sky Background level

At the summit of Mt. Maunakea, city lighting is relatively small, and quite often completely damped from cloud cover at the 2000-3000 m level. A county ordinance has been adopted, which restrict most lights of the Hawaii Island to low-pressure sodium lamps. Average sky brightness at zenith during dark time is given in the table 5.5. Note that night sky brightness in U-band increases by a factor of 5 at quarter moon and 65 at full moon. Corresponding values in V-band are 1.3 at quarter and 5 at full moon. These rough estimates are, of course, for clear (cirrus-free) nights. Figure 5.3 shows a typical spectrum of visible night sky emission at Mauna Kea.

As mentioned section § 1, we observed three OFF source points. These three OFF source points are apart from each other by only several arc minutes in right ascension, but the trigger rate observed by CheSS was quite different at each points. Figure 5.4 shows the observed trigger rates, which were ∼25Hz for 5min OFF, ∼15Hz for 10min OFF, and ∼8Hz for 12min OFF. This is because that the N.S.B has the strong effect on observed events below 100 GeV, as mentioned in Ch. 4. Figure 5.4 (d) shows the difference of ADC distributions at each OFF points, which are normalized by the number of counts between 4000 and 8000 ADC channel, where the cosmic-ray background is dominant and its count rate is expected to be the same value at each OFF points. The bumps around 2000 ch is due to the N.S.B, and the counts of them at each points is different by a factor ∼4.

According to these results: the data taken by the optical telescope; the trigger rate observed by CheSS; the result of simulations, the level of N.S.B. is expected to be 13 $\sim$ 17 ph.-e. within the gate time width of 20 nsec, which obviously exceed the number of Čerenkovphotons produced by a shower. Thus, at the first stage of the analysis, several selections for rejecting the N.S.B background photons were applied to the data.

Color	Equivalent λ (μm)	Brightness [mag/arcsec^2]	Flux [phot./cm^2/s/μsec/arcsec^2]
U	0.36	21.6	1.74×10^{-2}
B	0.44	22.3	1.76×10^{-2}
V	0.55	21.1	3.62×10^{-2}
R	0.64	20.3	5.50×10^{-2}
I	0.79	19.2	1.02×10^{-1}
J	1.23	14.8	2.49
H	1.66	13.4	4.20
K	2.22	12.6	3.98

Table 5.5: The sky background levels in each band(CFHT group 2004)

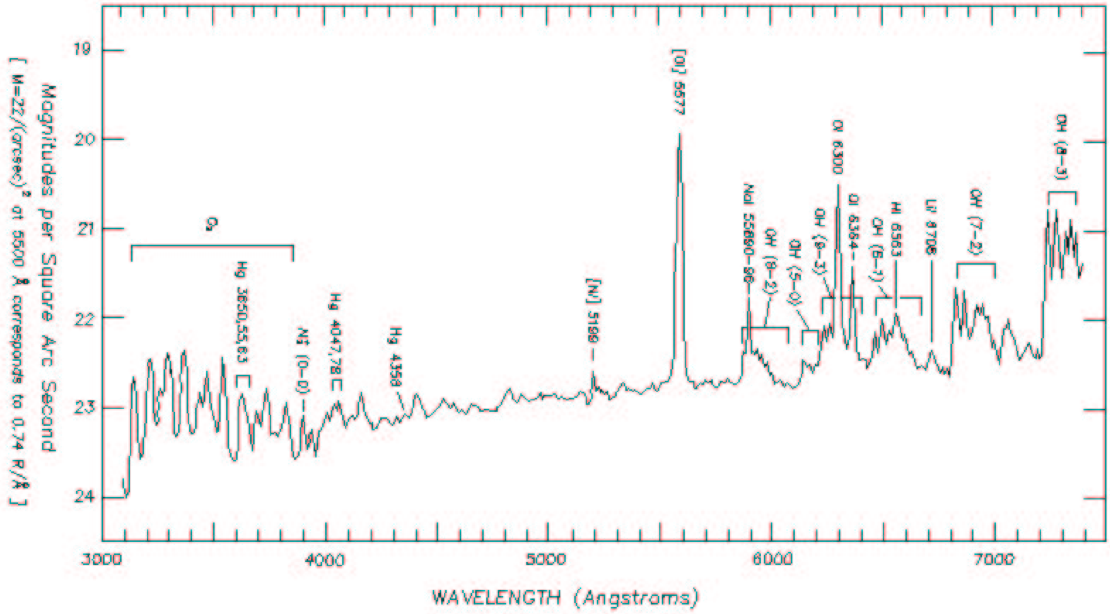

Figure 5.3: The sky background levels on the summit of Mt. Maunakea(CFHT group 2004).

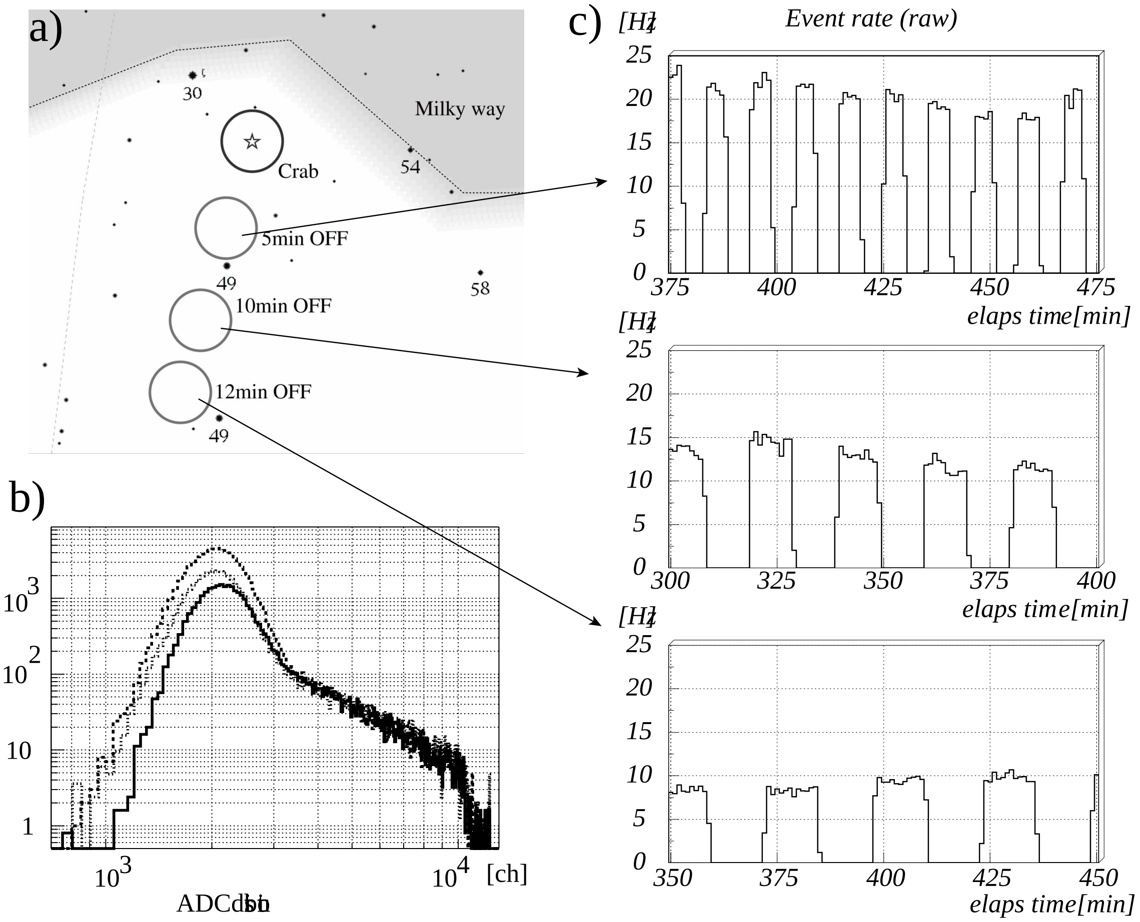

Figure 5.4: (a) Tracking points of Crab and 3 OFF points. (b) The ADC distributions at 12 min OFF point(solid line), 10 min OFF point (dotted line), and 5 min OFF point(dashed line). (c) The trigger rates at 5 min OFF point(Top), 10 min OFF(middle), 12 min OFF(bottom).

Chapter6

Analysis

> “It was much pleasanter at home,” thought poor Alice, “when one wasn’t always growing larger and smaller, and being ordered about by mice and rabbits. I almost wish I hadn’t gone down that rabbit-hole — and yet — it’s rather curious, you know, this sort of life! I do wonder what *can* have happened to me!”
>
> — *The Rabbit Sends in a Little Bill* —

The Čerenkov light are detected by the camera with 44 PMTs, and the arrival timing and charge of signals from PMTs is measured by two type of devices, TDC and ADC, respectively. TDC has 44 inputs for each PMT, and ADC has 3 inputs which are corresponding to 3 analog sum outputs from DSM (Fig. 3.10). Because of the limits of space and cost, each PMT is not equiped with ADC independently, and thus TDC data is quit important for the analysis of CheSS data.

Since CheSS has only 44 PMTs, the handling of TDC data is a little different from that for a standard IACT which has over 400 PMTs, such as CANGAROO. In this chapter, we introduce the correction and noise reduction methods which are effective for a camera with small FOV (~ 0.5) and small number of PMTs (~ 50).

§ 1 ADC distribution

ADCs measure charges of 3 analog sum outputs from DSM, i.e. the sum of three ADC channels shows the total number of Čerenkov photons detected by 44 PMTs, and it has a positive correlation with the energy of a primary particle. Hereafter, "ADC" means the sum of three ADC channels.

Figure 6.1(a) shows the distribution of ADC calculated from OFF source data without any cuts. The bump around 2500 channel is due to the N.S.B, and the power law component between 3000 and 9000 channel is due to the cosmic rays. The drop above 9000 channel is due to the saturation of the hardware.

The simple idea to reject N.S.B events is to discard the events which have too low ADC channel. For example, Figure 6.1(b) shows the observed trigger rate and event rate after the cut of ADC $<$ 3500 ch, as a function of the elapse time [min]. The event rate after the ADC cut depends on the elevation angle of the Subaru telescope (Fig. 6.1 c). The dependency on the elevation angle is one of the feature of cosmic-rays, and thus this result indicates that almost all events survived by this cut are due to cosmic rays. However, the event rate in Fig. 6.1(b) is too small, about 1Hz. According to our simulation (Ch.4 § 9), this event rate corresponds to the integral detection rate above 300 GeV for protons. Therefore, the cut condition of ADC $<$ 3500 ch is too tight, and discards significant number of low energy events.

Our simulation results suggests that we have to push the energy threshold down to at least 150 GeV for protons (corresponding to $\sim$ 100 GeV for γ-rays. See Fig.4.12.) in order to estimate γ-ray flux using 10 hour observation data. For this energy threshold, the integral detection rate must become 2 - 3 Hz.

In the analysis presented below, we request loose ADC cut $<$ 2300 channel to save the low energy data as much as possible.

§ 2 Hit timing distribution mesured by TDC

To explore the 10 GeV energy region, we need to improve the dynamic range of ADC in the lower channel. At the low ADC channel, the N.S.B hits blind us to the cosmic-ray shower image. Therefore, it is necessary to remove PMT hits due to the N.S.B as much as possible. The hit timings of 44 PMTs measured by TDC are useful for this purpose.

Figure 6.2 shows the raw distribution of PMT hit timing added up 44 PMTs.

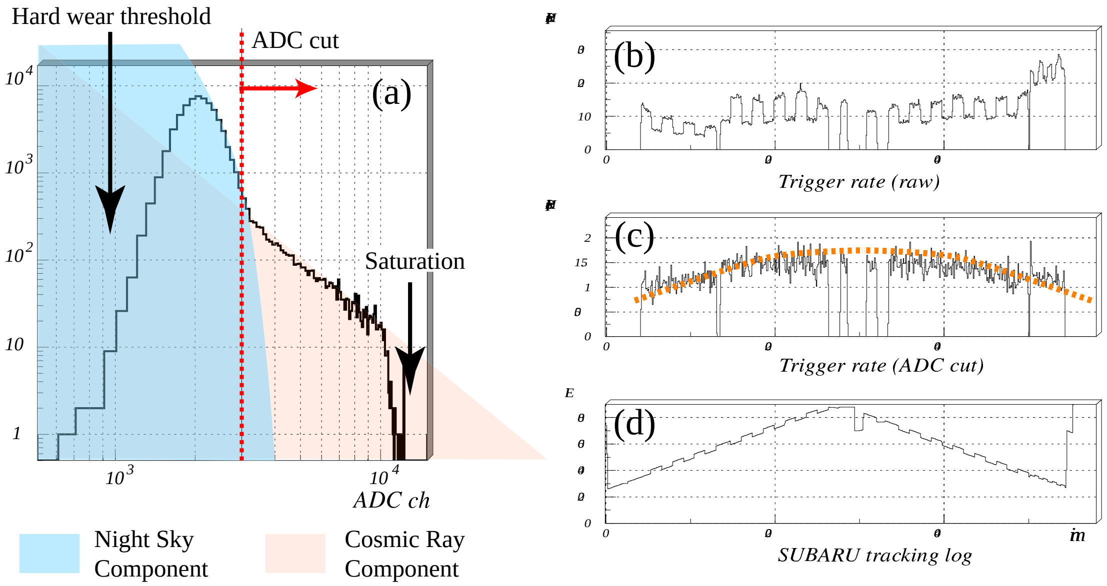

Figure 6.1: (a): ADC distribution without any cuts. (b): The event rate as a function of elaps time. (c):The event rate after cut of ADC $<$ 3500 ch. (d): The elevation angle of the Subaru telescope.

TDCs measure the arrival time of PMT hits within TDC gate time of about 1 μsec just before the TDC trigger is generated (COMMON STOP mode. See Fig. 6.3.). The uniform component in overall time is expected due to N.S.B. The spike around 500 nsec is composed by the signals which has generated the trigger pulse, and that is mainly due to cosmic ray showers. According to our simulation, the timing duration of Čerenkov photons generated by sub 100 GeV hadron showers is below 10 nsec. However, The time width of this spike in this figure is too wide, about 100 nsec. This duration is caused by;

1. the intrinsic timing jitter of the self-trigger system,
2. the effects of N.S.B.

In this section, we investigate the several corrections of TDC data and N.S.B reduction methods, and show that the timing width becomes much smaller.

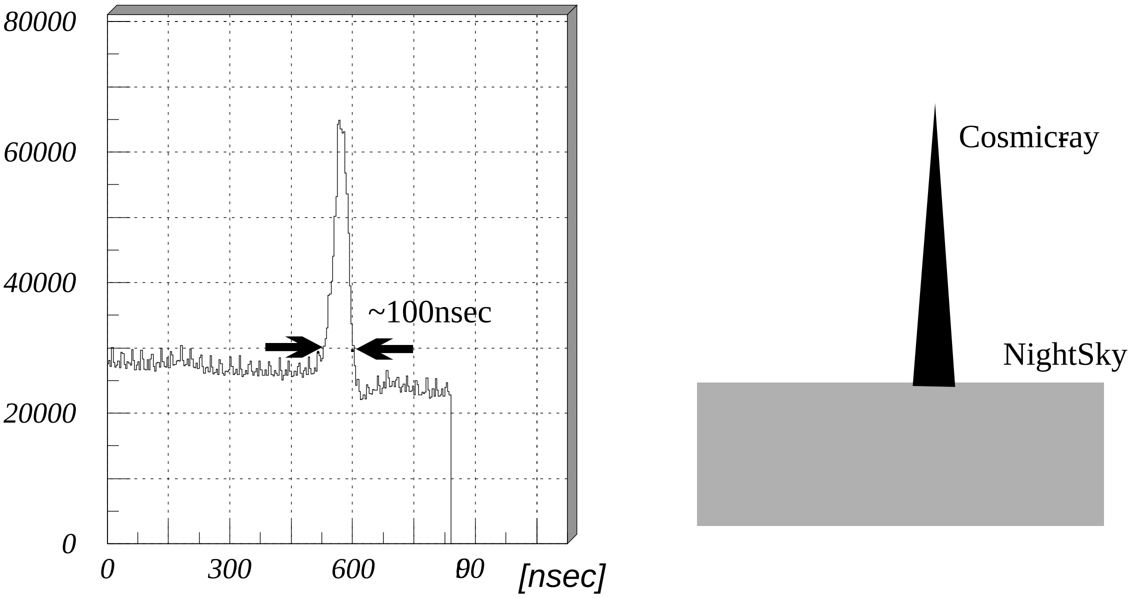

Figure 6.2: Left: raw TDC hit timing distribution without any cut. Right: the schematic diagram of the TDC distribution. N.S.B events distributes uniformly, and the Čerenkov photons caused by cosmic ray forms the peak shape.

2.1 Timing jitter of the self-trigger system

Since the common stop pulse for TDCs is generated by the PMT signal themselves (the self-trigger system, as shown in Fig. 6.3), the stating points of the data acuisition are not constant, but fluctuated by 10∼100 nsec event by event.

To correct these fluctuations, the CANGAROO telescope uses the "average correction" method(Asahara et al. 2004). This method is following;

1. The average timing of hit PMTs are calculated event by event.

2. Calculate Δt. Δt is the substitute of the standard point[1] and the average timing calculated above.

3. All TDC hit timings are substituted by Δt.

After this correction, the time width of spike is smaller (about 80 nsec) as shown in Fig. 6.4. Moreover, "S/U ratio" is also improved after correction, where the S/U ratio is defined as counts of the Spike component at 600 nsec over that of the

---

[1] The standard point has no physical mean. We defined it as the convenient point for analysis, 600 nsec.

Uniform component at 300 nsec, and means the ratio of the count caused by N.S.B. to that caused by cosmic-rays. Before and after the average correction, S/U is about 2.0 and 3.0, respectively.

However, the distribution of arrival timing (the width of spike components) is still large compared with those for standard IACTs (30nsec).

For CheSS, average correction seems not to be the best method to correct the offset. A standard IACT has sufficient number of PMTs. For example, the CANGAROO II has 512 PMTs and detect mean 100 hits per event. In contrast, the number of PMT installed in CheSS is only 44. Mean number of PMT hits is about 13 hit per event, and less in the lower energy bands. For below 10 hits, the average correction has the large statistical uncertainty. Moreover, since N.S.B. hits becomes dominant for a low energy event , the average of TDC hits doesn't mean the average of signal timing in such a low energy event.

Here, we propose another correction method. Instead of average value, we used the mode value in the histogram made from the TDC hit timing distribution. If we cannot find mode value, then we remake the histgram with larger binning. We applied this method to our data as following steps;

1. Make the histogram with 80 bin (1 bin = 12 nsec.) from the TDC hit timing distribution.

2. Search the bin giving the mode value in the histogram.

2'. If we find several mode bins, remake the histogram with the twice of bin width (40 bin. 1 bin = 24 nsec.), and search the bin giving the mode value in the new histogram.

2". If there are still several mode bins, remake the histogram with 20 bin. and search it again in the new histogram.

3. If we can find only one bin giving the mode value in process 2, Δt is calculated by the subtract the mode value from the standard point (here, we set it by 600 nsec).

4. Subtranct Δt from all TDC hit timings.

We called this method "mode correction method". After this correction, the

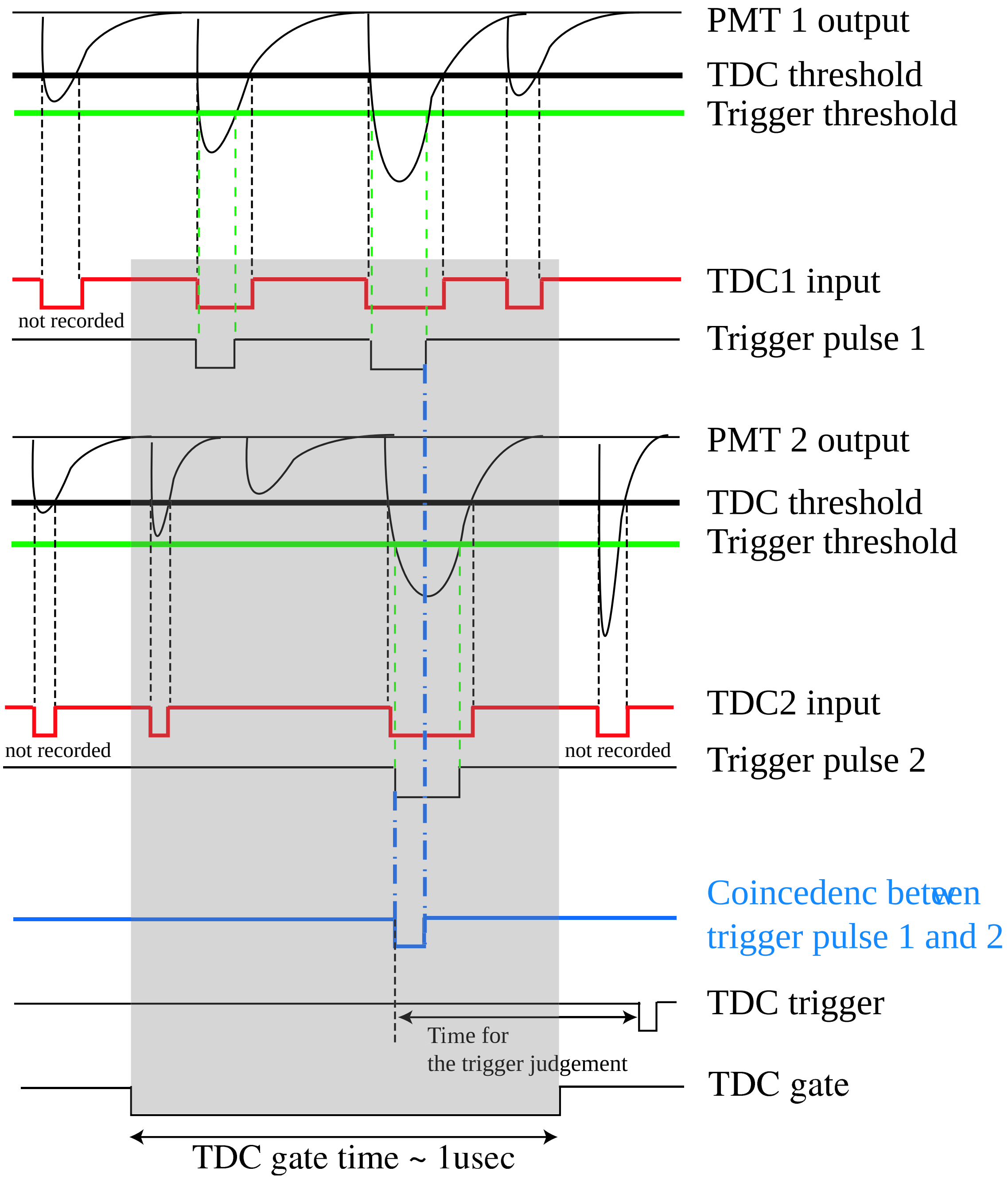

Figure 6.3: TDC data acquisition timing chart.

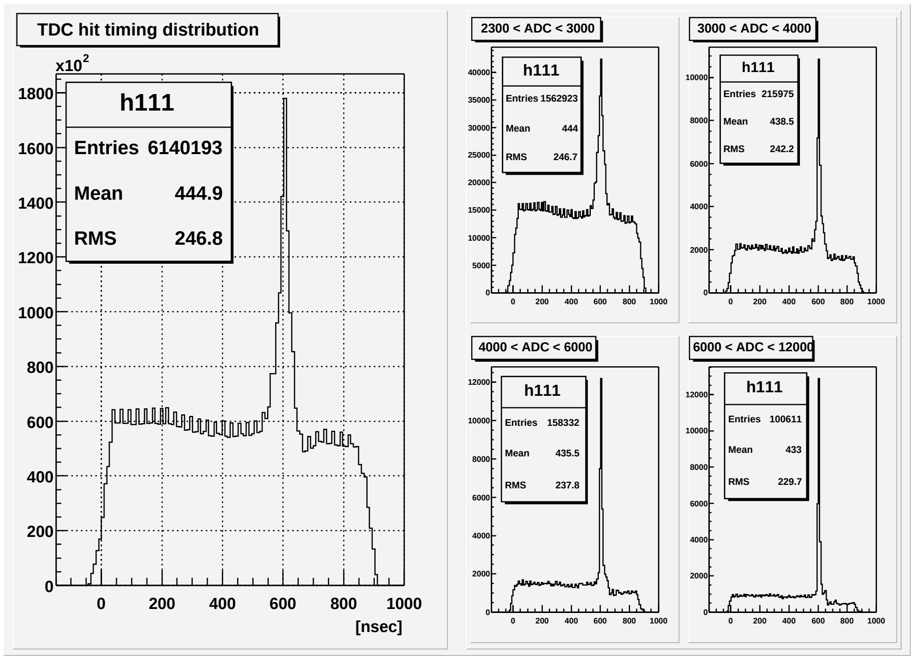

Figure 6.4: The TDC distribution after average correction.

timing distribution of shower events becomes about 70 nsec (Fig. 6.5). S/U is also improved from 3.0 to 3.5.

We checked that our new correction method don't make the fake spike from hits caused by N.S.B. Figure 6.6 shows the hit timing distributions before and after the mode correction, using the data recorded in N.S.B. runs. In this run, there is no cosmic-ray shower events (described in detail in Ch.5-§ 2). For the mode correction method, we can not find obviously fake spike. In contrast, the average correction method made fake small bump aground 600 nsec. Although the mode correction is simple procedure, it seems to be the powerful method to correct the timing jitter of TDC, especially for the camera with small number of PMTs.

2.2 Mode correction as the event cut method

Mode correction method is also useful as the cut method for N.S.B. events. The events caused by N.S.B. shows the flat distribution of TDC hit timings. If several bins giving the mode value still exist after the procedure 2" in the mode correction

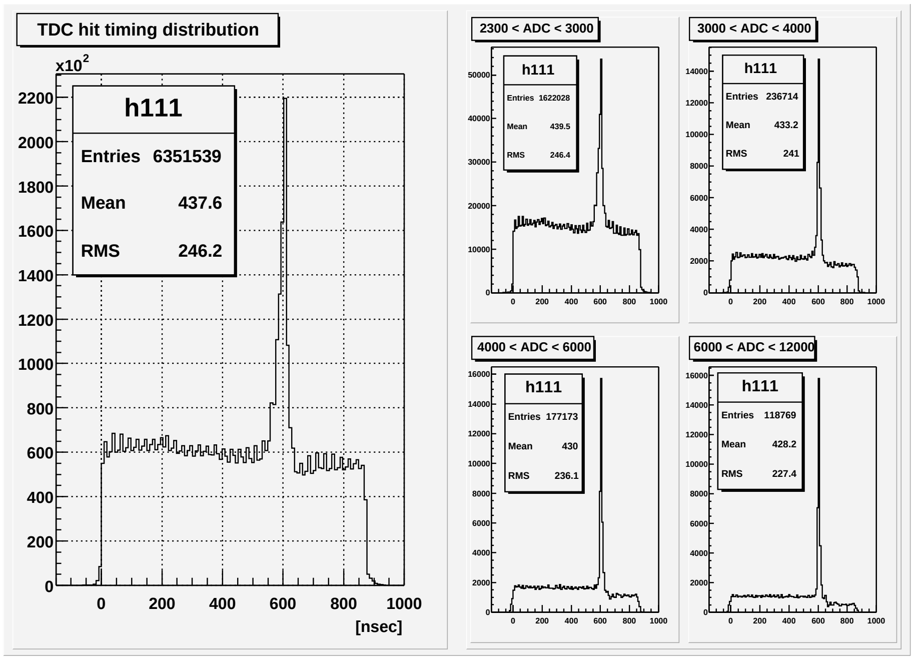

Figure 6.5: TDC hit timing distribution after mode correction.

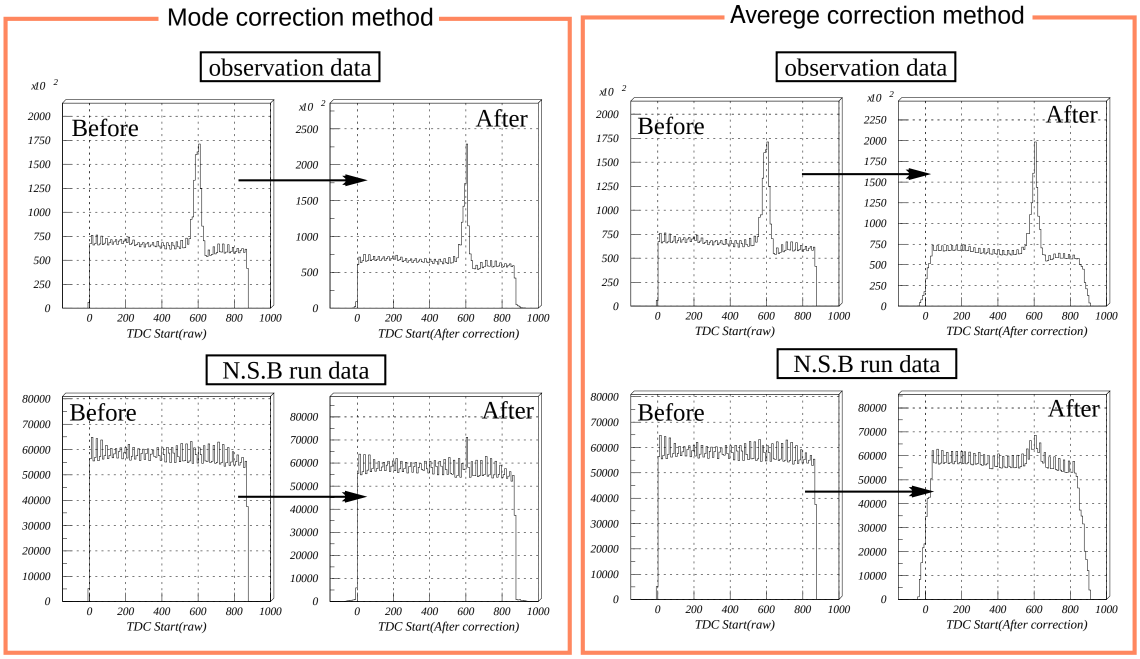

Figure 6.6: Hit timing distribution using observation data and the data recorded in N.S.B run, after mode correction and average correction.

method, that event is enough flat around 600 nsec, and likely to be caused by N.S.B. Here, we discard events having such a flat TDC hit timing distribution. Moreover, we request the mode bin to exceed the other bins by ≥ N counts (Fig. 6.7), and discard the event not having such a mode bin.

We examined the power of reduction in the variation of "N". Figure 6.8 shows the TDC timing distributions after the mode correction of N=2,3, and 4. In N=2, 3, and 4, the width of the timing distribution of shower events becomes about 60, 40, and 40 nsec, respectively. The S/U ratio is also improved, and at larger N, we can have a more improved S/U. However, at large N, we lost significant events, especially in lower energy band. Figure 6.9 shows the ADC spectra after the mode correction of N=2,3, and 4. For N = 3, the survived events is only 30 %, and thus we adopt the mode correction of N = 2. Figure 6.10 shows the hit timing distribution after mode cut of N=2. This cut is a relatively looser cut, but S/U is improved well, from 3.5 to 4.7.

Figure 6.11 shows the trigger rate after the mode cut. The trigger rate is reduced to about 5 Hz. However, we can't find that the trigger rate depends on the elevation angle. The data taken on 17th and 19th shows the uADC (refracts an energy spectrum. see next section.) of ON source exceed that of OFF source, but on 18 th data, both spectrum are almost same curve.

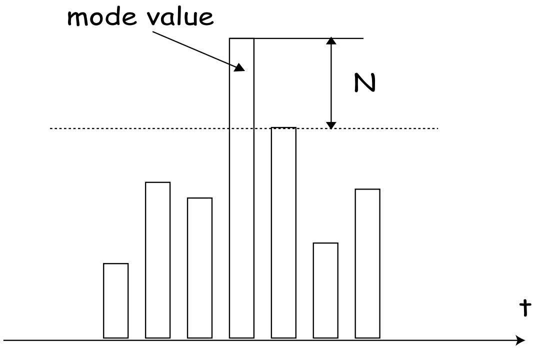

Figure 6.7: the define of "N"

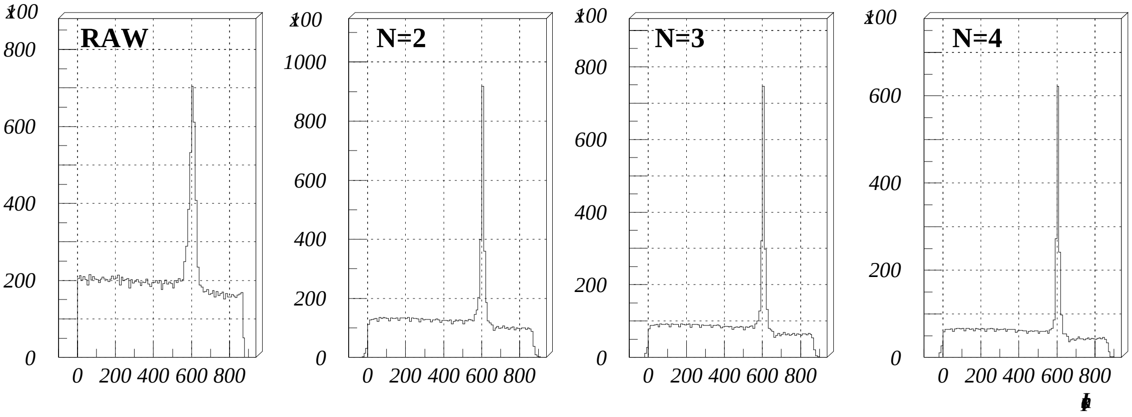

Figure 6.8: TDC timing distributions after the mode correction of N=2,3, and 4.

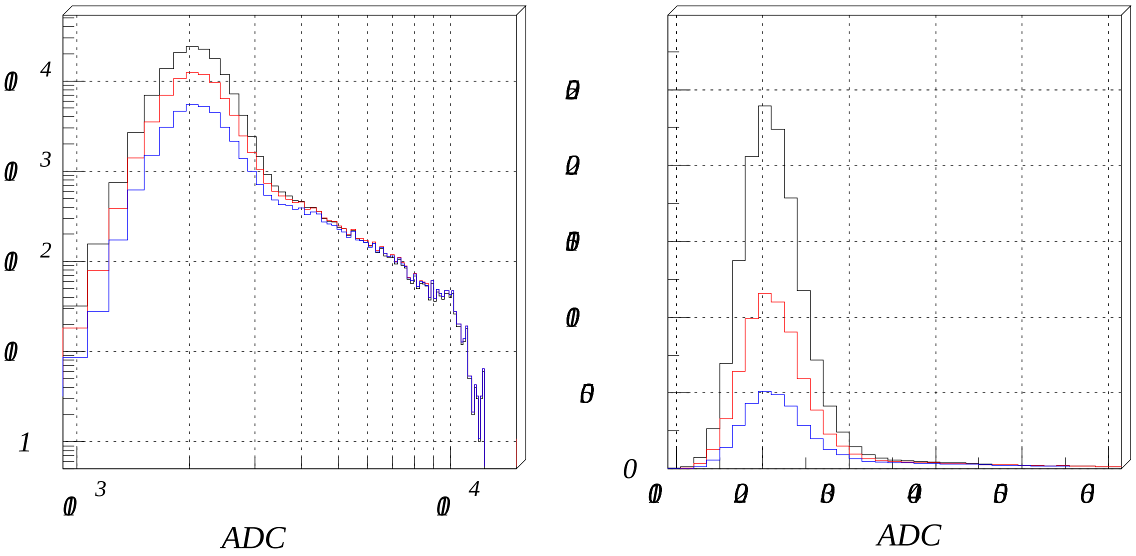

Figure 6.9: Black, red, and blue lines show raw ADC spectrum, after cut of "N"=2, and "N"=3. Left and right figure are shown by logarithmic and linear coordination, respectively (calculated from same data).

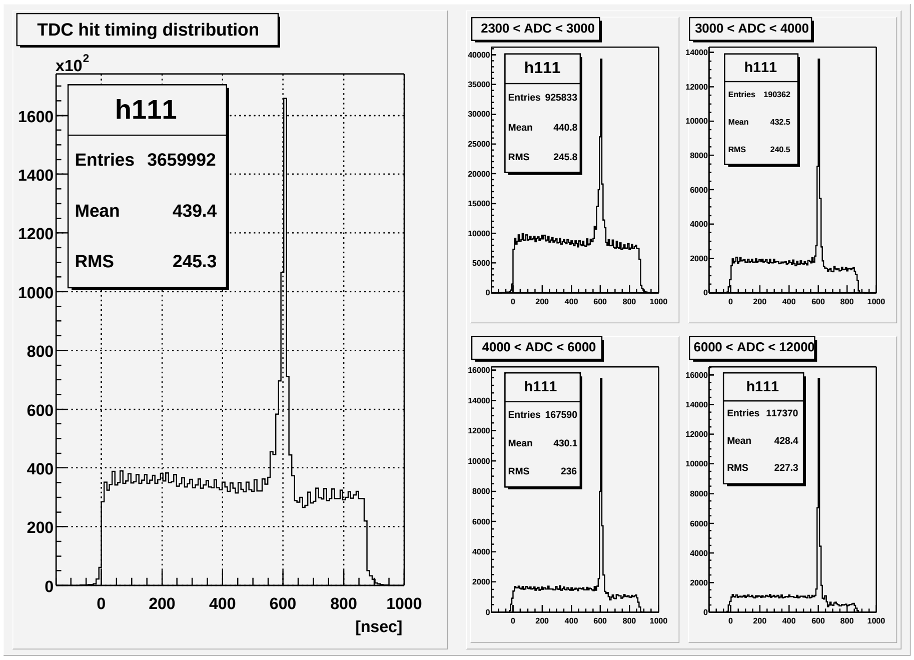

Figure 6.10: TDC hit timing distribution after mode cut.

§ 3 uADC

To extend the dainamic range of ADC to the lower energy band, we introduce "updating ADC (uADC)", which is defined as follows:

$$\text{uADC} \equiv \text{ ADC} - \Delta N_s \times \text{ ADC gate time} - \text{ Pedestal}$$

where "ΔN_s" is the ADC count of N.S.B. photon per 1 nsec per camera, and "Pedestal" is the ADC count induced by electronics noises with the offset value which ADC has intrinsically.

ADCs measure the total number of ph.-e. within the gate time of 100 nsec. That includes both ADC counts induced by cosmic-rays, and those by the N.S.B.(Fig. 6.12) If we eradicate the influence of N.S.B., the number of available events will increase, especially in lower energy band. However, unlike the Pedestal which give almost constant value throughout observation, the ADC count induced by the N.S.B. depends on the tracking points, and moreover, fluctuates event by event. To remove the incremental counts induced by N.S.B., we need to estimate it event by event.

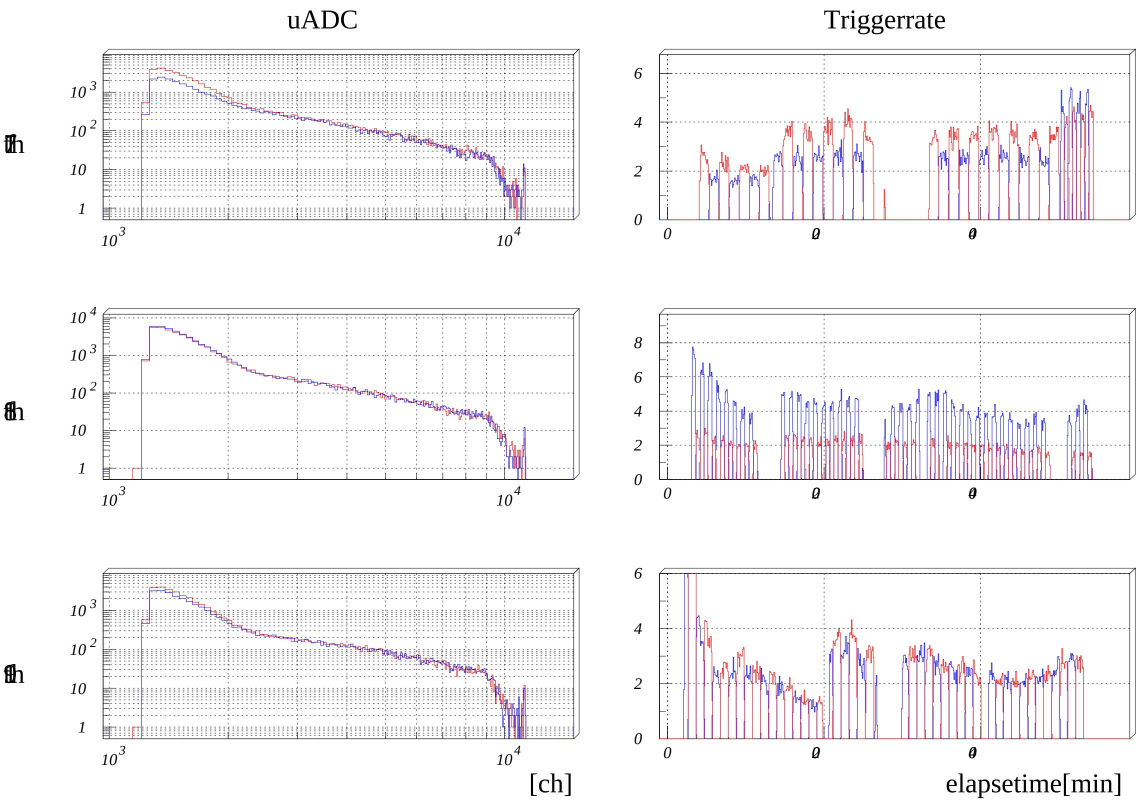

Figure 6.11: The uADC distribution and the event rate after mode cut, on Dec 17th (Top), Dec 18th (middle), and Dec 19th (bottom), where "uADC" is the ADC spectrum after N.S correction (§ 3). Red and blue line show ON and OFF source run, respectively.

We estimated the ADC count induced by N.S.B. using TDC hit timing distributions. Figure 6.12 shows the concept of it. Right figure shows the conceptional diagram of the hit timing distribution measured by TDCs. TDCs record not only the short spike composed by the trigger signals, but also the large fluctuations by the N.S.B during 1 μsec. Using these data except for 100 nsec around the peak region, we calculated the hit density of TDCs (D_{tdc} nsec^{-1}) induced by N.S.B. event by event.

Next, we need to estimate how much ADC channel corresponds to one hit of TDC caused by N.S.B. Figure 6.13 shows the 2 dimensional scatter plot of the number of PMT hit within the ADC gate time, and the sum of ADC calculated from the data recorded in the N.S.B. run. In N.S.B. run, the number of TDC hits within 100 nsec is mean 5.5, and we fit the relationship between the number of TDC hits and the sum of ADC by a linear function. The result shows that the sum of ADC increase by 32.5 channel as the number of TDC hits increasing by one. Consequently, we achieve ΔN_s as following;

$$\Delta N_s = D_{tdc} \times 32.5 \quad [\mathrm{nsec}^{-1}]$$

We can calculate ΔN_s event by event, and thus ΔN_s plays a role of the active canceler for N.S.B. The uADC value is expected to be close to the real ADC value without N.S.B. backgrounds. Figure 6.14 shows the comparison between ADC and uADC spectrum. The bump due to N.S.B. is moved to lower ADC channels, and the power law component is extended to the lower energy band.

§ 4 Noise Reduction Methods

After the correction of the hit timing distributions, the spike was the outstanding significance over N.S.B. components, and time width of spike becomes small enough, about 60 nsec. Further, we applied more two noise reduction methods.

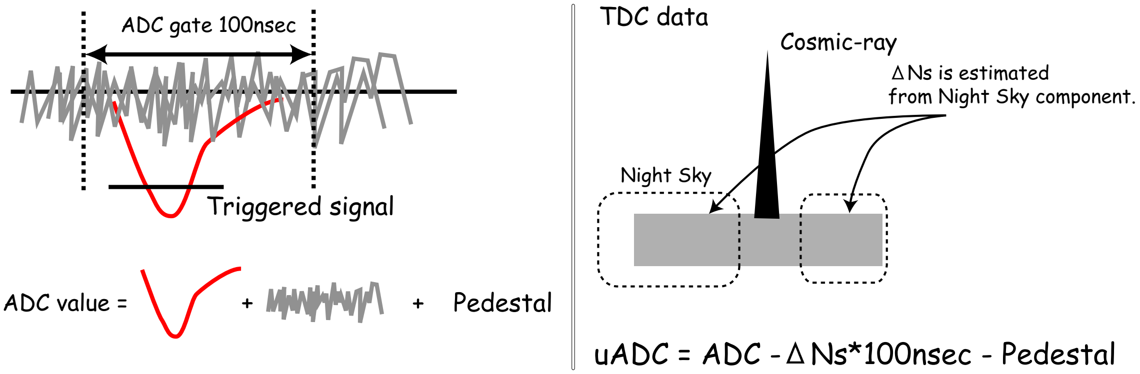

Figure 6.12: Schematic diagram of uADC

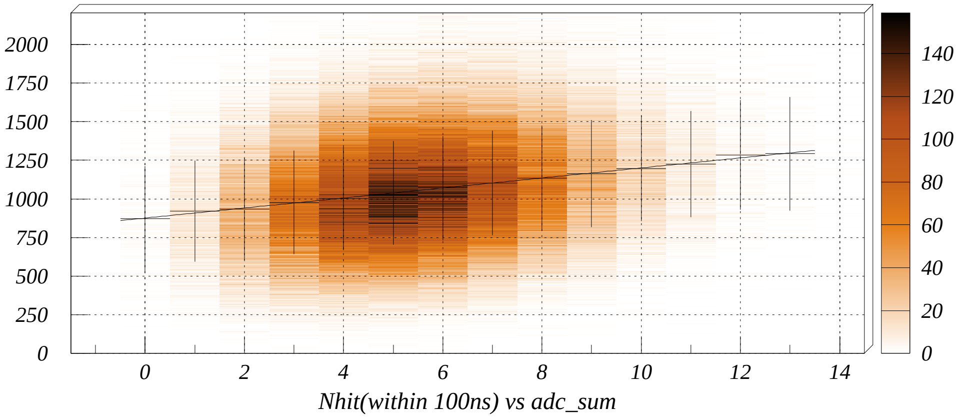

Figure 6.13: The relation between the number of PMT hit and the sum of ADC.

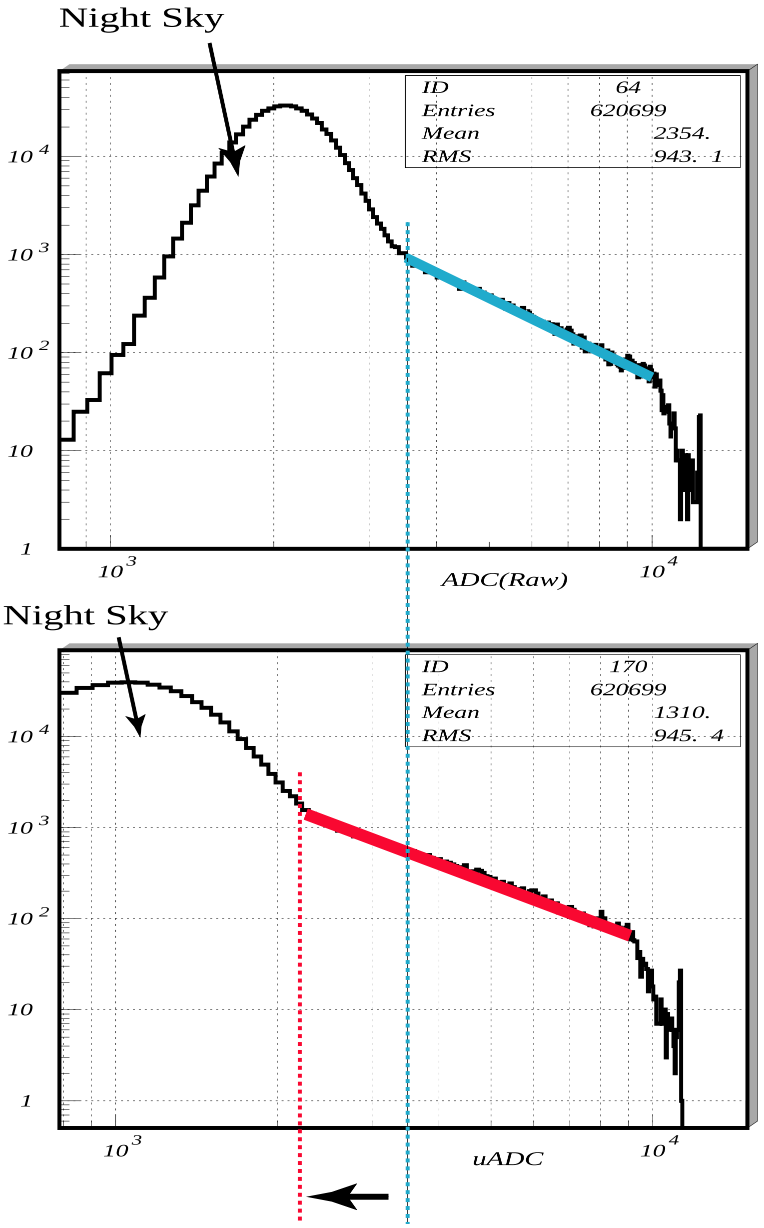

Figure 6.14: Top: ADC spectrum. Bottom: uADC spectrum.

4.1 RATIO cut

RATIO cut is the event cut method that use the “RATIO” of TDC hit density in the signal region to that in the noise region, where the signal region are defined as the 600 ± 20 nsec, and the noise region is others. Figure. 6.15 shows the concept of the RATIO cut.

The distribution of N.S.B. events shows flat character in overall TDC time. If the RATIO is significantly high, that is cosmic-ray events with high probability.

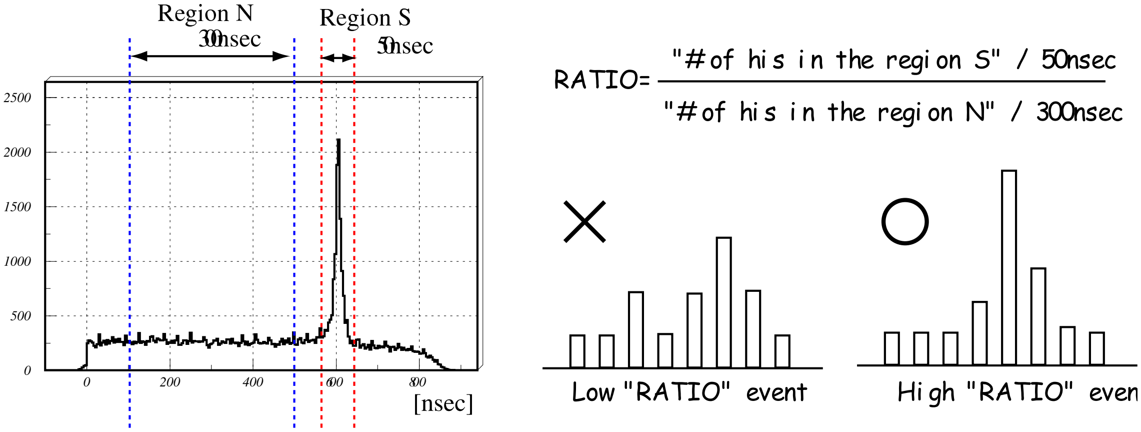

Figure 6.15: Schematic diagram of the RATIO cut.

Figure 6.16 shows the RATIO in several energy bands. If we request the cut of the RATIO of 3.0, we can remove events in low energy band (2300 < ADC < 3000) effectively without losts of events which have high ADC channel (> 3000). Figure 6.17 shows the distribution of the hit timing after the cut of RATIO > 3.0 . S/U was improved from 4.7 to 9.5, and the time width of spike was also improved to 50 nsec.

4.2 TDC width cut

As described in Ch.3-§ 8, the timing width of each PMT hit measured by TDCs has a positive correlation with the pulse hight of signals. Figure 6.18 shows the timing width of PMT hits in several kinds of runs. In a LED run (Fig. a), the voltage on a blue LED was set by -4.2 V which corresponds to the large ph.-e. event caused

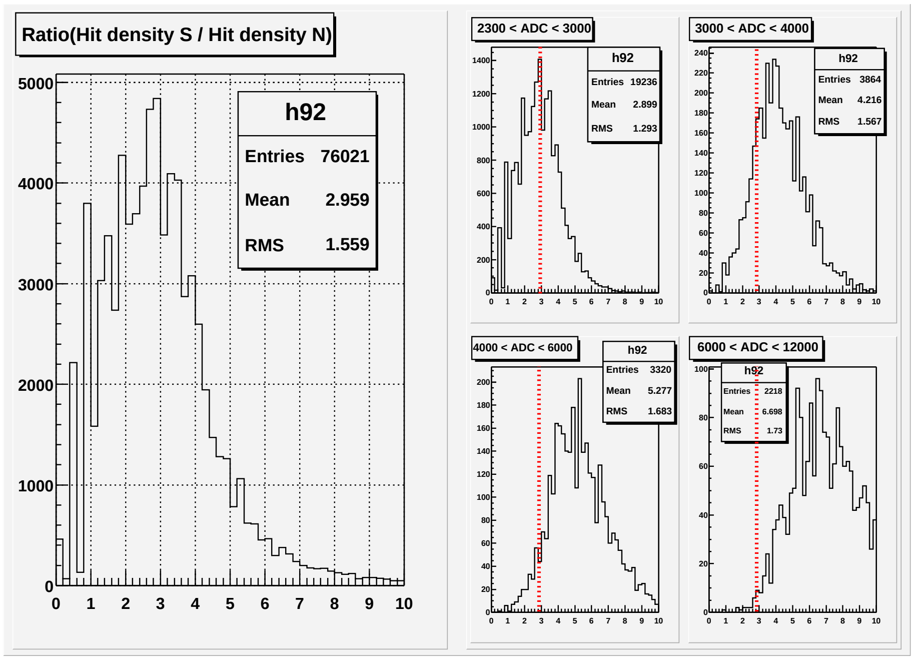

Figure 6.16: Left: The distribution of the RATIO, accumulated overall enegy. Right: The distributions of the RATIO sliced by ADC.

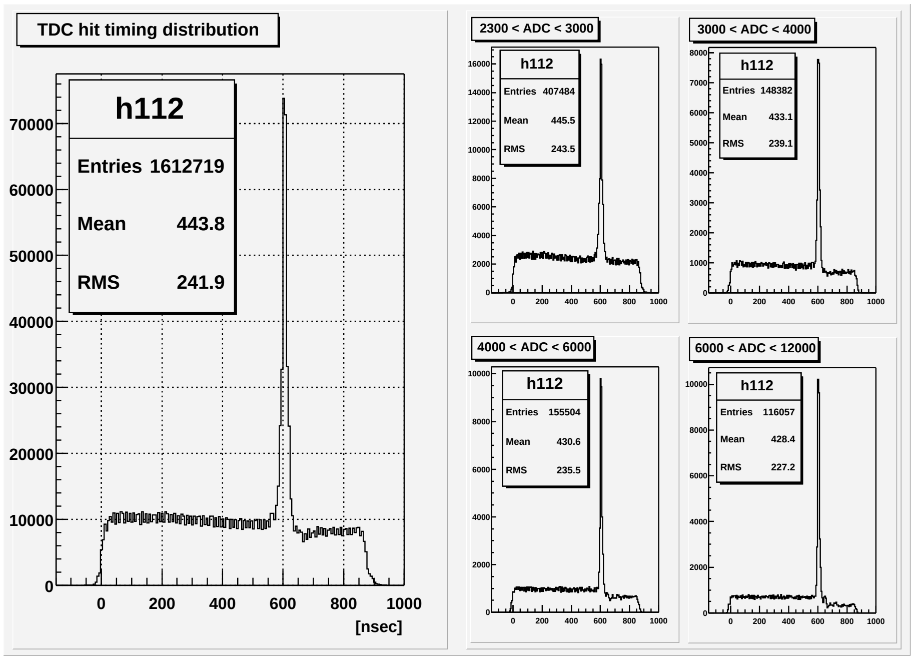

Figure 6.17: The distributions of TDC hit timing after RATIO cut.

by TeV or more energetic particle. Then, the maximum timing width caused by cosmic-rays must be about 150 nsec. In N.S.B. run (Fig. b), most timing width lie below 50 nsec, however, non-negligible number of counts exists over the maximum timing width of 200 nsec. In the N.S.B. run that forced external trigger ran, most of all events recorded by TDCs must be caused by N.S.B. photons. It seems that the huge width seems to be generated as shown in Fig. 6.19, namely, generated by overlapped by high frequent N.S.B. hits.

Figure 6.18 (c) shows the distribution of a LED run in astro-doom opened, where the voltage on a LED is the same as that in Fig. (a). The distribution is expected to be like the sum of (a) and (b). Since the rate of brighting LED is low (100 Hz), the counts caused by N.S.B. photons are overwhelmed to that cased by LED lights, but we can find a faint peak caused by LED around 80 nsec. Figure 6.18 (d) shows the distribution of a observation run pointing the Crab. According to the result of analysis on Fig. (a), (b), and (c), the timing width of over 150 nsec is unlikely to be caused by cosmic-rays, and must be caused by high frequent N.S.B. hits.

In contrast, too low width of below 10 nsec is also likely to be caused by N.S.B. TDCs installed on CheSS are not well enough to calculate the width of pulses by below 10 nsec resolution, and thus below 10 nsec means that TDC cannot detect the trailing edge because of too short pulse-width. The pulses that have such a short width must be cause by N.S.B. The cosmic-ray events would be within the timing width between 10 and 150 nsec. Consequently, we requested the TDC width cut of $10 < \text{width} < 150$ nsec.

4.3 Cluster cut

Since some accidental hits seems to be survived according to event patterns by eye scan, we applied the “cluster cut” to remove those fake images. Figure 6.20 shows the schematic diagram of the cluster cut. The image induced by a cosmic-ray is clustered, but that induced by N.S.B. shows at random in the camera. The cluster cut selects the clusters having at least “N” adjacent hit PMTs. Procedure is following;

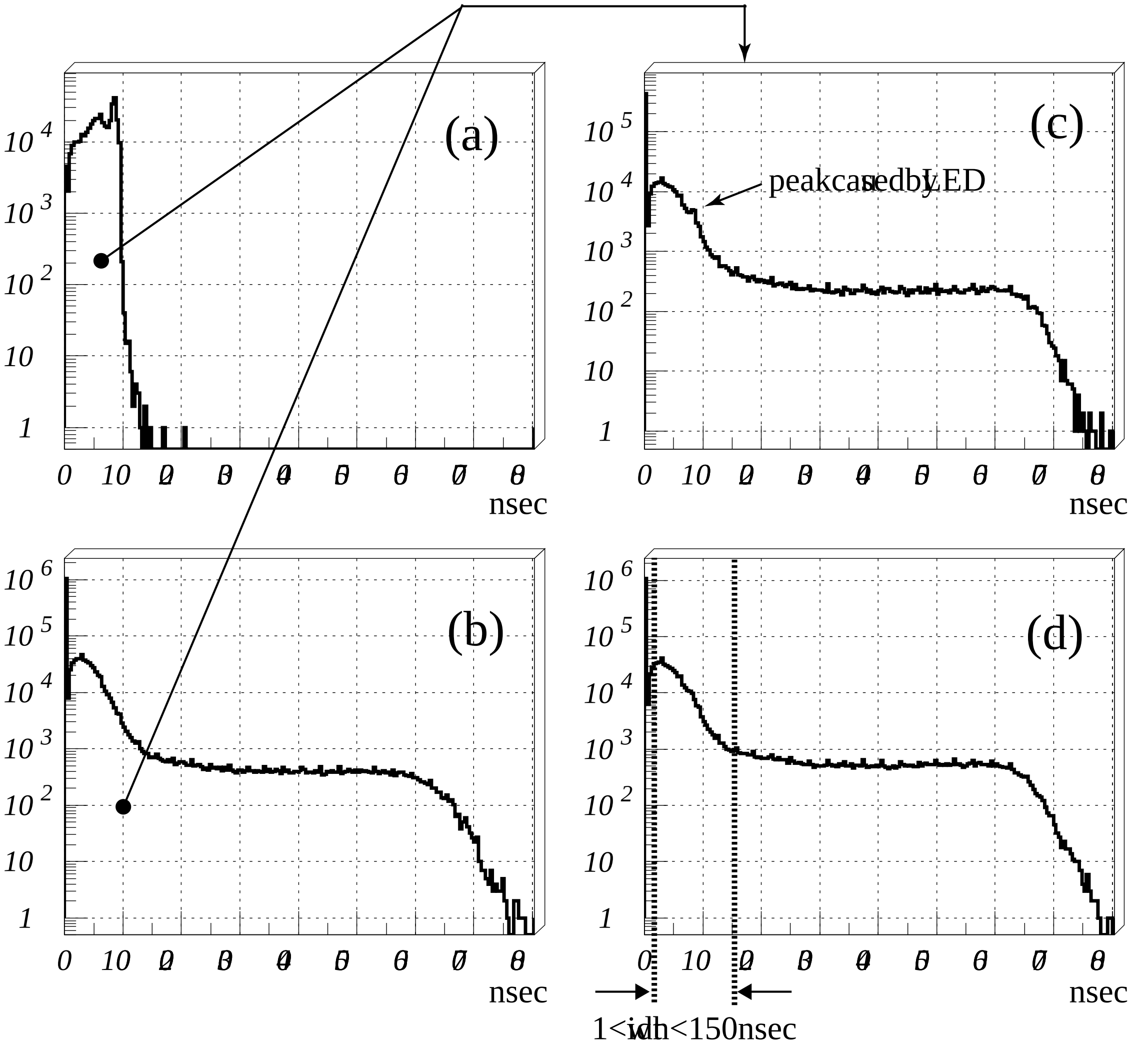

Figure 6.18: The distributions of TDC hit width. (a): the distribution in a LED run as the astro-doom is closed. (b): the distribution in a N.S.B run. (c): the distribution in a LED run as the astro-doom is opened. (d): the distribution in observation of the Crab.

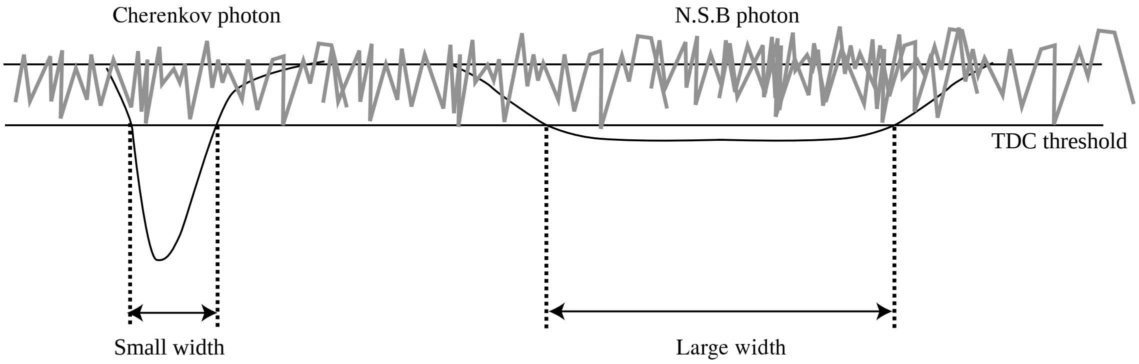

Figure 6.19: The explanation of huge width. Left: normal hits caused by cosmic-rays. Right: the huge width is recorded by contamination of many N.S.B. hits.

1. Reconstruct the image on the focal plane from TDC hits in the region S (See Fig. 6.15).
2. Clculate the size (number of hits) of each cluster.
3. Remove the clusters of which size is less than N.

The cut condition is described by "TNa", where N means the number of adjacent hit PMTs.

We examined the cut of T2a, T3a, and T4a. Figure 6.21 shows the uADC spectra after these cut conditions. T3a and T4a cut remove events around 1000 channel effectively, but also remove significant number of events at high channels. For example, for the cut of T4a, the counts at 4000 channels is about one fifths of that for before cut. Our simulation result also shows that T3a and T4a is too high cut and lost events, especially in lower energy bands. Figure 6.22 shows the number of hits induced by simulated gamma-rays and protons in several energies. The gamma-rays in an energy of 60 GeV induce only a few hits on the camera, and the cut of T3a or T4a discards a large part of events. Therefore, we decide to apply T2a cut throughout this paper. As shown in Fig. 6.22, T2a cut is enough to improve the time width of spike. The S/U of the hit timing distribution was also slightly improved after the clustering cut of T2a (Fig. 6.24).

In Fig. 6.21, we point out the fact that the bump around 1000 channels still exists after TNa cut, even if N=4. We discuss the origination of this bump in the next chapter.

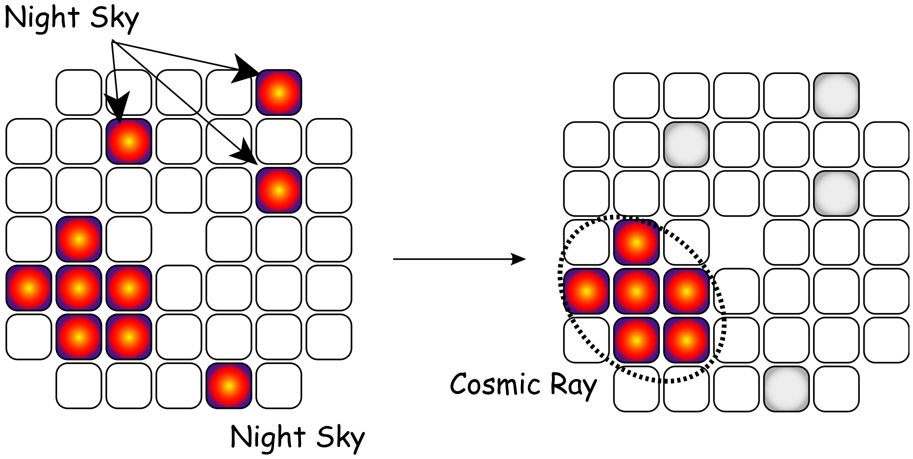

Figure 6.20: Schematic diagram of TNa cut

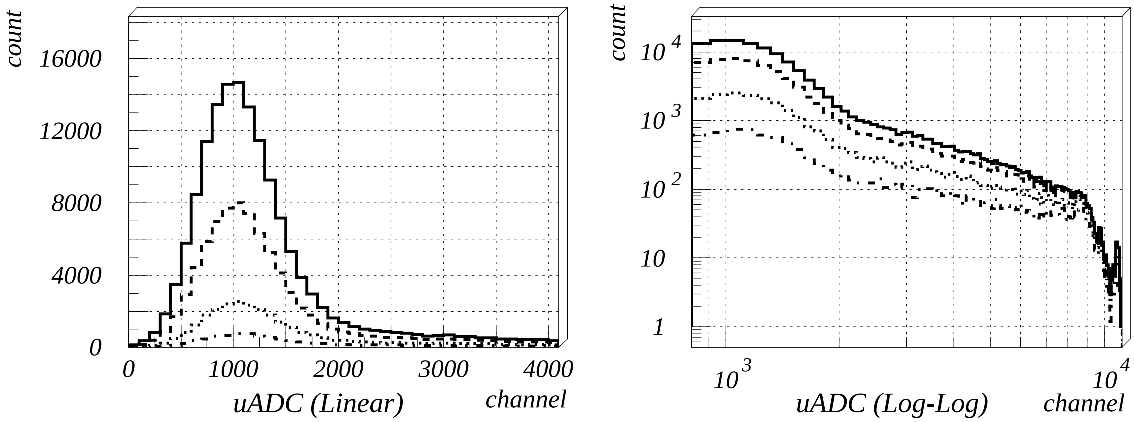

Figure 6.21: uADC spectra before the TNa cut (solid line) and after the T2a (dashed line), T3a (dotted line), and T4a (dash-dotted line). Left and right figure are shown by linear and logarithmic coordination, respectively (calculated from same data).

§ 5 Event rate

After all corrections and cuts introduced in this chapter, the event rate as the function of elapse time is shown in Fig. 6.25. Event rate is about 2 Hz around the

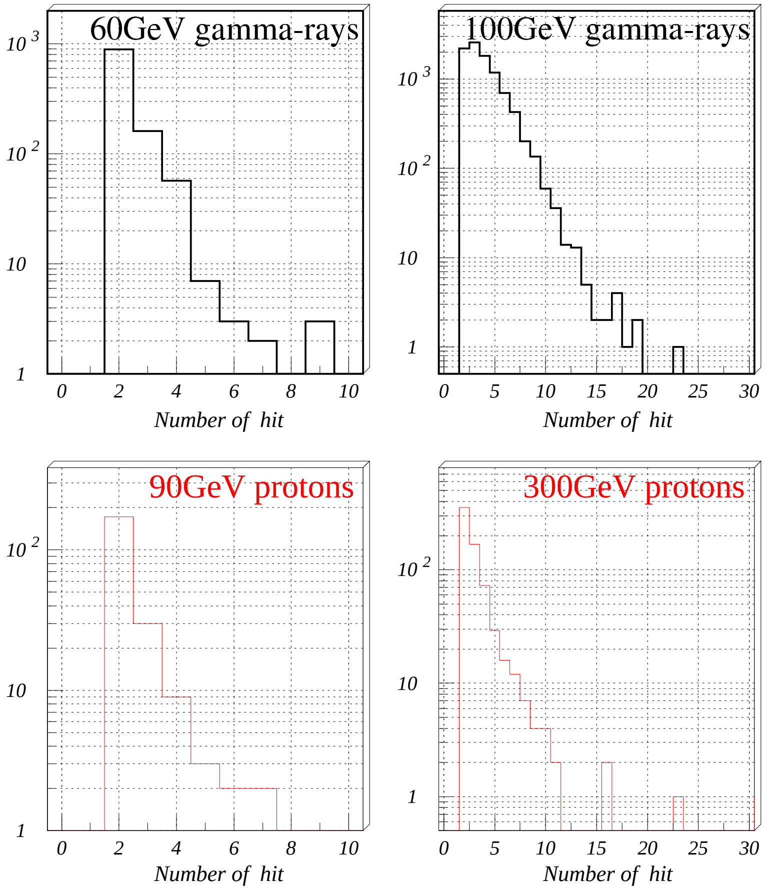

Figure 6.22: Number of PMT hits in simulation.

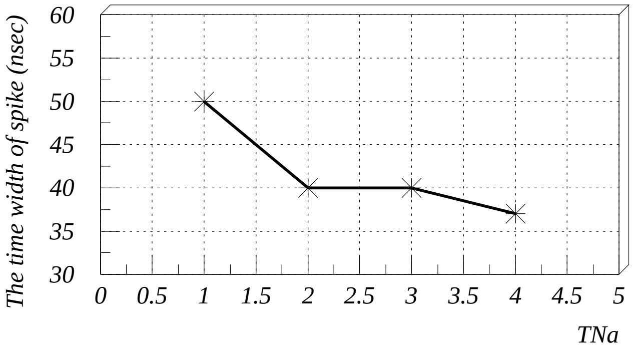

Figure 6.23: The time width of spikes after TNa cut of N=1, 2, 3, and 4.

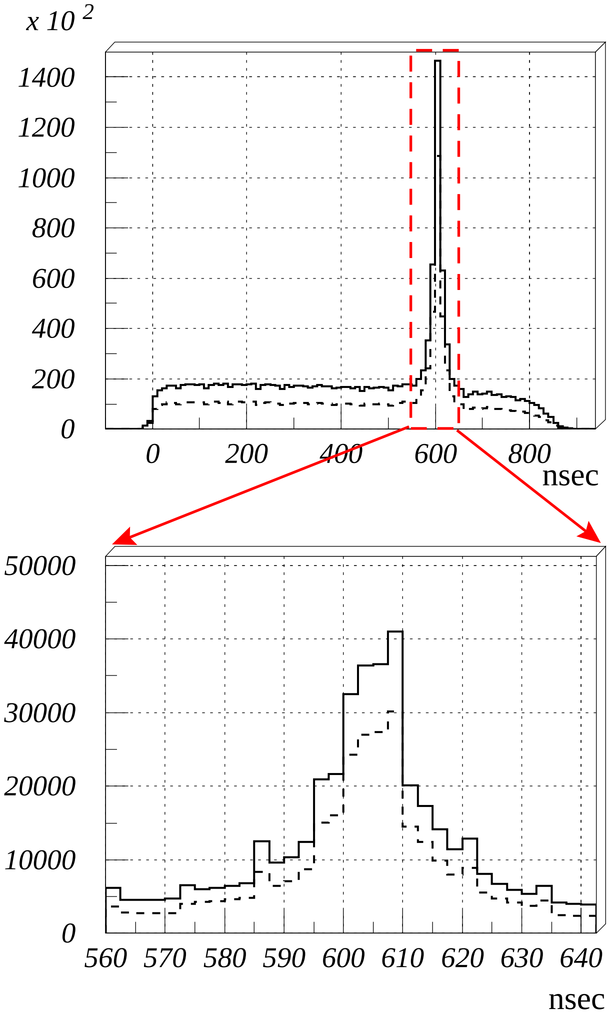

Figure 6.24: TDC hit timing distribution before and and after the TNa cut.

zenith.

We can see two discontinuous points in 17th and 19th light curves. These are due to the change of the threshold levels as described in Ch.5-§ 1.

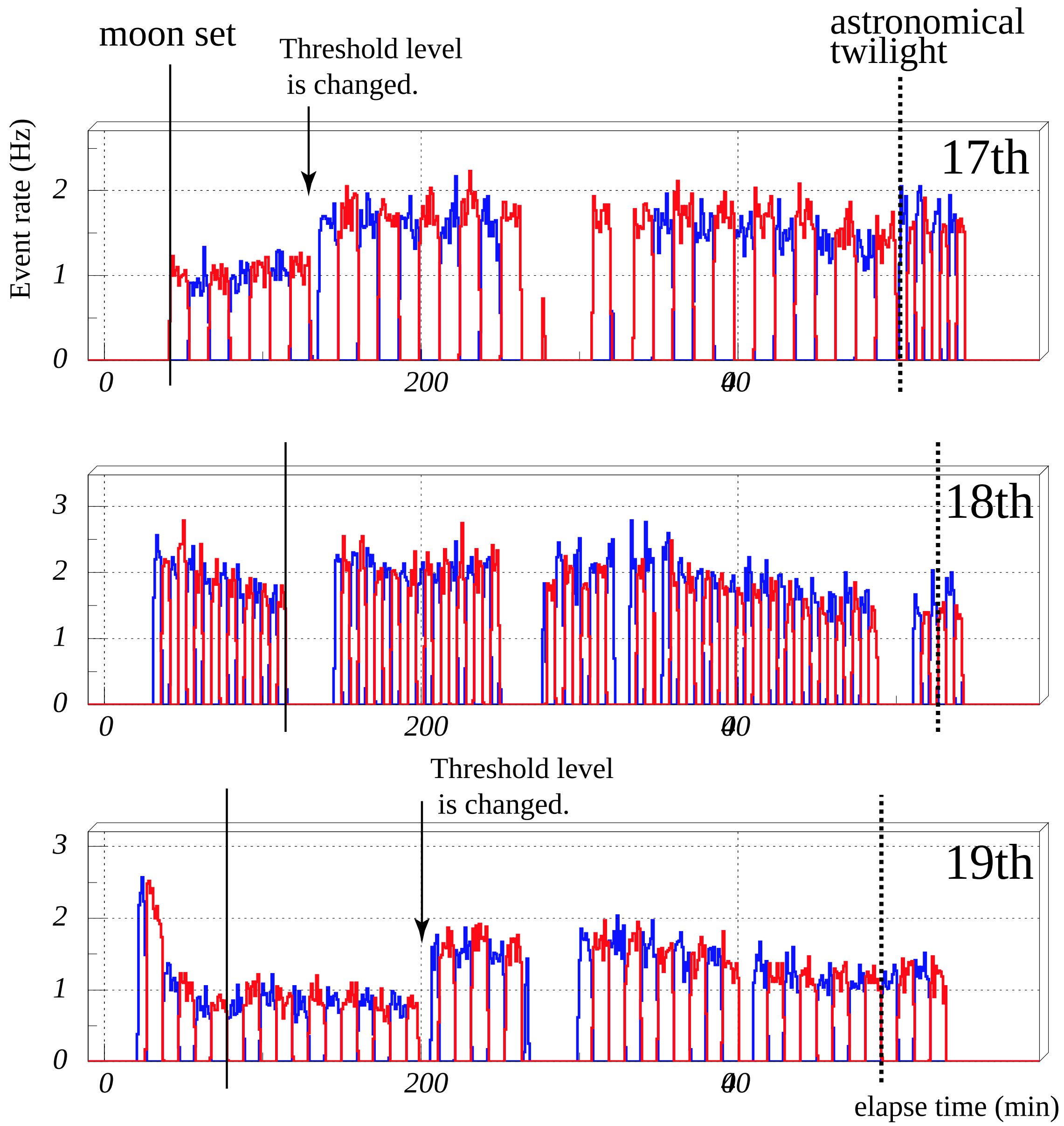

Figure 6.25: Event rate as the function of elapse time after ADC cut (< 2300), TDC mode correction, RATIO cut (> 3.0), TDC width cut ($1 <$ width < 150 nsec), and T2a cut.

Chapter7

Discussion

> “There’s more evidence to come yet, please your Majesty,” said the White Rabbit, jumping up in a great hurry: “this paper has just been picked up.”
>
> “What’s in it?” said the Queen.
>
> “I haven’t opened it yet,” said the White Rabbit; “but it seems to be a letter, written by the prisoner to – to somebody.”
>
> “It must have been that,” said the King, “unless it was written to nobody, which isn’t usual, you know.” — *Alice’s Evidence* —

§ 1 Comparison of ADC spectra between simulation and observation

In this section, we compare the ADC spectra between simulation and observation. However, the simulation results are provided by the unit of the number of ph.-e. At first, we calculated how much ADC counts corresponds to the number of ph.-e. Figure 7.1 shows the number of hits versus ADC counts in observation, and the number of hits versus sum of number of ph.-e. in simulation. We fitted two results by linear functions. The fitting results the slopes of 304 ± 0.520 counts/hit for observation, and 9.93 ± 0.259E-01 ph.-e./hit. for simulation. The Division for two slopes, 304 / 9.93, results 31 ± 0.18 [ADC/ph.-e.]. Hereafter, we convert the ADC count to number of ph.-e. using this results.

The trigger rates at the three OFF points that we observed in December 2001, were quite different from each other due to the fluctuation of the N.S.B. level, and were distributed between 7 Hz and 25Hz (Fig. 5.4). The N.S.B. level has a strong effect on the counting rate below 100 GeV, leads to large systematic errors, and thus we must reduce the N.S.B. event as much as possible in order to estimate the flux of gamma-rays using only conventional ON-OFF chopping methods. To reject N.S.B. hits, we tried a great number of cut method, and found that several methods of them are quite effective. Those methods are the RATIO cut, the Clustering cut, and TDC width cut, which have been already introduced in Ch.6. Figure 7.2 shows the timing distributions of PMT hits before and after N.S.B. rejection (RATIO $>$ 1.0, T2a clustering cut, and $1 <$ TDC width < 150). The hatched area corresponds to the hits due to N.S.B. photons within the gate time of ADC, and hits in this area distort the power-law spectrum measured by ADC. After rejection, the accidental events due to the N.S.B. were effectively removed, and hatched area becomes quite small, about one fifth.

Figure 7.3(a) shows the ADC distribution after N.S.B. rejection. We can still see a broad bump below 70 ph.-e. We tried to remove the bump by requesting a larger number of hits in the clustering cut, but to no avail. These results imply that this bump is not caused by the N.S.B.

Figure 7.3 (b) shows a simulated ADC distribution of CheSS, where we assume an observation time of 5 hours, which is the same as that in Fig. 7.3(a). For proton events, we translate the energy of proton showers in Fig. 4.10 to photo-electron. For muon events, we assume that the Čerenkovphotons have a Gaussian distribution with a mean of 37.7 ph.-e. and σ of 11.8 ph.-e. (Fig. 4.14). In addition, we apply the same N.S.B. rejection method as that for the observation data. The simulated ADC distribution replicates the bump below 65 ph.-e. This result concludes that the bump is not due to the N.S.B., but due to muon showers. Above 90 ph.-e., proton shower events are dominant. As shown in Fig. 7.3, both the simulated and observed ADC distributions are well fitted by a power law with the same index = -1.8, above 90 ph.-e.

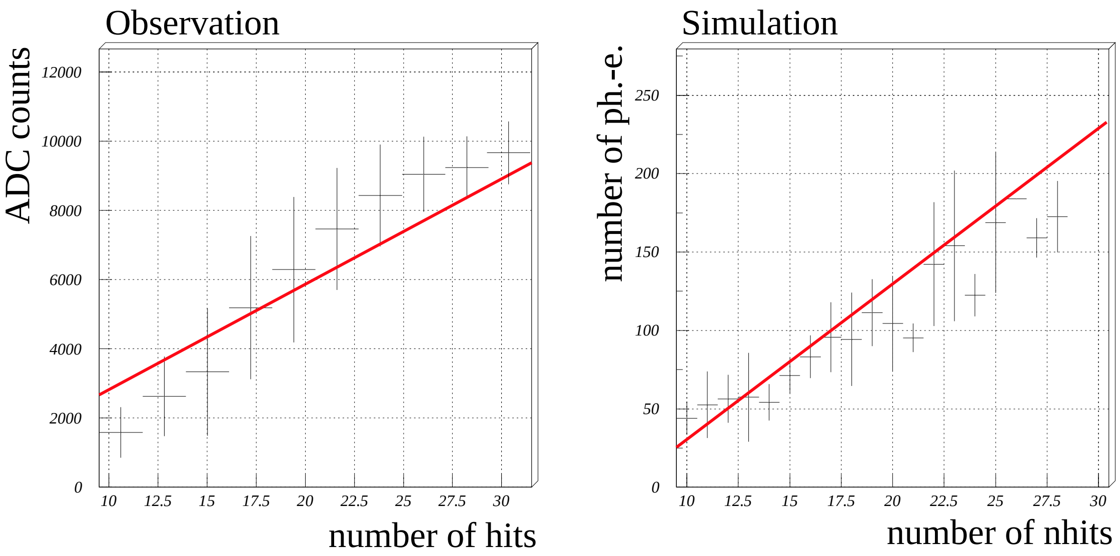

Figure 7.1: Left) the number of hits versus ADC counts in observation. The slope of the fitting line is 304 ± 0.520 counts/hit. Right) the number of hits versus sum of number of ph.-e. in simulation, where we assumed energy bands between 15 and 1000 GeV. The slope of the fitting line is 9.93 ± 0.0259 ph.-e./hit.

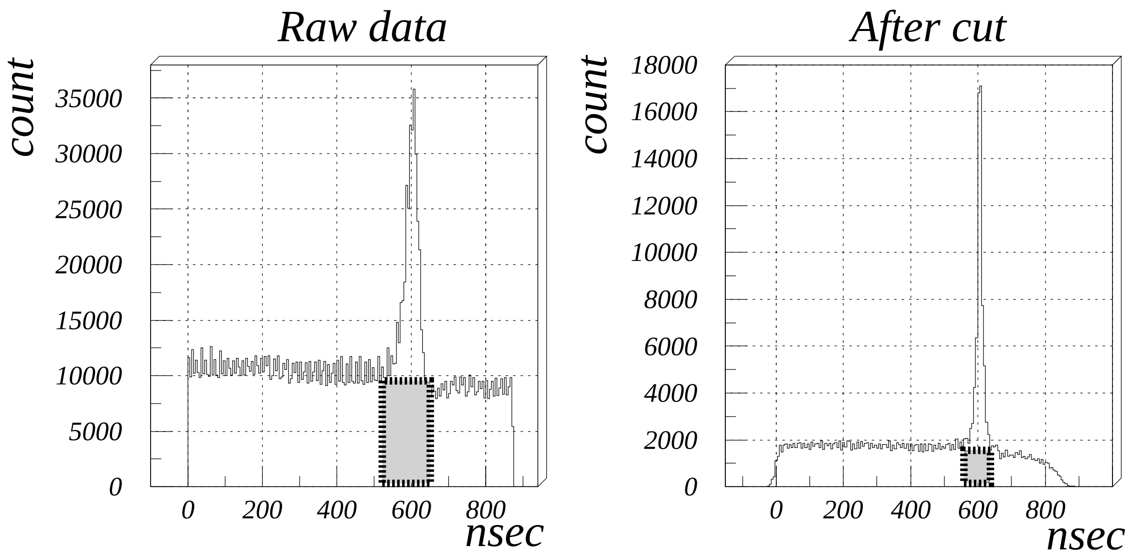

Figure 7.2: Hit timing distributions before (left) and after (right) N.S.B rejection, calculated from the observation data.

The hatched region shows the hits due to N.S.B. photons within the gate time of ADC.

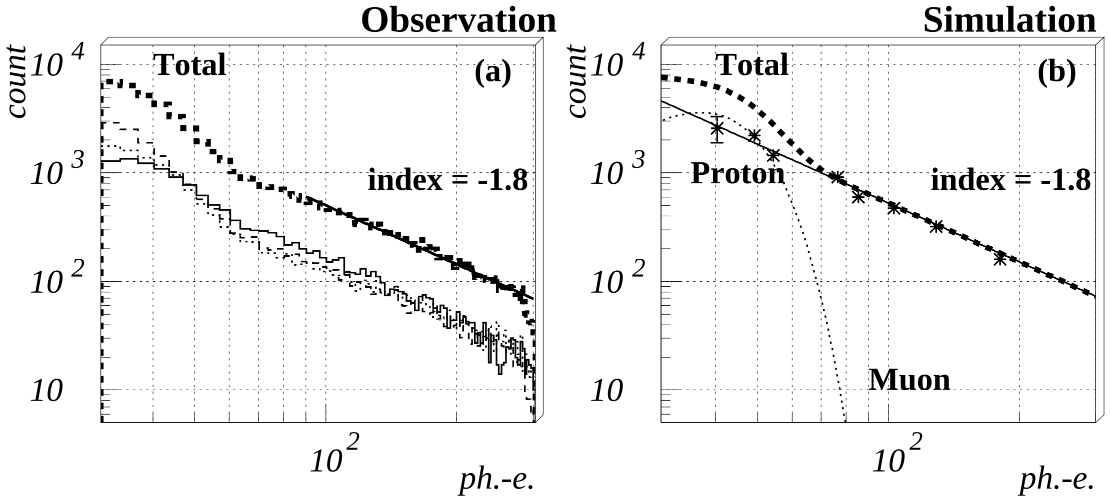

Figure 7.3: (a) Distribution of the ADC channel in an observation, where we apply the off-line rejection of N.S.B. events (hit timing cut & clustering cut). The solid, dashed and dotted line represent the distributions at 12 min OFF, 5 min OFF, and 10 min OFF points, respectively. The heavy-dashed line shows a total of 3 OFF points (5 hours of observation). The counts in the energy range between 90 and 250 ph.-e. are well fitted by a power law with an index= -1.8.

(b) Expected ADC spectrum calculated from simulation results of proton showers and muon showers. The result of proton showers is also well-fitted by a power law with an index of -1.8. The number of photons generated by muons has a Gaussian distribution of 38 ± 12 ph.-e. (See Fig. 4.14).

§ 2 LENGTH/SIZE parameter

In low ph.-e. bands, we found that muon events have strong effects on the ADC spectrum and the event rate. The Whipple telescope group proposed to remove muon events by using the parameter "LENGTH/SIZE" (Catanese et al. 1995), where LENGTH is the Image Parameter introduced in Ch.2-§ 3 and SIZE equals the number of ph.-e. The cut using "LENGTH/SIZE" parameter is quite effective to remove muon events for a standard IACT which has 3.0 degree FOV camera (we will show that in Ch. 8- § 5.). However, in the case of CheSS, the rejection power is much less because of the small FOV.

Figure 7.4 shows the LENGTH/SIZE parameters of simulated muon and gamma-ray events. The simulated energy bands for gamma-rays and muons are 30 - 100 GeV (the slope of energy spectrum are -2.0 and -2.7, respectively). We find that LENGTH/SIZE parameter has strong energy dependency. In lower energy band, the rejection power for muons tend to be stronger (Ch. 8- § 5). The energies of 30 - 100 GeV are the lowest bands for CheSS, but the LENGTH/SIZE parameter cannot distinguish between gamma-ray events and muon events.

Figure 7.5 shows the distributions of LENGTH/SIZE parameter in simulation and observation. The simulated energy band is 60 - 300 GeV and the slope of energy spectrum is -2.7. The distribution of LENGTH/SIZE parameter in observation is expected to be like the sum of the distribution of protons and that of muons. Indeed, both distributions shown in Fig. 7.5 resemble each other, except in the rage of LENGTH/SIZE >0.008. This fact implies that LENGTH/SIZE cut also cannot distinguish between muons and protons. Consequently, for a 0.75 degree FOV, the LENGTH/SIZE parameter is not effective cut for muon rejection.

§ 3 Diffecence between ON and OFF source run

Figure 7.6 shows uADC spectra in three different days after the N.S.B. rejection which includes RATIO > 1.0, T2a clustering cut, $1 <$ TDC width < 150. Moreover, we requested the elevation angle > 60 degrees. The significance in 17th, 18th, and

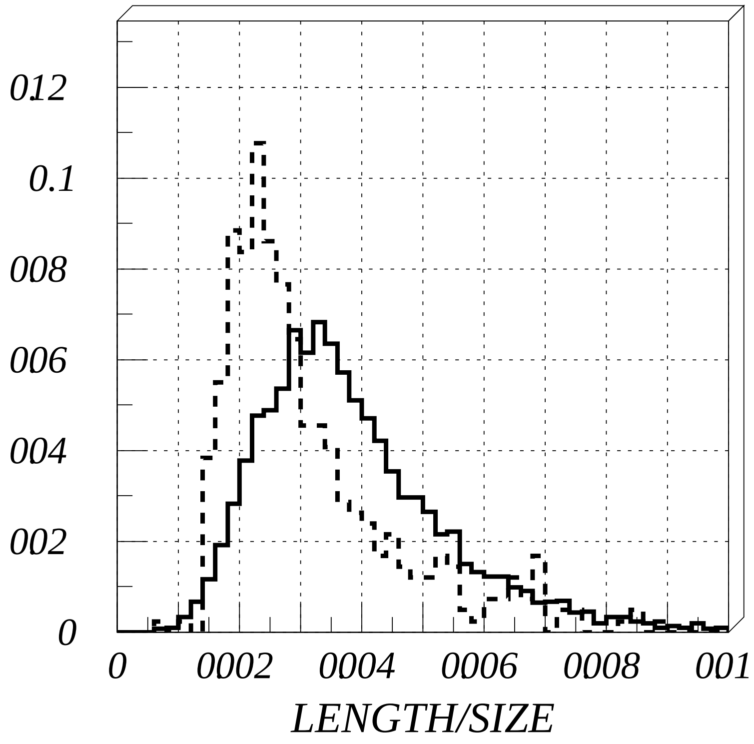

Figure 7.4: Distributions of the "LENGTH/SIZE" parameter of gamma-ray (solid line) and muon events (dashed line). The simulated energy band is 30 - 100 GeV.

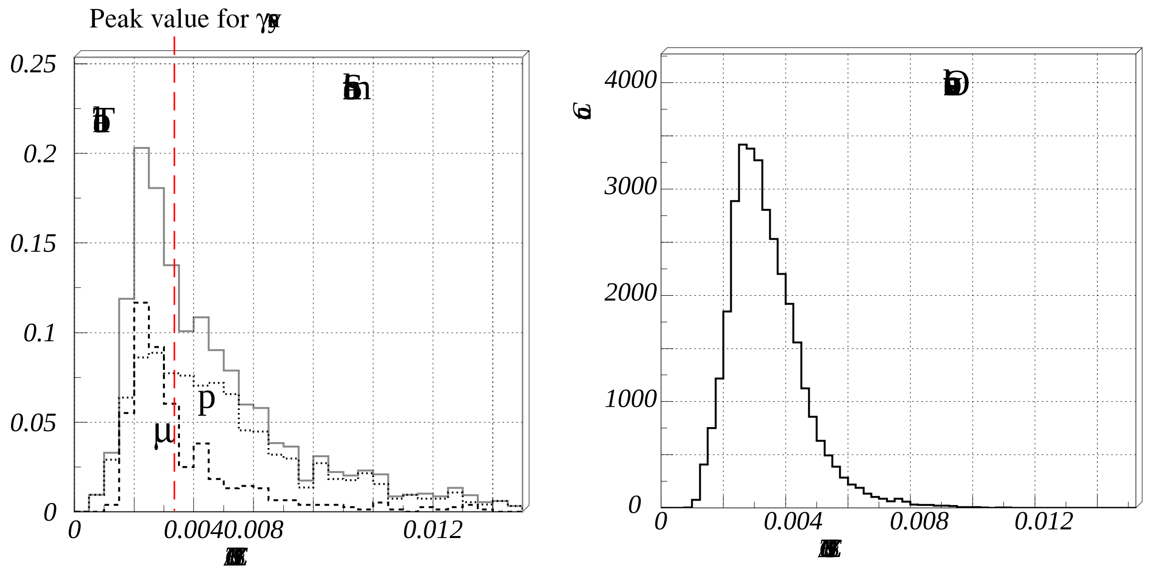

Figure 7.5: Distributions of the "LENGTH/SIZE" parameter in simulation (left) and observation (right).

19th is calculated from

$$\text{significance} = \frac{N_{ON} - N_{OFF}}{\sqrt{N_{ON} + N_{OFF}}} , \tag{7.1}$$

and found to be 4.9, -3.8, and -0.3 σ, respectively.

The significance of three days total is -0.2 σ, and thus we cannot find the difference of counts between ON and OFF source run. In this cut condition, spectra taken at four different points (3 OFF points and 1 ON point) are well accorded with each other. Therefore, the effects induced by N.S.B. events is completely removed.

§ 4 Timing analysis

We have not yet successed to estimate the unpulsed gamma-ray flux from the difference of count between ON and OFF source data. Analysis for gamma-rays is underway, but we can have a better understanding of pulsed gamma-rays using timing analysis.

A test for a periodic signal in sparse data (arrival times of photons) involves a test for uniformity (Mardia 1972). If the test rejects uniformity at a reasonable level of significance, we may accept the presence of a pulsed signal. The sensitivity depends on the "power" of the test, which is the probability that the test would identify a periodic signal with given pulsed strength and pulse profile. It is therefore desirable to use the most powerful test for identification. De Jager et al.(1989) discussed in their paper the power of various tests in X- and γ-ray astronomy. If we do not know which pulse profile to expect, a test would be needed to have moderate power against a wide range of possible pulse profiles. They concluded that a new test for uniformity called the "H-test" has a very good power against most light curve shapes encountered in X- and γ-ray astronomy, and thus makes the detection of sources with a larger variety of shapes possible. However, in our case, we have already known the pulse profile of Crab (period= 33 msec; double-peak). Figure 7.7 shows the power curves of various tests for Crab- and Vela-like double-peaked light curves. The Rayleigh-(Leahy et al. 1983) and Watson's U^2-tests (Watson 1961) perform poorly for all values of the signal strength. In contrast, the epoch folding

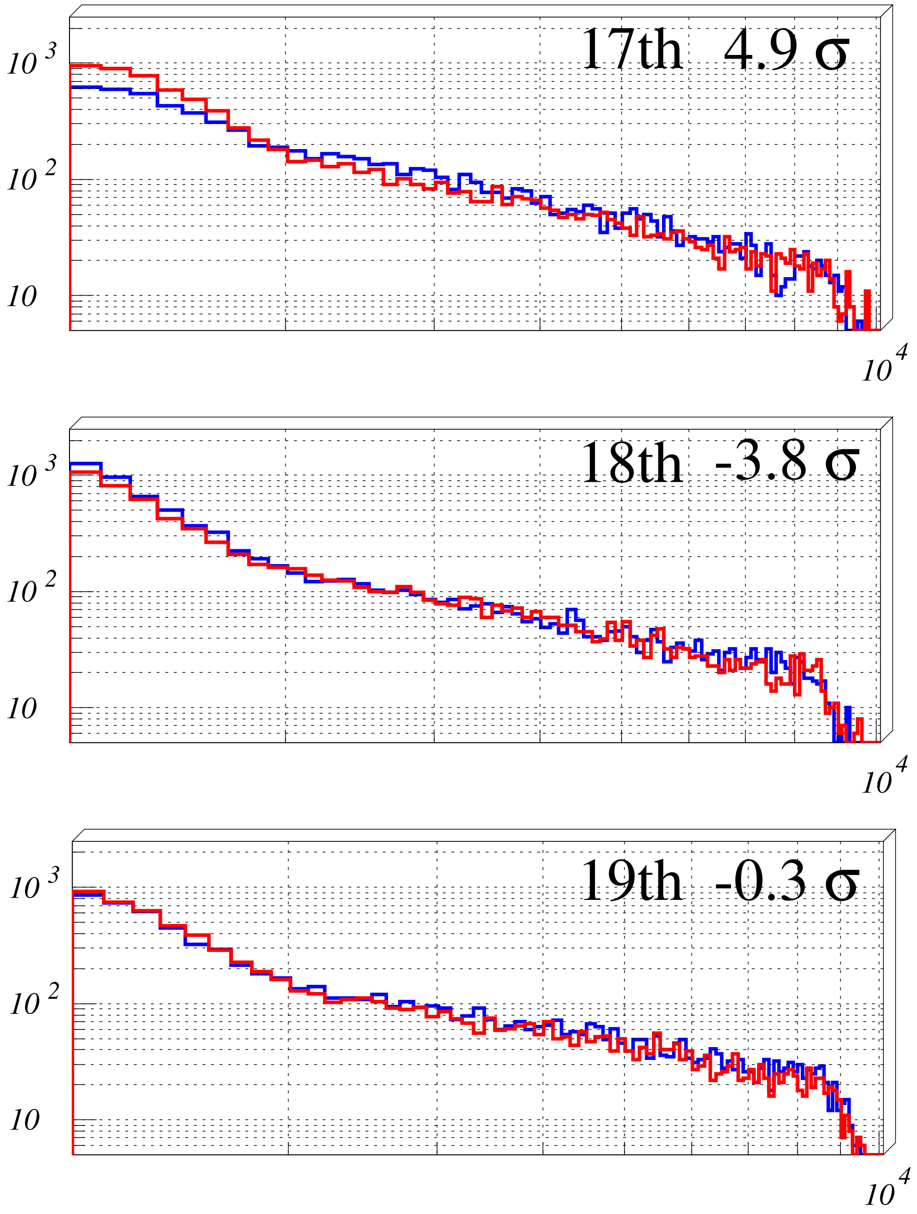

Figure 7.6: uADC spectra in 17th, 18th, and 19th Dec 2001 after N.S.B. rejection (RATIO > 1.0, T2a clustering cut, and $1 <$ TDC width < 150). The red and blue lines shows ON and OFF source data, respectively. The significances defined as $(N_{ON} - N_{OFF})/\sqrt{N_{ON} + N_{OFF}}$ are superimposed.

method is not the best, but significantly powerful. Under epoch folding, the data are folded modulo a trial period and then binned; Person's χ^2 is used to test the resulting light curve for uniformity. This statistic is χ^2_{n-1} distributed, where n is the number of phase bins. In Fig. 7.7, the symbol "χ^2_{19}" represents Person's χ^2-test with 20 bins. The algorithm of epoch folding is so simple that we can easily code it. Therefore, we adopted Person's χ^2-test with 20 bins for timing analysis.

In pre-analysis, the arrival time of each event must be transformed to the solar system barycentric (SSB) time because of the relatively short of the Crab pulsar (See appendix B). A derivative of the TEMPO programs (Taylor and Weisberg 1989),(Yoshikoshi 1996) is used for the transformation on the event arrival times. The solar system ephemeris used in the analysis comes from the Jet Propulsion Laboratory (JPL) and is based on epoch 2000. To conduct the epoch folding serch, we used our original epoch folding program, and the XRONOS package(Stella et al. 2001) for the cross-check. Both results were consistent with each other.

We applied the epoch folding to the same data set as § 3. Figure 7.8 shows the result of epoch folding, where the trial period range is $3.35312051841 \times 10^{-2} \pm 8 \times 10^{-7}$ sec. The value of $3.35312051841 \times 10^{-2}$ is the period of the Crab pulsar in 19 December 2001, observed by the radio telescope, Jodrell Bank Observatory (Lyne et al. 2002). We cannot find significant deviation from the uniform distribution. In order to cross-check this result, the Fast Fourier Transform was also applied to the same data set, and no significant excess is seen in the periods between 1 and 100 Hz.

§ 5 Upper limit for pulsed gamma-ray emission from Crab

We were not able to detect pulsed gamma-ray emission from Crab, but it is meaningful to estimate the upper limit for it.

At first, we estimated the energy of primary particles based on the simulation results. Figure 7.9 shows the same histogram as Fig. 7.3(a) superimposed simulation

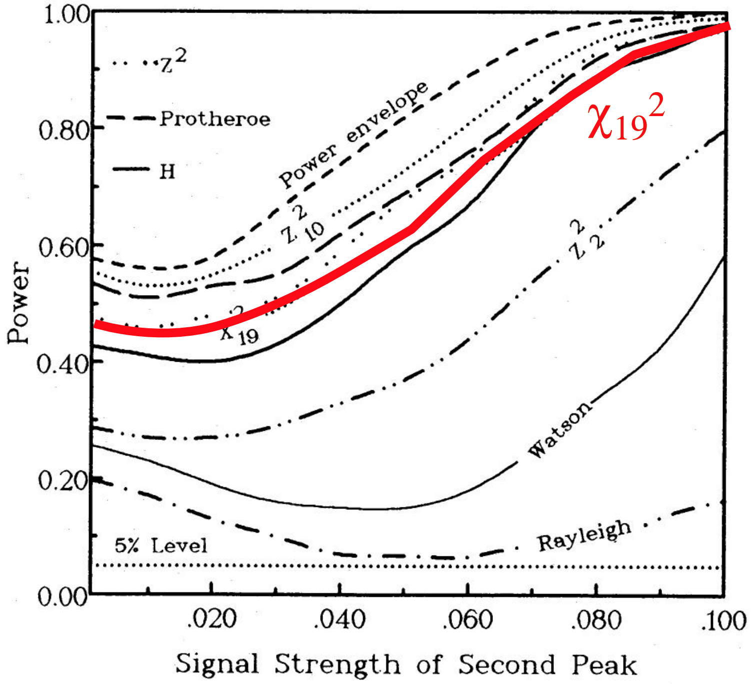

Figure 7.7: Power curves of various tests for Crab- and Vela-like double-peaked light curves (with 3.7% and 5.4% duty cycles respectively). The symbol "χ^2_{19}" represents Person's χ^2-test with 20 bins. The signal strength of the first peak is 5% and the power is drawn as function of the strength of the second peak. The sample size was again taken as 300 with a 5% detection threshold. The "power envelope" (the upper dashed curve) represents the best that any test can do in this case(de Jager et al. 1989).

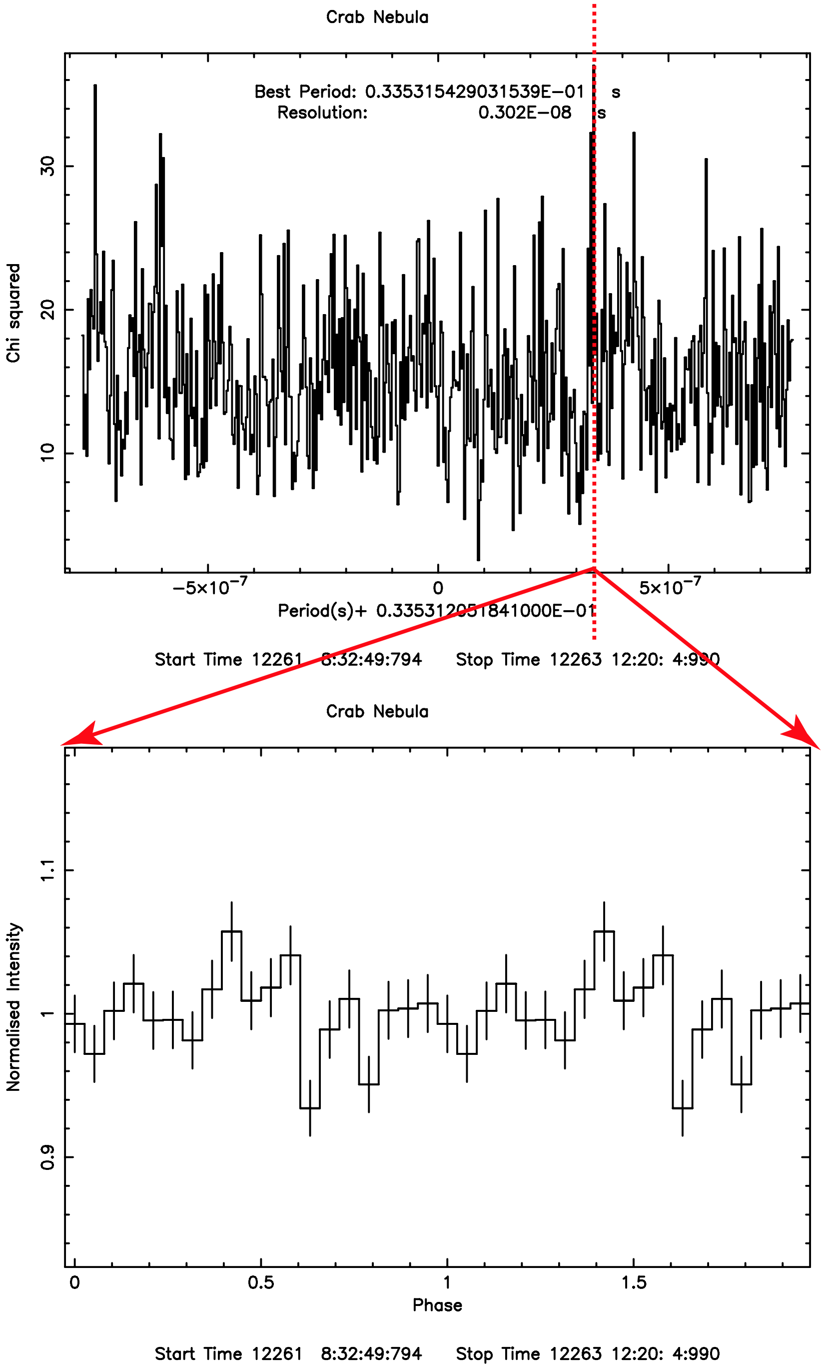

Figure 7.8: Result of the epoch folding search with 20 bins (Top). The pulse profile at the best period is also shown.

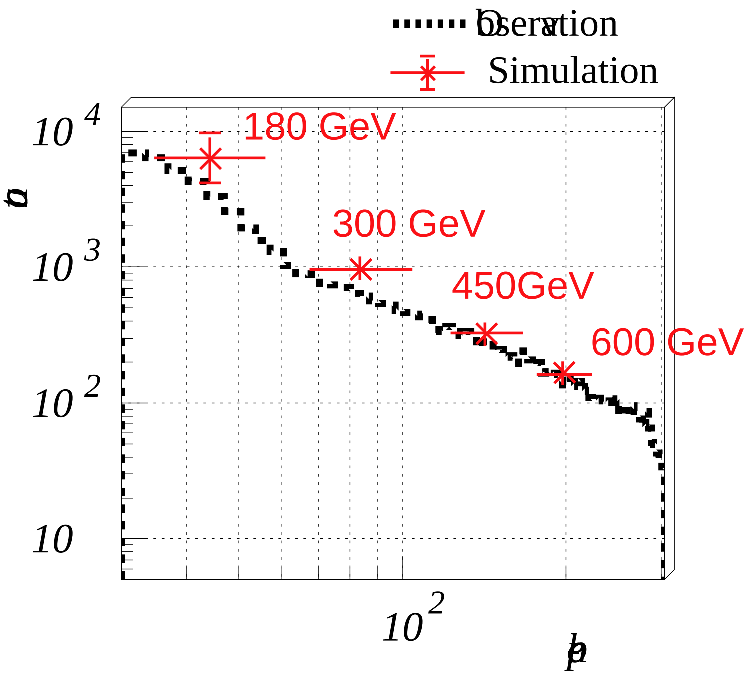

Figure 7.9: Distribution of the ADC channel in observation with the simulation results of proton showers having the energy of 180, 300, 450, 600 GeV.

results of proton showers having the energy of 180, 300, 450, 600 GeV. The number of ph.-e. induced by 180 GeV protons is equals to that induced by about 100 GeV gamma-rays (Fig. 4.12 (b)). Therefore, CheSS seems to have observed above 100 GeV gamma-rays.

If we requested the elevation angle > 60 degrees, total observation time of ON and OFF source run is 10 hours each. According to the significance lines calculated in Fig.4.17, we calculated the upper limit for pulsed gamma-ray emission from Crab, that is,

$$3.5 \times 10^{-5} \qquad [\mathrm{MeVcm^{-2}s^{-1}}] \qquad (> \ 100\mathrm{GeV}), \tag{7.2}$$

with 10 hours ON, 10 hours OFF, and 2 σ significance (Fig. 7.10). In this calculation, we didn't count the improvement significance due to the timing analysis, because we could not find how much duty cycle the Crab pulser has in the 100 GeV energy region.

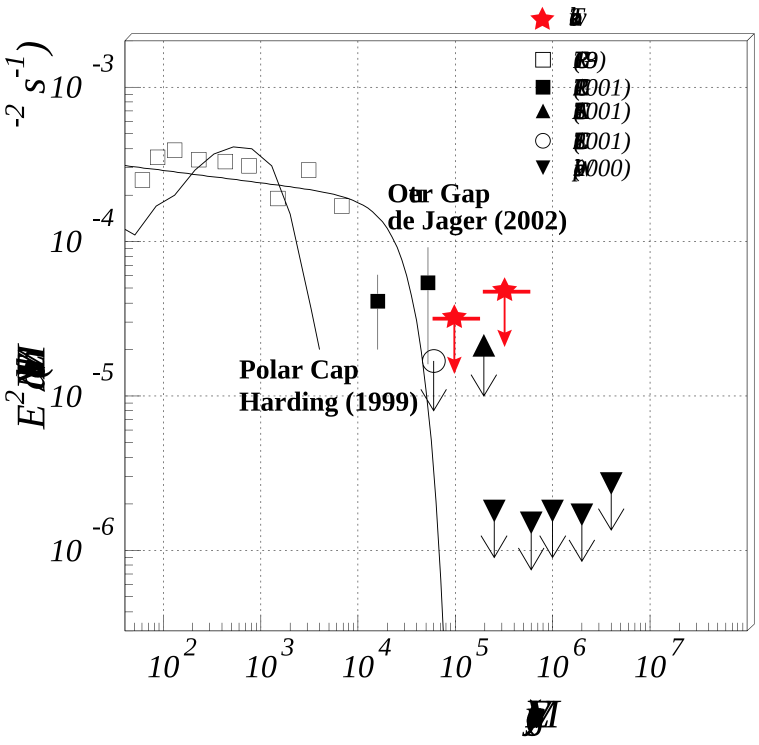

Figure 7.10: Spectra of the Crab reported by several instruments. Theoretical curves and the upper limit by CheSS are superimposed.

Chapter8

Simulation of a large FOV camera

> Alice was rather doubtful whether she ought not to lie down on her face like the three gardeners, but she could not remember ever having heard of such a rule at processions; "and besides, what would be the use of a procession," thought she, "if people had all to lie down on their faces, so that they couldn't see it?" So she stood where she was, and waited. — *The Queen's Croquet-Ground* —

Currently, a few detectors for use at high altitudes are being proposed, such as the "Hanle array" at 4500 m a.s.l(India). It is an array of 7 non-imaging telescopes based on the wavefront sampling technique(Cowsik et al. 2002). There is also the "5@5", located at 5000 m a.s.l(Chile), which is an array of 5 imaging air Čerenkov telescopes with 10 m diameter mirrors and based on the stereoscopic observations(Aharonian et al. 2001). In the near future, we will have to go to a high mountain location to detect a few GeV gamma-rays, because a 20 or 30 m diameter is the economical limit for enlarging a mirror. At those diameters, it is not sufficient to detect faint Čerenkov light caused by a few GeV particles. In this chapter, we disscuss the next generation IACT at high altitudes that must be constructed near future.

§ 1 Field of View

The Imaging Method fits an ellipse to Čerenkov images detected by a multi-pixel camera consisting of several hundred PMTs, and extracts the characteristic parameters from the images. Therefore, an IACT needs a large FOV of >3.0 degrees in order to detect a complete shower image induced by gamma-rays. For example, CANGAROO-III has an $\sim$ 4.0 degree FOV(Asahara et al. 2004), H.E.S.S has an $\sim$ 5.0 degree FOV(Hofmann et al. 2003), and MAGIC has an $\sim$ 4.0 degree FOV(Martinez et al. 2003). However, as mentioned in Ch.4, a Čerenkov-light image for tens of GeV energy is smaller than that for several 100 GeV, and thus we don't need such a large FOV for sub 100 GeV. Accoring to Fig. 4.3 and Fig. 4.5, a FOV of 3.0 degrees seems to be large enough to detect gamma-rays with energy below 500 GeV. In this section, we discuss the performance of an IACT with a 3.0-degree FOV camera at high altitudes based on the study of CheSS.

As shown in Fig. 8.1, the detection probability at a core distance of 100 m is still high for a large FOV. In this section, we describe shower simulations performed within a core distance between 0 and 200 m from a telescope. The showers induced by background particles were simulated within a solid angle of 5 degrees with the respect to the axis of the telescope. Since we simulated a "pure" IACT, we assumed the mirror reflectivity to be the same as that of CANGAROO III ($\sim$ 85% at a wavelength of $>$ 400nm). In addition, the zenith angle was fixed at 0 degrees to estimate the best performance of the IACT. Other simulation parameters, such as mirror dimensions, focal length, and a specification of each PMT, were the same as those of CheSS. They are listed in Table 8.1.

For a FOV of 3.0 degree, the number of N.S.B. photons is over 20-times larger than that of CheSS. We calculated that the N.S.B. within a gate time of 20 nsec is about 300 ph.-e. from the mirror reflectivity, the PMT quantum efficiency, and the N.S.B. data taken by the optical telescope at Mt. Mauna Kea. The simulations presented below include the mean 300 ph.-e./event N.S.B. with a Poisson distribution. Using a simple hardware trigger logic that is the same as that of CheSS is insufficient for noise reduction. Therefore, we adopted a more sophisticated trigger logic that is the same as 5@5(Aharonian et al. 2001). We assumed the following trigger logic: for signals above some critical threshold, "q_0" ph.-e. in "m" adjacent pixels, we say "$m/616 \geq q_0$". Here, "616" is the total number of PMTs.

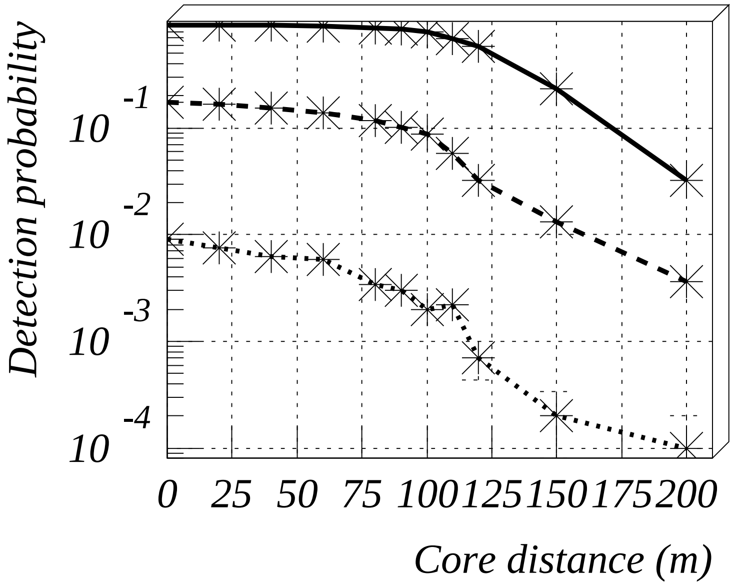

Figure 8.1: Detection probability as a function of the core distance, assuming the standard N.S.B. and 2/616 $\geq$ 6ph.-e. trigger condition. The solid, dashed, and dotted lines show 100 GeV, 30 GeV, and 10 GeV gamma-rays, respectively.

Table 8.1: Simulation parameters the 3.0-degree large FOV camera.

Mirror dimensions	$8.2m\phi$, $52.8m^2$ area, monolithic
Focal length	15m
Mirror Reflectivity	Ref. CANGAROO data (Asahara et al. 2004)
Correction lenses	none
Field of view	3.0 degrees
Camera pixels	615
Quantum efficiency	Ref. HAMAMATSU R2497 spec sheet (Hamamatsu Photonics K.K. 2004)
Site	Hawaii(4200m) or Chili(5000m)
Atmospheric model	U.S. standard atmosphere(Linsley 1988)

§ 2 Effective areas and energy spectra

Figure 8.2 shows the effective areas for gamma-rays as a function of the energy between 5 and 500 GeV, where we examine several trigger conditions of $2/616 \geq 4$ ph.-e., ≥ 5 ph.-e., and ≥ 6 ph.-e. For the trigger condition of $2/616 \geq 5$ ph.-e., the effective area is about 10^4 m^2 at 25 GeV, which corresponds to that at 100 GeV for CheSS. The detection area is strongly dependent on the energy below 30 GeV, as follows: $\mathrm{A}_{eff}(\mathrm{E}) \propto \mathrm{E}^{3.5}$; above 100 GeV, it settles down to $\mathrm{A}_{eff}(\mathrm{E}) \propto \mathrm{E}^{0.45}$, in the case of $2/616 \geq 5$ ph.-e.

Figure 8.3 shows the simulated differential detection rates for gamma-rays, protons, electrons, and muons. We used the same input fluxes as those described in Ch.4-§ 5. The spectra of gamma-rays and electrons over 100 GeV are well fitted by power laws. The energy threshold is about 15 GeV under the $\mathrm{q}_0 = 5$ or $\mathrm{q}_0 = 6$ trigger condition. Figure 8.4 shows the signal-to-noise ratio (S/N) for several of the hardware trigger conditions, where S/N is defined as the integral detection rate of gamma-rays over the square root of that of background particles,

$$\mathrm{S/N} = Rate_\gamma / \sqrt{Rate_p + Rate_e + Rate_\mu}\ . \tag{8.1}$$

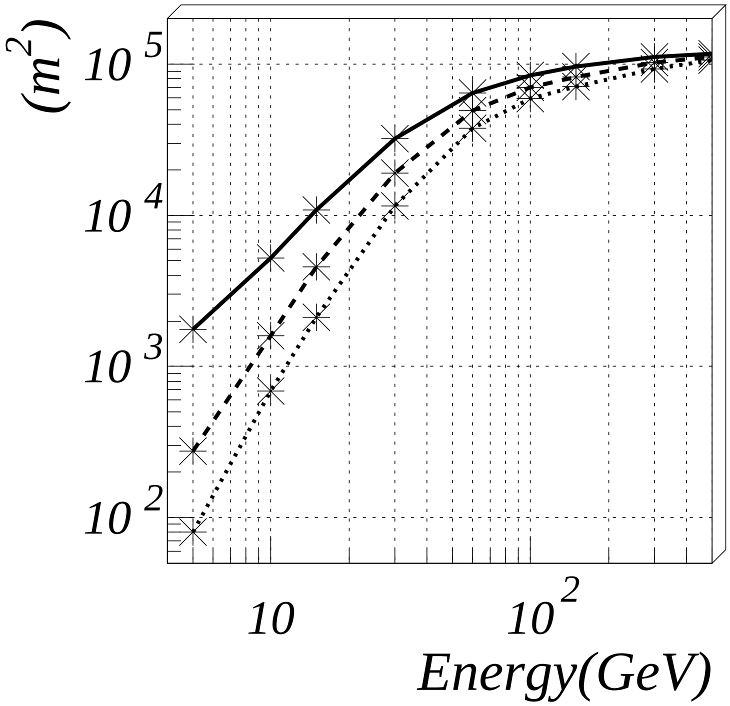

Figure 8.2: Effective area of an IACT with a 3.0-degrees FOV as a function of the gamma-ray energy, assuming trigger thresholds of q_0 = 4 (solid line), 5 (dashed line), 6 (dotted line) ph.-e.

For a threshold of 4 ph.-e. or lower, S/N is obviously low, since the background rates caused by the N.S.B. are quite high. We concluded that the trigger condition of 2/616 $\geq$ 5ph.-e. is the best in terms of S/N. For this trigger condition, the total event rate generated by these 4 particles is about 160 Hz.

§ 3 Proton background

Figure 8.5 shows the mean number of photo-electrons detected by the camera for gamma-rays and protons, where we request a hardware trigger of 2/616 $\geq$ 5 ph.-e. Just the same as in the case of CheSS, the mean number of photo-electrons induced

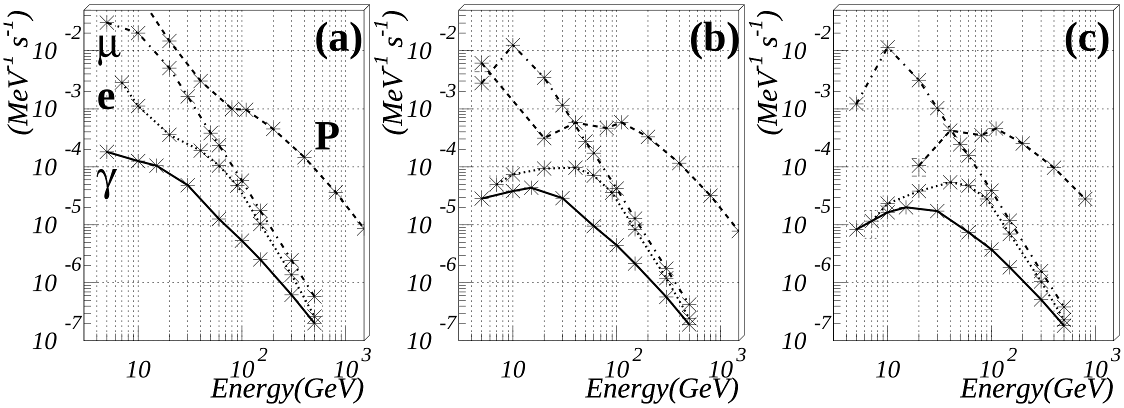

Figure 8.3: Expected detection rates. The solid, dashed, dotted, and dash-dotted lines represent gamma-rays, protons, electrons, and muons, respectively. We assumed three trigger conditions: 2/616 $\geq$ 4ph.-e. (a), 2/616 $\geq$ 5ph.-e. (b), and 2/616 $\geq$ 6ph.-e. (c).

by gamma-ray primaries is about 2.5-times larger than that by protons above 200 GeV. In contrast, below 30 GeV, both primaries generate the same number of photoelectrons.

For the 3.0-degree FOV camera, we can use the “Imaging Method” with 616 PMTs, and reject efficiently proton shower events. The rejection power is discussed in detail in section § 6.

§ 4 Electron background

For the 3.0-degree FOV camera, the integral detection rate of electrons becomes larger than that for CheSS. As shown in Fig. 8.3, the differential detection rate of electrons is about 5 times lager than that of gamma-rays at an energy of 40 GeV.

As mentioned in Ch.4-§ 7, it is difficult to distinguish electron and gamma-ray events using the shapes of their Čerenkov photon images. Hence, it seems to be meaningful to study the background reduction power of the GF. Cortina et al.

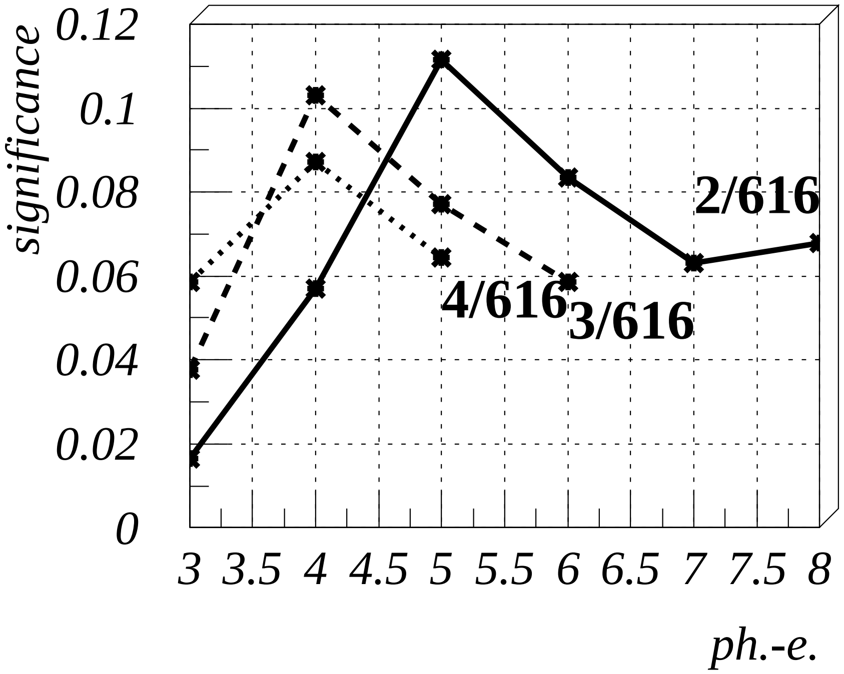

Figure 8.4: Signal-to-noise ratio (S/N) for a hardware trigger of "m/616 ≥ q0", where S/N is defined as the integral flux of gamma-rays over the square root of that of the background particles (protons, electrons, and muons); $Rate_\gamma/\sqrt{Rate_p + Rate_e + Rate_\mu}$.

We examined the case of m=2,3,4, and show the S/N as the function of q_0. The solid, dashed, and dotted lines represent the S/N for trigger conditions of 2/616 ≥ q0 ph.-e., 3/616 ≥ q0 ph.-e., and 4/616 ≥ q0 ph.-e., respectively. In the case of a trigger condition of 2/616 ≥ 5 ph.-e., we can reduce the trigger rate caused by background particles most effectively (S/N = 0.11).

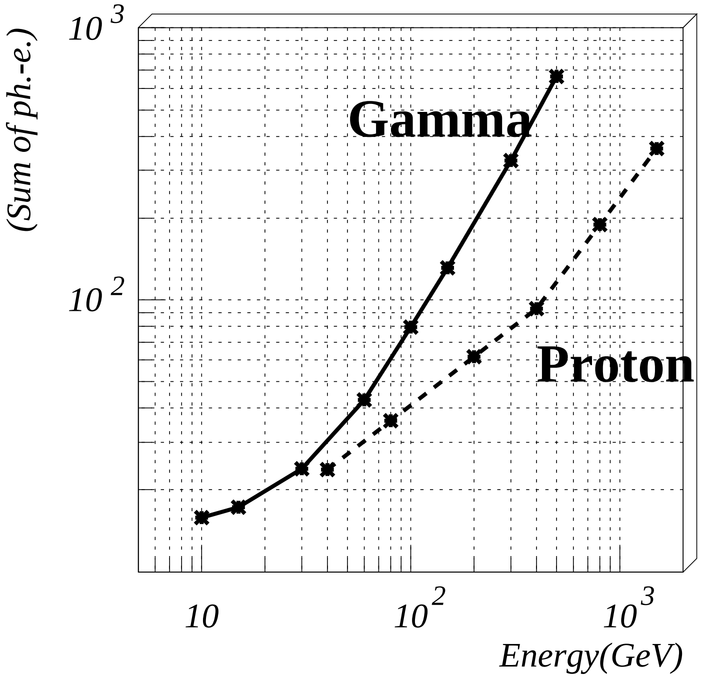

Figure 8.5: Total number of photo-electrons on the camera as a function of the energy, assuming $2/616 \geq 5$ph.-e.

have already discussed the effect of the GF at different locations on the Earth for the MAGIC telescope (15 m diameter mirror, 3.0 degrees FOV, and 2300 m a.s.l.)(Cortina and González 2001). Here, we consider the effect of the geomagnetic field at two specific locations, the Atacama Large Millimeter Array (ALMA) site (23°0' S, 67°30'W, 5000 m a.s.l.) and the Subaru telescope site (19°49' N, 155°28'W, 4200 m a.s.l.). These two sites are well known as ideal sites for the next-generation IACT to detect sub 100-GeV gamma-rays. The cut-off rigidity is about 11 GeV/c for the Subaru site and 13 GeV/c for the ALMA site in the vertical direction.

Figure 8.6 shows the detection rates of electrons at the Subaru and the ALMA sites, assuming trigger condition of $2/616 \geq 5$ph.-e. The expected integral detection rates are 9.4 Hz for the ALMA site and 2.2 Hz for the Subaru site. The higher trigger rate at the ALMA site is caused by the higher altitude and the weaker local GF. To estimate the net effect of the local GF, we also simulated the electron showers at an imaginary location having the same local GF as that at the ALMA site, and a same altitude as that at the Subaru site. The integral trigger rate becomes 8.5 Hz; that is, a difference in the latitude of only 3 degrees reduces the electron counting rate by 75%. Thus, the Subaru site is a better location than that of the ALMA from the viewpoint of electron rejection.

On the other hand, the ALMA site has the benefit of higher altitude, where the density of Čerenkov light is 20% larger than that at the Subaru site (Fig. 8.7). The 5@5 project proposes to built IACTs at this site. Below 10 GeV, the electron background interference becomes a serious problem, and then they plan to reject electron showers by stereoscopic observations composed of five telescopes. For a point-like source, the electron background can be significantly reduced if they select showers arriving from the direction of the gamma-ray source. Our simulation result shows that the integral counting rate of gamma-rays is 20% larger than that at the Subaru site, and that the energy threshold becomes about 10 GeV (Fig. 8.8). However, as mentioned above, the rate of electron background is four-times larger than that at the Subaru site. The increase in the electron counting rates seems to be more important than the slight improvement in the energy threshold, especially

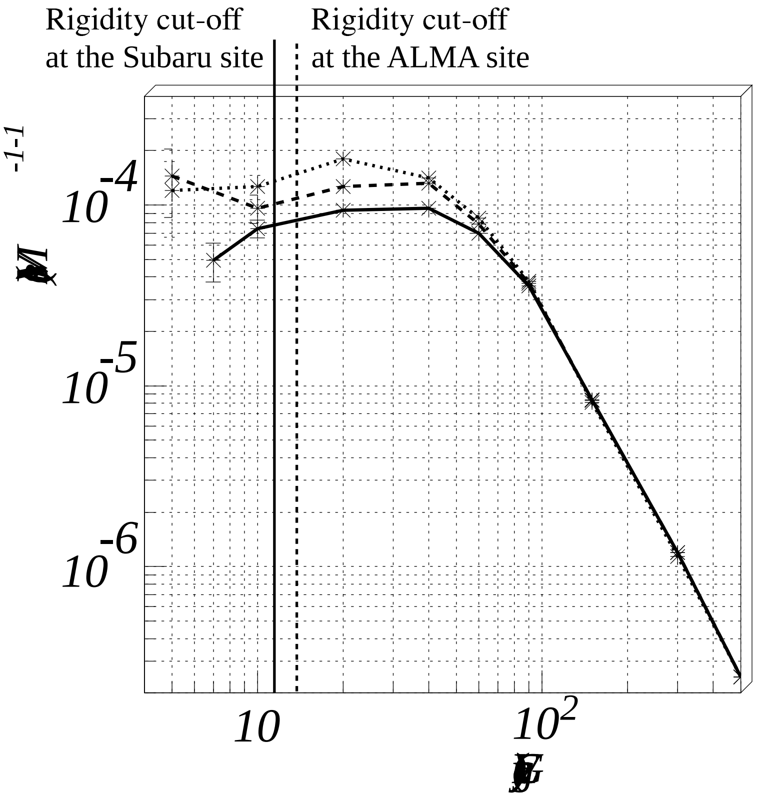

Figure 8.6: Differential detection rate of electrons at the Subaru site (solid line), at the ALMA site (dashed line), and at an imaginary location that has the same GF as that at the ALMA site and the same altitude as that at the Subaru site (dotted line), assuming a trigger condition of 2/616 ≥ 5ph.-e. The GF is (B_x,B_z)=(27.7 μT, 20.8 μT) for the Subaru site and (B_x,B_z)=(22.35 μT, -7.68 μT) for the ALMA site.

for a single telescope. Consequently, the Subaru site appears to be a better place to explore the 10-GeV energy region using the IACTech.

§ 5 Muon background

Just as in the case of CheSS, the effective area of muons is almost constant above 10 GeV, and exceeds those of protons and electrons below 50 GeV. Thus, it becomes the dominant background below 50 GeV. The number of photo-electrons induced by each muon shower is 38 ± 12 ph.-e. for a trigger condition of 2/616 ≥ 5ph.-e., independently of the energy of muons.

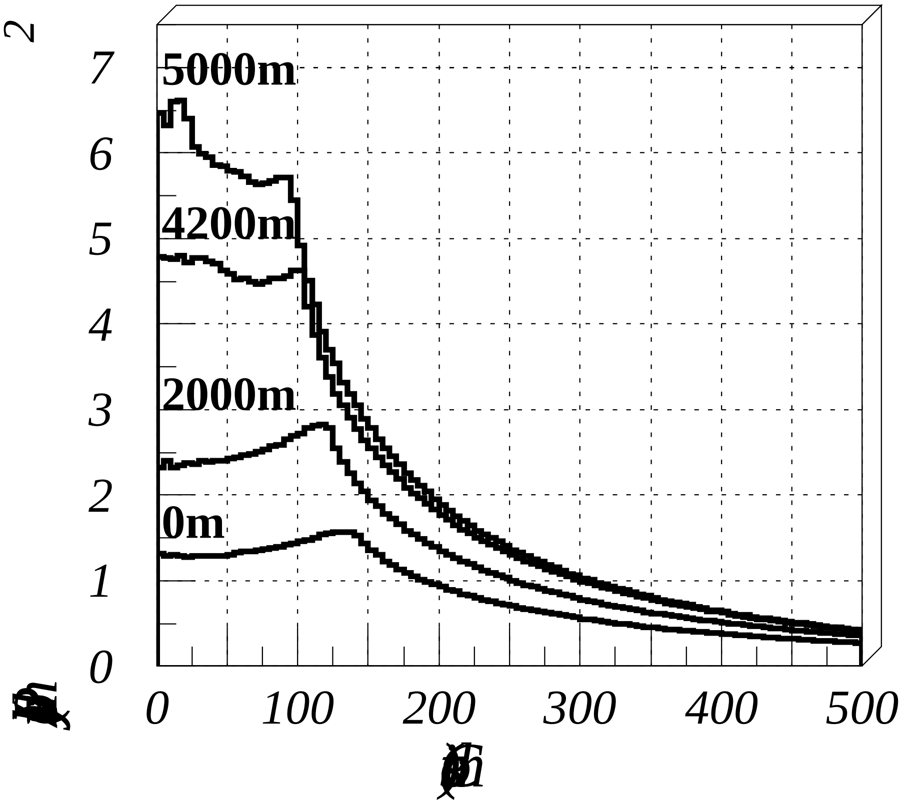

Figure 8.7: Density distributions of Čerenkov-light photon caused by 10 GeV gamma-ray at various altitudes, which are averaged over 1000 showers.

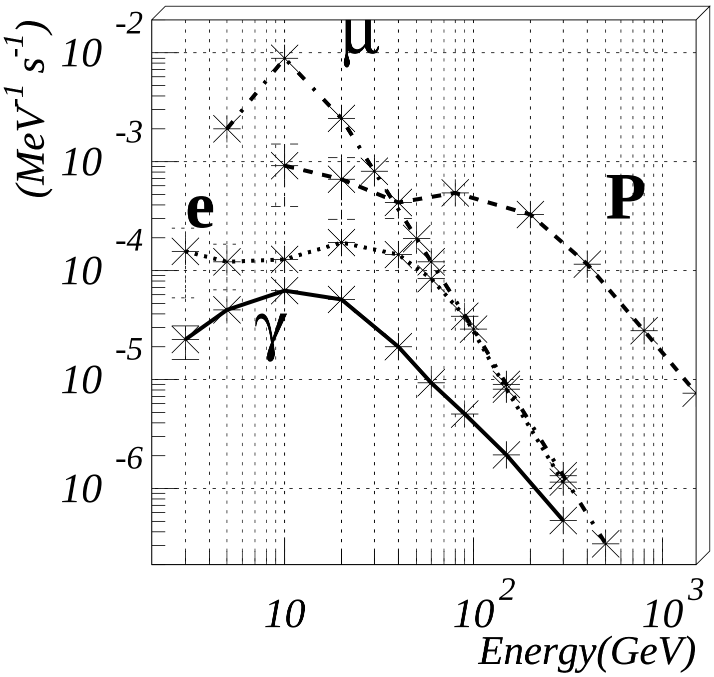

Figure 8.8: Expected detection rates at the ALMA site. The solid, dashed, dotted, and dash-dotted lines represent gamma-rays, protons, electrons, and muons, respectively.

Muon events that have a large number of ph.-e. make a complete ring, or a large arc-shape image. Such an event can be removed easily, which is, however, not a main part of the muon events. The definition of the arc shape requests at least 5 adjacent hit PMTs, and the average number of ph.-e. requested in an event with over 5 adjacent hit PMTs is roughly above 80 ph.-e. It is therefore obvious that most muon events make small arcs, like a gamma-ray image.Unlike the CheSS case, the LENGTH/SIZE cut removes muon events efficiently. Figure 8.9 shows the LENGTH/SIZE parameters of simulated muon and gamma-ray events. We also calculated the "WIDTH/SIZE" parameter. The simulated energy bands for gamma-rays and muons are 15 - 50 GeV (the slope of energy spectrum are -2.0 and -2.7, respectively; however, as we mentioned above, the number of ph.-e. does not depend on the energy of muons). The WIDTH/SIZE is also useful, but less effective than the LENGTH/SIZE.

A cut of LENGTH/SIZE < 0.002 can remove 80% of muon events, while more than 90% of the gamma-ray events survive in the energy range between 15 and 50 GeV. However, we should pay attention to the the energy dependency of LENGTH/SIZE, which is quite strong for gamma-rays, as shown in Fig. 8.10. We can find that LENGTH/SIZE cut is a powerful tool for muon rejection in a lower energy band, but for higher energy events, a cut of LENGTH/SIZE < 0.002 removes most gamma-ray events. Thus, an energy-dependent cut must be used. During observation, we have no way to know the energy of each particle, and thus the number of photo-electron (SIZE) is used in order to estimate it. Figure 8.11 shows scatter plots of SIZE versus LENGTH/SIZE for gamma-rays and muons. Using this plot, we calculated the best cut criteria for muon rejection,

$$\mathrm{LENGTH/SIZE} < -1.53 \times 10^{-5} \times \mathrm{SIZE} + 2.3 \times 10^{-3} \ . \tag{8.2}$$

This cut removes 55% of muon events, but only 6% of gamma-ray events in the energy range between 15 and 300 GeV.

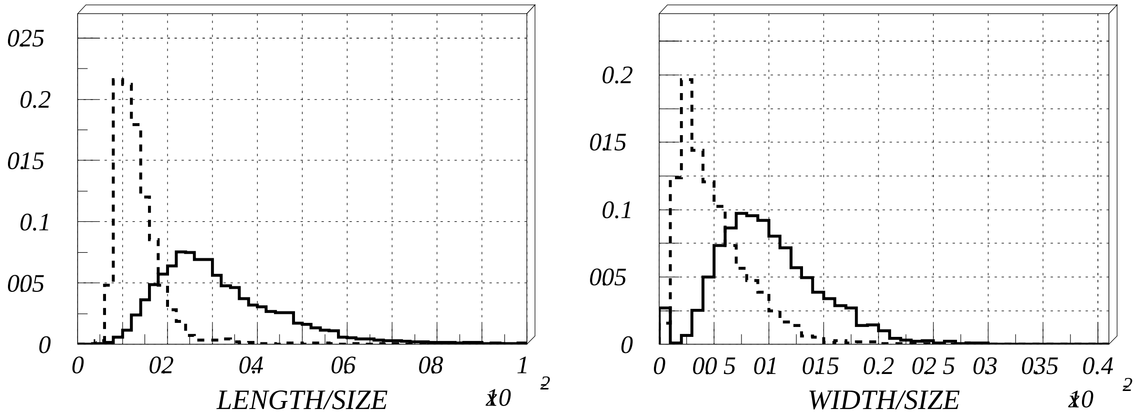

Figure 8.9: Distributions of the "LENGTH/SIZE" and "WIDTH/SIZE" parameters. The solid and dashed lines show gamma-ray and muon shower events. We assumed energy bands between 15 GeV and 50 GeV for each particle; the slopes of the energy spectra are -2.0 for gamma-rays and -2.7 for muons, respectively.

§ 6 Rejection power by the Imaging Method

In order to obtain the sensitivity of a large FOV camera, we must estimate the rejection power for proton events by the Imaging Method. At first, we defined the so-called Q-factor as Q $= \kappa_\gamma/\sqrt{\kappa_p}$, to evaluate the improvement of the signal-to-noise ratio after applying the Imaging Method, where κ_p and κ_γ are the efficiencies for isotropic proton showers and for point-source gamma-ray showers, respectively.

Figure 8.12 shows the ALPHA distributions of gamma-ray induced and proton-induced showers. We simulated gamma-ray showers weighted by a power-law with an index of -2.0 in the energy range of 10 - 50 GeV, based on the theoretical flux of the pulsed component of Crab(de Jager 2002). Proton showers were weighted by a power-law with an index of -2.7 in the energy range of 40 - 100 GeV. Note that we selected the each energy range in which gamma-rays and protons generate the same number of Čerenkov photons (Fig. 8.5). In this energy band, the ALPHA cut that gives the maximum Q-factor is 22 degrees (Q=1.4).

The Q-factor decreases as the energy of gamma-rays decreases, because the image size of the Čerenkov photons induced by gamma-rays becomes smaller as its energy

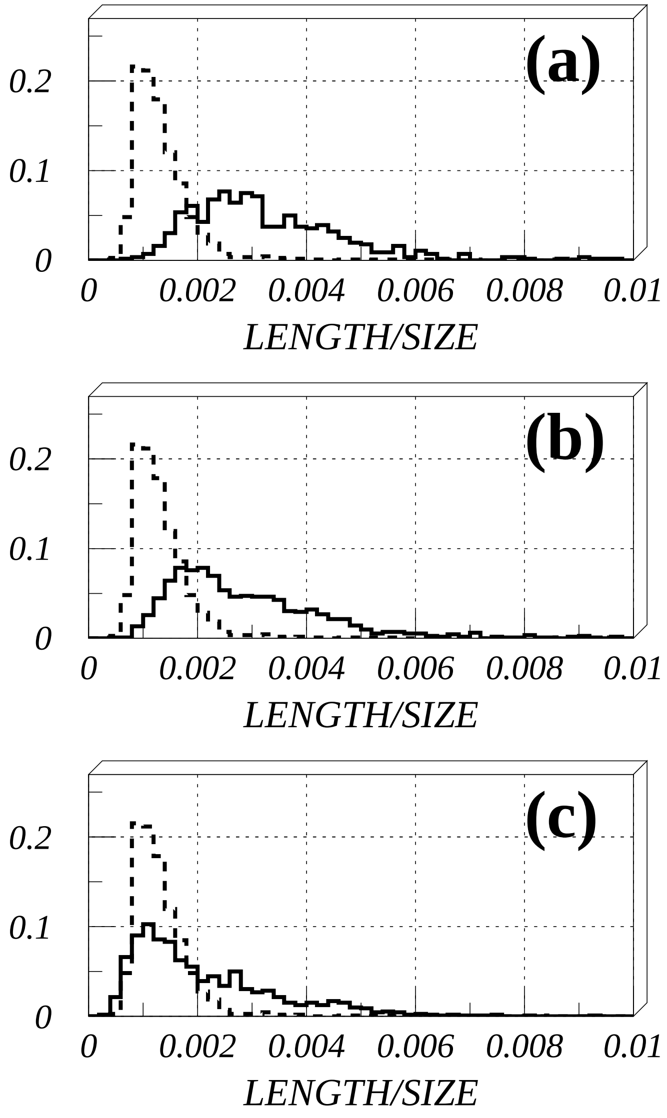

Figure 8.10: Distributions of the "LENGTH/SIZE" parameter of gamma-ray events. (a), (b), and (c) show energies of 30, 60, and 150 GeV, respectively. The distributions for muon events are superimposed (dashed-lines; the same lines shown in Fig. 8.9).

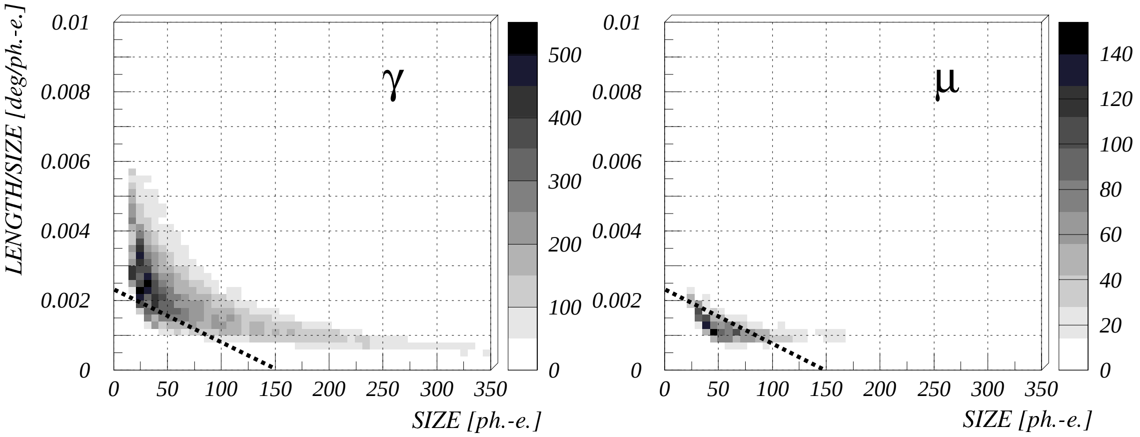

Figure 8.11: Scatter plot of SIZE versus LENGTH/SIZE for gamma-rays and muons. The simulated energy region is 15 - 300 GeV for each figure. The dotted lines represent LENGTH / SIZE = $-1.53 \times 10^{-5} \times$ SIZE $+2.3 \times 10^{-3}$.

decreases. Figure 8.13 shows the variation of the maximum Q-factors in that energy band, and the ALPHA values that give the maximum Q-factors. The ALPHA value giving the maximum Q-factor increases as the energy decreases, and becomes about 30 degrees at 20 GeV. This result suggests that the sensitivity for an extended source, such as supernova remnants, is dramatically worse at around 20 GeV. The stereoscopic observation method could improve the sensitivity for an extended source to some extent. However, the broad ALPHA peak implies that the intersection of the long axes of each Čerenkov images is obscure, and it does not seem to be easy to identify the emission point of each gamma-ray shower.

We also evaluated the efficiency of the WIDTH, LENGTH, and DISTANCE cut, proposed by Hillas(Hillas et al. 1985). These three parameters are commonly used in the Imaging Method. Figure 8.14 shows the WIDTH and LENGTH in the same energy bands as in Fig. 8.12. As shown in this figure, these two parameters can not distinguish between gamma-ray showers and proton showers. Figure 8.15 shows the DISTANCE parameter. Unlike WIDTH and LENGTH, the distributions of the DISTANCE parameter are quite different between a gamma-ray shower and a proton shower. In this low-energy band, the maximum Q-factor by the DISTANCE cut is slightly over 1.4, which exceeds that given by the ALPHA cut. This fact

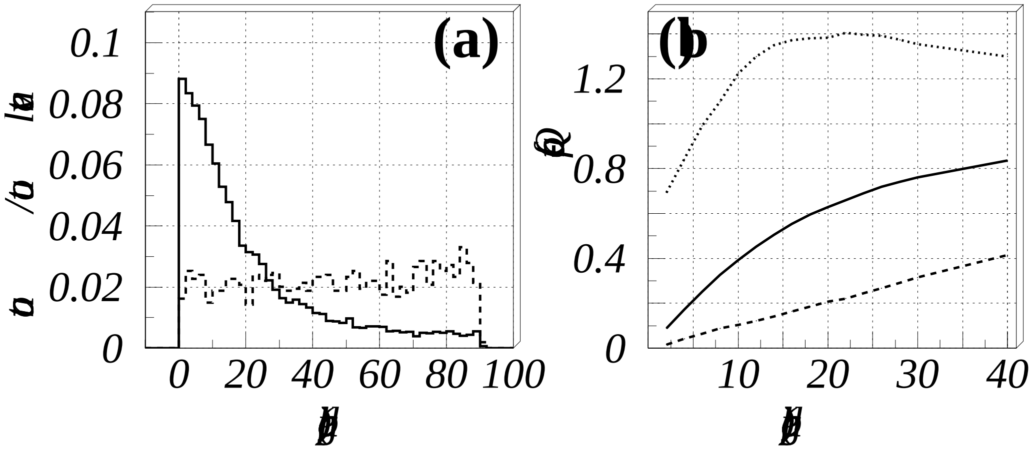

Figure 8.12: (a) Distribution of the "ALPHA" parameter. The solid and dashed line show gamma-ray and proton shower events. We assumed energy bands between 15 GeV and 50 GeV (slope of the energy spectrum is -2.0) for gamma-rays, and between 40 GeV and 100 GeV (slope of energy spectrum is -2.7) for protons. The simulated energy bands of gamma-rays and protons are different, because the energy of the particle that generates the same number of ph.-e. is different between gamma-rays and protons.

(b) Efficiency of the image cut for gamma-rays, κ_γ (solid line); that for protons, κ_p (dashed line); and the Q-factor (dotted line) as a function of ALPHA.

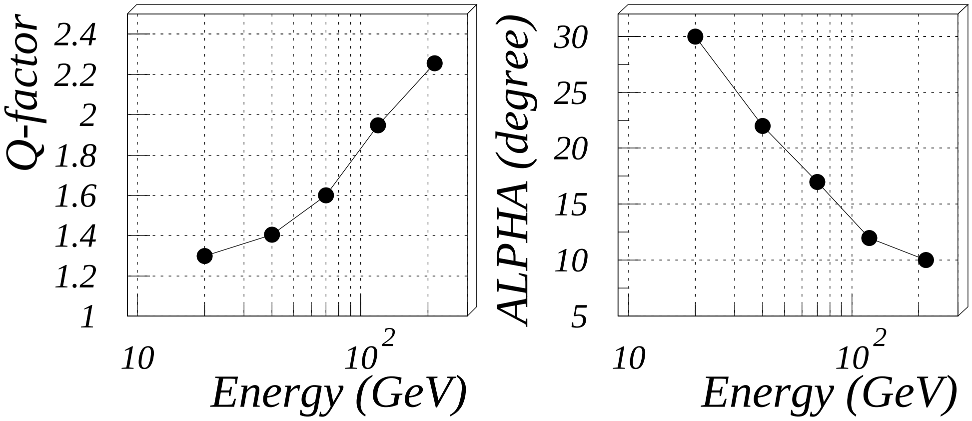

Figure 8.13: (a) Maximum Q-factor as a function of energy. The Q-factor has the lowest value (1.3) at an energy of 20 GeV.

(b) ALPHA that gives the maximum Q-factors.

indicates that below 50 GeV, the DISTANCE cut improves S/N rather than the ALPHA cut. Figure 8.16 shows the maximum Q-factor on DISTANCE, and also shows the DISTANCE values that give the maximum Q-factor. The Q-factor of the DISTANCE cut is almost constant between 20 and 200 GeV.

Using the two parameters, ALPHA and DISTANCE, the efficiency of proton rejection is more improved (Fig. 8.17). In the low-energy band between 15 and 50 GeV, κ_γ and κ_p are 0.608 and 0.0965; thus, the Q-factor becomes about 2.0. For electron and muon events, the ALPHA and DISTANCE cut is less effective than that for protons. However, for observations of a point-like source, the ALPHA and DISTANCE distributions is different between gamma-ray showers and isotropic background particles, and thus we can reject electrons and muons to some extent by using these parameters. Figure 8.17 shows two-dimensional histograms of the ALPHA and DISTANCE distributions of gamma-rays, electrons, and muons. The cut efficiencies are the following: $\kappa_\gamma = 0.608$, $\kappa_{electron} = 0.1$, $\kappa_\mu = 0.08$.

For observations of an extended gamma-ray source, the ALPHA distributions

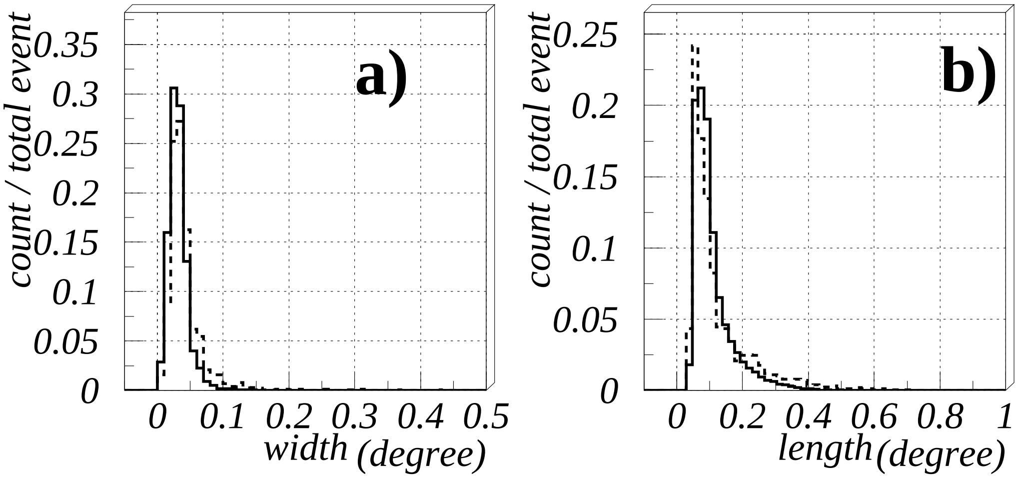

Figure 8.14: Figure (a) and (b) show the distribution of the WIDTH and LENGTH parameters. The solid and dashed lines show gamma-ray and proton shower events.

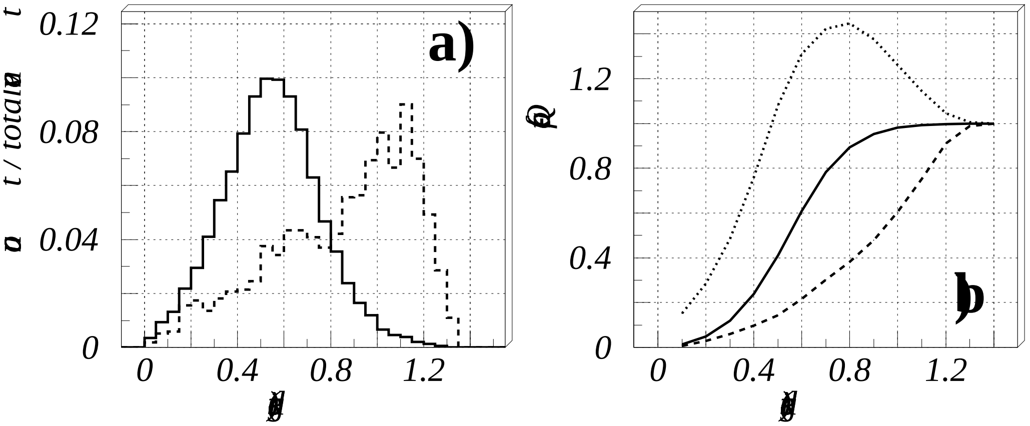

Figure 8.15: (a) Distribution of the DISTANCE parameter. The solid and dashed lines show gamma-ray and proton shower events. (b) Efficiency of the image cut for gamma-rays, κ_γ (solid line); that for protons, κ_p (dashed line); and the Q-factor (dotted line) as a function of DISTANCE.

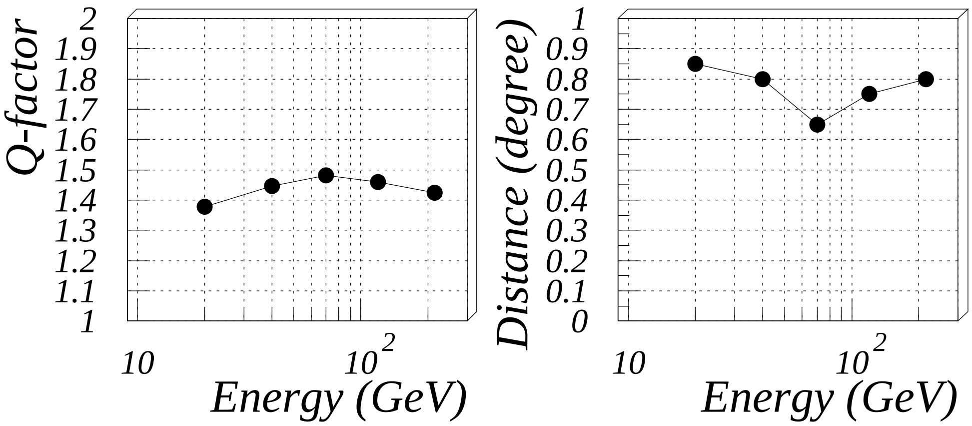

Figure 8.16: (a) Maximum Q-factor as a function of energy. (b) The DISTANCE that gives maximum Q-factors.

become broader and the DISTANCE value becomes larger. Therefore, the background rejection capability by the Imaging Method becomes much worse. We need additional simulations to estimate it.

§ 7 Sensitivity of a large FOV camera for pulsars

Figure 8.18 shows the expected integral counting rate of gamma-rays, protons, electrons, and muons, In Fig. 8.18 (a), we assume a hardware trigger of $2/616 \geq 5$ph.-e. In Fig. 8.18 (b), we assume the DISTANCE cut (> 0.8 degrees) and the ALPHA cut (> 22 degrees) for proton rejection. As mentioned in subsection § 5, the LENGTH/SIZE cut is effective for muon rejection, especially in the low-energy band below 50 GeV. In Fig. 8.18 (c), we assume the additional cut for muon rejection, LENGTH/SIZE $< -1.53 \times 10^{-5} \times$SIZE $+2.3 \times 10^{-3}$ (see subsection § 5).

Here, we defined significance as

$$\sigma = \frac{R_\gamma}{\sqrt{R_{proton} + R_{electron} + R_\gamma + R_\mu}} \sqrt{t_{obs}} \ , \tag{8.3}$$

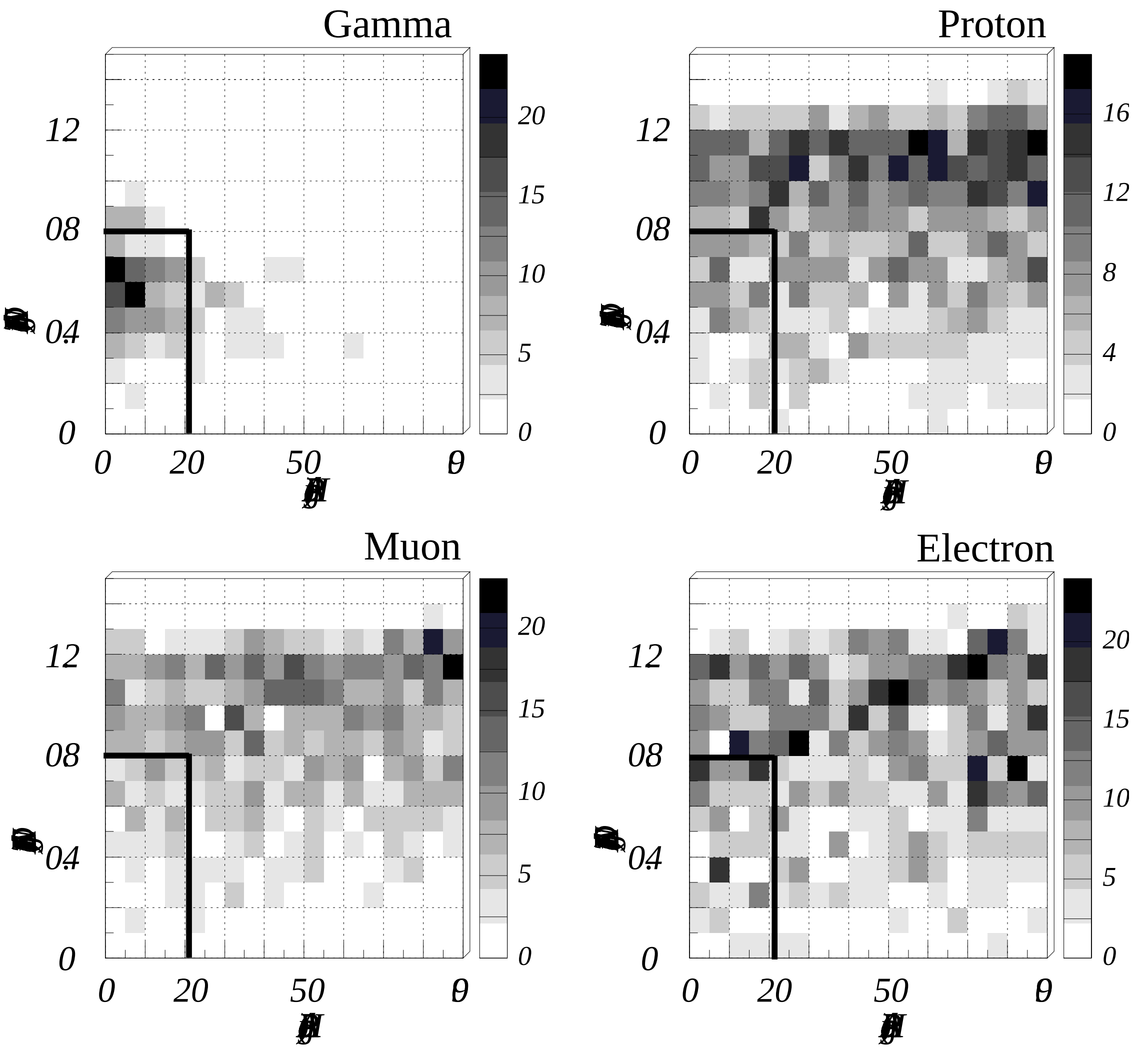

Figure 8.17: Two-dimensional histograms of the ALPHA and DISTANCE distribution of gamma-rays, protons, electrons, and muons. The solid lines in each figure represent DISTANCE=0.8° and ALPHA=22°.

where t_{obs} means the observation time; R_γ, R_{proton}, $R_{electron}$ and R_μ are the expected integral detection rates. According to Fig. 8.18 (c), the integral event rates of gamma-rays, protons, electrons, and muons above 5 GeV, are 0.52, 8.3, 0.33, and 1.8 Hz, respectively, and thus the signal-to-noise ratio becomes $\sim 0.1 \times \sqrt{t_{obs}(\mathrm{sec})}$. This results suggests that only a 1-hour observation would enable us to detect Crab with 6 σ significance. Assuming 10 hours of observation time and a 5σ significance, Figure 8.19 shows the sensitivity curve calculated from the integral counting rates of background particles. The theoretical fluxes of pulsed components of 6 gamma-ray pulsars detected by EGRET(de Jager 2002) is superimposed on it. Note that the ALPHA value giving the maximum Q-factor has an energy dependency as shown in Fig. 8.13. In this calculation, we assumed the ALPHA cut > 22 degrees to obtain the maximum Q-factor ($= 1.4$) at the low-energy band between 10 and 50 GeV.

Figure 8.19 suggests that a 10 m diameter class imaging Čerenkov telescope installed at 4000 m a.s.l. could detect 15 GeV gamma-rays, emitted from EGRET pulsars with only one exception, Geminga. To detect radio quiet pulsars, like Geminga, we must reduce the energy threshold to 10 GeV. To achieve such a low threshold, we need a higher altitude (about 5 km a.s.l.) or a larger mirror (15m aperture). Table 8.2 gives the energy threshold of an IACT with mirror diameters of 15 m and 8.2 m, at altitudes of 0 m, 4200 m, and 5000 m a.s.l. In this simulation, we changed only the observation altitudes and mirror diameters, and assumed a trigger condition that would reduces the trigger rate of background protons to under 200 Hz. This table indicates that an enlargement of the mirror could not efficiently reduce the energy threshold.

As shown in Fig. 8.7, the density of Čerenkov light at 4200 m a.s.l. is about 4-times larger for gamma-ray showers than at sea level. Moreover, the density of Čerenkov light induced by protons is only 2.5-times larger than that at sea level, and thus observations at high altitudes would lead to a significant improvement in the gamma/proton ratio(Aharonian et al. 2001). In contrast, increasing the mirror diameter would lead not only to a proportional increase in the density of Čerenkov photons, but also to an increase in the accidental rate caused by the N.S.B. The

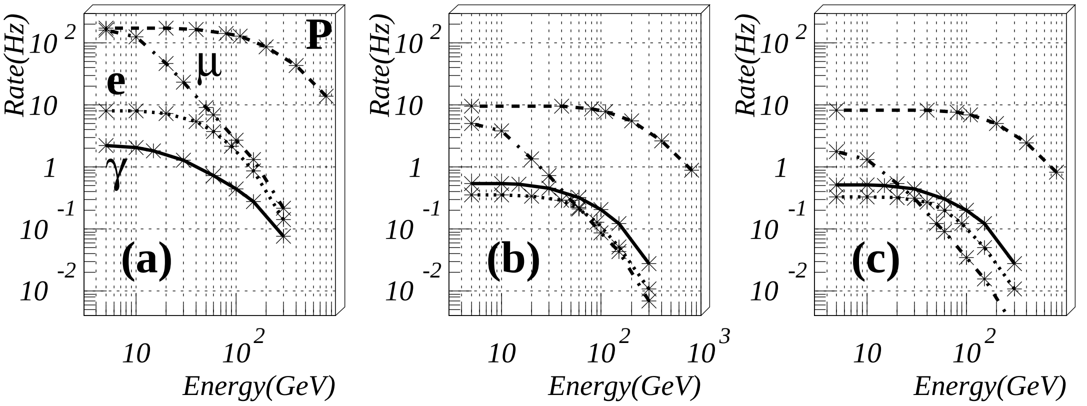

Figure 8.18: Integral flux of gamma-rays (solid-line), protons (dashed-line), electrons (dotted-line), and muons (dash-dotted line).

(a) Integral fluxes calculated from the surviving events after a hardware trigger of $2/616 \geq 5$ph.-e.

(b) Integral fluxes calculated from the surviving events after an ALPHA cut, > 22 degrees, and a DISTANCE cut, > 0.8 degrees (for proton rejection).

(c) Integral fluxes after the additional cut:

“ LENGTH / SIZE $< -1.53 \times 10^{-5} \times$SIZE $+2.3 \times 10^{-3}$ ” (for muon rejection).

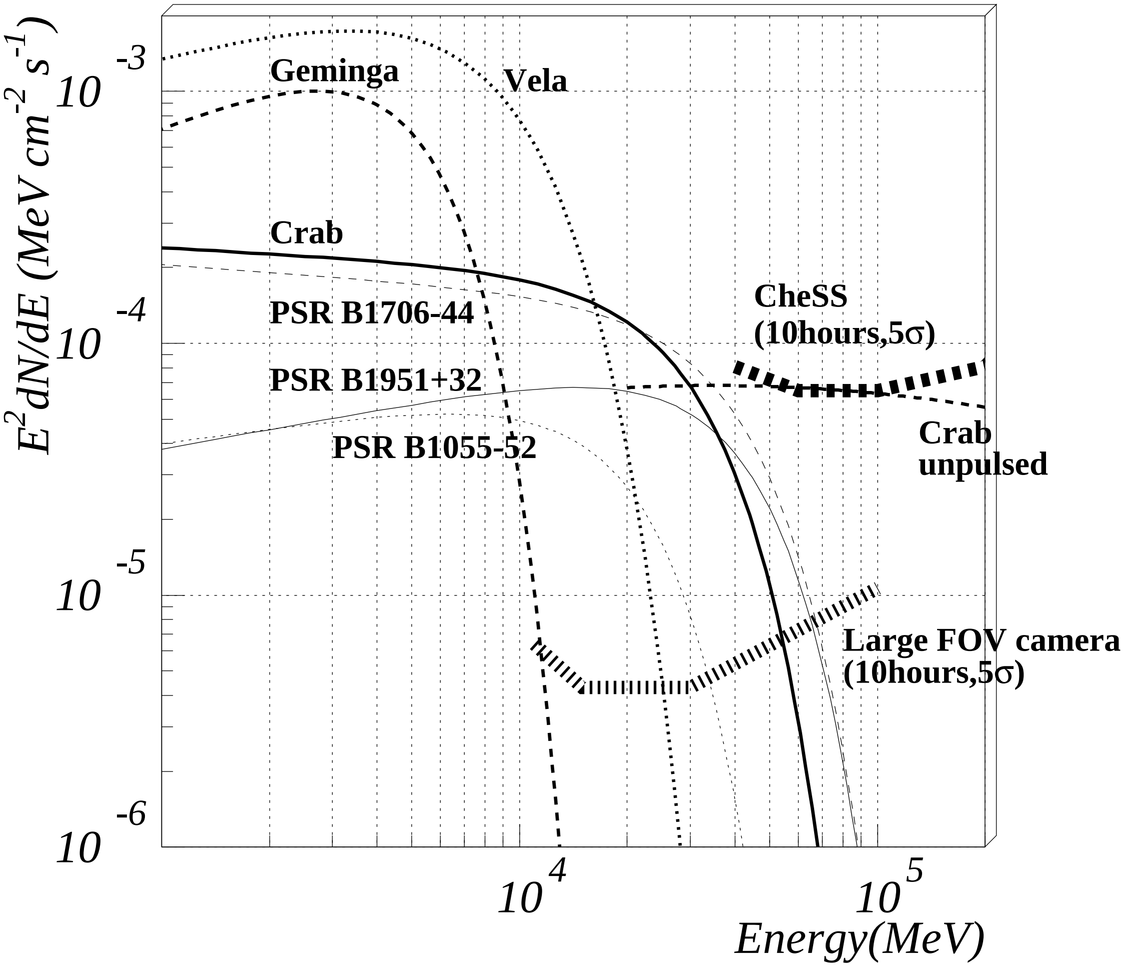

Figure 8.19: Theoretical fluxes of pulsed components of EGRET pulsars with the sensitivity line of CheSS. We did not take account of an improvement of the sensitivity due to a timing analysis.

MAGIC telescope has a 15 m diameter mirror, which is the largest among current IACTs. However, to detect several GeV gamma-rays at moderate altitudes, we need much larger mirror than that of MAGIC. The construct of such a huge mirror is not cost-effective method, because we need a lot of research and development for the mirror that we have never constructed before. Therefore, we propose that the ~ 15 m class mirror at altitudes of above 4000 m a.s.l. is the most practical solution to detect several GeV gamma-rays.

Table 8.2: Energy threshold of a single IACT with mirror diameters of 15m and 8.2 m, at three different altitudes. We assume a zenith angle of 0 degrees.

Mirror ϕ	sea level	4200 m a.s.l	5000 m a.s.l
8.2 m	150 GeV	15 GeV	10 GeV
15 m	100 GeV	10 GeV	7 GeV

§ 8 Trigger gate width

The trigger circuit installed on CheSS generates a 20 nsec trigger gate. A narrower gate may cause a lower trigger efficiency due to a deformed pulse and/or a miss adjustment of the internal delays in the circuit. Since the observation described in this paper was the first-light for CheSS, we gave preference to stable operation with a wide gate width over reducing the N.S.B with a narrow one. To estimate the net difference between 3.0 and 0.75-degree FOV, we assumed the same trigger gate width as that of CheSS for the 3.0-degree FOV camera discussed in this section. However, it is worth estimating the performance of the camera with a narrow trigger gate. In the 5@5 projects, they assume a quite narrow gate width of 5 nsec(Aharonian et al. 2001). We also simulated a camera installed with a trigger circuit having a gate time width of 5 nsec.

The number of N.S.B. within the 5 nsec gate would be 75 ph.-e., which is one forth of that within a 20 nsec gate. At such a low N.S.B. level, we can adapt a looser trigger condition without an exponential increase of the trigger rate. Table 8.3 gives the trigger conditions that produce the most effective data acquisition at each N.S.B. level. In this calculation, we used the same evaluation criteria as that mentioned in the subsection § 2 and Fig. 8.4. Table 8.3 also gives the signal-to-noise ratio for each N.S.B. level. We can find that a camera with a 5 nsec trigger gate can accumulate 2.3-times more gamma-ray events, and archive a two-times larger signal-to-noise ratio than that with a 20 nsec trigger. However, our simulation results show little improvement in the energy threshold (Fig. 8.20).

Table 8.3: Trigger conditions that give the most effective data acquisition at the 300 ph.-e. (20 nsec gate) and 75 ph.-e. (5 nsec gate) N.S.B. levels. The background rate includes proton, electron, and muon events. S/N is defined as the rate of gamma-rays over the square root of the rate of the background events.

gate time width (nsec)	suitable trigger	event rate of gamma-rays (Hz)	event rate of backgrounds (Hz)	S/N ($\times 10^{-1}$)
20	$2/616 \geq 5$ph.-e.	2.2	386	1.1
5	$2/616 \geq 3$ph.-e.	5.1	611	2.1

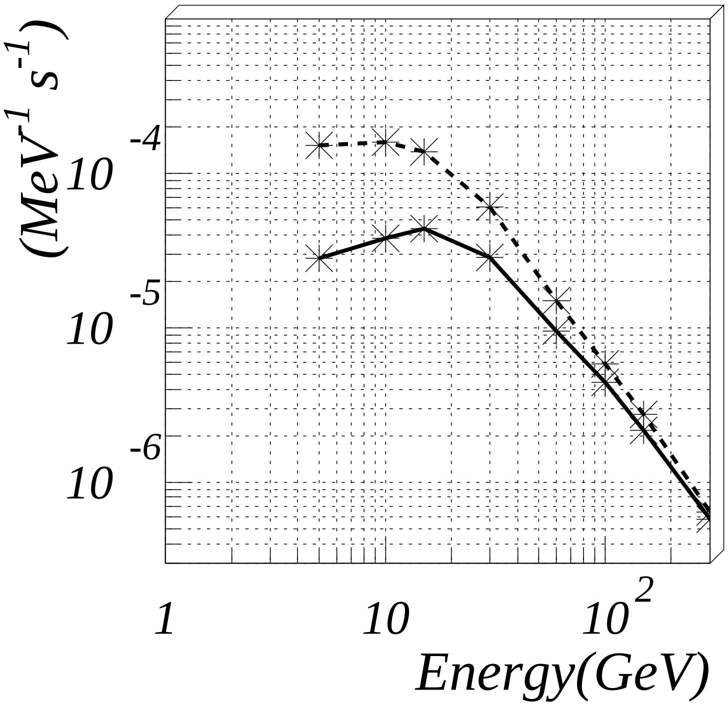

Figure 8.20: Differential detection rate of gamma-rays with a 20 nsec trigger gate (trigger condition of 2/616 $\geq$ 5 ph.-e., solid line) and a 5 nsec trigger gate (trigger condition of 2/616 $\geq$ 3 ph.-e., dashed line).

Chapter9

Conclusions

> "I thought you did," said the Mouse. "I proceed. 'Edwin and Morcar, the earls of Mercia and Northumbria, declared for him; and even Stigand, the patriotic archbishop of Canterbury, found it advisable —' "
>
> "Found *what*?" said the Duck.
>
> "Found *it*," the Mouse replied rather crossly: "of course you know what 'it' means."
>
> "I know what 'it' means well enough, when *I* find a thing," said the Duck: "it's generally a frog, or a worm. The question is, what did the archbishop find?"
>
> — *A Caucus-Race and a Long Tale* —

We have discussed the performance of high-altitude IACTs with two types of cameras. One type consists of 44 PMTs, and covers a field of view of 0.75 degrees, which is the same configuration as the CheSS installed at the Subaru telescope. The effect of electron showers is suppressed because its FOV is much smaller than that of a standard Čerenkovtelescope, and the geomagnetic cut-off is strong at low latitude, 19°49'42.6"N(Hawaii). From a comparison between the simulated and observed shower events, we found that the N.S.B and muon showers have significant effects on both the energy threshold and the energy spectrum. Our simulation results show that the energy threshold of CheSS is about 60 GeV; the expected integral detection rates above 60 GeV are about 0.036 Hz for gamma-rays from the Crab nebula/pulsar, 2.9 Hz for protons, 0.039 Hz for electrons, and 2.5 Hz for muons. The simulated integral rate is consistent with the observed event rate. Moreover, we can explain the profile of the observed ADC spectrum, especially the "bump" in the low-energy bands, using muon shower events. We could not found the significant excess induced by pulsed and/or unpulsed gamma-rays from the Crab. Almost all N.S.B. backgroun are removed. To extract gamma-ray events from Crab, we need to focus on proton and muon backgrounds, and try additional reduction methods for them. Our upper limit for gamma-rays from the Crab pulsar is 3.5×10^{-5} MeVcm^{-2}s^{-1} above 100 GeV, with 10 hours ON/OFF observation and 2 σ significance.

The other type involves 616 PMTs with a 3.0-degree FOV based on the standard camera used in the 10 m IACT. For a large FOV, the electron background increases below 100 GeV. The expected integral counting rate of electrons is about 9 Hz at the ALMA site, which is 4-times larger than at the Subaru site. We estimated the rejection power for background particles by the Imaging Method, especially for protons and muons which are dominant backgrounds. Regarding the proton background, we found that the DISTANCE parameter is quite important in the low-energy band. Below 50 GeV, the maximum Q-factor given by the DISTANCE cut is about 1.4 for proton showers, which exceeds that given by the ALPHA cut. For muon rejection, LENGTH/SIZE cut is effective. The cut of LENGTH / SIZE $< -1.53 \times 10^{-5} \times$ SIZE $+2.3 \times 10^{-3}$ removes 55% of the muon events, but only 6% of the gamma-ray events in the energy range between 15 and 300 GeV. The Q-factor, defined as $\kappa_\gamma / \sqrt{\kappa_\mu}$, is ~ 1.4. Our results show that this camera installed at an 8 m aperture telescope can achieve an energy threshold of 15 GeV, which does not depend on the gate time width.

AppendixA

Definition of Image Parameters

The definition of the image parameters used in this thesis is almost the same as that of the Hillas parameters originally used in the Whipple group. However, the following definition based on the Asymmetry Vector is convenient to make event maps as described in Section § 3. Suppose the i-th PMT is given by coordinates (x_i, y_i) in degrees and registers a signal s_i. The following is defined first:

$$\langle x\rangle = \frac{\sum_i s_i x_i}{\sum_i s_i}, \quad \langle y\rangle = \frac{\sum_i s_i y_i}{\sum_i s_i}, \tag{A.1}$$

$$\langle xy\rangle = \frac{\sum_i s_i x_i y_i}{\sum_i s_i}, \quad \langle x^2 y\rangle = \frac{\sum_i s_i x_i^2 y_i}{\sum_i s_i}, \quad \langle xy^2\rangle = \frac{\sum_i s_i x_i y_i^2}{\sum_i s_i}, \tag{A.2}$$

$$\langle x^2\rangle = \frac{\sum_i s_i x_i^2}{\sum_i s_i}, \quad \langle y^2\rangle = \frac{\sum_i s_i y_i^2}{\sum_i s_i}, \quad \langle x^3\rangle = \frac{\sum_i s_i x_i^3}{\sum_i s_i}, \quad \langle y^3\rangle = \frac{\sum_i s_i y_i^3}{\sum_i s_i}. \tag{A.3}$$

The coordinates $(\langle x\rangle, \langle y\rangle)$ correspond to the centroid of the image. The following parameters are further defined:

$$\sigma_{x^2} = \langle x^2\rangle - \langle x\rangle^2, \quad \sigma_{xy} = \langle xy\rangle - \langle x\rangle\langle y\rangle, \quad \sigma_{y^2} = \langle y^2\rangle - \langle y\rangle^2, \tag{A.4}$$

$$\begin{aligned}
\sigma_{x^3} &= \langle x^3\rangle - 3\langle x^2\rangle\langle x\rangle + 2\langle x\rangle^3, \\
\sigma_{y^3} &= \langle y^3\rangle - 3\langle y^2\rangle\langle y\rangle + 2\langle y\rangle^3, \qquad \text{(A.5)} \\
\sigma_{x^2 y} &= \langle x^2 y\rangle - 2\langle xy\rangle\langle x\rangle - \langle x^2\rangle\langle y\rangle + 2\langle x\rangle^2\langle y\rangle, \\
\sigma_{xy^2} &= \langle xy^2\rangle - 2\langle xy\rangle\langle y\rangle - \langle y^2\rangle\langle x\rangle + 2\langle y\rangle^2\langle x\rangle. \qquad \text{(A.6)}
\end{aligned}$$

If we define $d = \sigma_{y^2} - \sigma_{x^2}$ and $z = [d^2 + 4\sigma_{xy}]^{1/2}$, then

$$\text{Width} = \left(\frac{\sigma_{x^2} + \sigma_{y^2} - z}{2}\right)^{1/2}, \qquad \text{Length} = \left(\frac{\sigma_{x^2} + \sigma_{y^2} + z}{2}\right)^{1/2}. \tag{A.7}$$

If an assumed source position in the field of view is (x_s, y_s) and the Distance vector $\vec{D} = (x_D, y_D)$ is

$$\vec{D} = (x_s - \langle x\rangle, y_s - \langle y\rangle), \tag{A.8}$$

then

$$\text{Distance} \quad = \quad \sqrt{\langle D\rangle^2 + \langle D\rangle^2}. \tag{A.9}$$

$$\tag{A.10}$$

If the unit vector of the major axis, $\vec{u} = (x_u, y_u)$ is

$$\vec{u} = \left(\left(\frac{z-d}{2z}\right)^{1/2}, \quad \text{sign}(\sigma_{xy})\left(\frac{z+d}{2z}\right)^{1/2}\right), \tag{A.11}$$

then

$$\text{Alpha} = \cos^{-1}\left(\frac{x_u x_D + y_u y_D}{\text{Distance}}\right). \tag{A.12}$$

And Asymmetry vector $\vec{A} = (x_A, y_A)$ is

$$\vec{A} = -\sigma_A \vec{u}. \tag{A.13}$$

If the largest three PMT signals in the image is S_1 ,S_2 and S_3, Concentration is

$$\text{Conc} \quad = \quad \frac{s_{\text{max}} + s_{\text{2nd}} + s_{\text{3rd}}}{\sum_i s_i}. \tag{A.14}$$

AppendixB

Time Correction

In order to detect the sensitive pulsed emission from the fastest pulsing sources (a few milliseconds), we must have a timing accuracy within a fraction of the pulse period. Observed time is slightly inaccurate due to the observed position on the Earth. For example, CheSS records photon arrival times to an absolute accuracy of $\sim 1\,\mu$s, however, the radius of the Earth's orbit is 8 light-minutes. The variation of the Earth's position make a significant offset of the arrival time of photons from the celestial objects. Thus we need to translate all measured arrival times into Solar System Barycenter (SSB) times. The SSB time is the time when a photon would arrive at the solar system barycenter, if none of the mass of the solar system were present. The conversion between measured time (t_{UTC}) and barycenter time t_b is described as follows (Jones 1998) (Lyne and Smith 1998),

$$t_b = t_{UTC} + \Delta_{convention} + \Delta_{location} + \Delta_{Einstein} + \Delta_{Shapiro} \tag{B.1}$$

Each correction parameters: $\Delta_{convention}$, $\Delta_{location}$, $\Delta_{Einstein}$, and $\Delta_{Shapiro}$ is mentioned followings.

- $\Delta_{convention}$

  This correction translates Universal Time (UTC) to a monotonic sequentially time known as International Atomic Time:

  $$\Delta_{convention} = k + 32''.184 \tag{B.2}$$

  where k is the integral number of leap seconds since 1972.

- $\Delta_{location}$

  This correction is made for the position of the observatory. Since the pulsar is much further away from the barycenter than the observatory, the difference in path lengths is simple, and the arrival time is explained as follows,

$$\Delta_{location} = -\frac{\mathbf{s} \cdot \mathbf{r_{bo}}}{c} \tag{B.3}$$

where $\mathbf{s}$ is the unit vector pointing at the pulsar, and $\mathbf{r_{bo}}$ is the vector between the SSB and the observatory. In practice, this is the vector sum of the vector from the SSB to the center of the Sun, the vector from the Sun to the Earth, and the vector from the Earth to observatory. The position vectors from the Earth to Sun are taken from the standard ephemeris known as the Jet Propulsion Laboratory (JPL) ephemeris (Lyne and Smith 1998).

- $\Delta_{Einstein}$

  This correction, the Einstein delay, is relativistic in nature. It depends only on the depth of the potential of the observatory. Therefore, the Einstein delay is included in the JPL ephemeris. There is an additional term that results from the ellipticity of the Earth's orbit of the form $\mathbf{v_E} \cdot \mathbf{r_{bo}}/c^2$. The portion of this term due to the Earth's position is already included in International Atomic Time; we need only to add the part due to the observatory position:

$$\Delta_{Einstein} = \Delta_{Einstein}(JPL) + \frac{\mathbf{v_E} \cdot \mathbf{r_{bo}}}{c^2} \tag{B.4}$$

- $\Delta_{Shapiro}$

  This correction, the Shapiro delay, is also relativistic in nature, which induced by the gravitational potential in the region of the Sun and goes as

$$\Delta_{shapiro} \simeq \frac{2GM_{\odot}}{c^3} \ln(1 + \cos\theta) \tag{B.5}$$

  where θ is the angle between the vector of the observatory to the Sun and the vector from the observatory to the pulsar.

Combining all these corrections, the arrival time in the SSB frame as a function of the measured UTC time.

Bibliography

Aharonian, F. A. et al. (2001). 5@5 - a 5 GeV energy threshold array of imaging atmospheric Cherenkov telescopes at 5 km altitude. *Astroparticle Physics 15*, 335–356.

Asahara, A. et al. (2004). Performance of the 10m Imaging Atmospheric Cherenkov Telescope of CANGAROO. *Nucl. Instrum. Methods Phys. Res., Sect. A submitted*.

Asahara, A. et al. (2003). In *Particle Astrophysics Instrumentation. Edited by Peter W. Gorham. Proceedings of the SPIE, Volume 4858, pp. 347-357 (2003).*, pp. 347–357.

Backer, D. C. et al. (1986). Pulsar timing and general relativity. *Ann. Rev. Astron. Astrophys. 24*, 537–575.

Ball, R. et al. (1993). Unidaq. Technical report, University of Michigan.

Barger, V. D. et al. (1991). *Classical electricity and magnetism.* bai-fu-kan.

Becker, W. et al. (1997). The X-ray luminosity of rotation-powered neutron stars. *Astron. Astrophys. 326*, 682–691.

Beskin, V. et al. (1993). *Physics of the Pulsar Magnetoshere.* Cambridge University Press.

Boezio, M. et al. (1999). The Cosmic-Ray Proton and Helium Spectra between 0.4 and 200 GV. *Astrophys. J. 518*, 457–472.

Boezio, M. et al. (2000). Measurement of the flux of atmospheric muons with the CAPRICE94 apparatus. *Phys. Rev. D 62*, 32007–+.

Carraminana, A. et al. (1995). Pulsars at 1 MeV: The Crab and PSR 1509-58. *Advances in Space Research 15*, 65–.

Catanese, M. et al. (1995). In *Towards a Major Cherenkov Detector–IV*, pp. 335.

CFHT group, . (2004). http://www.cfht.hawaii.edu/Instruments/ObserverManual/chapter5.html.

Cheng, K. S. et al. (1986). Energetic Radiation from Rapidly Spinning Pulsars. II. VELA and Crab. *Astrophys. J. 300*, 522–+.

Cordes, J. M. et al. (1988). JPL pulsar timing observations. V - MACRO and microjumps in the VELA pulsar 0833-45. *Astrophys. J. 330*, 847–869.

Cortina, J. et al. (2001). The cosmic electron background in low energy imaging atmospheric Cherenkov telescopes: effect of the geomagnetic field. *Astroparticle Physics 15*, 203–210.

Cowsik, R. et al. (2002). An introduction to the Indian Astronomical Observatory, Hanle. *Bulletin of the Astronomical Society of India 30*, 105–114.

de Jager, O. C. (2002). Pulsar observations above 1 GeV with future ground-based gamma-ray telescopes. *Bulletin of the Astronomical Society of India 30*, 85–93.

de Jager, O. C. et al. (1989). A poweful test for weak periodic signals with unknown light curve shape in sparse data. *Astron. Astrophys. 221*, 180–190.

de Naurois, M. et al. (2002). Measurement of the Crab Flux above 60 GeV with the CELESTE Cerenkov Telescope. *Astrophys. J. 566*, 343–357.

Downs, G. S. (1982). JPL pulsar timing observations - Spinups in PSR 0525+21. *Astrophys. J. Letters 257*, L67–L70.

Fierro, J. M. et al. (1993). Pulsed high-energy gamma rays from PSR 1055-52. *Astrophys. J. Letters 413*, L27–L30.

Gómez, G. C. et al. (2001). A Reexamination of the Distribution of Galactic Free Electrons. *Astron. J. 122*, 908–920.

Gaisser, T. (1997). *Cosmic Rays an Particle Physics*. Maruzen.

Gehrels, N. et al. (1993). The Compton Gamma Ray Observatory. *Scientific American 269*, C38–+.

Gil, J. A. et al. (1998). On the radio-frequency emission from the Geminga pulsar. *Monthly Notices Roy. Astron. Soc. 298*, 1207–1211.

Goldreich, P. et al. (1969). Pulsar Electrodynamics. *Astrophys. J. 157*, 869–+.

Halpern, J. P. et al. (1992). Discovery of soft X-ray pulsations from the gamma-ray source Geminga. *357*, 222–224.

Hamamatsu Photonics K.K., . (2004). http://www.hpk.co.jp/Eng/main.html.

Harding, A. K. (2001). In *American Institute of Physics Conference Series*, pp. 115–+.

Harding, A. K. et al. (1997). Photon-splitting Cascades in Gamma-Ray Pulsars and the Spectrum of PSR 1509-58. *Astrophys. J. 476*, 246–+.

Heck, D. et al. (1998). Report **FZKA 6019**, Forschungszentrum Karlsruhe; http://www-ik3.fzk.de/˜heck/corsika/physics_description/corsika_phys.html.

Hewish, A. et al. (1968). Observation of a rapidly pulsating radio source. *Nature 217*, 709.

Hillas, A. M. (1982). *J. Phys. G 8*, 1475–1792.

Hillas, A. M. (1985). In *19th Internat. Cosmic Ray Conf., La Jolla*, Volume 3, pp. 445–448.

Hillas, A. M. et al. (1985). In *19th Internat. Cosmic Ray Conf., La Jolla*, Volume 3, pp. 44.

Hillas, A. M. et al. (1998). The Spectrum of TeV Gamma Rays from the Crab Nebula. *Astrophys. J. 503*, 744–+.

Hofmann, W. et al. (2003). In *28th Internat. Cosmic Ray Conf., Tsukuba*, pp. 2811–.

Hoyle, F. et al. (1964). . *Nature 203*, 914–+.

Iye, M. et al. (2000). In *Proc. SPIE Vol. 4008, p. 18-27, Optical and IR Telescope Instrumentation and Detectors, Masanori Iye; Alan F. Moorwood; Eds.*, Volume 4008, pp. 18–27.

Jelley, J. V. (1958). *ČerenkovRadiatioin and its Applications.* Pergamon Press.

Jones, B. (1998). Ph. D. thesis, Stanford University.

Kamae, T. et al. (2000). Studying the High-Energy Gamma-Ray Sky with Glast. *Advances in Space Research 25*, 905–910.

Kanbach, G. (2002). *astro-ph 0209021.*

Kifune, T. et al. (1995). Very high energy gamma rays from PSR 1706-44. *Astrophys. J. Letters 438*, L91–L94.

Komiyama, Y. (2001). private communication. Technical report, SUBARU telescope, NAOJ.

Kubo, H. et al. (2004). In *New Astronomy Reviews*, pp. in press.

Kuiper, L. et al. (2001). The Crab pulsar in the 0.75-30 MeV range as seen by CGRO COMPTEL. A coherent high-energy picture from soft X-rays up to high-energy gamma-rays. *Astron. Astrophys. 378*, 918–935.

Kuiper, L. et al. (1999). COMPTEL detection of pulsed gamma -ray emission from PSR B1509-58 up to at least 10 MeV. *Astron. Astrophys. 351*, 119–132.

Kushida, J. (2003). *Study of the TeV Gamma-Ray Emission Mechanism of PSR 1706–44 Based on the Multi-Wavelength Spectrum.* Ph. D. thesis, Tokyo Tech.

Leahy, D. A. (2003). Hollow-Cone Accretion Columns and Light-bending Effects. *Astrophys. J. 596*, 1131–1136.

Leahy, D. A. et al. (1983). On searches for periodic pulsed emission - The Rayleigh test compared to epoch folding. *Astrophys. J. 272*, 256–258.

Lessard, R. W. et al. (2000). Search for Pulsed TEV Gamma-Ray Emission from the Crab Pulsar. *Astrophys. J. 531*, 942–948.

Linsley, J. (1988). private communication by M. Hillas.

Longair, M. S. (1997). *High Energy Astrophysics.* Cambridge University Press.

Lyne, A. et al. (1998). *Pulsar Astronomy.* Cambridge University Press.

Lyne, A. G. et al. (2002). Jodrell Bank Crab Pulsar Timing Results Monthly Ephemeris. Technical report.

Lyne, A. G. et al. (1988). Crab pulsar timing 1982-87. *Monthly Notices Roy. Astron. Soc. 233*, 667–676.

Manchester, R. N. (2003). pp. in his presentation.

Maraschi, L. et al. (1977). On the gamma-ray source CG 195 plus 4 /Geminga/. *Astron. Astrophys. 61*, L11–L13.

Mardia, K. V. (1972). *Statistics of Directional Data.* London Academic.

Martinez, M. et al. (2003). In *28th Internat. Cosmic Ray Conf., Tsukuba*, pp. 2815–.

Mayer-Hasselwander, H. A. et al. (1994). High-energy gamma radiation from Geminga observed by EGRET. *Astrophys. J. 421*, 276–283.

Moffett, D. A. et al. (1996). Multifrequency Radio Observations of the Crab Pulsar. *Astrophys. J. 468*, 779–+.

Mori, M. (2001). Estimated by m. mori using the data presented by d. thompson et al. at gamma-ray astrophysics 2001 symposium.

NAOJ, . (2001).
http://www.naoj.org/Observing/Telescope/reflect.html.

Nolan, P. L. et al. (1993). Observations of the Crab pulsar and nebula by the EGRET telescope on the Compton Gamma-Ray Observatory. *Astrophys. J. 409*, 697–704.

Oda, M. et al. (1989). *Cosmic Ray Astrophysics.* Asakura.

Ong, R. A. (1998). Very high-energy gamma-ray astronomy. *Physics Report 305*, 93–202.

Oser, S. et al. (2001). High-Energy Gamma-Ray Observations of the Crab Nebula and Pulsar with the Solar Tower Atmospheric Cerenkov Effect Experiment. *Astrophys. J. 547*, 949–958.

Pacini, F. et al. (1967). . *Nature 216*, 567–+.

Ramanamurthy, P. V. et al. (1995). EGRET Detection of Pulsed Gamma Radiation from PSR B1951+32. *Astrophys. J. Letters 447*, L109+.

Ruderman, M. A. (1989). In *The EGRET symposium, Greenbelt, NASA Conf.*, Volume No.3071.

Ruderman, M. A. et al. (1975). Theory of pulsars - Polar caps, sparks, and coherent microwave radiation. *Astrophys. J. 196*, 51–72.

Schönfelder, V. et al. (2000). The first COMPTEL source catalogue. *Astron. Astrophys. Suppl. 143*, 145–179.

Seward, F. D. et al. (1982). A new, fast X-ray pulsar in the supernova remnant MSH 15-52. *Astrophys. J. Letters 256*, L45–L47.

Shapiro, S. L. et al. (1983). *Black Holes, White Dwarfs, and Netron Stars.* A Wiley-Interscience Publication.

Shearer, A. et al. (1998). Possible pulsed optical emission from Geminga. *Astron. Astrophys. 335*, L21–L24.

Shemar, S. L. et al. (1996). *MNRAS 282*, 667.

Sokolsky, P. (1989). *Introduction to ultrahigh energy cosmic ray physics.* Addison-Wesley.

Stella, L. et al. (2001). Xronos: http://xronos.gsfc.nasa.gov/.

Sturrock, P. A. (1971). A Model of Pulsars. *Astrophys. J. 164*, 529–+.

Sunagawa, S. (1964). *Rirondenzikigaku (in Japanese).* kinokuniya.

Swanenburg, B. N. et al. (1981). Second COS B catalog of high-energy gamma-ray sources. *Astrophys. J. Letters 243*, L69–L73.

Tanimori, T. et al. (1995). In *Towards a Major Cherenkov Detector–IV*, pp. 316.

Taylor, J. H. et al. (1989). *Astrophys. J. 345*, 434–450.

Thompson, B. J. et al. (1999). SOHO/EIT Observations of the 1997 April 7 Coronal Transient: Possible Evidence of Coronal Moreton Waves. *Astrophys. J. Letters 517*, L151–L154.

Thompson, D. J. (2004). In *Young Neutron Stars and Their Environments, IAU Symposium.*, Volume 218.

Thompson, D. J. et al. (1992). Pulsed high-energy gamma-rays from the radio pulsar PSR1706-44. *359*, 615–+.

Torii, S. et al. (2001). The Energy Spectrum of Cosmic-Ray Electrons from 10 to 100 GeV Observed with a Highly Granulated Imaging Calorimeter. *Astrophys. J. 559*, 973–984.

Trimble, V. (1968). Motions and Structure of the Filamentary Envelope of the Crab Nebula. *Astron. J. 73*, 535–+.

V., R. M. P. et al. (1986). *Gamma-ray astronomy*. Cambridge University Press.

Wakely, S. P. et al. (2003). In *28th Internat. Cosmic Ray Conf., Tsukuba*, pp. 2803–.

Watson, G. S. (1961). *Biometrika 48*, 109.

Weber, J. (1960). *Phys. Rev. 117*, 306.

Weekes, T. C. (1988). *Phys. Rep. 160*, 1.

Wolszczan, A. et al. (1989). A 110-ms pulsar, with negative period derivative, in the globular cluster M15. *Nature 337*, 531–533.

Woltjer, L. (1968). The Nature of Pulsating Radio Sources. *Astrophys. J. Letters 152*, L179+.

Yoshikoshi, T. (1996). Ph. D. thesis, Tokyo Institute of Technology.